ISBN 978-82-326-3610-5 (printed version)
ISBN 978-82-326-3611-2 (electronic version)
ISSN 1503-8181

NTNU
Norwegian University of
Science and Technology

Jan-Tore Horn

Doctoral Thesis

Doctoral theses at NTNU, 2018:409

NTNU
Norwegian University of
Science and Technology
Faculty of Engineering
Department of MarineTechnology

NTNU

Doctoral theses at NTNU, 2018:409

Jan-Tore Horn

Statistical and Modelling Uncertainties in the Design of Offshore Wind Turbines

NTNU
Norwegian University of
Science and Technology

Jan-Tore Horn

Statistical and Modelling Uncertainties in the Design of Offshore Wind Turbines

Thesis for the degree of Philosophiae Doctor

Trondheim, December 2018

Norwegian University of Science and Technology
Faculty of Engineering
Department of MarineTechnology

NTNU
Norwegian University of
Science and Technology

NTNU
Norwegian University of Science and Technology

Thesis for the degree of Philosophiae Doctor

Faculty of Engineering
Department of MarineTechnology

ISBN 978-82-326-3610-5 (printed version)
ISBN 978-82-326-3611-2 (electronic version)
ISSN 1503-8181

Doctoral theses at NTNU, 2018:409

MILJØMERKET 241 TRYKKSAK 731
Printed by Skipnes Kommunikasjon as

Abstract

This thesis aims to contribute to lowering the cost of offshore wind energy by minimizing design conservatism. By increased confidence in the structural design, the total cost of energy can be reduced through less material consumption or extending the operational lifetime. Both model- and statistical uncertainties in the design of offshore wind turbines have been systematically addressed in this thesis to evaluate the potential design conservatism. Two major research objectives (RO) have been formulated:

RO1 Assessment of environmental load effects and their impact on the reliability of a monopile-mounted offshore wind turbine

RO2 Develop methodologies to reduce excessive design conservatism by means of high-fidelity models and time-domain simulations in a probabilistic analysis framework

To date, all commercial offshore wind farms are bottom-fixed, and the monopile foundation is currently the most cost-effective design at shallow to intermediate water depths. Hence, the case studies in this thesis are based on the next-generation monopile-mounted offshore wind turbines with a rated capacity of 10 MW. Numerical, fully coupled, aero-servo-hydro-elastic simulations and statistical analysis have been the main methodologies in this thesis.

As future wind farms are being planned in deeper water far from shore, the impact from wave loads on the final design of the sub-structure is increasing. Hence, more accurate methods are needed to capture important load and response phenomena, such as wave diffraction and ringing. It has been observed that new and improved methods may lead to both lower and higher characteristic response values to be used in the design phase. In this thesis, the model-specific hydrodynamic load effect uncertainties have been identified and their impact on the partial safety factors are discussed and exemplified.

An improved probabilistic description of the ocean environment is proposed. The joint probability distribution includes state-of-the-art models for wind speed and wind sea, and is extended to include their respective directions, separation of swell, and astronomical tide. For offshore wind turbines, directional descriptions are important due to the large aerodynamic damping induced by the rotor in the fore-aft direction. The impact of directional models on the foundation fatigue and structural reliability have been investigated. It has been shown that separation of wind sea and swell reduces the foundation fatigue damage.

An engineering problem will often consist of model uncertainties, which may be improved by research, and statistical uncertainties that can only be handled by gathering more data and performing more simulations. It has been shown in the present work that both short- and long-term statistical uncertainties can be reduced by smart simulation techniques, efficient use of computational resources and structural reliability analysis.

Acknowledgements

I would like to thank my supervisors, Prof. Jørgen Amdahl, Prof. II Jørgen R. Krokstad and Prof. Asgeir J. Sørensen at the Department of Marine Technology and Centre for Autonomous Marine Operations and Systems (NTNU AMOS). They have continuously asked critical questions to improve my work and develop myself as a researcher. Also, they have been very positive to my cross-disciplinary work and collaborations with researchers at DTU and DNV GL.

Further, I would like to thank others at NTNU for feedback and good discussion. Prof. Bernt J. Leira has been helpful in matters of structural safety analysis and is a frequent co-author in my papers. Also, Zhen Gao and Erin E. Bachynski at the department have provided feedback on several occasions.

Next, I would like to thank Prof. Emeritus Jørgen Juncher Jensen at DTU for interesting discussions and collaboration on one of my conference papers. I also stayed at DTU for several weeks by invitation from Ass. Prof. Henrik Bredmose to collaborate on his novel wave load model. I really enjoyed my weeks at DTU, and thank you to the PhDs and Post Docs there for welcoming me so warmly. Unfortunately, there was not time to finish a paper on the work together with Henrik to be included in this thesis.

I would like to express my gratitude to Olav Rognebakke at DNV GL for providing me with a desk during my frequent stays in Oslo. At DNV GL, I need to thank one of my co-authors Elzbieta M. Bitner-Gregersen, and Torfinn Hørte for rewarding conversations in matters of environmental models, structural reliability, and their efforts in providing me with a Proban license.

Furthermore, I would like to thank Steven R. Winterstein for his co-authorship and rewarding discussions. Finally, Tore Holmås has been very helpful and responsive to my requirements regarding the time-domain simulation tool *vpOne*, which needed some modifications to handle external controllers, arbitrary load input and distributed computing.

A special thanks goes to my classmates and friends from the first day at Tyholt and throughout the PhD period; my roomie Jan Vidar Ulveseter, Carl Fredrik Rehn, Emil Smilden, Pal Takle Bore, Ole Alexander Eidsvik, Øyvind Øksnes Dalheim, John Martin Kleven Godø and Henrik Schmidt. I also wish to thank my significant other Elise for her moral support and unshakeable believe in my doings.

List of Papers

This thesis consists of an introductory part and a collection of seven papers as follows:

Paper I:

Jan-Tore Horn, Jørgen R. Krokstad, and Jørgen Amdahl, 2016. Hydro-Elastic Contributions to Fatigue Damage on a Large Monopile. *Energy Procedia.*

Paper II:

Jan-Tore Horn and Jørgen Juncher Jensen, 2016. Reducing uncertainty of Monte Carlo estimated fatigue damage in offshore wind turbines using FORM. In: *Proceedings of the 13th International Symposium on Practical Design of Ships and Other Floating Structures (PRADS).*

Paper III:

Jan-Tore Horn, Jørgen R. Krokstad, and Jørgen Amdahl, 2018. Long-Term Fatigue Damage Sensitivity to Wave Directionality in Extra Large Monopile Foundations. *Journal of Engineering for the Maritime Environment.*

Paper IV:

Jan-Tore Horn et al., 2018. A new combination of conditional environmental distributions. *Applied Ocean Research.*

Paper V:

Jan-Tore Horn and Steven R. Winterstein, 2018. Extreme response estimation of offshore wind turbines with an extended contour-line method. *Journal of Physics: Conference Series.*

Paper VI:

Jan-Tore Horn and Bernt J. Leira, 2018. Fatigue reliability assessment of offshore wind turbines with stochastic availability. *Accepted to: Reliability Engineering & System Safety.*

Paper VII:

Jan-Tore Horn, Jørgen R. Krokstad, and Bernt J. Leira, 2018. Impact of model uncertainties on the fatigue reliability of offshore wind turbines. *Marine Structures.*

The following two conference papers were also written in relation to the PhD work. Paper C1 is excluded due to scope and Paper C4 is excluded due to overlap with Paper IV.

Paper C1:

Jan-Tore Horn, Jørgen Amdahl, and Sverre K. Haver, 2015. Dynamic Amplification of Drag Dominated Structures in Irregular Seas. In: *Proceedings of OCEANS'15 MTS/IEEE Washington Conference & Exhibition.*

Paper C4:

Jan-Tore Horn, Jørgen R. Krokstad, and Jørgen Amdahl, 2017. Joint probability distribution of environmental conditions for design of offshore wind turbines. In: *Proceedings of the International Conference on Offshore Mechanics and Arctic Engineering - OMAE.*

The following two journal papers representing underlying studies were written in cooperation with Emil Smilden and Stian Høegh Sørum, respectively:

Paper C2:

Emil Smilden et al., 2016. Reduced Order Model for Control Applications in Offshore Wind Turbines. In: *The 10th IFAC Conference on Control Applications in Marine Systems (CAMS).*

Paper J2:

Stian H. Sørum, Jan-Tore Horn, and Jørgen Amdahl, 2017. Comparison of numerical response predictions for a bottom-fixed offshore wind turbine. *Energy Procedia.*

Contents

Appended papers . . .

1 | Introduction

This chapter gives an overview of the motivation and objectives for this doctoral thesis. Furthermore, the papers that form the basis of this thesis are presented.

1.1 Motivation

Harnessing wind power has long traditions, from the first known practical plant from the 7th century in the middle east, to the modern, electricity-producing wind turbine. At first, wind mills where used for mechanical loads, such as pumping water and grinding grain. Today, the wind energy is mainly used for electricity production, and has gained increased attention in light of climate change and limiting the emissions of greenhouse gases. In 2017, Denmark produced enough energy from their wind turbines, onshore and offshore, to cover 44% of the energy consumption [`danskenergi.dk`]. At the time of writing, China is producing 5 times more energy from wind than Norway is consuming, on average. The future seems bright for the wind energy industry which, in combination with solar panels, will be an important part of the energy mixture. To utilize the full potential for wind energy, the industry is moving offshore, where there is an abundance of areas with less visual and environmental impact from the installation. Furthermore, offshore wind conditions will provide stronger and less turbulent wind, which will make power production more economically feasible.

In Europe, more than 600 offshore wind turbines were erected in 2017 (WindEurope 2017), which is enough to provide energy to approximately 650 000 average Norwegian households, or approximately 13 TWh yearly. The installed capacity continues to increase, and so do the turbine size, average water depth, and distance from shore. Measures to reduce the cost of energy from offshore wind relies heavily on research and engineering. Increased knowledge is a key component to reduce the risks involved when installing and operating wind farms far from shore in harsh conditions. The current boom in offshore wind is the result of many years of research on bottom-fixed offshore wind turbines, and the cost-efficient design of the monopile substructure is still dominant. Hence, a next-generation large wind turbine mounted on a monopile is chosen for the cases studied in this thesis. The year 2017 also saw the installation of the first floating offshore wind farm, Hywind Scotand, leading the way for these concepts. In other words, this thesis aims to contribute to the relatively new offshore wind energy industry which is growing fast and is an area where Norway can contribute with substantial knowledge from the oil and gas industry.

1.2 Research context and sponsor

This work has been carried out at the Centre for Autonomous Marine Operations and Systems (NTNU AMOS) and Project 3: Risk management and maximized operability of ships and ocean structures. The Norwegian Research Council is acknowledged as the main sponsor of NTNU AMOS. This work was supported by the Research Council of Norway through the Centres of Excellence funding scheme, Project number 223254.

1.3 Research objectives

The role of academic researchers in the field of wind energy has been partly to develop theory and methods to allow for safe and efficient construction, installation and operation. New models for wave loading is of special interest when the waves become a design driver due to deeper waters, exposed areas and larger substructures. One objective of this thesis is to adapt these wave load theories into probabilistic design of offshore wind turbines. The first research objective is formulated as:

- RO1: Assessment of environmental load effects and their impact on the reliability of a monopile-mounted offshore wind turbine

A significant background knowledge of existing load theories and their statistics is required to fulfil this research objective. Here, the focus will be on wave loads and the long-term statistics of environmental parameters such as; wind speed, significant wave height, wave peak period, directions, and swell.

Once the systematic uncertainties related to engineering models for loads and environment are quantified, they can be included in a probabilistic design procedure to determine the corresponding partial safety factors. What remains then are statistical, or aleatory, uncertainties, related to the stochastic nature of physical wind and wave processes and their underlying long-term statistics. These are uncertainties that are often handled by partial safety factors but can also be mitigated by increasing the amount of data from e.g. time-domain simulations, or by using reliability-based methods. A second research objective is formulated as:

- RO2: Develop methodologies to reduce excessive design conservatism by means of high-fidelity models and time-domain simulations in a probabilistic analysis framework

In relation to RO2, methods to avoid the use of overly conservative characteristic values are explored. For instance, how to treat the two main states of an offshore wind turbine, operational and idling, in a consistent manner with respect to the failure probability. The research objectives formulated above will be discussed by means of numerical experiments in this thesis, which are presented in the appended papers and Chapter 3. A summary of the specific contributions and their relation to the research objectives are given in the conclusions and discussions in Chapter 5.

1.4 Publications

The papers that form the basis of this thesis, and additional papers for professional development and background knowledge are shown in Fig. 1.1. Other scientific papers are also shown in the figure to show their relations. Papers that are appended in this thesis are clearly marked with Paper I etc. and sorted thematically. The knowledge domains that are relevant for this thesis in terms contributions are; offshore environment, hydrodynamics, structural reliability and wind turbine control. Some papers deal purely with e.g. hydrodynamics or environmental modelling, while other combine several fields in probabilistic analysis, especially the two last papers (Paper VI and VII). Other important areas like structural analysis and aerodynamics are also important fields of knowledge for design of offshore wind turbines and are pre-requisites for performing the integrated analysis.

Publications are marked according to their status as journal paper (J), conference article (C) or poster (P). In Tab. 1.1, publications associated with conferences are listed, while journal papers are listed in Tab. 1.2.

Table 1.1: Published conference publications

Name	Year	Location	Presentation	Publication
OCEANS	2015	Washington DC	Oral	C1
EERA DeepWind	2016	Trondheim	Oral	J1
CAMS	2016	Trondheim	-	C2
PRADS	2016	Copenhagen	Oral	C3
EERA DeepWind	2017	Trondheim	Poster	P1
OMAE	2017	Trondheim	Oral	C4
EERA DeepWind	2018	Trondheim	Poster	J5

Table 1.2: Journal publications

Name	Year	Publication	Status
Energy Procedia	2016	J1	Published
Energy Procedia	2017	J2	Published
JEME*	2017	J3	Published
Applied Ocean Research	2018	J4	Published
Journal of Physics: Conference Series	2018	J5	Published
Reliability Engineering & System Safety	2018	J6	Accepted
Marine Structures	2018	J7	Published

* Proceedings of the Institution of Mechanical Engineers, Part M: Journal of Engineering for the Maritime Environment - Special Issue on Marine Renewable Energy

1.4.1 Declaration of authorship and relevance to this thesis

Below, a short description of the relevance of each paper is given, including main contributions and declaration of authorship.

Paper I An initial study regarding the effect of multiple wave load models on the characteristic fatigue of an offshore wind turbine foundations was conducted. The paper is a continuation of my Master's thesis. My co-supervisor Jørgen R. Krokstad has provided useful insight, but all calculations are performed by myself using a simple wind turbine model in *vpOne*. The paper has given useful answers to the questions regarding importance of consistent wave modelling on fatigue estimation which is an important part of **RO1**.

Paper II A co-operation with Jørgen J. Jensen at DTU was initiated in relation to a PhD course regarding structural reliability. A hypothesis was made that the statistical uncertainty of fatigue damage introduced by wave loads can be reduced using a reliability-based approach. Professor Jensen contributed with the basic idea, which was further developed by myself, and implemented on the same model as used in Paper I. It was shown that by combining Monte Carlo simulations and FORM, critical wave realizations for fatigue damage can be found faster and potentially reduce the computational time and result uncertainty, which is in line with **RO2**.

Paper III In this journal paper, the effect on fatigue damage from wind sea and swell separation was investigated. The paper contributes to **RO2** in terms of reduced conservatism while maintaining the same level of reliability. I performed all time-domain simulations and writing, with input from my supervisors, Krokstad and Amdahl.

Paper IV In Paper IV, a collaboration with Bitner-Gregersen at DNV GL was initiated from my side. She has many publications on the subject of probabilistic environmental models and associated uncertainties. The paper significantly expands on Paper C4 (Horn, Krokstad, and Amdahl 2017) by including absolute directions and swell. After many iterations I suggested an environmental model, which was approved by my co-authors. The model has been used extensively in all investigations during the course of this thesis, and has been important for both **RO1** and **RO2**. A version of the associated program will be made available on GitHub.

Paper V I met Steven R. Winterstein at DNV GL where he presented a method to use the *contour-line* method for different directional sectors, or sub-populations. We agreed to initiate a collaboration to examine the operational and idling state of an offshore wind turbine with this new approach in order to obtain a consistent 50-year extreme value. The work relates to **RO2** in terms of reducing the uncertainty related to the long-term extreme values when only one operational state is assumed to be dominating. I made all calculations and simulations and had invaluable discussions with Steve.

Paper VI This paper is inspired by Paper V, but focuses on fatigue in the foundation. It is proposed to treat the operational states of the turbine separately in a reliability analysis, which opens for the use of a stochastic availability parameter. Hence, conservatism can be reduced by replacing a conservative characteristic downtime percentage with a Beta-distributed variable. This paper is one of the main contributors to **RO2**, and was developed solely by myself, but with useful discussions with Prof. Bernt J. Leira.

Paper VII The purpose of the final paper was to wrap up any loose ends by showing the combined impact of previous works during probabilistic design of an offshore wind turbine. Here, load models from Paper I, environmental model from Paper IV and sub-populations from Paper V/VI are used to demonstrate the relative impact on the case-specific partial safety factors. It is an attempt to combine **RO1** and **RO2** to make the PhD thesis complete. The development of necessary models and extensive time-domain simulations were performed by me, with Jørgen Krokstad providing critical questions in order to make the topic relevant for future guidelines, and with support from Prof. Leira on matters of structural reliability.

In summary, the work on the above papers have been very rewarding and provided interesting results. Most of all, I found the discussions with other researchers and professors both educational and inspiring. The papers span over a wide range of topics related to structural design of offshore wind turbines, but they all have the same overall purpose and goal, founded in the presented research objectives. An overview of how the different papers relates to the research questions can be found in Fig. 1.2.

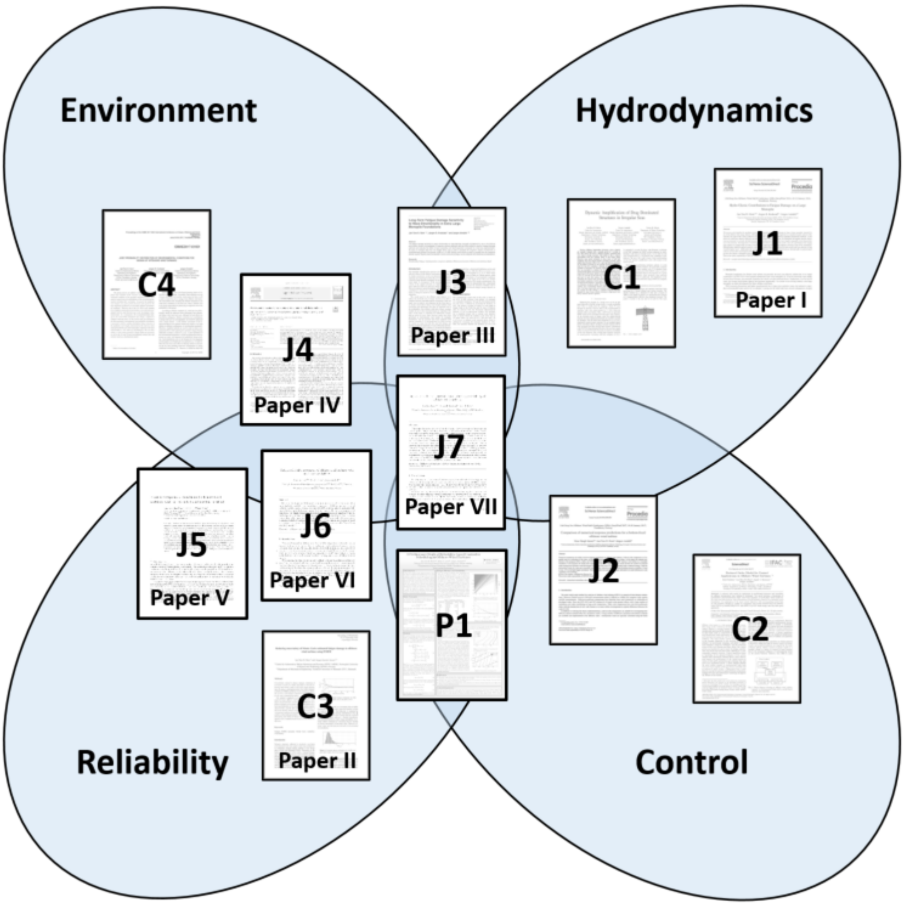

Figure 1.1: Thematic overview of publications; appended papers and additional publications.

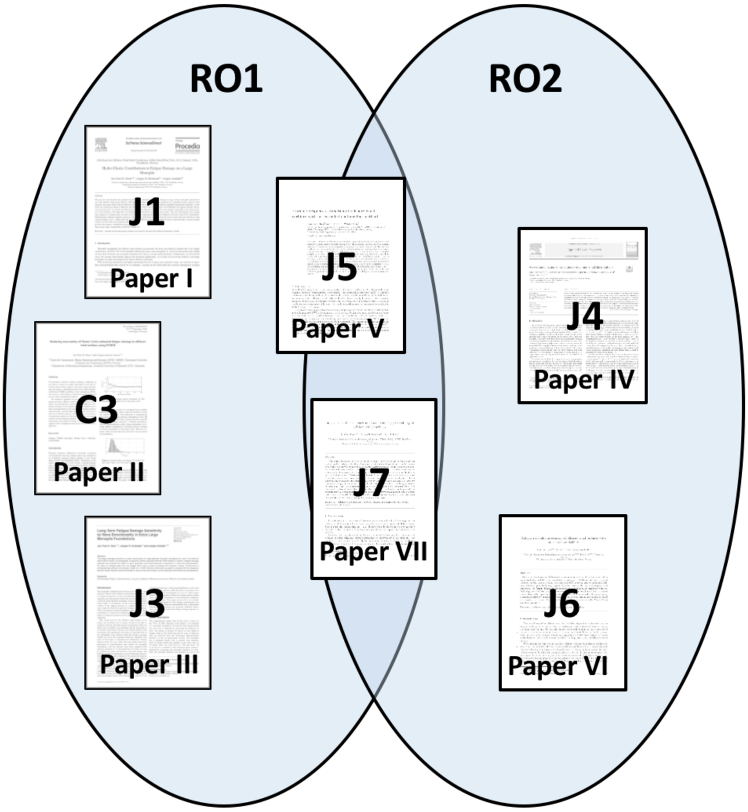

Figure 1.2: Graphical representation of the relation between research objectives (ROs) and appended papers.

2 | Background

An overview of the current status of offshore wind energy industry and design requirements is given in this chapter. First, the reader is introduced to the most important considerations when designing an offshore wind turbine. Secondly, areas allowing for increased competitiveness of offshore wind energy are presented, and how research and development can contribute are discussed.

2.1 Offshore wind energy

The offshore wind industry continues to expand and has currently a total of 16 GW installed capacity (WindEurope 2017), mainly in the North Sea. In Fig. 2.1, the locations of operational, consented, planned and wind farms under construction are illustrated. From the figure, one can see that current wind farms are located in shallow water close to shore. However, a significant number of consented farms are located further from shore, in a harsher environment. In this thesis, the location of interest is Dogger Bank, which is located to the north west in Fig. 2.1. More information on the assessment of Dogger Bank as a suitable location for offshore wind farms can be found in e.g. Forewind (2010).

To date, the by far most popular and cost-effective foundation for offshore wind turbines have been the monopile, illustrated in Fig. 2.2. Its simplicity during construction, consisting of only one cylindrical pile and transition piece has been more important than the material usage. However, it is expected that the monopile will not be feasible in water deeper than approximately 40 meters. The jacket type foundation consumes less steel but is more expensive to produce. For waters deeper than 50-60 meters, floating wind turbines is expected to be most cost efficient. To date, there are only a few prototypes of floating wind turbines in operation, in addition to the Hywind pilot park outside Scotland consisting of five spar-type platforms.

2.2 Design principles of offshore wind turbines

This section will briefly explain the requirements and common practice regarding structural design of offshore wind turbines.

2.2.1 Design criteria

In general, an offshore wind turbine shall be designed to (DNV GL 2014):

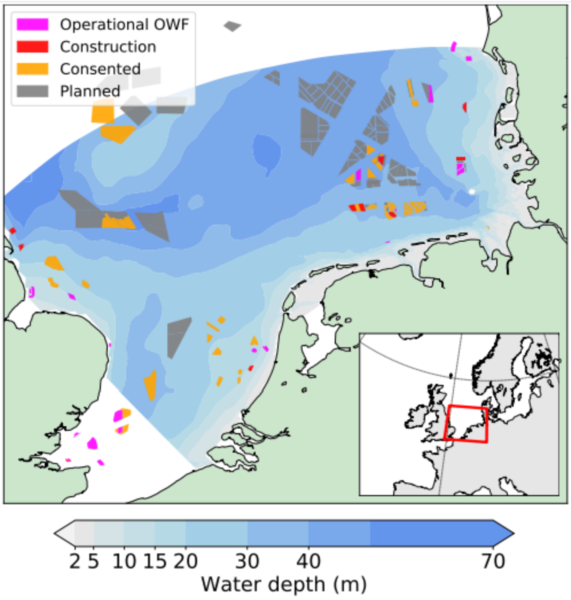

Figure 2.1: Offshore wind farms in the North Sea, from Slavik et al. 2017.

- Sustain all occurring loads
- Ensure acceptable structural safety during design life
- Maintain acceptable safety for personnel and environment
- Resist deterioration during design life

Even though offshore wind turbines are unmanned, there is still some risk of personnel injuries, pollution and economical losses if a component should fail. Hence, an offshore wind turbine structure is categorized according to the *normal* safety class (DNV GL 2014), implying that an annual failure probability of less than 10^{-4} (International Electrotechnical Commission 2009) shall be maintained during the design lifetime. The target safety level is

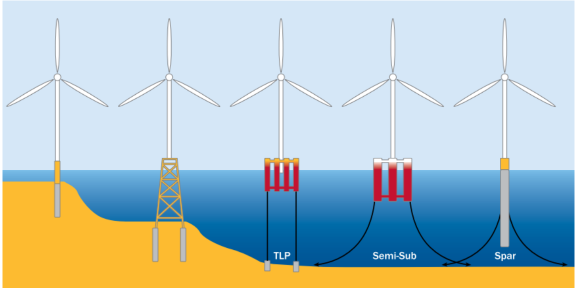

Figure 2.2: Examples of offshore wind turbine foundations, taken from EWEA (2013). From left to right: monopile, jacket, tension-leg platform (TLP), semi-submersible and spar-type.

meant to cover the entire structure but is in practice used for each individual failure mode, or for the weakest link in a series system. In the thesis work, two different approaches to reach a satisfactory safety level will be considered:

- design by partial safety factors with direct simulation of combined load effects,

and

- probability-based design.

The first approach is by far the most commonly used, but probability-based design might be necessary for completely new systems or to calibrate the partial safety factors. Later it will be discussed how probability-based methods are used throughout the papers.

In the work associated with this thesis, fully coupled, non-linear time-domain simulations using a finite element method (FEM) is the main method for load effect evaluations. Guidelines for which load effects to consider are given in International Electrotechnical Commission (2009) and DNV GL (2016a), representing different failure modes and limit states. A limit state is a condition where the structure is no longer satisfying the target safety level. Standards for offshore wind turbines consider four limit states:

Fatigue limit state	(FLS)	- material failure due to cyclic loading,
Ultimate limit state	(ULS)	- exceedence of the structural resistance,
Serviceability limit state	(SLS)	- a tolerance criteria is superceeded, or
Accidental limit state	(ALS)	- failure due to accidental/rare loads.

Next, design methods for FLS and SLS are discussed as they are most relevant for the scope of this thesis.

2.2.2 Fatigue limit state (FLS)

For extra-large, monopile-mounted offshore wind turbines, fatigue is expected to be the dominating failure mode. Hence, focus is placed on FLS. It is limited to the monopile foundation itself, which is significantly affected by both wind and wave loads. When a design check using partial safety factors is performed, the following requirement must be satisfied:

$$D_d \leq 1.0 \tag{2.1}$$

where $D_d = D_c \cdot DFF$ is the design fatigue utilization for the lifetime of the structure. D_c is the characteristic fatigue damage, calculated using the characteristic SN-curve (DNV GL 2005) and other characteristic values ensuring a conservative estimate of D_c. Finally, a *design fatigue factor* (DFF), which is pre-calibrated and given in the design standards (DNV GL 2016a; International Electrotechnical Commission 2009), is added to guarantee the minimum safety level. For the foundation below seabed, where no inspection to detect fatigue cracks is possible, a DFF of 3.0 should be applied according to e.g. DNV GL (2005) and DNV GL (2016b).

The above procedure is used before the construction phase to ensure sufficient structural capacity. However, the environmental loads and dynamic properties that the wind turbine is experiencing may differ significantly from what was used in the design phase. Most of these uncertainties are taken care of by the DFF, assuming that a reasonable design approach was performed. A part of the scope of this thesis, is to include these uncertainties in a less conservative manner through a design procedure. As a consequence, a probability-based design procedure is required, which should comply with the following requirement:

$$P[D > \Delta] \leq 10^{-4} \tag{2.2}$$

where D is the total fatigue damage, often assumed to be Weibull distributed, and Δ is the fatigue capacity of the structure, usually Lognormally distributed with an expected value of 1.0 (DNV GL 2015). This approach opens for using probability distributions of the random variables instead of their respective characteristic values, as demonstrated in Paper V for turbine availability.

Since fatigue damage is a cumulative measure, inspections are required throughout the lifetime to reduce the risk of failure due to crack propagation. Several schemes for inspection planning and structural monitoring have been proposed to keep track of the safety level (see e.g. Nielsen and Sørensen (2011), Florian and Sørensen (2017), and Martinez-Luengo, Kolios, and Wang (2016)). For the submerged foundation however, one can only rely on monitoring and continuous information about the response. Figure 2.3 illustrates how the principal of material degradation leads to a reduced capacity as was predicted in the design analysis, while a monitoring scheme may reduce the uncertainty related to the time-varying capacity.

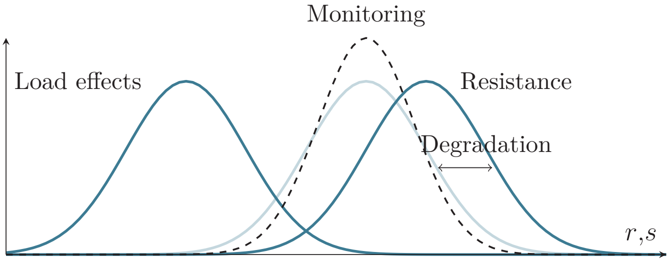

Figure 2.3: Structural load effect (s) and resistance (r) distributions. No monitoring bias is assumed.

2.2.3 Serviceability limit state (SLS)

While ULS considers complete or partial loss of structural resistance, like yielding, buckling or capsizing, SLS sets of limits to deflections, vibrations etc. to maintain a state where the turbine can operate efficiently (DNV GL 2014). A review of these requirements can be found in e.g. Arany et al. (2015). Paper IV addresses the SLS for maximum allowable acceleration of the nacelle, and the pile translation due to bending moment from wind and waves. Typical requirements are an acceleration less than $0.5g$ in the nacelle and a horizontal translation of less than 0.2 meters at the seabed for bottom-fixed structures. The requirement in SLS can be formulated as:

$$R/\gamma_m \geq \gamma_s \cdot S_c \tag{2.3}$$

where R is the SLS requirement, S_c is the characteristic value of the load effect, and γ_s and γ_m are the partial safety factors for the load effect and material factor, respectively. In Paper V, it is investigated whether the 50-year characteristic load effect corresponding to S_c can be found by an extended contour-line method (Winterstein et al. 1993) for offshore wind turbines, where both the power-producing and idling states are included.

2.3 Reducing the cost of energy

The development of an offshore wind farm is a capital-intensive project, with high initial investment costs related to construction, installation and infrastructure. A typical cost breakdown for a single offshore turbine is shown in Fig. 2.4. As indicated in Gonzalez-Rodriguez (2017), there are significant variations between different farms. There is still a large potential for cost reduction by optimization of the foundation and the structure, and improved methods for installation.

The operation and maintenance costs (OPEX) are also a significant contributor to the total cost of energy (CoE). An overview of some types of operational costs can be found in e.g. GL Garrad Hassan (2013), which is also included in an overview of OPEX reports in Crabtree, Zappalá, and Hogg (2015). It is found that the OPEX can contribute to 40% of the total life cycle costs of an offshore wind farm. The OPEX fraction is smaller compared to traditional oil and gas structures. This is mainly due to the absence of fuel costs, as the wind energy in itself is still free, if it can be captured. Still, a significant reduction in the total CoE can be achieved by managing the operation and maintenance schedules (see e.g. Sarker and Faiz (2016) and Nielsen and Sørensen (2011)).

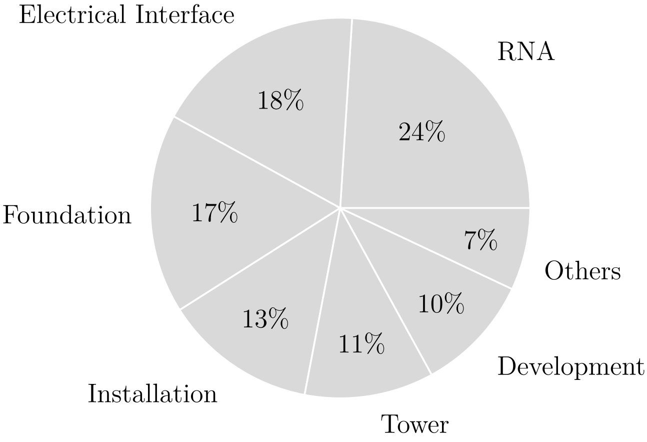

Figure 2.4: Typical capital cost breakdown for offshore wind turbines

Reducing the CAPEX and/or OPEX is one way to reduce the CoE of offshore wind farms. Another approach is to maximize the total energy production, either by achieving a higher capacity factor (Abed and El-Mallah 1997), or increasing the operational lifetime (Ziegler et al. 2018). The latter option is compared to a CAPEX-reducing approach by structural reliability analysis in Horn, Leira, and Amdahl (2017) as a preliminary study for this thesis. It was concluded that a lifetime extension using reliability-based methods has more potential for cost savings than incremental reductions of the CAPEX.

For the offshore wind industry to thrive, the cost of energy must be lower than the energy supplied from fossil-fueled plants, for instance coal-fired plants. According to The Crown Estate (2012), the key opportunities for cost reductions related to the supply chain and technology development can be summarized as follows:

- New turbines with higher reliability and energy capture, and lower operating costs
- Increased competition in supply markets
- Improved Front End Engineering Design (FEED) and extensive site surveys
- Economies of scale and productivity improvements
- Optimization of installation methods
- Mass production of support structures for water depths larger than 35 meters

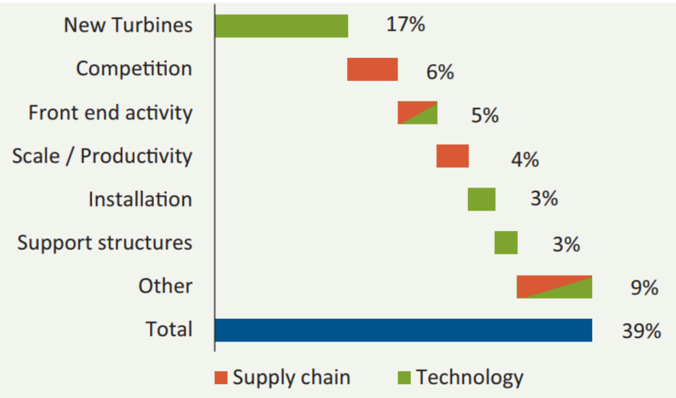

Figure 2.5: Cost reductions as predicted by the Crown Estate (The Crown Estate 2012)

with a graphical representation in Fig. 2.5. As expected, a significant part of cost reduction is obtained through engineering and technology development. In the area of marine engineering, extensive knowledge related to structural reliability and modelling of the external environment are important contributions to the overall cost reduction. This thesis contributes indirectly to cost reduction through new turbine technology with the potential for higher reliability and improved engineering methods for design of support structures.

3 | Software

An overview of relevant software and the work flow for large-scale time-domain simulations of offshore wind turbines is briefly presented in this chapter.

3.1 Software for integrated analysis

Verification of offshore wind turbines according to the limit states design format requires simulations of combined load effects. Such analysis include interaction between hydrodynamic and aerodynamic loads, as well as the wind turbine controller. It is stated in DNV GL (2016b) that "the linear combination model of the partial safety factor method may be inadequate in cases where the load effect associated with one of the applied load processes depends on structural properties which are sensitive to the characteristics of one or more of the other load processes."

For bottom-fixed wind turbine structures, the soil interaction is also important for the dynamic response. In order to capture non-linear load effects from waves and the impact of aerodynamic damping induced by the rotor an control system, time domain simulations have been carried out in this work. Methods based on frequency domain analysis have proven efficient for fatigue analysis in an early stage of the design process with sufficient accuracy (Schløer et al. 2018).

Details regarding aerodynamic modelling using the *blade element momentum* (BEM) theory will not be presented here, the reader is referred to Hansen (2013). For further insight into the dynamics of a wind turbine rotor, Hansen (2016) gives good insight into how the modal properties changes with rotational velocity and wind speed. Also, details regarding FEM modelling of the blade sections can be found in e.g. Hansen et al. (2006). The remaining part of this section will present the software used in the coupled, dynamic time-domain simulations.

A substantial amount of code has been written in relation with this thesis. The purpose has mostly been to improve workflow and software couplings. For a time-domain simulation given a set of input variables, the workflow is illustrated in Fig. 3.2. First, all necessary pre-processing is performed before the coupled time-domain simulation is performed. The pre-processing includes; generation of wave kinematics using *WaveSim*, wind field generation using *TurbSim* (Kelley and Jonkman 2007), and automatic creation of a wind turbine model based on the 10MW reference wind turbine by DTU (Bak et al. 2013) which is presented later.

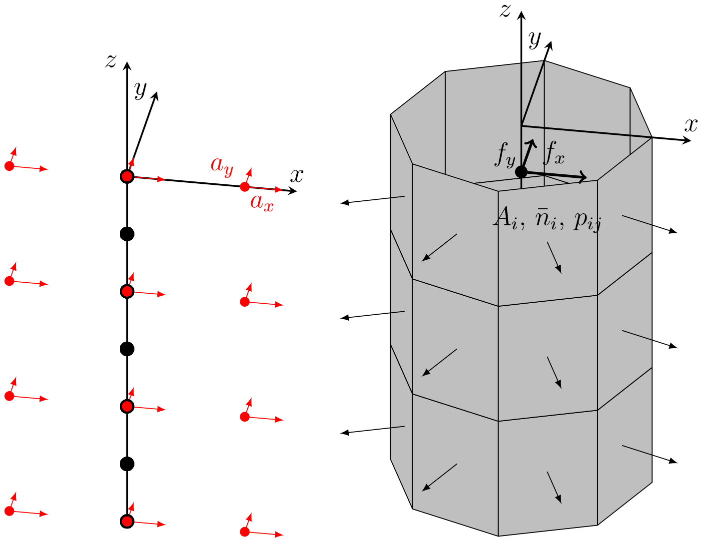

(a) Wave kinematics grid and structural nodes **(b)** Mapping of panel pressures from WAMIT to nodal forces

Figure 3.1: Mapping of wave loads to beam elements and nodes using a Morison type formulation with incident kinematics (a) or nodal loads from integration of panel pressures (b).

3.1.1 WaveSim

WaveSim is Matlab and Octave compatible, and was developed during the early stages of this thesis. *WaveSim* is a tool for the generation of incident wave kinematics for pre-defined spatial coordinates. To compensate for fluid-structure interaction it allows for the MacCamy & Fuchs correction on the linear components and mapping of forces computed by the panel-code WAMIT (WAMIT Inc 2011). Two procedures for exporting equivalent loads are illustrated in Fig. 3.1. The equivalent wave kinematics used in the Morison equation imported by *vpOne* for time-domain simulations. An efficient evaluation of second-order kinematics (Sharma, Golubchik, and Govindan 2010) using a two-dimensional FFT algorithm has also been implemented. Only minor movements of the cylinder are assumed with the current description. Further details on the hydrodynamic modelling can be found in Section 4.2.

3.1.2 TurbSim

TurbSim (Kelley and Jonkman 2007) is developed by NREL and is a full-field simulator for coherent turbulence. The code incorporates many spectral models and fluid dynamic features of turbulent flows. To facilitate integration into the current workflow, the source-code was modified to output a format readable by *vpOne*. Generating the full wind field is a relatively time-consuming process, using approximately 30% of the total simulation time for 10-minute time-domain simulations.

3.1.3 vpOne

vpOne is a non-linear time-domain simulation tool based on the USFOS software (SINTEF and NTNU 2003). Its performance is demonstrated in Hansen et al. (2009), and it was found suitable for this work due to its flexibility in load input and easy integration in a Linux environment for distributed computing. Beam elements are used for modelling the foundation, tower, drive-train and blades. For aerodynamic modelling, BEM theory with corrections for tip-loss, tower shadow and dynamic wake is used. Further description of the aerodynamic modelling can be found in Sørum, Horn, and Amdahl (2017). The interaction between the soil and structure is modelled using non-linear springs based on site-specific data. The soil model is presented in Section 4.1.3.

3.1.4 Controller

The controller is the up-to-date version of the *basic DTU wind energy controller* presented in Hansen (2013) which is openly available on *GitHub*. Both *vpOne* and the controller had to be modified for a common DLL interface. The model-specific controller is further described in Section 4.1.2.

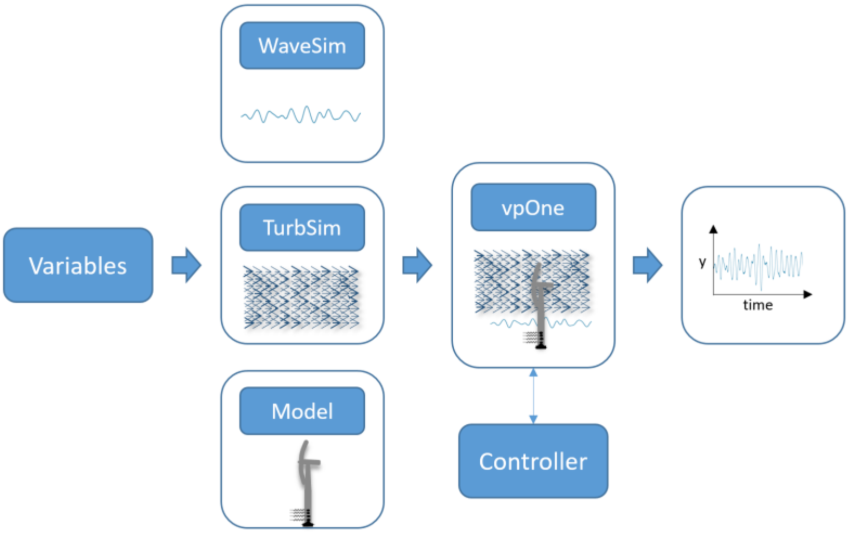

Figure 3.2: Workflow for a single time-domain realization

3.2 Computational resources and work flow

The results from tens of thousands of simulations hours form the basis of the calculations performed in this thesis. To enable running and re-running of large batch simulations, a procedure for using local machines in a cluster and cloud-based computers has been developed. A brief description of the set-up including implementation tips is given below.

First, the coupled time-domain simulation must be able to run on a Linux distribution with minimal modifications. This means that all standalone executables in the coupled simulations must be compatible with e.g. Ubuntu, and work flow scripts must be written in common scripting languages such as Bash and Python. For modules written in Matlab, only small modifications should be necessary to run the program using the open-source alternative GNU Octave.

Second, a framework for file sharing, job distribution, progress monitoring, time-series storage and result evaluation is required for a fully automated process. The set-up is shown in Fig. 3.3. The main engine is called *BatSim* (batch simulations) which first distributes the numerical model to all nodes in the cluster, before sending individual commands containing the input variables for the next time-domain realization. Say there are 4 nodes in the cluster with 20 threads available for each numerical experiment, then there is a total of 80 parallel commands from the host machine. After each simulation is finished, the results are transferred to a cloud storage solution, e.g. DropBox and Amazon S3. The results can then be evaluated in real time by the host machine, which decides whether this information shall be used to update the settings of the sampler.

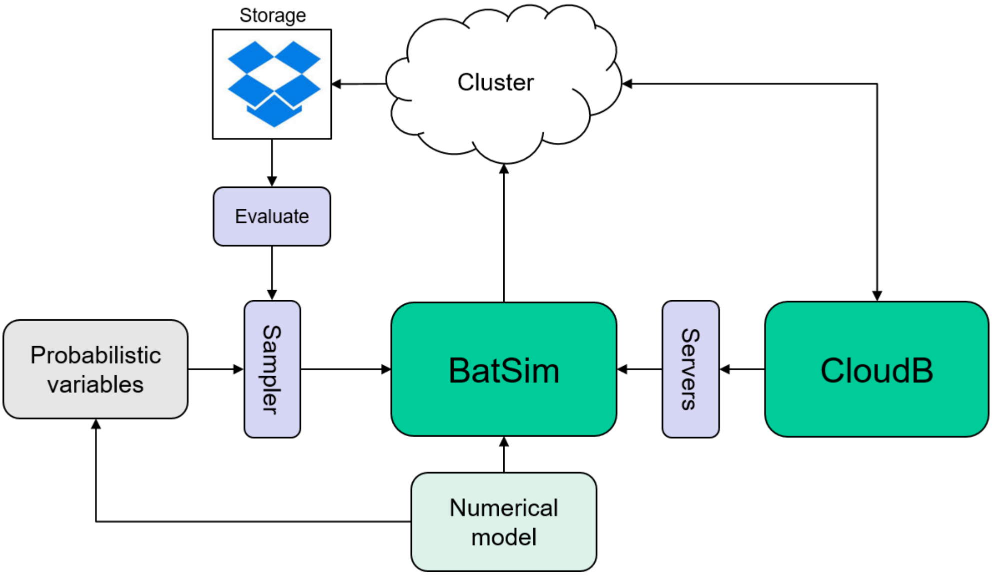

Figure 3.3: Work flow for large-scale batch simulations

The sampler samples from all standard probability distributions, including some distributions without analytical CDFs, such as the von Mises distribution (Forbes et al. 2010). To support dependencies between the probabilistic variables, for instance wind speed dependent significant wave height, a general Markov chain Monte Carlo algorithm (Gibbs sampler) is implemented.

To start and maintain a computing cluster, an external program is developed, called *CloudB*. It makes sure that pre-defined local workstation is available and may reduce the utilized capacity if the computer is already in use by other users. The total workload can also be scheduled to leave some available capacity for the user during the daytime and increase after the workday has ended. Also, a wanted number of Amazon servers can be started and added to the list of available servers for *BatSim*. To reduce the cost related to external usage of computational resources, *CloudB* uses spot instances in the Amazon Elastic Compute Cloud (Amazon EC2), which are 60-80% cheaper than instances with a pre-defined renting period. The disadvantage is that the instance will shut down if the market price exceeds the bid price set by the user. Future development includes a dynamic allocation of computational resources to the cheapest cloud solutions, and distribution to several cloud computing providers.

4 | Numerical Models

This chapter gives a short introduction of the numerical wind turbine model, and an overview of several hydrodynamic load models used in this work.

4.1 Reference model

In this section, the reference wind turbine model used in the thesis work is presented. The model is based on the DTU 10 MW reference wind turbine, mounted on an extra-large monopile foundation in 30 meters water depth at Dogger Bank in the central North Sea.

4.1.1 Main dimensions

The main dimensions of the rotor-nacelle assembly (RNA) of the 10MW DTU reference wind turbine can be found in Bak et al. (2013). Some characteristics are reproduced in Tab. 4.1. The aerodynamic properties of the blade sections are unchanged from the reference version, along with all other parameters related to the RNA. In order to have a realistic tower, that is not too soft in comparison to the stiff foundation, the original tower thickness is increased by 20% (Bachynski and Ormberg 2015). This ensures that the natural period is below the 1P period.

Table 4.1: Characteristics of rotor-nacelle assembly (RNA)

Hub height over MSL	[m]	119
Hub weight	[ton]	105
Blade length	[m]	89
Blade weight	[ton]	41
Nacelle weight	[ton]	446

The monopile and transition piece is based on a preliminary design at NTNU (Velarde 2016) and the main particulars are shown in Fig. 4.1. The transition piece spans from the tower base at 10 meters above to 10 meters below the mean sea level (MSL) where the monopile foundation continues to the seabed and 42 meters into the soil. Both the transition piece and monopile have a diameter of 9 meters, while the equivalent thickness is 11 cm for the monopile and 15 cm for the transition piece. The first and second mode shape and eigenperiod related to fore-aft and side-side vibration of the model are shown in Fig. 4.2.

For a bottom-fixed wind turbine, the eigenperiods depend on the soil stiffness model, which is further described in Section 4.1.3.

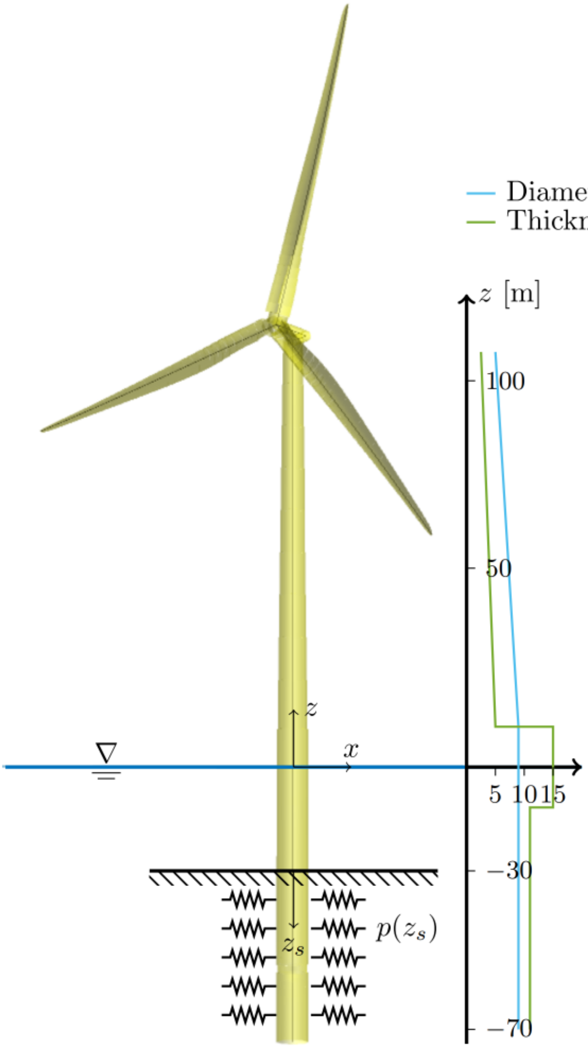

Figure 4.1: Structural model in *vpOne* with cylinder diameter and thickness as function of the vertical coordinate.

4.1.2 Controller properties

The controller is an important part of any wind turbine. Its properties determine the key characteristics; power quality, noise, fatigue and extreme responses. During the develop-

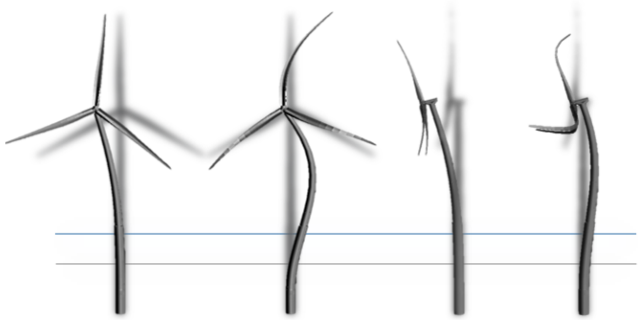

Figure 4.2: Vibrational modes, from left to right: 1st side-side (4.6s), 2nd side-side (0.9s), 1st fore-aft (4.6s), 2nd fore-aft (0.9s). Seabed and mean water level is included.

ment of the model, a conventional PI controller was used for both generator torque and blade pitch as implemented in Hansen (2013). A wind turbine controller require tuning to ensure stability and robustness (Merz 2016), and it is usually performed in the frequency domain for computational efficiency. However, the controller performance may alter significantly between frequency domain and between different aero-elastic simulation codes. Hence, additional tuning in time-domain is often required to obtain satisfactory performance. During the initial phase of this thesis, the gains were tuned in order to have a well performing controller, with minimal negative impact on the foundation fatigue. To verify the dynamic behavior, a comparison study between three different aero-servo-hydro-elastic codes was performed. The reference wind turbine model was modelled in FAST, SIMA and vpOne, and typical verification tests for the controller, natural periods and fatigue estimates were performed. The resulting characteristics are shown in Fig. 4.3 for wind speed stepping of 1 m/s every 50 seconds and in Fig. 4.4 for steady wind cases. It is seen that the performance for the DTU 10 MW monopile-mounted turbine is comparable for all three codes; FAST, SIMA and vpOne. The study is published in Sørum, Horn, and Amdahl (2017).

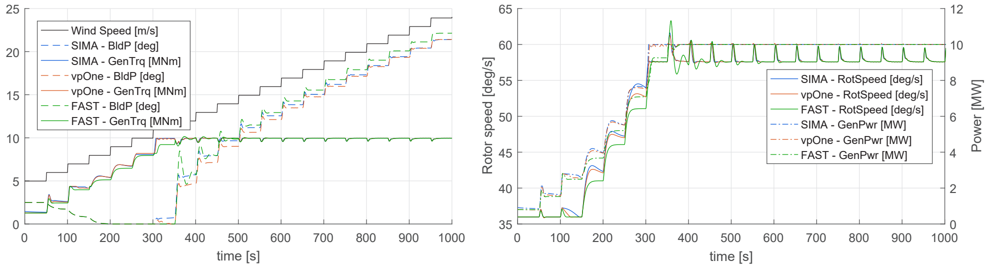

(a) Blade pitch angle and generator torque

(b) Rotational speed and power

Figure 4.3: Wind speed stepping for 5 to 25 m/s, from Sørum, Horn, and Amdahl (2017).

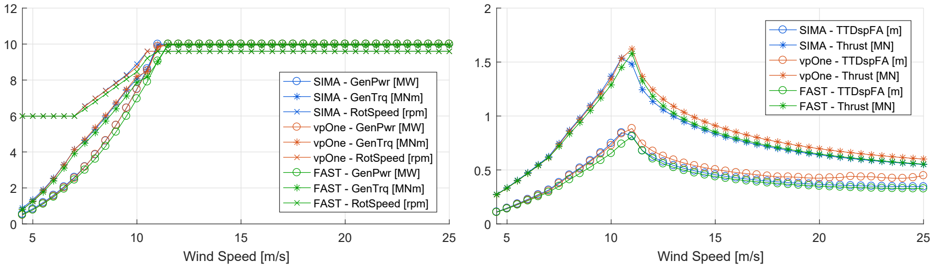

(a) Generator torque, power and rotational speed

(b) Aerodynamic thrust and fore-aft tower-top displacement

Figure 4.4: Response parameters for steady wind, from Sørum, Horn, and Amdahl (2017).

4.1.3 Soil model

This section presents the soil model used in the present work. A probabilistic soil model is outlined, which is used to obtain the characteristic soil stiffness curves, but may also be used in future reliability studies. The model can then be used to compensate for uncertainty related to the engineering model for soil-structure interaction as described in e.g. DNV GL (2016b). In the literature, several probabilistic models are presented (see e.g. Damgaard et al. (2015), Haldar, Sharma, and Basu (2018), and DNV (1996)).

The elastic soil properties are commonly modelled using *py*-curves as described in e.g. DNV GL (2016b) and American Petroleum Institute (API) and International Organization for Standarization (ISO) (2011). For large-diameter cylinders, the validity of this approach is questionable (Lesny 2010; Doherty and Gavin 2011; Carswell et al. 2015), unless the *py*-curves are calibrated to FEM analyses (see e.g. Velarde (2016)). Recently, new methods for increased confidence in geotechnical designs were developed (Page et al. 2017). In this work, classical non-linear *py*-curves have been used with characteristics as described below.

Clay

By standard description of *py*-curves for clay, it can be shown that the static ultimate lateral loading resistance per unit area valid in the present large-diameter case is:

$$p_u = 2a(3s_u + \gamma' z_s) + J s_u z_s \tag{4.1}$$

for a pile with radius a, and a clay shear strength of s_u at the vertical soil coordinate z_s illustrated in Fig. 4.1. Here, γ' is the effective unit weight of the soil and J is an empirical constant taken as 0.5 (DNV GL 2016b). For cyclic loading, the *py*-curve can be generated with:

$$p = \frac{p_u}{2}\left(\frac{y}{y_c}\right)^{1/3} \tag{4.2}$$

for a lateral displacement y, where $y_c = 5\epsilon_c a$ with ϵ_c as an empirical constant. Since the non-linear soil stiffness curves need to be represented by a piecewise linear curve, the first part is important as it describes the initial stiffness and hence eigenvalues. It is suggested in DNV GL (2016b) that $y_1 = 0.1\, y_c$ be used as the first point on the piecewise linear curve. The remaining points are chosen so that $y_2 = 3\, y_1$ and $y_3 = 10\, y_1$. The presented formulation will be used for $z_s \geq 2$, as the uppermost soil layer is sand (Horn 2015).

Quantitative values obtained from measurements campaigns at Dogger Bank are used as a basis for the current py-curves. The data are also presented in Paper I. Data for the clay shear strength are plotted in Fig. 4.5a with linear fits for the upper and lower estimate found as:

$$s_u^{hi}(z_s) = 4.66 \cdot z_s + 114 \tag{4.3a}$$

$$s_u^{lo}(z_s) = 2.33 \cdot z_s + 57 \tag{4.3b}$$

where the vertical soil coordinate z_s is related to the global z-coordinate through: $z_s = -(z + h)$. All parameters used in the probabilistic soil model are presented in Tab. 4.2. Note that all variables are assumed to be lognormally distributed, meaning that the lateral resistance p_u is also lognormal. In Fig. 4.5b, three different models for s_u are presented; a uniform distribution using the high and low estimate from the data, and two lognormal distributions. The lognormal distribution with a CoV of 0.20 was chosen to represent the soil model in this thesis.

Variable		Distribution	Mean	CoV [%]
s_u	[kPa]	Lognormal	$0.5\,(s_u^{hi} + s_u^{lo})$	20
γ'	[kN/m^3]	Lognormal	10	5
$\tilde{z}_s$	[m]	Lognormal	z_s	10
J	[-]	Lognormal	0.5	10
ϵ_c	[-]	Lognormal	0.01	5

Table 4.2: Probabilistic soil parameters

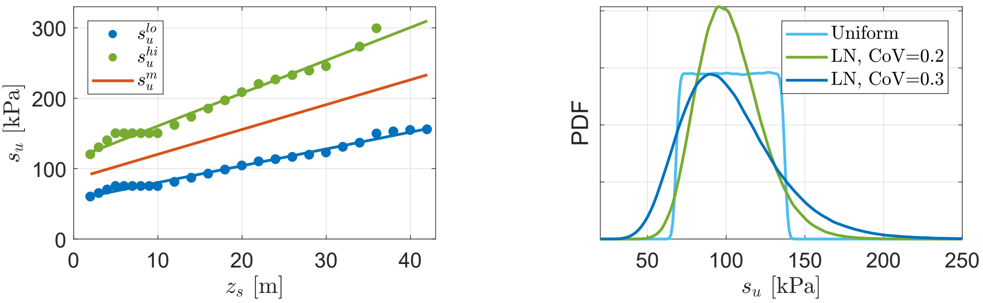

(a) Measurement data with linear fits and mean value s_u^m

(b) Alternative probability distributions for the shear strength s_u

Figure 4.5: Clay shear strength

By pure Monte Carlo simulations (MCS), the resulting distributions for p_u at given soil levels are obtained as shown in Fig. 4.6a. The parameters for the corresponding lognormal distributions are plotted in Fig. 4.6b as a function of the soil depth. Not surprisingly, both the soil stiffness and its variance increase with the depth. Now, the soil stiffness at any level z_s can be found with:

$$p_u(z_s) = F_{LN}^{-1}(\alpha_s; \mu_{p_u}(\tilde{z}_s), \sigma_{p_u}(\tilde{z}_s)) \tag{4.4}$$

where $\alpha_s \sim \mathcal{U}[0,1]$, and ν_{p_u} and σ_{p_u} are defined in Fig. 4.6b. Furthermore, it is assumed full correlation between the soil layers, which is expected to be a conservative assumption. Consequently, only one α_s is used to describe the full soil profile.

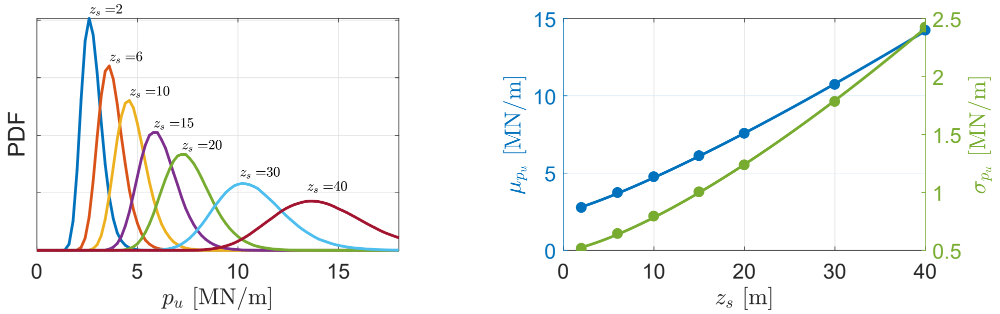

(a) Distributions of p_u after MCS analysis of the probabilistic description for various depths

(b) Parameters for a Lognormal distribution of p_u as function of depth below seabed

Figure 4.6: Probabilistic description of the soil resistance p_u

Sand

The soil resistance due to sand in the top layer of the soil profile can be described with (DNV GL 2016b):

$$p_u = (C_1\, z_s + 2\, a\, C_2)\, \gamma'\, z_s \tag{4.5}$$

where C_1 and C_2 are functions of the internal friction angle of sand. With a current friction angle of 47 degrees, it is found that $C_1 = 8.5$ and $C_2 = 6.3$ (International Electrotechnical Commission 2009). The soil resistance per area of the pile can then be found as:

$$p = 0.9\, p_u \tanh\left(\frac{k\, z_s\, y}{0.9\, p_u}\right) \tag{4.6}$$

where k is an empirical value dependent on the internal friction angle (DNV GL 2016b), and the remaining parameters are similar to those used for clay. The uncertainty related to the soil stiffness in sand layers are assumed to be uncorrelated with the clay layers.

Implementation and impact on eigenperiod

The stochastic soil model has a significant impact on the dynamic properties. Both the modal shapes and eigen periods of the system changes as a function of the soil stiffness. The variation in the first fore-aft eigenperiod based on 10 000 MCS is shown in Fig. 4.7 along with the cumulative density function (CDF). The scatter for a given α_s is due to the uncertainty assigned to ϵ_c, which determines the initial stiffness of the soil springs.

It is suggested in DNV GL (2016b) that a soil stiffness corresponding to a fractile of 0.05 or 0.95, whichever yields the most conservative results, should be used for design. For the present model, it is expected that a fractile of 0.05 will yield the most conservative result due to increased dynamic amplification at higher eigenperiods for lower stiffness. In the present work, a fractile of 0.5 ($\alpha_s = 0.5$) is chosen when the soil is modelled deterministically, which is the case for all appended papers. This yields a fore-aft period of approximately 4.6 seconds, although this value varies slightly between the different case studies due to small changes in the numerical model. The current foundation is stiff compared to the tower as seen by the eigenmodes in Fig. 4.2. As a result, a softer soil model will yield more contributions from wave loads on the dynamic response. Hence, the soil model must not be too stiff as it will result in non-conservative results. Using a probabilistic soil model in the reliability analysis is left for future studies.

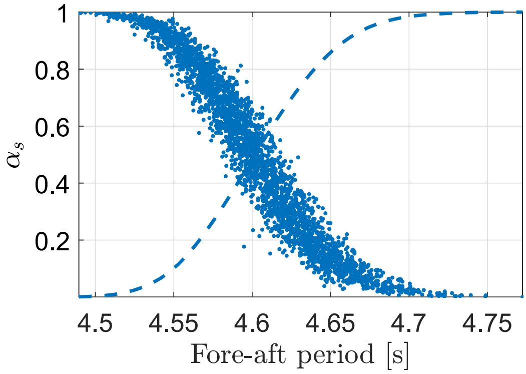

Figure 4.7: Eigenperiod variation due to stochastic soil model. CDF in dashed.

4.2 Hydrodynamic modelling

Several different hydrodynamic models were used to estimate the wave loads on an offshore wind turbine with a large monopile foundation. The hydrodynamic modelling can be divided into a description of the incident wave kinematics, as if there were no structure present, and the wave force calculation while accounting for fluid-structure interaction. Both kinematics and fluid-structure interaction calculation have several alternatives, varying in accuracy and computational complexity. The aim of this section is to present the wave load models used in this work and give the reader some supplementary insight.

4.2.1 Incident wave

For the incident wave kinematics, the most widely used approach is the linear formulation, or Airy formulation (Faltinsen, Newman, and Vinje 1995). The approach is fast and often sufficiently accurate for slender structures where little fluid-structure interaction is present and in sea-states will small steepness. By stretching the linear kinematics to the linear free surface, some higher-order components are obtained (Horn 2015). However, the order of the total load, and hence response, will be inconsistent (Paper I). Figure 4.8 is reproduced form Paper I, and illustrates wave stretching and which components to include for consistent order of horizontal wave load.

The main reasons for adopting higher order wave kinematics is to capture non-linear effects which are present for steep waves, shallow water, all forms of breaking waves, and non-linear interactions between individual wave components. However, the importance of increased accuracy depends highly on the response characteristics. For instance, a linear model might be sufficient for fatigue estimation in some cases (Paper I), while a higher-order model is required to describe non-linear phenomena such as ringing. It has been observed that second order theory gives the most important increase in load effects for FLS, while the third order, which is important for ringing is most relevant for ULS analysis where the waves are longer and steeper. Design computations are usually performed using potential flow theory, neglecting viscous effects in the fluid. If breaking waves are important, they must currently be modelled using CFD (Chella et al. 2016). . Here, methods concerning a potential flow formulation are discussed.

The degree of wave non-linearity for sea-states modelled using potential flow can be estimated by comparing a linear description with a highly- or fully non-linear description.

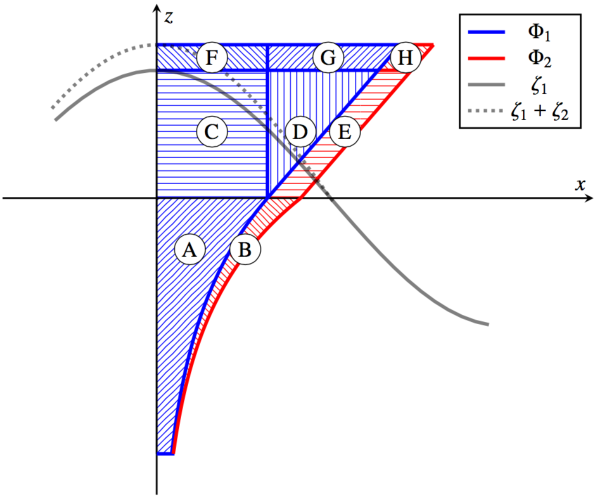

Figure 4.8: Wave kinematics stretching for first and second order incident wave potential. Reproduced from Paper I. The order of the horizontal force is dependent on which contributions that are accounted for: first (A), second (B+C), third (D+E+F), and fourth order (G+H).

OceanWave3D (Engsig-Karup, Bingham, and Lindberg 2009) is an example of a fully non-linear solver of the Laplace equation, while the higher-order spectral method (HOSM) solves the non-linear surface conditions to desired accuracy by Taylor expansions (Dommermuth and Yue 1987). A comparison between OceanWave3D and a HOSM solver was conducted in Guillaume et al. (2011). Here, HOSM using a solver to the third order will be the reference for a non-linear sea-state as it captures the most important non-linear effects. The difference of the power spectrum density (PSD) using linear and a non-linear solver is exemplified in Fig. 4.9. It is seen that a linear description will yield significantly less energy around the most important natural frequency of the reference model. Clearly a non-linear method is needed in order to model important wave components that can potentially excite the corresponding vibrational mode.

A linear realization of a given sea-state will yield a Gaussian surface elevation, wave particle velocity and acceleration. In other words, the third and fourth moment, skewness and kurtosis, will be zero and three, respectively. Consequently, the wave elevation will be normally distributed with zero mean, and the statistics of the wave crests will be similar to the wave troughs. The out-crossing rates for two sea-states are shown in Fig. 4.10. The sea-state in Fig. 4.10a has a close to Gaussian surface elevation as seen by the symmetry about $\eta = 0$, while the sea-state in Fig. 4.10b is heavily skewed towards positive η indicating a non-Gaussian process. The skewness and kurtosis using HOSM simulations are shown in Fig. 4.11, indicating an increase in the moments for large significant wave height compared to the peak period, i.e. larger steepness. It indicates that the joint probability distribution of the significant wave height and peak period is important to account for since the most non-Gaussian waves does not occur for the most probable pairs of H_S and T_P.

4.2.2 Wave load models

For the reference model, wave inertia forces proportional to the wave particle acceleration are dominating due to the large diameter of the foundation (Paper I). Viscous effects are accounted for by the drag term in the Morison equation with an appropriate drag coefficient

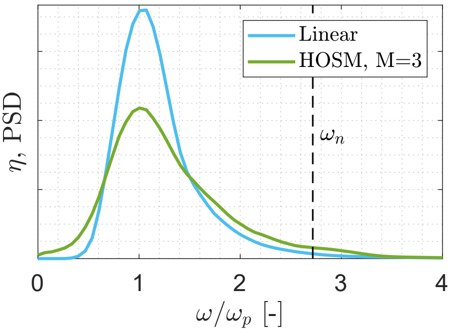

Figure 4.9: Example linear simulation vs. non-linear simulation of wave elevation with indication first fore-aft frequency of the structure

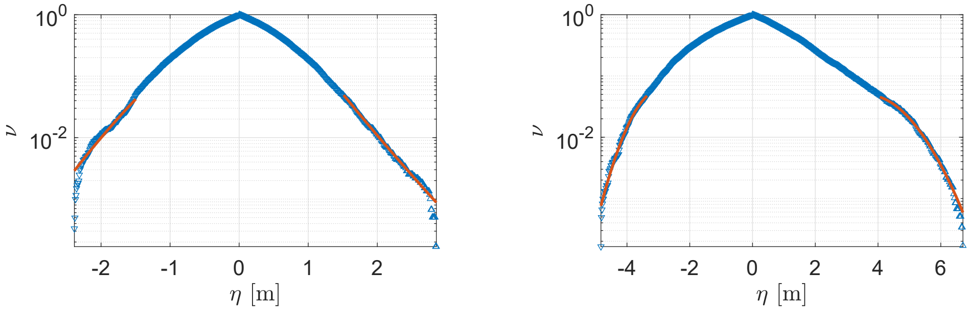

(a) $H_S = 3.0$m and $T_P = 8$s

(b) $H_S = 7.5$m and $T_P = 12$s

Figure 4.10: Wave elevation out-crossing rates for two different sea-states at a water depth of 30 meters, indicating the degree of non-linearity. Tail fits are included, using the ACER method (Moan and Naess 2013)

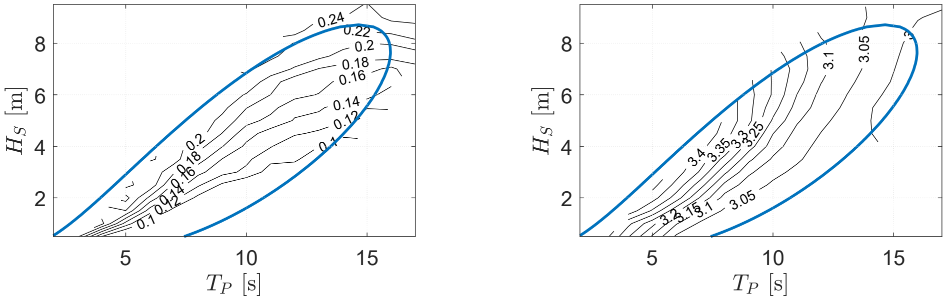

(a) Skewness

(b) Kurtosis

Figure 4.11: Isoquants for the wave elevation skewness and kurtosis from HOSM realization of the surface elevation at 30 meters water depth and JONSWAP spectrum with default peak shape factor. The 50-year contour line is shown to indicate the most frequent combinations of H_S and T_P.

and Morison elements. The drag term is evaluated using the incident wave particle velocity and has the same formulation regardless of which method is used for calculating the inertia forces which are influenced by the fluid-structure interaction. In Fig. 4.12, the non-linear wave load caused by the drag term in the Morison equation is shown as a fraction of the total force root-mean-square (RMS). As expected, the loading on the large-diameter cylinder in question is mostly dominated by inertial forces (Paper I).

The Morison equation without any corrections of the added-mass coefficient is not suitable for load calculations on a large monopile foundation (Paper I). A constant added-mass coefficient is very conservative, and frequency dependency should be introduced to capture the wave scattering/diffraction effects when the wave length is in the same order of

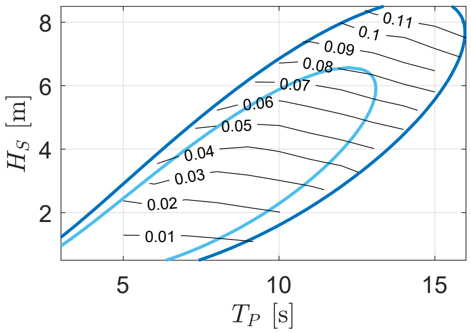

Figure 4.12: Contribution to total force variation from the non-linear drag term in Morison equation using linear wave theory. 1- and 50-year contour lines are shown.

magnitude as the foundation diameter. The implications of accounting for wave diffraction in a linear wave realization is shown in Fig. 4.13 for two different foundation diameters. It can be seen that the benefits in terms of reduced wave loading is significant for a diameter of 9 meters, but somewhat less important for a diameter of 5 meters.

Several hydrodynamic load models have been used throughout this thesis. The different load models are listed in Tab. 4.3 along with some additional models, and they all have individual advantages and limitations. In the appended papers, the load models are ranging from *1a* to *2b*. Brief comments are made below to each load model.

Morison The Morison load model is the most widely used approach for calculation of wave forces on slender objects (Morison, Johnson, and Schaaf 1950). Strip theory is assumed valid,

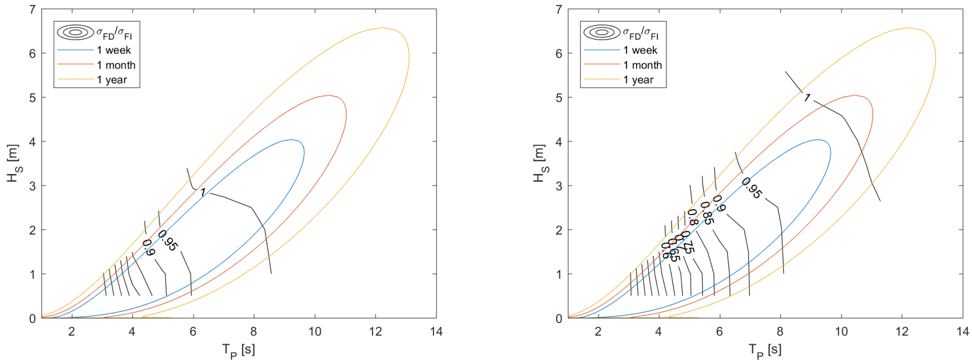

(a) Diameter of 5 meters

(b) Diameter of 9 meters

Figure 4.13: Isoquants of the RMS of the horizontal wave load using linear diffraction (D), normalized with respect to the incident wave load (I). Both at a water depth of 30 meters using a JONSWAP spectrum. Contour lines are shown for several return periods.

Table 4.3: Wave kinematics- and load models sorted after complexity. Indication of the associated main limitation and/or challenge.

No.	Kinematics	Load model	Limitation/challenge
1a	Linear	Morison	Fixed added mass
1b	Linear	MacCamy & Fuchs	Fixed cylinder
1c	Linear	FNV	Long wave assumption
1d	Linear	WAMIT 1st order	Hybrid time/frequency
2a	2nd order	WAMIT 2nd order	Hybrid time/frequency
2b	2nd order	Morison	Fixed added mass
3a	HOSM	Morison	Fixed added mass
3b	HOSM	FNV	Long wave assumption
3c	HOSM	SFM	Fixed cylindrical structure

meaning no hydrodynamic interaction along the length of the structure, and the structure is not influencing the incident waves significantly, i.e. wave scattering is neglected. This simple approach is sufficiently accurate in small to moderate seas as demonstrated in Paper I.

MacCamy & Fuchs For increasing cylinder diameter, fluid-structure interaction become a significant contribution to the total wave force. An analytical solution was presented in MacCamy and Fuchs (1954) for linear wave scattering about a circular cylinder. Recently, the method has been adopted to monopile foundations as the diameter increases to support larger turbines. It has been shown that excessive conservatism, primarily in FLS, can be expected when wave diffraction is not accounted for (Paper I). The MacCamy & Fuchs solution with linear extrapolation to the linear free surface has been the preferred method during this thesis when the hydrodynamic modelling has not been of primary importance.

FNV The Faltinsen-Newman-Vinje (FNV) load model was first developed in Faltinsen, Newman, and Vinje (1995) with the goal of representing the ringing phenomena, dominated by third order wave forces. Lately, a new formulation was presented for arbitrary water depths (Kristiansen and Faltinsen 2017) which shows good agreement with model tests for small to intermediate wave steepness. The method was tested in Paper I to quantify the third order wave load contributions to fatigue on a monopile foundation. Overall, a small contribution can be expected. This was agreed with conclusions made by Bachynski and Moan (2014) for tension leg platforms.

WAMIT The commercial panel code WAMIT (WAMIT Inc 2011) is widely used for calculating the hydrodynamic properties of large-volume structures assuming potential flow. The frequency-dependent added mass and potential damping can be applied in time-domain simulations by means of convolution, or the wave forces can be obtained by inverse FFT. The latter formulation was used in Paper I and VII, which is considered to be a good approach for a fixed structure. A second order solution can also be obtained. However, WAMIT will only calculate wave loads to the mean free surface. In order to calculate wave loads to the true surface, panel methods in time-domain must be adopted, for instance based on e.g. Rankine source method (Feng et al. 2016), HPC (Shao and Faltinsen 2014) or other numerical wave tanks.

SFM The spectral force method (SFM) is a novel method with the goal of filling the gap between Morison-based wave load models and CFD, while retaining the non-linearity in the incident wave and allowing for non-linear fluid-structure interaction (i.e. diffraction). An initial numerical solution scheme was proposed in Bredmose and Andersen (2014) and updated in Bredmose and Andersen (2016) with results from regular waves. Further development of the SFM may be an important contribution to reduce the wave load uncertainties while maintaining a reasonable computational efficiency. Also, it would be advantageous to have a method for calculating wave loads with no assumptions made on the initial wave field or diameter of the cylinder. Hence, the kinematics can be calculated using tools such as HOSM to a high degree of accuracy, while the wave scattering of a cylinder can still be accounted for by an efficient algorithm.

5 | Research Findings

In this chapter, the main research findings and the contributions from the individual papers to the overall research objectives are presented. The findings are sorted thematically with references to relevant publications. Where appropriate, supplementary investigations are provided for educational purposes.

5.1 Environment

The description of the site-specific environment forms the basis of the structural design and evaluation of the system reliability. Hence, a significant part of this thesis is devoted to the development of a new environmental model suitable for detailed design with probabilistic methods. As indicated in Fig. 1.1, the most relevant papers are IV and VII.

In this work, the environmental model is fitted to hindcast data for wind and wave parameters provided by the Norwegian Meteorological Institute (Reistad et al. 2011) for the location shown in Fig. 5.1. The figure also includes an estimate of the highest astronomical tide (HAT) collected from [`worldtides.info`], which is needed for the extreme load cases in the industry guidelines (DNV GL 2016a).

For an offshore wind turbine, the response in the rotor-nacelle assembly (RNA) and tower is mainly dominated by the wind loads. Depending on the type on foundation, wind loads may dominate the design criteria for foundation displacement and tilting. Wave loads have proven important in both FLS and SLS/ULS design of extra large monopile foundations in deeper waters. Considering both the energy production and large induced loads at the RNA, wind speed is the most important environmental parameters. This is not the case for traditional oil and gas structures (DNV GL 2017), where the significant wave height is often used as the main parameter. Also, the relative direction of propagation for the wind speed and wave-train is important, especially for a bottom-fixed offshore wind turbine due to sideways response excitation (Paper III and VII, and (Bachynski et al. 2014)). A 4-dimensional joint probability density function (JPDF) was developed and presented in Paper C4 (Horn, Krokstad, and Amdahl 2017). The misalignment angle was chosen to be the main parameter, with a conditional wind speed, significant wave height and peak period. Contour plots showing the four parameters are given in Fig. 5.2. This initial model represented only the absolute value of the relative direction and total sea, so the work was significantly extended in Paper IV. The new model describes absolute directions and separates wind sea and swell. The resulting JPDF is formulated as:

$$f_{\mathbf{X}_e} = f_{V,\Theta_v,H_S^w,T_P^w,\Theta_r^w} \cdot f_{H_S^s,T_P^s,\Theta^s} \cdot f_{H_t} \tag{5.1}$$

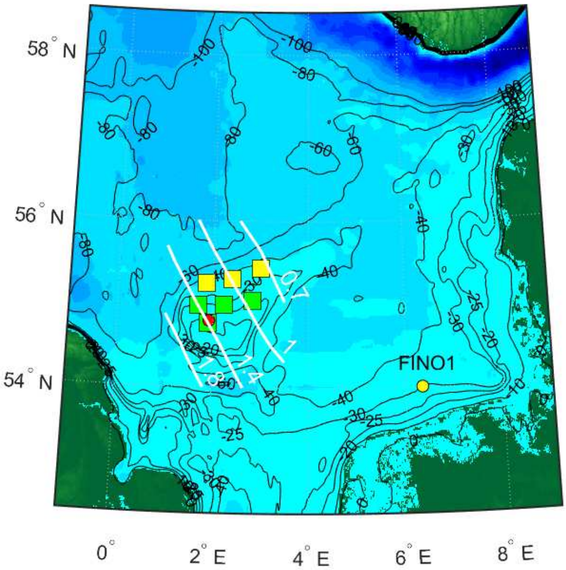

Figure 5.1: Central and southern North Sea with location for hindcast data (red), consented offshore wind farms (green), planned farms (yellow) and location of the FINO1 research platform. White lines indicate HAT.

where the different parameters are briefly described in Tab. 5.1. The reader is referred to Paper IV for the complete description of the model, including dependence modelling and validation of accuracy.

In Fig 5.3, the conditional three-parameter Weibull distribution of significant wave height and the von Mises model for wind speed dependent wind direction are shown. To the author's knowledge, a 3-parameter Weibull distribution has not previously been modelled with conditional parameters. A two-step procedure for robust fitting of the parameters are provided in Paper IV. It was found that a 2-parameter Weibull distribution is insufficient for

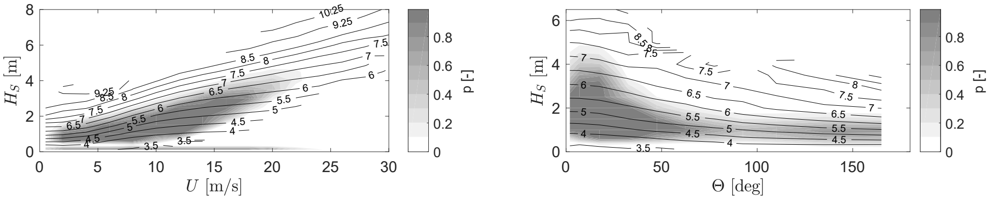

(a) Expected up-crossing period as function of wind speed and significant wave height

(b) Expected up-crossing period as function of misalignment angle and significant wave height

Figure 5.2: Contours of expected up-crossing period (T_Z) with annual probability of exceedence

modelling the wind sea significant wave height, and that the additional location parameter is needed for a good fit. Furthermore, the von Mises distribution was proven to be suitable for modelling the wind and swell directions. A novel procedure for dependency modelling on the wind speed was also introduced in Paper IV. Several uni-directional von Mises distribution were summed with weighting factors as a function of the wind speed. A reasonable fit can be seen in Fig. 5.3, where the wind direction of 220 degrees is weighted proportionally with the wind speed.

Paper VII also elaborated on the uncertainty related to spatial fatigue damage distribution introduced by the wind speed directional model. It was concluded that any non-uniform wind directional distribution will most likely yield increased fatigue damage. Hence, the directional properties must be accounted for by simulations or partial safety factors.

Table 5.1: Marginal distribution types and description of environmental parameters

	Parameter		Distribution	Description	Unit
Wind sea	V	v	3-p Weibull	Wind speed at 100 m.a.s.l.	[m/s]
	Θ_v	θ_v	von Mises mix	Wind direction at 100 m.a.s.l.	[deg]
	H_S^w	h_w	3-p Weibull	Significant wave height for wind sea	[m]
	T_P^w	t_w	Lognormal	Peak period for wind sea spectrum	[m]
	Θ_w^r	θ_w	Trunc. Normal	Relative wind-wave direction	[deg]
Swell	H_S^s	h_s	3-p Weibull	Significant wave height for swell	[m]
	T_P^s	t_s	Lognormal	Peak period for swell spectrum	[s]
	Θ_s	θ_s	von Mises mix	Swell direction	[deg]
	H_t	H	Normal mix	Water level	[m]

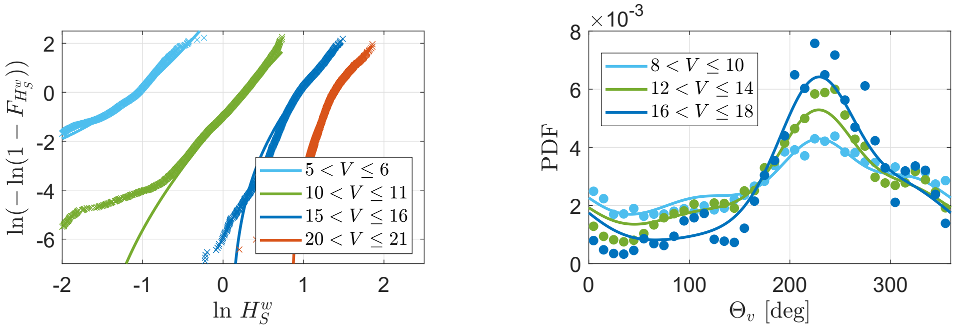

(a) Parameters for 3-parameter Weibull distribution of wind sea significant wave height as function of wind speed

(b) Wind directional distribution conditioned on wind speed

Figure 5.3: Example conditional descriptions of environmental variables reproduced from Paper IV. Scatters indicate binned hindcast data points.

5.1.1 Wind-wave misalignment

The wind-wave misalignment is an important parameter for determining the fatigue life of an offshore bottom-fixed wind turbine. According to design standards, misalignment shall be considered in both FLS, SLS and ULS checks. As demonstrated in Paper VII, the misalignment angle has a significant impact on the fatigue lifetime. The reason for this is the dramatic reduction in damping level when the structure is excited by waves from another direction than the wind and rotor plane as shown in Fig. 5.4a. A case specific partial safety factor of 1.28 was found when not considering the wind-wave misalignment in fatigue (Paper VII).

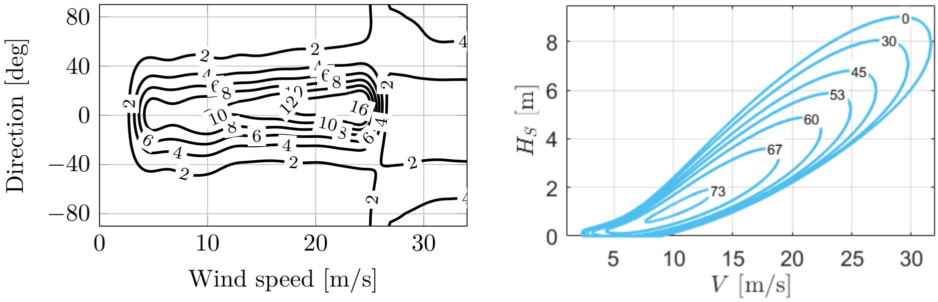

(a) Aerodynamic damping coefficient (%) as function of wind speed and vibration direction. Zero degrees is fore-aft motion.

(b) Maximum misalignment angle for a 50-year combined return period of wind speed and significant wave height

Figure 5.4: Misalignment considerations

For ULS and SLS, the relative wind-wave direction is expected to be less important, especially for a parked turbine. The issue of extreme misalignment angles for ULS/SLS analysis while maintaining a consistent return period for the response level was briefly touched upon in Paper C4 (Horn, Krokstad, and Amdahl 2017). A similar presentation can be found in Fig. 5.4b, where the maximum misalignment angle to be expected with a return period of 50 years or less is given as a function of wind speed and significant wave height. The values are valid for any peak period, and will be conservative compared to the use of a probabilistic peak period. At the cut-out wind speed, the maximum misalignment angle to be expected is 53 degrees, for a sea-state with dramatically reduced significant wave height. In the IEC standard for offshore wind turbines (International Electrotechnical Commission 2009) it is suggested that the significant wave height is to be taken as constant for misalignment angles up to 30 degrees. Figure 5.4b shows that this is slightly conservative. However, for misalignment angles above 30 degrees, it appears to be very important to reduce the significant wave height to avoid excessive conservatism. It is specified in the load cases DLC 6.1, 6.2 and 6.3 in DNV GL (2016a) that misalignment angles up to ±30 degrees shall be used.

Initially, only the absolute value of the misalignment angle was modelled (Horn, Krokstad, and Amdahl 2017). However, it was later extended to include both positive and negative misalignment angles using a normal distribution (Paper IV). This is important due to the non-symmetric response behavior of the wind turbine about the pure fore-aft motion as seen in Fig 5.4a. Here, a positive misalignment angle means that the wave direction has an incoming direction which is shifted counter-clockwise compared to the wind direction.

Another interesting finding is the correlation between expected misalignment angle and significant wave height. Using a truncated normal distribution for the misalignment angle, the standard deviation is seen to be constant while the mean misalignment is decreasing linearly with the significant wave height as seen in Fig. 5.5a. This phenomenon is expected to be site-specific and is due to the rotation of weather and increased inertia for larger sea states. The effect on fatigue damage normalized for each wind speed can be seen in Fig. 5.5b. By combining this knowledge with the asymmetric response behavior in Fig. 5.4a, the difference in fatigue damage in the foundation for a turbine rotating clockwise and counter-clockwise may be significant. This effect has not been quantified, and is merely an interesting observation.

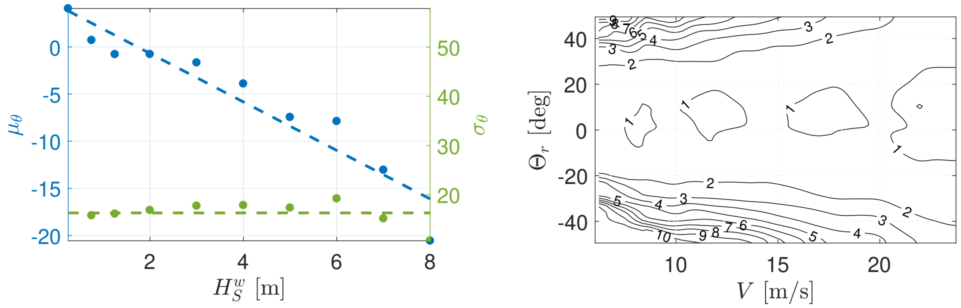

(a) Parameters for normally distributed wind-wave misalignment as function of significant wave height.

(b) Effect of misalignment on the maximum fatigue around the foundation pile circumference. Normalized for each wind speed.

Figure 5.5: Wind-wave misalignment and its impact on fatigue

5.2 Hydrodynamics

In this section, the research findings related to sensitivity studies for hydrodynamic modelling and the corresponding load effects are presented. The first three papers focus entirely on hydrodynamic loads and load effect, and the subject was revisited in the final paper for analysis in a structural reliability framework.

Hydrodynamic load effects

In Paper I, several approaches with varying degree of modelling fidelity was compared with respect to the foundation fatigue of the reference wind turbine model. The different hydrodynamic models are described in more detail in Section 4.2.

Some of the results regarding fatigue damage uncertainty and maximum overturning moment are presented in Fig. 5.6. It is concluded that the MacCamy & Fuchs correction must be accounted for when performing analysis on large monopiles, and that the higher-order models significantly increases the fatigue damage if the significant wave height is more than four meters. Hence, depending on the site and environmental joint distribution, second order load models may have a significant impact on the lifetime of the foundation. For the maximum base moment, wave diffraction does not influence the result dramatically as seen in Fig. 5.6b. However, higher-order models should be adopted for SLS/ULS analysis.

The sensitivity of the results with respect to the soil model and stiffness of the foundation should be included in future analysis. Comparing with the frequently used Wheeler stretching is also of interest, and left for future work.

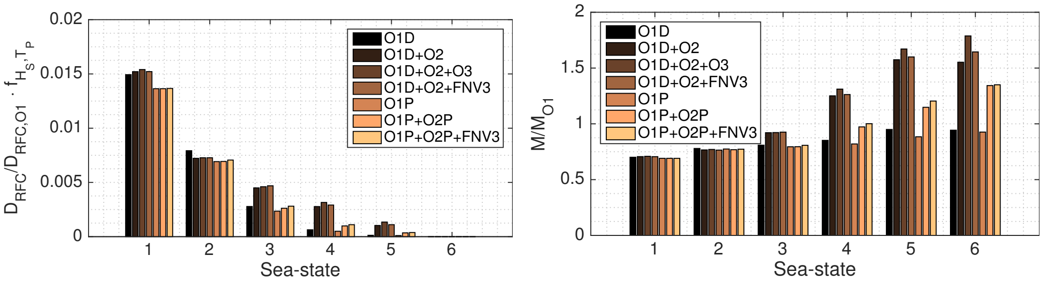

(a) Fatigue damage normalized with respect to load model O1 and weighted with probability of occurrence.

(b) Maximum base moment normalized with respect to load case O1.

Figure 5.6: Results from Paper I regarding fatigue and maximum load sensitivity with respect to hydrodynamic model.

Short-term variability

The modelling uncertainty introduced by the short-term variability due to the stochastic nature of the wave climate has been investigated (Paper II). An example is shown in Fig. 5.7a for convergence of the foundation fatigue as a function of the number of short-term simulations. The underlying fatigue damage distribution can be approximated by the histogram in Fig. 5.7b. According to design standards (DNV GL 2016a; International Electrotechnical Commission 2009), it is in general required to conduct a total of at least 60 minutes of time domain simulations to obtain a confident fatigue damage estimate in each sea-state. In Paper II, the goal was to reduce the short-term variability by a combination of MCS and FORM to allow for shorter simulation lengths.

The short-term simulation time must be chosen so that all important dynamic response characteristics are captured. For the reference model with dominating natural period of 4.5 seconds, it is assumed that a 100-second simulation will yield a sufficient number of load-effect cycles to calculate a reasonable fatigue damage when only wave loads are applied (Paper II). The short simulation time is chosen as a first step in order to limit the number of wave components in the wave train to be able to perform the inverse FORM method. For each sinusoidal wave component, one or two stochastic variables exist depending on the modelling method (Tucker, Challenor, and Carter 1984). Hence, a 100-second simulation requires 40 or 80 random variables (Paper II) to avoid repetition of the surface elevation. A method for only including the most important wave components in the gradient-based optimization scheme using inverse FORM was introduced (Paper II).

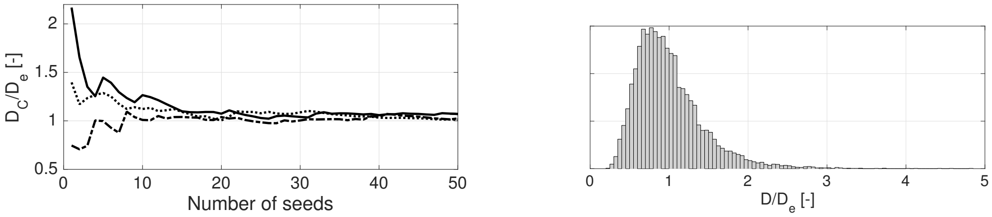

(a) Foundation fatigue damage as function of the number of 100-second simulations

(b) Fatigue damage distribution for 10,000 samples in moderate conditions with H_S = 1.5m and T_P = 4.7s.

Figure 5.7: Convergence and short-term variability of mudline foundation fatigue damage. D_e is the expected fatigue damage used for normalization.

The procedure used in Paper II can be summarized as follows: the first-order reliability method (FORM) was used to find a wave realization giving a very large short-term fatigue damage (D_{ext}). This realization is used to represent all sea-states which may introduce result variability by introducing a linear (or quadratic) fit for the corresponding reliability index (β_{FORM}) and fatigue damage as shown in Fig. 5.8a. Consequently, the sea-states leading to increased fatigue are accounted while having a reduced impact on the result variability as seen in Fig. 5.8b. It is seen that the best performing method is the quadratic fit (Q), which reduces the standard deviation significantly.

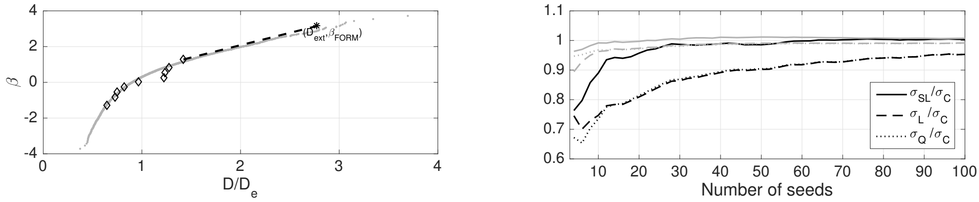

(a) Example fit using the "sum+linear" (SL) method with linear fit between the FORM-constructed point and the worst of the remaining sea-states

(b) Standard deviation of fatigue damage estimation given number of seeds (N) of 100s simulations with only wave loads. Gray lines are the mean fatigue normalized with true damage.

Figure 5.8: Results from Paper II, where FORM is used for variance reduction of the estimated foundation fatigue damage

Wind sea, swell and spreading

The effect of separating the total sea into wind sea and swell, and short-crested modelling has been investigated with respect to fatigue damage. Hindcast data containing both wind sea and swell, and their respective directions, were used in the experiment. Instead of using the joint probability model as described earlier by Eq. 5.1, the hindcast data were used directly for simulations until an acceptable CoV of the fatigue estimate was obtained. For short-crested sea, there is no data to support the choice of spreading function for the reference location. However, it was shown that larger spreading in co-directional sea will yield lower fatigue due to directionally distributed energy and less excitation in critical directions (Paper III). The results are shown in Fig. 5.9 for the frequency domain simulation case and circumferential fatigue damage. For the reference wind turbine model with Dogger Bank hindcast data, it was found that swell separation yielded approximately 30% lower fatigue damage in the foundation at the critical location.

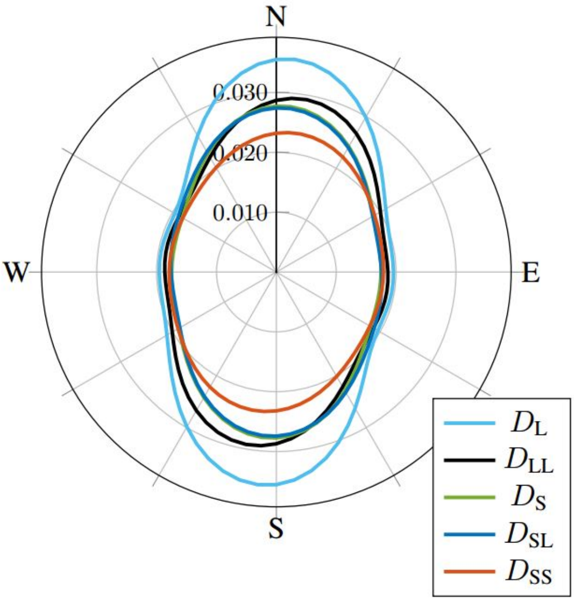

Figure 5.9: 20-year circumferential fatigue damage at mudline using frequency domain simulations, 20 years of data and 90% availability. SN-curve with exponent $m = 5$ and spreading exponent s = 9 have been used. Cases: long-crested total sea (L), long-crested wind sea and swell (LL), short-crested total sea (S), Short-crested wind sea and long crested swell (SL), and short crested wind sea and swell (SS).

In contrast to separate modelling of wind sea and swell, the sea spreading is rarely supported by site-specific measurement data. It is clear that a long-crested formulation will yield conservative fatigue estimates for the present model as seen in Fig. 5.9. Various models for description of the short-term directional spreading was investigated in Paper VII, with and without frequency dependence. Results showed that a frequency dependence would yield slightly larger fatigue damage than equal spreading for all frequencies. Site-evaluations in the literature support a frequency-dependent spreading is more realistic. An example CDF of a spreading function is shown in Fig. 5.10, where little spreading is allowed at the peak frequency, while more spreading is expected for higher and lower wave frequencies. A challenge with introducing wave spreading is the increase in computational efforts. In DNV GL (2017), it is suggested that 11 discrete directions should be used when introducing short-crestedness. If n wave components are required by the FFT algorithm to avoid repetition of the surface elevation, a total of $11 \cdot n$ wave components are present in the wave field. This means 11 times more computational efforts when generating wave kinematics unless some countermeasures are introduced. In this work, a sampling method to retain n wave components also for short-crested sea has been used. The principle is shown in Fig. 5.10, where a single direction is sampled for each wave frequency. If $\Delta\omega$ is sufficiently small, it can be shown that the result will be similar for both approaches. Care should be taken in having a sufficient number of components to ensure a homogenous wave elevation. Some additional short-term statistical uncertainty is introduced, and the solution may require a few additional simulations before the target CoV is reached, but the total computational efforts are reduced with approximately 80% depending on the number of discrete directions. The method is implemented in *WaveSim*.

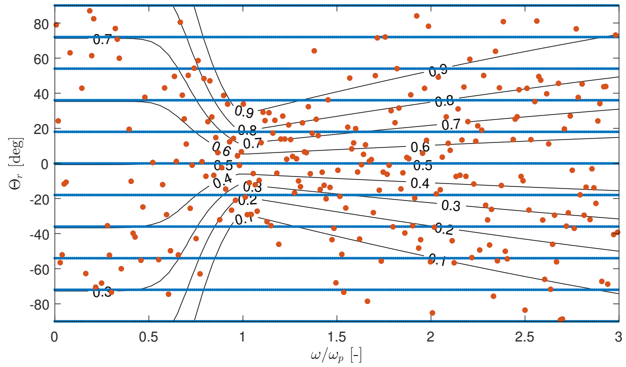

Figure 5.10: Wave spreading CDF showed as isoquants for wave frequencies normalized by the peak frequency of the sea state. Blue dots indicate deterministic wave components, while red dots are the sampled directions. Note how the variance sampled direction is changing as a function of the frequency.

Impact of hydrodynamic model on fatigue reliability

The final paper in this thesis (Paper VII) investigates the impact of the hydrodynamic load effect uncertainty on the fatigue lifetime of the reference foundation. Using a second order WAMIT model, the uncertainty is found as the relative difference in fatigue between linear and second order solution. This is performed for both operational and idling turbine. As expected, the load effect sensitivity is largest for an idling turbine. A comparable study was recently published (Colone, Natarajan, and Dimitrov 2018), although without second order contributions, diffraction effects and environmental uncertainties. In Paper VII, the wave load uncertainty is calculated by accounting for the variation in the significant wave height and peak period for a given wind speed. Consequently, the stress variation increases due to the strong dependency on the wave steepness as seen in Fig. 5.11. A case-specific partial safety factor of 1.2 was found for the wave load uncertainty for the linear wave load model, if the second order model is taken as a reference for the true loading.

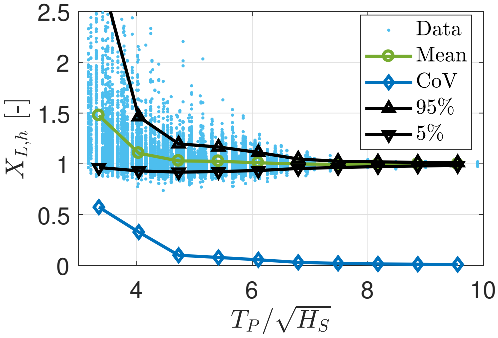

Figure 5.11: Uncertainty of the stress range in the foundation as function of the inverse wave steepness. The uncertainty is measured as the relative difference between the damage-equivalent stress for linear and non-linear wave load (see Paper VII).

5.3 Structural reliability analysis

Structural reliability analysis has been an important tool in this thesis to evaluate the impact of different modelling techniques on the fatigue reliability. It has given a deeper understanding of the results sensitivities compared to fatigue analysis using characteristic values and partial safety factors.

Relevant literature on general structural reliability analysis (SRA) can be found in e.g. Toft-Christensen and Murotsu (1986) and Madsen, Krenk, and Lind (1986). In Sørensen and Toft (2010), an overview of probabilistic design of wind turbines is presented, including uncertainties related to environmental models and stress calculations. Load effects uncertainties may also include in-situ measurements (Ambühl et al. 2015). For a given set of load effects, partial safety factors for a given level of reliability can be calculated as demonstrated in e.g. Marquez-Dominguez and Sorensen (2012). In this section, some challenges and remedies to structural reliability analysis of offshore wind turbines in both FLS and SLS are discussed.

5.3.1 Response sub-populations

An important difference between an offshore wind turbine from traditional oil and gas structures is the controllable loads on the rotor. There is no way to quickly influence the dynamic response of a jacket platform after installation. For an offshore wind turbine, the aerodynamic loads on the rotor are adjusted with the control system for blade pitch and generator torque. In Fig. 4.3 and 4.4, some properties of a wind turbine control system was presented. Here, the focus is placed on the effects of the control system on the foundation fatigue. In Paper VI it was found that an idling turbine will accumulate material damage in the foundation on average 3.6 times faster than an operational turbine. This can be explained by the significant aerodynamic damping introduced by induced velocities on the blade section, and control system (see Paper III). The result is a dramatic reduction of the dynamic amplification of the support structure. Furthermore, additional modifications can be made to the control system in order to reduce the fatigue accumulation rate even more. New load mitigating control algorithms in combination with structural monitoring have enabled lifetime extensions, and has the potential to compensate for other load uncertainties as described in Horn, Leira, and Amdahl (2017). Here, only two control strategies will be considered; operational turbine using a controller with no additional attempts of reducing the load effects, and a controller for an idling turbine, resulting in a slowly rotating rotor. The latter setting is assumed to cover all shut-down situations, where the rotor-induced damping is minimal.

Depending on the availability α and wind speed V, the wind turbine states may be classified as shown in Fig. 5.12. The idea behind the classification is to limit the amount of total simulations by focusing on the most important sub-populations, and to facilitate arbitrary weighting of the sub-populations (Paper VI). In Section 5.4, a supplementary simulation algorithm using each wind speed bin as a sub-population is presented. Here, the usage of response sub-populations for FLS and SLS analysis is presented.

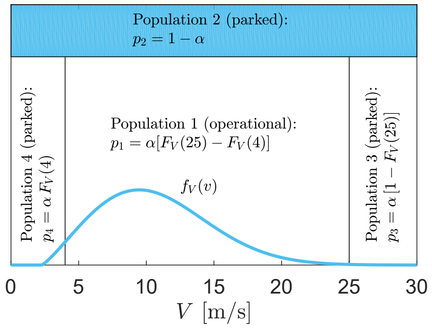

Figure 5.12: Wind turbine response sub-populations

5.3.2 SLS

For SLS and ULS, the total failure probability for several response sub-populations can be formulated as a nested reliability problem. The total failure probability can be expressed as the sum of all independent populations using the law of total probability:

$$p_f = \sum_{i=1}^{4} p_i \, P[g_i \geq 0] \tag{5.2}$$

where g_i represents the failure surface, simply formulated as:

$$g_i = R - S_i \tag{5.3}$$

where R represents the capacity or allowable load effect, and S_i is the stochastic load effect in population i. $P[g_i > 0]$, is the failure probability considering the load effect in population i. In Paper V, the combined 50-year nacelle acceleration and bending moment at seabed is found using the procedure outlined above, except that Eq. 5.2 is formulated as:

$$F_X(x) = \sum_{i=1}^{4} p_i \, F_{X_i}(x) \tag{5.4}$$

where $F_{X_i}(x) = P[x - X_i \geq 0]$ is the CDF for the response parameter x in population i. Typical response parameters for SLS and ULS design checks include; nacelle acceleration, lateral pile displacement in soil, moments at critical locations along the support structure, and responses in drive-train and blades.

The usage of the above formulation for finding a consistent 50-year extreme response by accounting for all sub-populations was demonstrated for the nacelle acceleration and mudline moment (Paper V). The extreme value distributions for the nacelle acceleration is shown in Fig. 5.13a for sub-population 1 and 2, which are assumed to be dominating. By using Eq. 5.4 and setting $F_X(x_{50}) = 1/50 \cdot 365 \cdot 24$, the 50-year level for the 1-hour extreme response is shown in Fig. 5.13b. It can be seen that the combined 50-year response corresponds approximately to the 75-year extreme value in sub-population 1 and 9-year extreme value in sub-population 2, as shown in Fig. 5.13a. Finding the true 50-year response value is not straight-forward by other means than the presented method (Paper V), although some other promising approaches have been published (Li, Gao, and Moan 2016; Li, Gao, and Moan 2017).

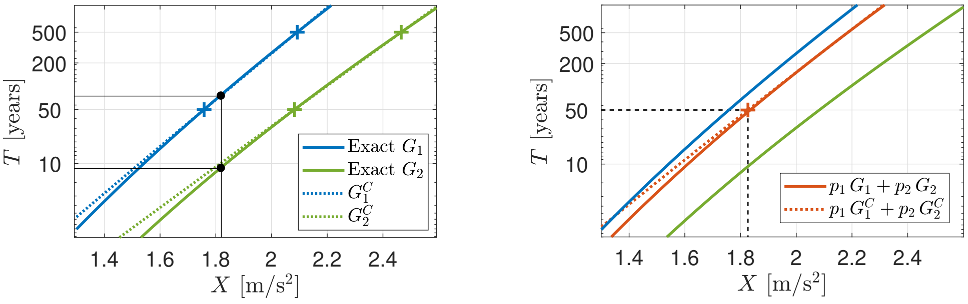

(a) Exceedance plot for the nacelle acceleration for sub-population 1 and 2, assuming either are present throughout the lifetime. Return periods corresponding to the true 50-year response are shown.

(b) Individual exceedance plots and weighted exceedance plot for the combined response. The combined 50-year value is found as approx. 1.82 m/s.

Figure 5.13: Long-term extreme response functions for sub-populations 1 and 2; unweighted curves and weighted total extreme response curve

5.3.3 FLS

In contrast to SLS/ULS, FLS is a cumulative measure. Consequently, the failure probability must be found by considering all sub-populations simultaneously with a common material capacity, and the approach in Eq. 5.2 is invalid. For a total failure probability of $p_f = P[g \geq 0]$, the limit state equation is formulated as:

$$g = \Delta - n \sum_{i=1}^{4} p_i \, D_i \tag{5.5}$$

for n years of operation with yearly fatigue accumulation rate D_i in population i. Δ is the allowed fatigue utilization, usually assumed lognormally distributed (DNV GL 2015). The individual weights p_i are defined in Fig. 5.12. Since the accumulation of fatigue damage over n years in independent of the chronology of the downtime period, a simple weighted summation is valid. The probabilistic parameters used to describe each D_i can be found in Paper VI. In short, D_i contains parameters related to the Weibull-distributed stress ranges, SN-curve and load effect uncertainties. The failure probability can then be found by FORM, SORM or Monte Carlo simulations, where the latter has proven to be the most robust when the limit state surface is ill-behaving.

The failure probability in FLS for combined sub-populations is found using a stochastic availability parameter modelled with a Beta distribution (Paper VI). Contributions from the two dominating sub-populations are shown in Fig. 5.14 as a function of the number of MCS. It is clear that population 2 gives a significant contribution to the failure probability. Populations 3 and 4 do not contribute to any noteworthy fatigue during the lifetime and is therefore neglected completely.

5.4 Simulation optimization

Computing the lifetime fatigue damage of an offshore wind turbine is a computationally demanding task. This section provides an overview of novel methods used in this work for

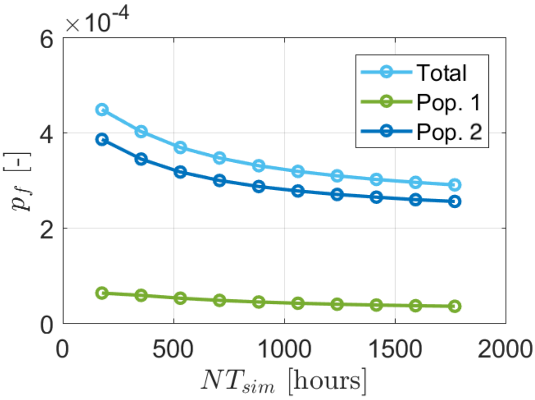

Figure 5.14: Convergence of the 25-year failure probability in FLS for sub-populations 1 and 2

minimizing the variance of time-domain simulation results while maintaining or even reduce the total computational time.

The purpose of a long-term fatigue analysis is to obtain an estimate of the material degradation during the lifetime of structural components. Due to epistemic and aleatory uncertainties in the environmental variables and numerical models, an estimate is obtained by accounting for the probability distributions of these variables and how they affect the average damage accumulation. The long-term annual average fatigue accumulation can be expressed as:

$$D_e = \int_{\mathbf{x}_e} \int_{\mathbf{x}_m} d_e(\mathbf{x}_e, \mathbf{x}_m)\, f_{\mathbf{X}_m}(\mathbf{x}_m)\, d\mathbf{x}_m\, f_{\mathbf{X}_e}(\mathbf{x}_e) d\mathbf{x}_e \tag{5.6}$$

where $d_e(\mathbf{x}_e, \mathbf{x}_m)$ is the average annual damage for a given structural component given the probabilistic environmental variables in $\mathbf{x}_e$ and model uncertainties in $\mathbf{x}_m$. Traditionally, Eq. 5.6 is evaluated by numerical integration using a binning procedure. However, as the dimensions of $\mathbf{x}_e$ and $\mathbf{x}_m$ increases, numerical integration becomes computationally demanding. A alternative approach is to use Monte Carlo simulation or similar sampling procedures to approximate the multi-dimensional integral. The solution can then be approximated as the mean of all MCS samples. The approach was used to analyze the fatigue damage at mudline for the present numerical wind turbine model, and it was shown to converge as illustrated in Fig. 5.15a. A comparison between several simulation lengths is shown in Fig. 5.15b. Industry standards typically require sat least 10-minute simulations in order to capture all important dynamic effects. However, it is here shown that the result converges faster for shorter simulation lengths. For a bottom-fixed turbine with low dominating eigen period, it is expected that most of the important dynamics can be captured during 200 second simulations. Although this will probably not be the case for a floating turbine, where slowly varying processes will be of importance.

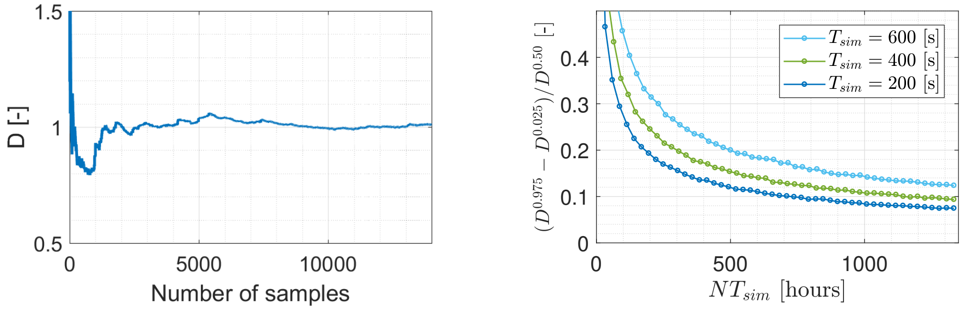

(a) Convergence of normalized fatigue damage at the mudline

(b) Convergence of the 5-percentile range for several short-term simulation lengths

Figure 5.15: Convergence plots

The downside of pure MCS is the potentially large number of samples needed for convergence. Hence, it is proposed to use a combination of binning of variables and MCS to obtain results with a constraint on the accuracy. As the control system characteristic and hence the dynamics of the wind turbine is mainly dominated by the wind speed, it is chosen to perform discretization on the wind speed parameter, V, into N bins. The outcome is an adaptive importance sampling procedure, with an optimization problem stated as:

$$\begin{aligned} &\text{minimize} && \sum_{i=1}^{N} n_i \\ &\text{subject to} && \sqrt{\sum_{i=1}^{N} \left(p_i\, \sigma_{d,i}\right)^2} \leq \gamma_d \sum_{i=1}^{N} p_i\, \mu_{d,i} \end{aligned} \tag{5.7}$$

where n_i is the number of simulations in bin i, p_i is the probability of bin i, which is defined as: $p_i = f_V(v_i)\,\Delta v_i$. Furthermore, μ_d is the average fatigue damage rate and σ_d is the standard deviation of the damage rate. The parameter γ_d is the CoV of the end result, D_e. The target CoV is 10% in the present simulations.

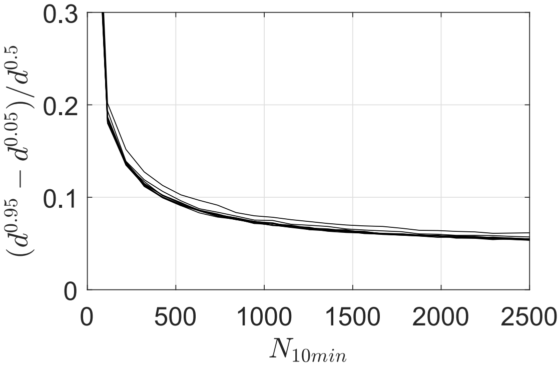

Figure 5.16: Convergence of fatigue damage for several wind speed bins

Figure. 5.16 shows the range of the 90% confidence interval for a number of wind speeds as a function of the number of Monte Carlo samples. Each sample represent a 10-minute time-domain analysis for the wind speed corresponding to the bin, and significant wave height, peak period, tidal elevation etc., conditioned on this wind speed. It is suggested that the fatigue in all wind speed bins are initialized with some n_{ini} to get an initial estimate on μ_i and σ_i. After that, the algorithm described above automatically performs more simulations in the most important wind speed bins. An example is shown in Fig. 5.17. It is not surprising to see that the number of simulations in each bin is proportional to the relative contribution of fatigue damage. Hence, the simulations performed in bin i is approximately: $n_i = N\,\mu_d(v_i)/\sum_i \mu_d(v_i)$.

With the above approach, computational efforts can be reduced dramatically without the need for a priori knowledge of the system dynamics and a case-specific binning procedure. Furthermore, the error estimate is available throughout the simulations which is not the case for binning methods. Consequently, the method is also suitable for probabilistic analysis with a high number of random variables.

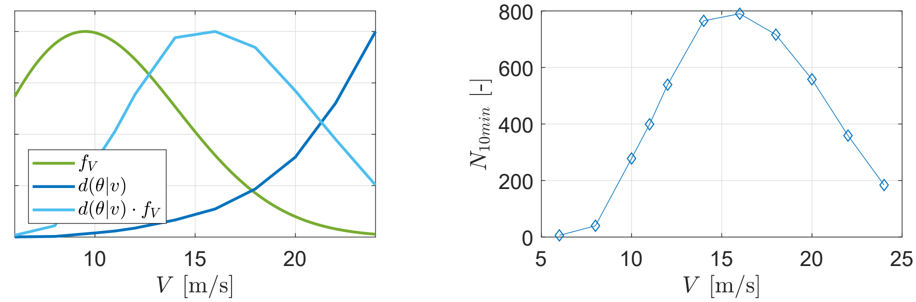

(a) Fatigue distribution as function of wind speed after weighting with wind speed marginal distribution

(b) Number of simulations required in each wind bin to satisfy a total CoV of less than 10%

Figure 5.17: Fatigue simulation optimization

6 Conclusions and recommendations for further work

The current chapter summarizes the contributions to the research on offshore wind turbines in this thesis. Suggestions for further work are made with basis in the appended papers.

6.1 Conclusions

This thesis deals with uncertainties related to the hydrodynamic, environmental and numerical modelling in the design of offshore wind turbines. All cases are performed with a large bottom-fixed, monopile-mounted offshore wind turbine with 10MW rated capacity. Short- and long-term analysis using stochastic environmental modelling and non-linear time-domain simulation tools have been the main research methodology.

As a baseline for long-term analysis of offshore wind turbines, a new combination of environmental joint distributions was developed. The model allows for large-scale stochastic simulations for any stationary offshore structure where the short-term sea state can be described by means of the long-term distribution of wind, wind sea, swell and tidal parameters. It was found that the design conservatism can be reduced by introducing more environmental parameters, e.g. swell, for the present case. This will contribute to reduce the cost of energy.

It was demonstrated that expanding the number of environmental variables to include separation of wind sea and swell yields reduced fatigue damage for the present model. The fatigue reduction is mainly due to introduction of directional parameters, spreading the wave energy to more directions. The same conclusion goes for directional spreading of wind sea. It is therefore suggested to facilitate the use of swell sea (Paper III and IV) and investigate the site-specific wave spreading for potential cost savings.

From the comparison different wave load models for large monopile type foundations, it is clear that the wave diffraction effects must be taken into account to avoid excessive conservatism. On the other hand, higher-order methods might reduce the fatigue lifetime. It has been shown that improved numerical modelling of waves increases the safety margin compared to simpler methods. This may introduce excessive conservatism depending on the uncertainties accounted for by the safety factors defined in design standards. Hence, a partial safety factor depending on the degree of model complexity might be required to avoid excessive conservatism.

A method for combining response sub-populations (such as idling and operational conditions) for design analysis in FLS and SLS/ULS is proposed (Paper V). For the reference model, reduced fatigue conservatism in the foundation is found when using a probabilistic availability model. For SLS/ULS, it is important to account for the extreme response caused by both an operational and idling turbine. The wave loads have proven dominating for an idling turbine, and higher-order loads may increase the load effects further. In contrast, an operational turbine is less sensitive to wave loads and the response is mainly driven by the aerodynamic loads. Depending on the specific wind turbine model, bottom-fixed or floating, the two states will contribute differently. An extended contour-line method for finding a consistent characteristic extreme response is presented, while accounting for the load effects in both populations. The method significantly influenced the extreme nacelle acceleration of the present numerical model, where the true extreme value was influenced by both the operational and idling state.

To summarize, a complete reliability model using an efficient simulation scheme was implemented to evaluate the impact of environmental loads on the support structure reliability as stated in RO1. The impact of environmental load effects on the fatigue lifetime has been well documented in several of the appended research papers. In relation to RO2, a new environmental model was developed to investigate the effect of modelling uncertainty on the expected lifetime of the support structure. It is seen that the introduction of new variables has a tendency to reduce the modelling uncertainty into statistical uncertainties. These uncertainties can be handled more easily by increased computational efforts. However, reducing the model uncertainty of the environmental load models by high-fidelity methods is likely to yield larger load effects. To justify calibration of new partial safety factors, the reduction of model uncertainties presented in this thesis must be verified by experimental methods or full-scale measurements. The introduction of a stochastic availability parameter (Paper V) contributes to RO2 by limiting the design conservatism through probabilistic analysis. It is a good example on how increased knowledge can be used to reduce design conservatism and energy costs.

6.2 Recommendations for further work

With basis in the work conducted in Paper I to VII, the following suggestions are made for future work:

- Significant non-linear load effects from waves may occur for the present model, indicating that the diffraction problem and non-linear loading should be incorporated in the same hydrodynamic load model. Hence, further development of efficient methods as the SFM, FNV and time-domain panel methods are strongly suggested to reduce load effect uncertainties.

- It was found that an inverse reliability method can be used to reduce the load effect uncertainty of fatigue damage. However, it was concluded that the numerical model of an operational wind turbine has too many short-term stochastic variables for the method to be efficient. Hence, it is suggested that a similar method is applied to the outer-domain stochastic environmental variables. Such a method is expected to reduce the number of combinations of wind speed, significant wave height etc. needed to get a good estimate on the fatigue damage.

- In this thesis, the external parameters are treated as random. However, the model uncertainties may also be included in similar manner. Especially the soil model uncertainty which is likely to yield significant variations in fatigue damage, should get more attention in holistic probabilistic design of bottom-fixed offshore wind turbines. For floating offshore wind turbines, some model uncertainties may be related to the hybrid frequency/time-domain evaluation of the floater dynamics.
- It is suggested to establish a design procedure for offshore wind turbines by including the dynamic properties induced by the control system. For instance, the presented subpopulations should be extended to separate between the wind speeds below and above rated where the pitch controller is activated. Hence, different pitch control strategies and their impact on the lifetime of the structure can be handled more easily.
- As more data becomes available for the drivers of wind turbine downtime, the availability can be modelled with more sophisticated models, by for instance accounting for dependencies between environmental conditions and downtime. Consequently, the downtime caused by inspections and maintenance performed at low wind speeds can be accounted for separately.

Bibliography

Abed, K. A. and A. A. El-Mallah (1997). "Capacity Factor of Wind Turbines". In: *Energy* 22.5, pp. 487–491.

Ambühl, Simon et al. (2015). "Fatigue reliability and calibration of fatigue design factors of wave energy converters". In: *International Journal of Marine Energy* 10, pp. 17–38. ISSN: 22141669.

American Petroleum Institute (API) and International Organization for Standarization (ISO) (2011). *Geotechnical and Foundation Design Considerations for Offshore Structures.* Tech. rep.

Arany, Laszlo et al. (2015). "A Critical Review of Serviceability Limit State Requirements for Monopile Foundations of Offshore Wind Turbines". In: *Proceedings of the Annual Offshore Technology Conference*, pp. 2570–2587. ISSN: 01603663.

Bachynski, Erin E. and Torgeir Moan (2014). "Ringing loads on tension leg platform wind turbines". In: *Ocean Engineering* 84, pp. 237–248. ISSN: 00298018.

Bachynski, Erin E. and Harald Ormberg (2015). "Hydrodynamic modeling of large-diameter bottom-fixed offshore wind turbines". In: *Proceedings of the ASME 34th International Conference on Ocean, Offshore and Arctic Engineering.* St. Johns, Canada: ASME.

Bachynski, Erin E et al. (2014). "Wind-Wave Misalignment Effects on Floating Wind Turbines: Motions and Tower Load Effects". In: *Journal of Offshore Mechanics and Arctic Engineering* 136.4, p. 41902.

Bak, Christian et al. (2013). *Description of the DTU 10 MW Reference Wind Turbine.* Tech. rep. DTU.

Bredmose, H and S J Andersen (2014). "Towards a higher-order spectral force model for vertical circular cylinders". In: 1, pp. 1–4.

— (2016). "Higher-order spectral modelling of the diffraction force around a vertical circular cylinder". In: 2.1, pp. 1–4.

Carswell, Wystan et al. (2015). "Soil-structure reliability of offshore wind turbine monopile foundations". In: *Wind Energy* 18.3. ISSN: 10991824.

Chella, Mayilvahanan Alagan et al. (2016). "Numerical and Experimental Investigation of Breaking Wave Interaction with a Vertical Slender Cylinder". In: *Energy Procedia* 94, pp. 443–451. ISSN: 1876-6102.

Colone, Lorenzo, Anand Natarajan, and Nikolay Dimitrov (2018). "Impact of turbulence induced loads and wave kinematic models on fatigue reliability estimates of o ff shore wind turbine monopiles". In: *Ocean Engineering* 155, pp. 295–309. ISSN: 00298018.

Crabtree, Christopher J., Donatella Zappalá, and Simon I. Hogg (2015). "Wind energy: UK experiences and offshore operational challenges". In: *Proceedings of the Institution of*

Mechanical Engineers, Part A: Journal of Power and Energy 229.7, pp. 727–746. ISSN: 20412967.

DNV GL (2005). *RP-C203 Fatigue design of offshore steel structures.*

— (2014). *OS-J101 Design of Offshore Wind Turbine Structures.*

— (2015). *RP-C210 Probabilistic methods for planning of inspection for fatigue cracks in offshore structures.*

— (2016a). *Loads and site conditions for wind turbines.*

— (2016b). *Support structures for wind turbines.*

— (2017). *RP-C205 Environmental conditions and environmental loads.* Tech. rep.

DNV (1996). *Guideline for offshore structural reliability analysis: application to jacket platforms.* Tech. rep.

Damgaard, M. et al. (2015). "A probabilistic analysis of the dynamic response of monopile foundations: Soil variability and its consequences". In: *Probabilistic Engineering Mechanics* 41, pp. 46–59. ISSN: 02668920.

Doherty, P. and K. Gavin (2011). "Laterally loaded monopile design for offshore wind farms". In: *Proceedings of the Institution of Civil Engineers.*

Dommermuth, Douglas G and Dick K P Yue (1987). "A high-order spectral method for the study of nonlinear gravity waves". In: *J. Fluid Mech.* 184.1987, pp. 267–288. ISSN: 1098-6596.

EWEA (2013). *Deep water - The next step for offshore wind energy.* July, p. 51. ISBN: 9782930670041.

Engsig-Karup, A P, H B Bingham, and O Lindberg (2009). "An efficient flexible-order model for 3D nonlinear water waves". In: *Journal of Computational Physics* 228.6, pp. 2100–2118. ISSN: 0021-9991.

Faltinsen, O. M., J. N. Newman, and T. Vinje (1995). "Nonlinear wave loads on a slender vertical cylinder". English. In: *Journal of Fluid Mechanics* 289, p. 179. ISSN: 0022-1120.

Feng, Aichun et al. (2016). "A Rankine source method solution of a finite depth, wave–body interaction problem". In: *Journal of Fluids and Structures* 62. ISSN: 0889-9746.

Florian, Mihai and John Dalsgaard Sørensen (2017). "Risk-based planning of operation and maintenance for offshore wind farms". In: *Energy Procedia* 137, pp. 261–272. ISSN: 18766102.

Forbes, Catherine et al. (2010). "von Mises Distribution". In: *Statistical Distributions.* John Wiley & Sons, Inc., pp. 191–192. ISBN: 9780470627242.

Forewind (2010). *Dogger Bank - Environmental Impact Assessment Scoping Report.* Tech. rep. October.

GL Garrad Hassan (2013). *A guide to UK offshore wind operations and maintenance.* Tech. rep.

Gonzalez-Rodriguez, Angel G. (2017). "Review of offshore wind farm cost components". In: *Energy for Sustainable Development* 37, pp. 10–19. ISSN: 09730826.

Guillaume, Ducrozet et al. (2011). "A comparative study of two fast nonlinear free-surface water wave models". In: *International Journal for Numerical Methods in Fluids* 69.11, pp. 1818–1834. ISSN: 0271-2091.

Haldar, Sumanta, Jitendra Sharma, and Dipanjan Basu (2018). “Probabilistic analysis of monopile-supported offshore wind turbine in clay”. In: *Soil Dynamics and Earthquake Engineering* 105, pp. 171–183. ISSN: 0267-7261.

Hansen, M.O.L. et al. (2006). “State of the art in wind turbine aerodynamics and aeroelasticity”. In: *Progress in Aerospace Sciences* 42.4, pp. 285–330. ISSN: 03760421.

Hansen, Martin O L (2013). *Aerodynamics of wind turbines, Second edition.* Vol. 9781849770, pp. 1–181.

Hansen, Martin Otto Laver et al. (2009). “vpOne - a new FEM based servo-, hydro- and aeroelastic code for wind turbines”. In: *Offshore Wind Energy.*

Hansen, Morten Hartvig (2016). “Modal dynamics of structures with bladed isotropic rotors and its complexity for 2-bladed rotors”. In: *Wind Energy Science* 1, pp. 271–296. ISSN: 2366-7621.

Horn, Jan-Tore (2015). *Stochastic Dynamic Analysis of Offshore Bottom-Fixed Structures.* Tech. rep. NTNU/AMOS, p. 139.

Horn, Jan-Tore, Jørgen Amdahl, and Sverre K. Haver (2015). “Dynamic Amplification of Drag Dominated Structures in Irregular Seas”. In: *Proceedings of OCEANS’15 MTS/IEEE Washington Conference & Exhibition.* IEEE conference proceedings. ISBN: 978-0-933957-43-5.

Horn, Jan-Tore and Jørgen Juncher Jensen (2016). “Reducing uncertainty of Monte Carlo estimated fatigue damage in offshore wind turbines using FORM”. In: *Proceedings of the 13th International Symposium on Practical Design of Ships and Other Floating Structures (PRADS).* Copenhagen, Denmark. ISBN: 9788774754732.

Horn, Jan-Tore, Jørgen R. Krokstad, and Jørgen Amdahl (2016). “Hydro-Elastic Contributions to Fatigue Damage on a Large Monopile”. In: *Energy Procedia* 94, pp. 102–114.

— (2017). “Joint probability distribution of environmental conditions for design of offshore wind turbines”. In: *Proceedings of the International Conference on Offshore Mechanics and Arctic Engineering - OMAE.* Trondheim, Norway. ISBN: 9780791857786.

— (2018). “Long-Term Fatigue Damage Sensitivity to Wave Directionality in Extra Large Monopile Foundations”. In: *Journal of Engineering for the Maritime Environment* 232, pp. 37–49.

Horn, Jan-Tore, Jørgen R. Krokstad, and Bernt J. Leira (2018). “Impact of model uncertainties on the fatigue reliability of offshore wind turbines”. In: *Marine Structures* 64, pp. 174–185.

Horn, Jan-Tore and Bernt J. Leira (2018). “Fatigue reliability assessment of offshore wind turbines with stochastic availability”. In: *Accepted to: Reliability Engineering & System Safety.*

Horn, Jan-Tore, Bernt J. Leira, and Jørgen Amdahl (2017). “A Preliminary Study of Reliability-based Controller Scheduling in Offshore Wind Turbines (poster)”. In: *EERA DeepWind’2017, 14th Deep Sea Offshore Wind R&D Conference.* Trondheim, Norway.

Horn, Jan-Tore and Steven R. Winterstein (2018). “Extreme response estimation of offshore wind turbines with an extended contour-line method”. In: *Journal of Physics: Conference Series* 1104, pp. 1–10.

Horn, Jan-Tore et al. (2018). “A new combination of conditional environmental distributions”. In: *Applied Ocean Research* 73, pp. 17–26. ISSN: 0141-1187.

International Electrotechnical Commission (2009). *IEC 61400-3, Wind turbines—Part 3: design requirements for offshore wind turbines.* Tech. rep.

Kelley, N.D. and B.J. Jonkman (2007). *Overview of the TurbSim stochastic inflow turbulence simulator.* Tech. rep.

Kristiansen, Trygve and Odd M Faltinsen (2017). "Ringing loads on a vertical cylinder in finite water depth". In: *Journal of Fluid Mechanics* 3, pp. 1–4.

Lesny, Kerstin (2010). *Foundations for Offshore Wind Turbines: Tools for Planning and Design.* VGE Verlag.

Li, Qinyuan, Zhen Gao, and Torgeir Moan (2016). "Modified environmental contour method for predicting long-term extreme responses of bottom-fixed offshore wind turbines". In: *Marine Structures* 48, pp. 15–32. ISSN: 09518339.

— (2017). "Modified environmental contour method to determine the long-term extreme responses of a semi-submersible wind turbine". In: *Ocean Engineering* 142.July, pp. 563–576. ISSN: 00298018.

MacCamy, R. C. and R. A. Fuchs (1954). *Wave Forces on Piles: A Diffraction Theory.*

Madsen, H.O., S. Krenk, and N.C. Lind (1986). *Methods of Structural Safety.* Prentice-Hall, Inc.

Marquez-Dominguez, Sergio and John D Sorensen (2012). "Fatigue Reliability and Calibration of Fatigue Design Factors for Offshore Wind Turbines". In: *Energies* 5.6, pp. 1816–1834. ISSN: 1996-1073.

Martinez-Luengo, Maria, Athanasios Kolios, and Lin Wang (2016). "Structural health monitoring of offshore wind turbines: A review through the Statistical Pattern Recognition Paradigm". In: *Renewable and Sustainable Energy Reviews* 64, pp. 91–105. ISSN: 18790690.

Merz, Karl O. (2016). "Basic controller tuning for large offshore wind turbines". In: *Wind Energy Science* 1.2, pp. 153–175. ISSN: 2366-7451.

Moan, Torgeir and Arvid Naess (2013). *Stochastic Dynamics of Marine Structures.* Cambridge University Press.

Morison, J.R., J.W. Johnson, and S.A. Schaaf (1950). "The Force Exerted by Surface Waves on Piles". In: *Journal of Petroleum Technology* 2.05, pp. 149–154. ISSN: 0149-2136.

Nielsen, Jannie Jessen and John Dalsgaard Sørensen (2011). "On risk-based operation and maintenance of offshore wind turbine components". In: *Reliability Engineering and System Safety* 96.1, pp. 218–229. ISSN: 09518320.

Page, Ana M. et al. (2017). "A New Foundation Model for Integrated Analyses of Monopile-based Offshore Wind Turbines". In: *Energy Procedia* 137, pp. 100–107. ISSN: 18766102.

Reistad, Magnar et al. (2011). "A high-resolution hindcast of wind and waves for the North Sea, the Norwegian Sea, and the Barents Sea". In: *Journal of Geophysical Research: Oceans* 116.5, pp. 1–18.

SINTEF and NTNU (2003). *USFOS.*

Sarker, Bhaba R. and Tasnim Ibn Faiz (2016). "Minimizing maintenance cost for offshore wind turbines following multi-level opportunistic preventive strategy". In: *Renewable Energy* 85, pp. 104–113. ISSN: 18790682.

Schløer, Signe et al. (2018). "A model for Quick Load Analysis for monopile-type offshore wind turbine substructures". In: *Wind Energy Science* 3, pp. 57–73. ISSN: 17426596.

Shao, Yan-lin and Odd M Faltinsen (2014). “A harmonic polynomial cell (HPC) method for 3D Laplace equation with application in marine hydrodynamics”. In: *Journal of Computational Physics* 274, pp. 312–332. ISSN: 0021-9991.

Sharma, Abhishek B, Leana Golubchik, and Ramesh Govindan (2010). “Sensor Faults: Detection Methods and Prevalence in Real-world Datasets”. In: *ACM Trans. Sen. Netw.* 6.3, 23:1–23:39. ISSN: 1550-4859.

Slavik, Kaela et al. (2017). *The large scale impact of offshore wind farm structures on pelagic primary production in the southern North Sea.* Tech. rep. arXiv: `1709.02386`.

Smilden, Emil et al. (2016). “Reduced Order Model for Control Applications in Offshore Wind Turbines”. In: *The 10th IFAC Conference on Control Applications in Marine Systems (CAMS).* Vol. 49. 23. Trondheim, Norway.

Sørensen, John D. and Henrik S. Toft (2010). “Probabilistic Design of Wind Turbines”. In: *Energies* 3.2, pp. 241–257. ISSN: 19961073.

Sørum, Stian H., Jan-Tore Horn, and Jørgen Amdahl (2017). “Comparison of numerical response predictions for a bottom-fixed offshore wind turbine”. In: *Energy Procedia* 137, pp. 89–99.

The Crown Estate (2012). *Offshore wind cost reduction-Pathways study.* Tech. rep., 88 pp.

Toft-Christensen, Palle and Yoshisada Murotsu (1986). *Application of Structural Systems Reliability Theory.* Springer. ISBN: 978-3-642-82764-8.

Tucker, M.J., P.G. Challenor, and D.J.T. Carter (1984). “Numerical simulation of a random sea: a common error and its effect upon wave group statistics”. In: *Applied Ocean Research* 6.2, pp. 118–122. ISSN: 01411187.

Velarde, Joey (2016). *Master thesis: Design of monopile foundations to support the DTU 10MW wind turbine.* Tech. rep. Norwegian Univeristy of Science and Technology.

WAMIT Inc (2011). *Wamit user manual 7.0.* Tech. rep.

WindEurope (2017). *Offshore wind in Europe - key trends and statistics 2017.* Tech. rep.

Winterstein, Steven R. et al. (1993). “Environmental parameters for extreme response: Inverse FORM with omission factors”. In: *Proc. 6th Int. Conf. on Structural Safety and Reliability, Innsbruck, Austria.*

Ziegler, Lisa et al. (2018). “Lifetime extension of onshore wind turbines: A review covering Germany, Spain, Denmark, and the UK”. In: *Renewable and Sustainable Energy Reviews* 82.October 2017, pp. 1261–1271. ISSN: 18790690.

Appended papers

Paper I

Hydro-Elastic Contributions to Fatigue Damage on a Large Monopile

Jan-Tore Horn, Jørgen R. Krokstad, and Jørgen Amdahl

Energy Procedia, 2016

Abstract The present work identifies the qualitative hydro-elastic contributions to fatigue damage on large volume monopiles intended for use in the offshore wind energy industry. Although aerodynamic effects cannot be neglected in a complete dynamic analysis of the structure, the scope of this work is limited to wave loads and soil effects on a turbine in simplified operational conditions. As the rotors are scaled up to improve efficiency and reduce the overall costs in wind farms, the foundation and support structure dimen- sions are increased. As a result, the fluid-structure interaction becomes important for wave-lengths comparable to the characteristic size of the structure. The importance of including diffraction effects is present in the results. Also, the contributions from ringing type response in a fatigue-limit sea-state is investigated by applying the third order Faltinsen, Newman, Vinje (FNV) formulation. Hydrodynamic loading is applied as particle velocities in a spatial time variant grid for first and second order wave theories in long crested irregular waves. Additionally, the second order diffraction forces are calculated using an internationally recognized panel code for second order sum-frequency diffraction forces.

Available online at www.sciencedirect.com

ScienceDirect

Energy Procedia 94 (2016) 102 – 114

Energy Procedia

13th Deep Sea Offshore Wind R&D Conference, EERA DeepWind'2016, 20-22 January 2016, Trondheim, Norway

Hydro-Elastic Contributions to Fatigue Damage on a Large Monopile

Jan-Tore H. Horn[a,b,*], Jorgen R. Krokstad[b,c], Jorgen Amdahl[a,b]

[a] *Centre for Autonomous Marine Operations and Systems (AMOS), NTNU, 7491 Trondheim, Norway*
[b] *Department of Marine Technology, NTNU, 7491 Trondheim, Norway*
[c] *Statkraft, Sluppenvegen 17B, 7037 Trondheim, Norway*

Abstract

The present work identifies the qualitative hydro-elastic contributions to fatigue damage on large volume monopiles intended for use in the offshore wind energy industry. Although aerodynamic effects cannot be neglected in a complete dynamic analysis of the structure, the scope of this work is limited to wave loads and soil effects on a turbine in simplified operational conditions. As the rotors are scaled up to improve efficiency and reduce the overall costs in wind farms, the foundation and support structure dimensions are increased. As a result, the fluid-structure interaction becomes important for wave-lengths comparable to the characteristic size of the structure. The importance of including diffraction effects is present in the results. Also, the contributions from ringing type response in a fatigue-limit sea-state is investigated by applying the third order Faltinsen, Newman, Vinje (FNV) formulation. Hydrodynamic loading is applied as particle velocities in a spatial time variant grid for first and second order wave theories in long crested irregular waves. Additionally, the second order diffraction forces are calculated using an internationally recognized panel code for second order sum-frequency diffraction forces.

Peer-review under responsibility of SINTEF Energi AS

Keywords: monopile;wind turbine;fatigue;nonlinear;wave loads;fnv;maccamy;fuchs;diffraction;kinematics;cylinder;

---

1. Introduction

Monopile foundations for offshore wind turbines are presently the most cost-effective solution due to its simple construction. In 2014, 91% of the installed substructure types were monopiles [1]. Even for increasing water depths of more than 30 meters, the monopile foundation has shown to be the preferred choice. Furthermore, over the last 10 years, the average wind turbine capacity has increased significantly. As a result of an evolving industry, extra large monopiles are under development for future offshore wind farms.

With increasing dimensions and higher natural periods due to large rotors and drive-trains, the methods to reproduce environmental loads need to be re-evaluated. Leaving out the wind loads have several consequences strongly

---

[*] Corresponding author. Tel.: +47 971 56 990.
E-mail address: jan-tore.horn@ntnu.no

Peer-review under responsibility of SINTEF Energi AS
doi:10.1016/j.egypro.2016.09.203

depending on the turbine, environmental conditions and water depth. The wind is in general expected to contribute to fatigue damage compared to wave-only simulations if the aerodynamic damping is accounted for in both cases. For a mis-aligned or idling case, the wave-induced fatigue damage may be dominating due to the low damping. An analysis of wind/wave contributions can be found in [2], where the wave contribution with interaction effects on a jacket foundation may pose up to 35% of long-term fatigue damage. On a large monopile, wave loads are expected to be even more prominent, but more research is needed on this topic.

In the present paper, several well-known methods for estimating hydrodynamic loads and their effect upon fatigue damage are compared when used in the analysis of a large-diameter monopile (D=9m). The model used is comparable to the DTU 10MW reference wind turbine [3], with regards to mass of nacelle (446tons) and rotor (228tons). For nonlinear time-domain simulations, the space frame analysis program USFOS [4] has been used. Although USFOS supports first order wave loads, all wave kinematics are pre-generated in a MATLAB program, verified in [5], and applied in a spatial grid of velocities and accelerations. The kinematics are converted to loads by USFOS with the Morison equation. Also, second order forces are calculated from the quadratic transfer function (QTF) obtained with the SESAM software HydroD and Wadam [6] and later applied as local forces during simulation. This procedure is similar to what is presented in [7], but on a deep water TLP wind turbine. In this paper, a location at Dogger Bank with 30m depth is considered.

2. Simulation model

For the purely hydro-elastic analysis performed in this study, the monopile with the tower is modeled as a cantilever beam. The rotor and nacelle masses are both lumped onto the top of the tower as only constant aerodynamic forces and damping are accounted for. Still, it is important to get correct mode shapes and periods for the time-domain analysis. Therefore, also the soil is modeled with care to reflect the soil layers from the specific area. Geotechnical considerations are done using API standards for sand and stiff clay, and further implemented as equivalent nonlinear springs on the pile. Fig. 1 shows the main dimensions of the model whose pile is hammered down 42 meters into the soil, and the modal shapes for the two largest eigenvalues.

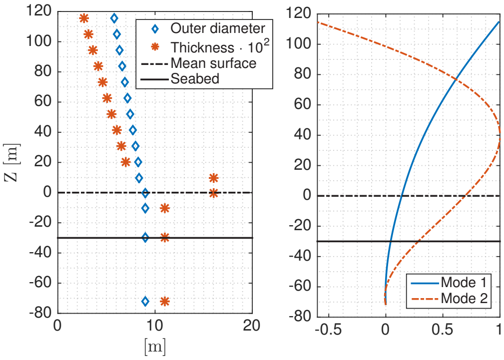

(a) (b)

Fig. 1. Main dimensions of monopile with tower in (a) and normalized modeshapes in (b).

The first tower bending mode has an eigenperiod of 4.1 seconds, while the second eigenperiod is 1.0 seconds. Damping is modeled as a Rayleigh structural damping of 1% at the first and second eigenperiod, giving Rayleigh parameters of 0.0256 and 0.0025, respectively. For higher damping ratios, the parameters are increased linearly. In addition, the dissipation of energy due to soil damping is modeled as a hysteresis damping equal to a energy loss of about 4% [8] per each oscillatory cycle in a decay test. An equivalent Rayleigh damping of 3% satisfies this contribution for the present model, including a small compensation for missing aerodynamic damping. Later, variation of damping will be introduced in the analyses to compare responses for lightly damped operational conditions, such as mis-aligned wind and waves.

3. First order wave kinematics

3.1. Finite water depth

The Airy theory wave potential for finite water depth in (1) is used for calculating first order irregular wave kinematics. The dispersion relation is given by (3) and the surface elevation, particle velocity and accelerations can be found with (2), (4) and (5), respectively [9]. For $z > 0$, i.e. above the mean water line, the kinematics are stretched according to Section 6.

$$\Phi_{1,n}(x,z,t) = \Im\left\{\frac{g\zeta_{a,n}}{\omega_n}\frac{\cosh(k_n(z+h))}{\cosh(k_n h)}e^{-i\phi_n(x,t)}\right\} \tag{1}$$

$$\zeta_1(x,t) = \Re\left\{\sum_{n=1}^{N}\zeta_{a,n}e^{-i\phi_n(x,t)}\right\} \tag{2}$$

$$\omega_n^2 = k_n g \tanh(k_n h) \tag{3}$$

$$u_1(x,z,t) = \sum_{n=1}^{N}\frac{\partial\Phi_{1,n}(x,z,t)}{\partial x} \tag{4}$$

$$a_1(x,z,t) = \sum_{n=1}^{N}\frac{\partial^2\Phi_{1,n}(x,z,t)}{\partial x\partial t} \tag{5}$$

Here, elevation and kinematics are obtained by summation over N wave components with frequency ω_n and amplitude $\zeta_{a,n}$. The phase, ϕ for each wave is given by (6) for propagation along the positive x-axis, where ϵ is a random phase angle, uniformly distributed between 0 and 2π.

$$\phi_n(x,t) = \omega_n t - k_n x + \epsilon \tag{6}$$

The summations in the equations above are evaluated using a Fast Fourier Transform (FFT) algorithm in MATLAB. See e.g. [10] for details of implementation. How the random wave amplitudes are obtained is described in Section 7.3.2.

3.2. Linear diffraction theory

When the monopile diameter is in the same order of magnitude as the wave length, diffraction forces should be accounted for, more specific, when $\pi D > 0.5\lambda$, as given in [11] for first order wave theory. The analytical solution for the scattering of a wave around a circular cylinder is known as the MacCamy and Fuchs correction and can be found in e.g. [12]. Here, the formulation is applied as a correction of the acceleration components equivalent to the magnitude of the inertia coefficient, C_M. With C_M constantly equal to 2, the acceleration is modified according to the function seen in Fig. 2, which is similar to the built-in correction in USFOS. The fitted function is used to avoid table look-ups and continuous evaluation of Bessel functions. A similar function is fitted to the phase lag present at diffraction [12]. A significant reduction in the equivalent diffracted acceleration is seen for short waves and large diameters. Note that a homogenous vertical column is assumed since the solution is not valid for conical shapes. The movement of the cylinder is also neglected when the kinematics are calculated and forces are applied, this is expected to be a good approximation as the horizontal displacements are very small at the mean surface (< 0.1m).

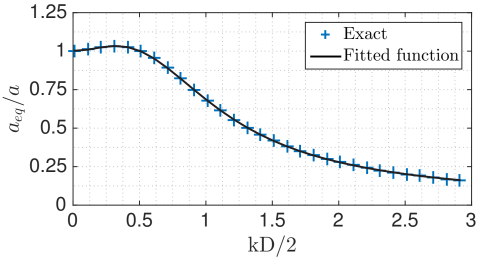

Fig. 2. Equivalent diffracted wave acceleration relative to incident wave acceleration, as a function of diameter and wave number

3.3. Panel code pressure and acceleration

The panel code has been used to verify the linear diffraction theory results. Linear panel pressures are found for the complete model, consisting of over 3000 panels. These are integrated in the frequency domain and the resulting non-dimensional horizontal pressure is found throughout the depth with (7), where $A_n \cdot n_{x,n}$ is the effective area in x-direction for panel n and $p_n(z_i, \omega_m)$ is the linear non-dimensional complex pressure evaluated by the panel code at $z = z_i$ and $\omega = \omega_m$.

$$\bar{p}_x(z_i, \omega_j) = \frac{\sum_{n=1}^{N} p_n(z_i, \omega_j) \cdot A_{n,i} \cdot n_{x,n,i}}{\sum_{n=1}^{N} A_{n,i} \cdot n_{x,n,i}} \tag{7}$$

Further, the pressure is linearly interpolated from $\bar{p}_x(z_i, \omega_j)$ to $\tilde{p}_x(z, \omega_m)$ for the targeted values of z and ω_m. Transformation to time-domain and re-dimensionalizing is done with (8).

$$p_x(z,t) = \Re\left\{\sum_{m=1}^{M} \rho \cdot g \cdot \tilde{p}_x(z, \omega_m) \cdot \zeta_{a,m} \cdot e^{-i\phi_m}\right\} \tag{8}$$

Finally, equivalent accelerations are found according to (9) for $C_M = 2$, which are to be used in the Morison equation (16).

$$a_x(z,t) = \frac{p_x(z,t)}{\rho \frac{\pi^2}{4} D} \tag{9}$$

4. Second order wave kinematics

4.1. Finite water depth

For second order incident wave kinematics, the formulation presented in [13] is used for sum-frequency wave components. Difference-frequency terms are neglected in this study due to a structural system with high eigenfrequencies. The term H^+_{mn} in (10) is the sum-frequency transfer function dependent on wave components and vertical coordinate. Particle velocity and acceleration can be found by differentiation of the potential, while the sum-frequency wave elevation is found according to (11).

$$\Phi_2(x,z,t) = \Im\left\{\sum_{n=1}^{N}\sum_{m=1}^{M} \zeta_{a,n}\zeta_{a,m} H^+_{mn}(z) e^{-i\phi^+_{mn}(x,t)}\right\} \tag{10}$$

$$\zeta_2(x,t) = \Re\left\{\sum_{n=1}^{N}\sum_{m=1}^{N} \zeta_{a,n}\zeta_{a,m} V^+_{mn} e^{-i\phi^+_{mn}(x,t)}\right\} \tag{11}$$

Here, H^+_{mn} and V^+_{mn} can be found in [13], and $\phi^+_{mn}(x,t) = \phi_n(x,t) + \phi_m(x,t)$. The double summations are evaluated using a two-dimensional FFT algorithm in MATLAB, which is very efficient, but memory demanding for long realizations. Hence, simulations in this study are limited to 30 minutes with a time-step of 0.1 seconds. The complete second order horizontal particle velocity can be modeled up to the free surface elevation by the use of a Taylor expansion [14]. The procedure can be found in e.g. [11]. The horizontal velocity can then be found as:

$$u(z) = \begin{cases} u_1(z) + u_2(z) & \text{for } z \leq 0 \\ u_1(0) + z\frac{\partial u_1(z)}{\partial z}\big|_{z=0} + u_2(0) & \text{for } z > 0 \end{cases} \tag{12}$$

where u_1 and u_2 are the linear and second order sum-frequency contributions. Similar stretching is performed on the acceleration term. However, this method does not provide a consistent order in the integrated force or moment, see Section 6 for further discussion.

4.2. Panel code QTF

For second order diffraction forces, analytical solutions are available and presented in e.g. [15]. This solution is not implemented in the present work, as the Wadam panel code in HydroD is used instead. A QTF for the total second order force is evaluated in the current frequency range with a 60×60 frequency resolution. For such analysis, HydroD requires a circular second order surface model. In shallow water, the radius of the surface mesh is suggested to be at least equal to the water depth [16]. Here, a radius twice the depth and an element size of maximum 1.0m are used, which is also consistent with [17]. The resulting QTF for total second order pitch force on the monopile is shown in Fig. 3 (a) along with the corresponding phase in Fig. 3 (b).

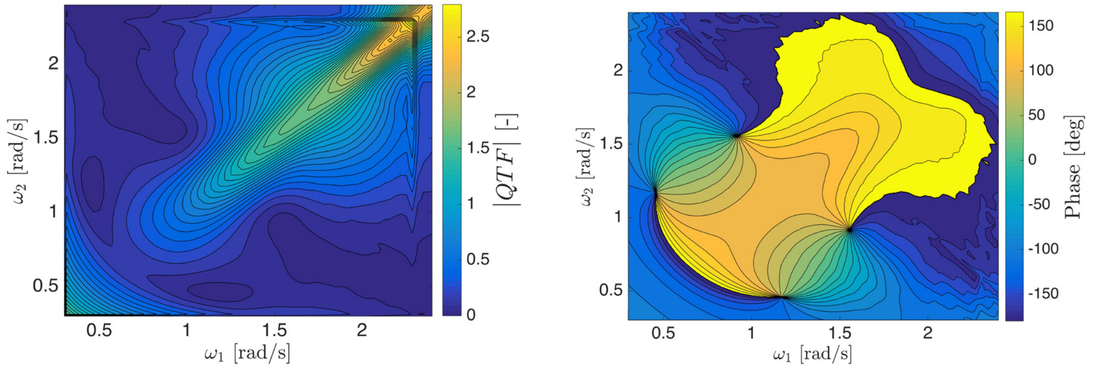

(a)

(b)

Fig. 3. Example pitch force QTF (a), phase (b) for monopile

The total second order horizontal force are lumped to the mean surface using (13), where subscript denotes the degree-of-freedom. The force/moment is found using (14), where Θ is the phase found in Fig. 3 (b) and D is the diameter. A 2D FFT is necessary for fast evaluation of the double summation.

$$F^{(2)}|_{z=0} = F_1^{(2)}|_{z=0} + F_5^{(2)}|_{z=0}/h \tag{13}$$

$$\frac{F_i^{(2)}|_{z=0}}{\rho g D^{\lceil 2i/7 \rceil}} = \Re\left\{\sum_{n=1}^{N}\sum_{m=1}^{M}\zeta_{an}\zeta_{am}QTFe^{-i(\phi_{mn}^{+}+\Theta_{mn})}\right\} \tag{14}$$

Further, the load is applied as a nodeload at the mean surface in USFOS during simulation. The validity and accuracy of this assumption can be discussed. However, by investigation of some simple load cases in Fig. 5, it is easily seen from the moment diagrams in Fig. 6 that converting the moment to a point load is more correct, especially for short waves concentrating the load at the top of the cylinder. To obtain even more reliable results and include the correct pressure distribution, which is penetrating deeper than e^{2kz}, the complete second order panel pressures should be taken directly from Wadam and applied in the kinematics grid. This is illustrated in Fig. 4, but it is computationally demanding. A conclusion is made that applying the second order panel code force as a point load is regarded as sufficiently accurate in this case. For the dominating linear panel code pressures, it would be fairly overconservative to apply the pressure as a point force, due to the interaction with the eigenmodes in Fig. 1 (b).

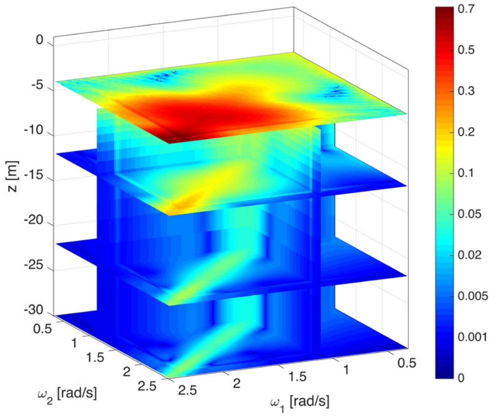

Fig. 4. Complete second order non-dimenpressure QTF from panel code

5. Third order ringing force

To model the high order ringing response, which is known to occur in steep waves, the third order FNV long-wave formulation is applied. Some of the observed criteria for ringing loads to occur include [18]: low Keulegan-Carpenter (KC) number (<5), low D/λ ratio (< 0.2) and large enough eigenperiod to have significant dynamic responses. It is expected that the monopile in question will experience ringing loads under certain wave conditions. The third order

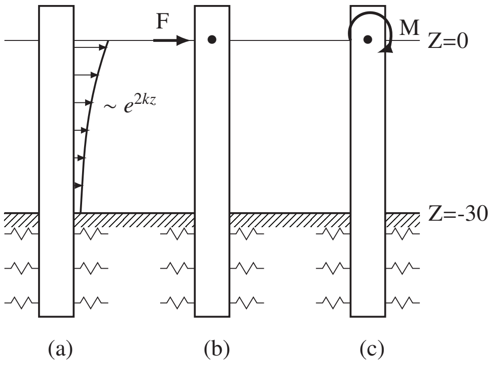

Fig. 5. Monopiles with different loadings

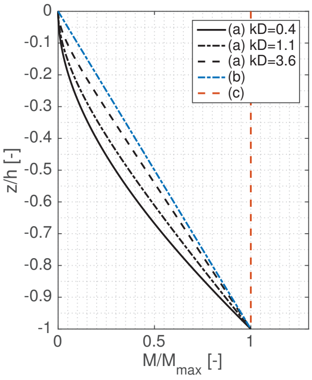

Fig. 6. Moment distributions for cases in Fig. 5 with k=0.08. Very stiff soil springs are assumed.

horizontal force is presented in [19] and [20] and reproduced in (15). Differentiation is given by subscripts.

$$F_x^{FNV(3)} = \rho\pi a^2 \left[\zeta_1 \left(\zeta_1 u_{tz} + 2ww_x + uu_x - \frac{2}{g} u_t w_t \right) - \left(\frac{u_t}{g} \right) (u^2 + w^2) + \frac{\beta}{g} u^2 u_t \right] \Bigg|_{z=0} \tag{15}$$

It can be shown that $\beta \to 4$, when $h/D \to \infty$. However, by using the formulations found in [19], it is seen that β converges very quickly, and that using $\beta = 4$ is a good approximation. This solution is based on a derivation assuming deep water which is not the case for large sea-states in the present study. It is therefore expected that the dominating last term in (15) will lead to some still unquantified underprediction of the third order force.

Implementation and evaluation of the original third order FNV formulation above is very efficient as it is only based on the first order potential. The resultant horizontal force from (15) is applied as a nodal force at the mean waterline during simulation. The direct implementation does introduce some unwanted difference-frequency terms, and an alternative would be to use the bandwidth-limited FNV formulation by Johannessen in [21]. For this study, the original formulation is used due to its simplicity and extremely efficient evaluation.

6. Overview of wave kinematics

Wave kinematics are evaluated according to the order of the corresponding integrated horizontal force. For velocity potential and wave elevation up to second order, the contributions are illustrated in Fig. 7 and described in Table 1. For evaluation of the order $O(F_x)$, the relations $k\zeta_a = O(\epsilon)$ and $kD = O(\delta)$ are used. In other words, both the wave amplitude and structural diameter are assumed small compared to the wave length. Further, it is reasonable to assume that the amplitude and diameter are of the same order, so that $\epsilon \approx \delta$. The resulting orders are comparable to those in [19] and [22]. Note also that field G also contains a fifth order term due to linear stretching which is neglected in Table 1.

Here, the force due to wave elevation is only included in second or higher order terms, to be consistent with forces from the panel code and the order of

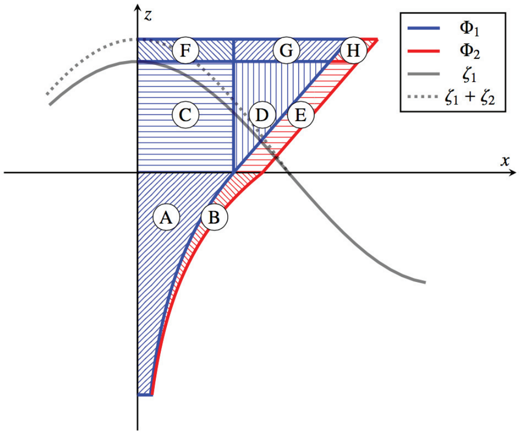

Fig. 7. Wave kinematics stretching for first and second order incident wave potential.

Table 1. Horizontal inertia force characteristics

Fig. 7	$F_x/(0.5\pi\rho D^2)$	$O(F_x)$	$F_x \propto$	Frequency	Comment
A	$\int_{-h}^{0} u_{1,t}(z)dz$	$\epsilon\delta^2$	ζ_a	1ω	Morison inertia force
B	$\int_{-h}^{0} u_{2,t}(z)dz$	$\epsilon^2\delta^2$	ζ_a^2	2ω	Second order force from second order potential
C	$\int_{0}^{\max(0,\zeta_1)} u_{1,t}(0)dz$	$\epsilon^2\delta^2$	ζ_a^2	2ω	Second order due to first order potential with Airy stretching
D	$\int_{0}^{\max(0,\zeta_1)} zu_{1,tz}dz$	$\epsilon^3\delta^2$	ζ_a^3	$1\omega + 3\omega$	Third order force due to linear extrapolation of first order kinematics
E	$\int_{0}^{\max(0,\zeta_1)} u_{2,t}(0)dz$	$\epsilon^3\delta^2$	ζ_a^3	$1\omega + 3\omega$	Third order force due to vertical extrapolation of second order kinematics
F	$\int_{\max(0,\zeta_1)}^{\max(0,\zeta_1+\zeta_2)} u_{1,t}(0)dz$	$\epsilon^3\delta^2$	ζ_a^3	$1\omega + 3\omega$	Third order force from Airy stretching to second order surface
G	$\int_{\max(0,\zeta_1)}^{\max(0,\zeta_1+\zeta_2)} zu_{1,tz}(0)dz$	$\epsilon^4\delta^2$	ζ_a^4	4ω	Fourth order force from linear stretching to second order surface
H	$\int_{\max(0,\zeta_1)}^{\max(0,\zeta_1+\zeta_2)} u_{2,t}(0)dz$	$\epsilon^4\delta^2$	ζ_a^4	4ω	Fourth order force due to stretching of second order kinematics

integrated horizontal force. The first order wave elevation term corresponding to field C in Fig. 7 has shown to be of large significance for drag-dominated, small diameter structures [23], as the maximum velocity is found at the wave crest. In contrast, the maximum force occurs with a phase of approximately $\pi/2$ [rad] before the wave crest for an inertia dominated cylinder. This makes the higher order forces less dominating for the baseline moment for a small diameter structure. In fact, for the regular wave in Fig. 7, the acceleration will be zero at the crest on a slender structure, but phase lag due to diffraction will shift the acceleration peak closer to the wave crest [5].

By investigating Fig. 7 and taking into account the stretching technique given in (12), the expressions for horizontal forces are found in column two in Table 1. Term A corresponds to the first order Morison inertia force without the inclusion of wave elevation. Term D corresponds to the first term in the third order FNV solution given in (15), but only for $\zeta_1(t) \geq 0$. This is illustrated in Fig. 8. As a consequence, the third order force from stretching will act slightly above the mean surface, which can be of significance for steep waves. Some inconsistency arises with the present kinematics scheme, namely a varying order of the horizontal force, dependent on $\zeta_1(t)$. Term F is the third order force dependent on the second order elevation. This corresponds to the 4th, 5th and 6th term in (15), but with different definition and perturbation for ζ_2. The remaining terms in the third order FNV solution are due to linear and non-linear diffraction potentials.

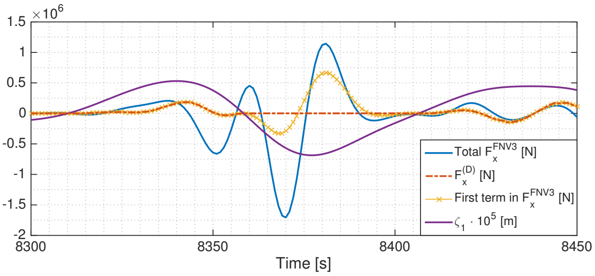

Fig. 8. Third order forcing terms with linear surface elevation

7. Dynamic simulations

7.1. Hydrodynamic models

The wave elevation and kinematics are calculated using a MATLAB script utilizing the FFT, see [10] for details. Due to some limitations in matrix size, half hour simulations are carried out as opposed to the recommended one hour. However, for a qualitative comparison study, this is of no significant importance. To reduce the impact of single, highly non-linear surface realizations, results are presented as the average findings for three 30 minute simulations for each sea-state.

The different notations and descriptions for the hydrodynamic load models used in the analyses are shown in Table 2. Combinations of these will be superimposed in time-domain. For the models O1, O1D, O2, O3 and O1P the load transfer is performed with the Morison equation given in (16). Due to the large diameter, the drag loads are small, but the particle velocities are still present in the kinematics grid as they will influence the load with large amplitude waves. For low KC numbers and large surface piercing cylinders, it is recommended to use C_M=2 and C_D=1 [24]. These coefficients are the theoretical values for large-diameter cylinders [25], although C_M is wave number dependent. This is, as mentioned, taken care of in the particle acceleration. Variation of C_D should be performed if the drag force is significant, but kept constant in this study. Note that the incident particle velocity with corresponding order is used when evaluating the drag loads for *all* load models, except the O2P and FNV3 load cases, which only contain inertia forces.

$$dF_x(t,z) = \frac{\rho\pi^2 D^2}{4} C_M u_t(t,z)dz + \frac{\rho D}{2} C_D u(t,z)|u(t,z)|dz \tag{16}$$

Table 2. Hydrodynamic load models

Notation	Fields in Fig. 7	Description
O1	A	First order incident wave potential
O1D	A	First order incident wave potential w/diffraction
O2	B+C	Second order incident wave potential and stretched first order potential
O3	D+E+F+G+H	Third and fourth order force from stretched first and second order potential
O1P	A	First order diffraction pressure from panel code modeled as acceleration
O2P	B+C	Total second order diffraction force from panel code
FNV3	N/A	Third order FNV ringing force based on first order incident potential

7.2. Wave kinematics grid

The wave kinematics acting on the structural elements are found by interpolating in a time variant grid containing particle velocities and accelerations. Since long crested waves are assumed, and the kinematics are evaluated at the vertical centerline of the monopile, only variation of the vertical component is needed. Fig. 9 shows an example distribution of gridpoints in the z-direction, which are chosen to be distributed with a cumulative function increasing logarithmically. This is to ensure sufficient amount of datapoints between the most probable extreme wave crest $E[\zeta_m]$ and the lowest trough. Note that these values are both time and sea-state dependent. For all simulations, 40 points in the vertical direction is used, which has shown to give accurate results.

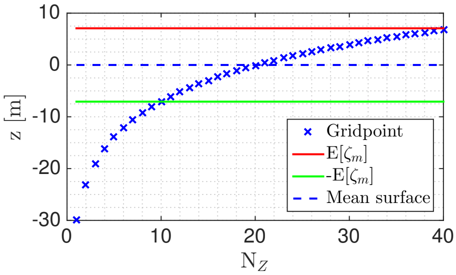

Fig. 9. Vertical distribution of gridpoints for sea-state no. 5

7.3. Environmental conditions

7.3.1. Sea-states

The sea-states are chosen to reflect a wide range of FLS conditions at Dogger Bank. In Table 3 all sea-states except number 6, are based on metocean data with the corresponding annual probability of occurrence. As seen from the KC number estimated from maximum linear particle velocity and average wave period, all conditions are expected to have dominating contributions from inertia forces, while sea-states 1-3 will also be in the wave diffraction regime [11]. Sea-state no. 6 is an additional contribution to see if an even larger T_P has any effects upon the third order FNV excitation.

Table 3. Chosen sea-states for Dogger Bank conditions. (*Additional sea-state)

No.	H_S [m]	T_P [s]	f_{H_S,T_P}[-]	KC_{max}[-]	kD/2 [-]
1	1.46	4.72	0.1002	0.5	1.28
2	2.95	6.18	0.0314	1.0	0.75
3	4.79	7.50	0.0092	1.7	0.50
4	6.54	8.76	0.0016	2.3	0.37
5	8.13	9.88	0.0002	3.0	0.29
6*	8.13	13.00	0.0000	3.5	0.17

7.3.2. Wave Spectrum

For all simulations, a JONSWAP spectrum with peak parameter equal 3.3 is used. Also, the spectrum is appropriately truncated to avoid calculation of the QTF where there are no significant contributions from wave heights. Truncation of the spectrum is very important to avoid ill behaved higher order contributions to the kinematics, as discussed in [26]. It is found that a cut-off frequency recommended in [11] and the following restrictions to the frequency space are applicable while maintaining statistical properties for the current sea-states:

$$\omega_{cut} = \min\left(2.5, \sqrt{\frac{2g}{H_S}}\right) \tag{17}$$

$$S'(\omega) = \begin{cases} S(\omega) & \text{for } 0.3 \leq \omega \leq \omega_{cut} \\ 0 & \text{for } \omega_{cut} < \omega \\ 0 & \text{for } \omega < 0.3 \end{cases} \tag{18}$$

The Rayleigh distributed random wave amplitudes are calculated according to (19), where $f_R^{-1}(\bar{u}, \sigma)$ is the inverse Rayleigh distribution with a scale parameter $\sigma = S'(\omega)\Delta\omega$, and $\bar{u} \sim \mathcal{U}(0, 1)$. This way, the statistical properties of the surface elevation, and thus kinematics, are completely retained [27]. A consequence is larger variance between the seeds, which is taken into account when the results are presented.

$$\zeta_a = f_R^{-1}(\bar{u}, S'(\omega)\Delta\omega) \tag{19}$$

7.3.3. Wind

As mentioned in the introduction, a constant thrust model has been used. This means that the baseline moment from the aerodynamic thrust will approximately equal the mean moment, which is disregarded in fatigue damage estimations.

7.4. Fatigue damage calculation

Fatigue damage is calculated using S-N curves obtained from [28] for a structure in seawater with cathodic protection, and the material parameters obtained are given in Table 4 for a bi-linear curve. The fatigue damage is then obtained with a rainflow counting (RFC) method, which is regarded at the most correct. The Palmgren-Miner rule for accumulated damage is given in (20), where S_j is the rainflow filtered stress range for S-N curve j [29] and n_j is the rainflow counted number of cycles.

$$D_{RFC} = \sum_j \frac{n_j}{N_j} = \sum_j n_j K_j^{-1} S_j^{m_j} \tag{20}$$

Table 4. Parameters for S-N curves.

m_1	4.0
m_2	5.0
$\log K_1$	11.764
$\log K_2$	15.606
Fatigue limit [MPa]	52.63

The stress is found from the overturning moment at the seabed level with for waves propagating in the x-direction, giving only a moment about the y-axis.

8. Results

All results presented below are from an average of three 30 minute long simulations for each sea-state and load model. Only small variances between the seeds are observed.

8.1. Baseline moment

The results for the moment at the seabed are shown in Fig. 10, where the maximum moment for each analysis is given as a fraction of the maximum moment obtained with an irregular first order incident wave. As expected, the moments for the small sea-states (1-3) are significantly influenced by the MacCamy and Fuchs correction on the first order particle acceleration terms. For the larger sea-states, it is seen that the second order contributions are significant as they are correlated with the wave height and steepness. The integration up to the incident second order surface elevation has indeed a large influence on the moment. Also, the third order FNV load shows contributions, but smaller than what is obtained with including O3.

When comparing the results in Fig. 10 with a lightly damped structure, there are significant increases in the maximum moment as seen in Fig. 11. If some uncertainty is assumed, there are very small relative differences between the load models when damping level is reduced. By lightly damped, it is meant that the structural damping of the structure is reduced from 3% to 1% of critical damping. This results in an unrealistically low damping, but it is only for illustrational purposes.

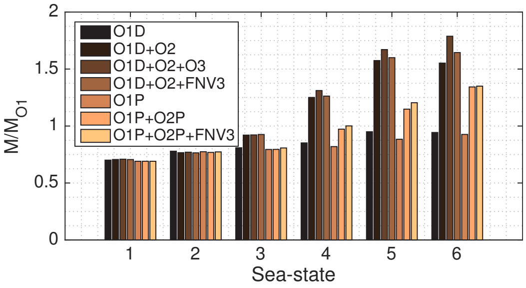

Fig. 10. Maximum base moment normalized with respect to load model O1.

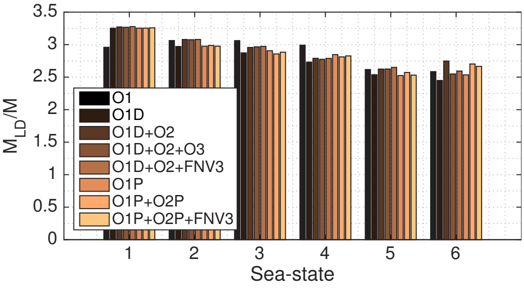

Fig. 11. Increase in maximum base moment for lightly damped (LD) system.

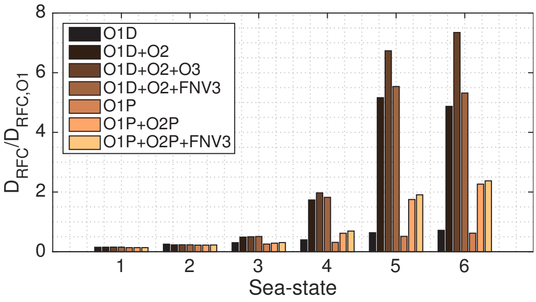

Fig. 12. Fatigue damage normalized with respect to load model O1.

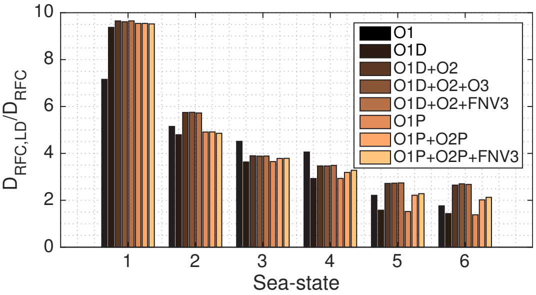

Fig. 13. Increase in fatigue damage for lightly damped (LD) system.

8.2. *Fatigue damage*

For fatigue damage, the variation in results are even larger. By Fig. 12, it is clear that a second order incident wave will contribute to an extremely high fatigue damage for the sea-states with $H_S > 6[m]$. These sea-states are not expected to be in the diffraction regime, although some effects are present on the O1D and O1P (first order diffraction) load case. Again, it is clear that in the sea-states 1-3, diffraction must be accounted for and higher order contributions are rather small.

The high fatigue damage for the higher order load cases is amplified with the utilized bi-linear S-N curves. It is observed that these load cases are sensitive to the choice of the material constant m_1 and is the component giving stress ranges above the fatigue limit stress. The panel-code-computed second order contributions are smaller than the undisturbed wave force (O2), but is still doubling the fatigue damage in the analyses in Fig. 12 for sea-states 4-6 when compared to O1D and O1P. For a lightly damped structure, results are shown in Fig. 13. Damping is without doubt a very important factor for total fatigue damage. Investigating the figure more closely reveals that the higher order forces are the most sensitive to low damping, as expected.

For a more realistic impression of the total fatigue damage contributions, it is necessary to include the probability of occurrence for each environmental state. The results after this correction is shown in Fig. 14, where the domination of the large sea-states are reduced. Now, significant contributions from higher order forces are prominent for sea-state 3-5.

Further, an analysis excluding the viscous forces have been carried out and is presented in Fig. 15. Due to the correlation between particle velocity and surface elevation, a reduction in fatigue damage proportional to the significant wave height is observed. The effect is largest when second order surface elevation is included in the kinematics stretching. Some reduction is also seen in the cases with no wave elevation (O1, O1D and O1P) where the KC number is largest.

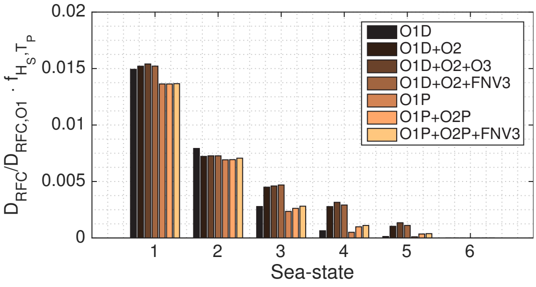

Fig. 14. Fatigue damage normalized with respect to load model O1 and multiplied with probability of occurrence.

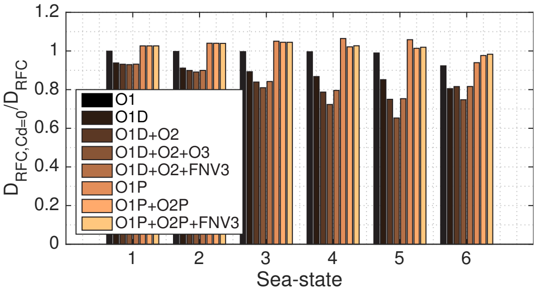

Fig. 15. Relative fatigue damage without contribution from drag force.

9. Conclusion

Interesting results are obtained for the fatigue damage estimation on an extra large monopile with regard to applicable wave load theories. As expected, the MacCamy and Fuchs correction is an essential contribution in the wave diffraction regime and compares well to the first order pressure from the panel code. In contrast, the second order undisturbed wave forces are predicting a large damage compared to the second order force from the Wadam model. These results are consistent with [22], where the *second* order FNV also overpredicts the forces. The quadratic FNV formulation is based on the same long-wave assumption as the second order model used in this paper, which also shows overprediction trends. It is observed that the large third/fourth order moment and fatigue contribution is due to an incident wave elevation influenced by the sum-frequency components. Therefore, it might be over-conservative to stretch all higher order kinematics to the undisturbed second order surface. This will have to be further verified with experiments.

The third order FNV force has previously shown to agree well with the third order terms in experiments [30], and does seem to reasonably increase the moment and fatigue damage for ringing exposed sea-states in these results. As for the relative importance of higher order loads in an operational condition with reduced damping, it is found that the fatigue damage contributions will be significant for sea-states with approximately $H_S > D/2$. It is also seen that even for KC< 3, the higher order drag forces may contribute to 20-30% of the estimated fatigue damage if the second order wave elevation is modeled.

Acknowledgment

This work has been carried out at the Centre for Autonomous Marine Operations and Systems (AMOS). The Norwegian Research Council is acknowledged as the main sponsor of AMOS. This work was supported by the Research Council of Norway through the Centres of Excellence funding scheme, Project number 223254 - AMOS.

The authors would like to thank Lene Eliassen and Loup Suja Thauvin (NTNU/Statkraft) for the foundation and tower model and soil data.

References

[1] EWEA, . The European offshore wind industry - key trends and statistics 2014. Tech. Rep. January; 2015.

[2] Dong, W., Moan, T., Gao, Z.. Long-term fatigue analysis of multi-planar tubular joints for jacket-type offshore wind turbine in time domain. Engineering Structures 2011;33(6):2002–2014. URL: https://www.engineeringvillage.com/share/document.url?mid=cpx_134e4fb12f277716deM782b2061377553&database=cpx. doi:10.1016/j.engstruct.2011.02.037.

[3] Bak, C., Zahle, F., Bitsche, R., Yde, A., Henriksen, L.C., Nata, A., et al. Description of the DTU 10 MW Reference Wind Turbine 2013;(July).

[4] SINTEF, , NTNU, . USFOS. 2003. URL: http://www.usfos.no.

[5] Horn, J.T.H.. Stochastic Dynamic Analysis of Offshore Bottom-Fixed Structures. Tech. Rep.; NTNU/AMOS; 2015.

[6] DNV, . Sesam HydroD. 2015. URL: https://www.dnvgl.com/services/software-for-hydrodynamic-and-stability-analysis-sesam-hydrod-2410.

[7] Bachynski, E.E., Moan, T.. Ringing loads on tension leg platform wind turbines. Ocean Engineering 2014;84:237–248. doi:10.1016/j.oceaneng.2014.04.007.

[8] Langen, I., Sigbjörnsson, R.. Dynamisk analyse av konstruksjoner. [Trondheim]: Tapir; 1979. ISBN 82-519-0362-9.

[9] Faltinsen, O.M.. Sea Loads on Ships and Offshore Structures. Cambridge University Press; 1990.

[10] Moan, T., Zheng, X.Y., Quek, S.T.. Frequency-domain analysis of non-linear wave effects on offshore platform responses. International Journal of Non-Linear Mechanics 2007;42(3):555–565. doi:10.1016/j.ijnonlinmec.2006.08.006.

[11] DNV GL, . RP-C205 Environmental conditions and environmental loads. Tech. Rep.; 2010.

[12] Mei, C.. The Applied Dynamics of Ocean Surface Waves. 1989.

[13] Sharma, J.N., Dean, R.G.. Contributions to second order directional sea simulation and wave forces. In: Proceedings of the International Conference on Offshore Mechanics and Arctic Engineering - OMAE; vol. 5. San Diego, CA. ISBN 0791842711; 9780791842713; 2007, p. 361–370. doi:10.1115/OMAE2007-29634.

[14] Stansberg, C.T., Amundsen, A., Fouques, S., Økland, O.D.. Second-Order random wave kinematics and resulting loads on a bottom-Fixed slender monopile. In: Proceedings of the International Conference on Offshore Mechanics and Arctic Engineering - OMAE; vol. 8. Nantes. ISBN 9780791855423; 2013,doi:10.1115/OMAE2013-11405.

[15] Kim, M.H., Yue, D.K.P.. The complete second-order diffraction solution for an axisymmetric body. Journal of Fluid Mechanics 1989;.

[16] DNV, . HydroD User Manual 2011;.

[17] Bachynski, E.E., Moan, T.. Hydrodynamic Modeling of Tension Leg Platform Wind Turbines. In: Volume 8: Ocean Renewable Energy. ASME. ISBN 978-0-7918-5542-3; 2013,doi:10.1115/OMAE2013-10120.

[18] Tromans, P., Swan, C., Masterton, S.. Nonlinear potential flow forcing : the ringing of concrete gravity based structures. Tech. Rep.; 2006.

[19] Faltinsen, O.M., Newman, J.N., Vinje, T.. Nonlinear wave loads on a slender vertical cylinder. Journal of Fluid Mechanics 1995;289:179. URL: http://journals.cambridge.org/abstract_S0022112095001297. doi:10.1017/S0022112095001297.

[20] Newman, J.N.. Nonlinear Scattering of Long Waves by a Vertical Cylinder. In: Waves and Nonlinear Processes in Hydrodynamics. 1996,.

[21] Johannessen, T.B.. Nonlinear Superposition Methods Applied to Continuous Ocean Wave Spectra. Journal of Offshore Mechanics and Arctic Engineering 2012;134(February 2012):011302. doi:10.1115/1.4003518.

[22] Krokstad, J., Stansberg, C., Nestegaard, A., Marthinsen, T.. A New Nonslender Ringing Load Approach Verified Against Experiments. Journal of Offshore Mechanics and Arctic Engineering 1998;120(1):20. doi:10.1115/1.2829515.

[23] Horn, J.T.H., Amdahl, J., Haver, S.K.. Dynamic Amplification of Drag Dominated Structures in Irregular Seas. In: Proceedings of OCEANS'15 MTS/IEEE Washington Conference & Exhibition. IEEE conference proceedings. ISBN 978-0-933957-43-5; 2015,.

[24] NORSOK, . N-003 Action and Action Effects. 2 ed. September; Standards Norway; 2007,.

[25] Chakrabarti, S.. Hydrodynamics of Offshore Structures. Computational Mechanics Publications; 1987.

[26] Johannessen, T.B.. On the use of linear and weakly nonlinear wave theory in continuous ocean wave spectra: Convergence with respect to frequency. In: Proceedings of the International Conference on Offshore Mechanics and Arctic Engineering - OMAE; vol. 4. Berlin. ISBN 9780791848210; 2008, p. 211–217. doi:10.1115/OMAE2008-57355.

[27] Tucker, M., Challenor, P., Carter, D.. Numerical simulation of a random sea: a common error and its effect upon wave group statistics. Applied Ocean Research 1984;6(2):118–122. doi:10.1016/0141-1187(84)90050-6.

[28] DNV GL, . RP-C203 Fatigue design of offshore steel structures. Tech. Rep. April; 2005.

[29] Moan, T., Naess, A.. Stochastic Dynamics of Marine Structures. Cambridge University Press; 2013.

[30] Stansberg, C.T.. Comparing ringing loads from experiments with cylinders of different diameters: an empirical study. [Trondheim]: Marintek, SINTEF-gruppen; 1997.

Paper II

Reducing uncertainty of Monte Carlo estimated fatigue damage in offshore wind turbines using FORM

Jan-Tore Horn and Jørgen Juncher Jensen

Proceedings of the 13th International Symposium on Practical Design of Ships and Other Floating Structures (PRADS), 2016

Abstract Uncertainties related to fatigue damage estimation of non-linear systems are highly dependent on the tail behaviour and extreme values of the stress range distribution. By using a combination of the First Order Reliability Method (FORM) and Monte Carlo simulations (MCS), the accuracy of the fatigue estimations may be improved for the same computational efforts. The method is applied to a bottom-fixed, monopilesupported large offshore wind turbine, which is a nonlinear and dynamically sensitive system. Different curve fitting techniques to the fatigue damage distribution have been used depending on the sea-state dependent response characteristics, and the effect of a bi-linear S-N curve is discussed. Finally, analyses are performed on several environmental conditions to investigate the long-term applicability of this multistep method. Wave loads are calculated using state-of-the-art theory, while wind loads are applied with a simplified model based on rotor thrust coefficients.

Reducing Uncertainty of Monte Carlo Estimated Fatigue Damage in Offshore Wind Turbines Using FORM

Jan-Tore H. Horn, Jørgen Juncher Jensen

Abstract—Uncertainties related to fatigue damage estimation of non-linear systems are highly dependent on the tail behaviour and extreme values of the stress range distribution. By using a combination of the First Order Reliability Method (FORM) and Monte Carlo simulations (MCS), the accuracy of the fatigue estimations may be improved for the same computational efforts.

The method is applied to a bottom-fixed, monopile-supported large offshore wind turbine, which is a non-linear and dynamically sensitive system. Different curve fitting techniques to the fatigue damage distribution have been used depending on the sea-state dependent response characteristics, and the effect of a bi-linear S-N curve is discussed. Finally, analyses are performed on several environmental conditions to investigate the long-term applicability of this multistep method. Wave loads are calculated using state-of-the-art theory, while wind loads are applied with a simplified model based on rotor thrust coefficients.

Keywords—Fatigue damage, FORM, monopile, monte carlo simulation, reliability, wind turbine.

I. INTRODUCTION

DYNAMIC structures subjected to stochastic, non-linear environmental loads may require many long simulations to confidently estimate fatigue damage in the design phase [1]. Depending on the degree of non-linearity in the system, computed fatigue may vary significantly between each simulation [2], and extreme values may have large impact on the expected lifetime estimation. An example is illustrated in Fig. 1 for the mudline fatigue damage on a 10MW monopile mounted offshore wind turbine. The conventional seed averaging method (D_C) is normalized with the expected damage (D_e).

It is clear that the results are converging, but are highly dependent on extreme values when the number of seeds are small to moderate. The behaviour is explained by investigating the fatigue damage distribution in Fig. 2. Extreme values are five times greater than the expected value, and the shape indicates a Weibull distribution. The present distribution yields a larger probability of extreme outliers compared to a Gaussian process, leading to slower convergence of the mean value. However, extreme values are also physical and need to be accounted for nonetheless.

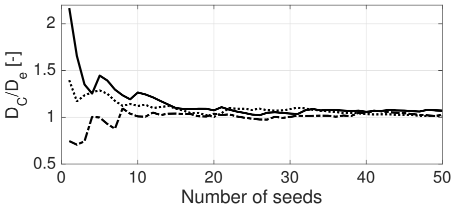

Fig. 1. Three example fatigue estimations for 100s simulations with U=6m/s, H_S=1.5m, and T_P=4.7s

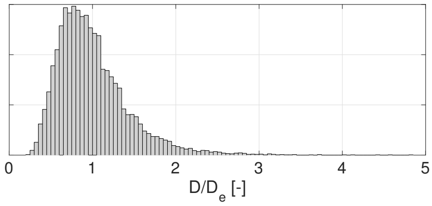

Fig. 2. Example fatigue distribution for 10,000 samples with U=6m/s, H_S=1.5m, and T_P=4.7s

The proposed method in [2] is to replace the large values with a FORM evaluation of the extremes in the fatigue distribution tail. As a result, outliers are accounted for in each fatigue estimation, but with less impact on the variance. The paper is built up as follows: First, an introduction to FORM analysis is given. Then, fatigue damage calculation methods are presented, both conventional, the method from [2], and new proposals for representation of the fatigue probability density function (PDF). A more detailed description of the procedure is found in Section II-G, while the simulation models are presented in Section III. Finally, results are presented in Section IV.

II. BACKGROUND

A. FORM

The objective of the FORM analysis is to minimize the function

$$G(\mathbf{u}) = D_{ext} - D(\mathbf{u}) \tag{1}$$

to determine the design-point $D(\mathbf{u}^*) \approx D_{ext}$ by a linear approximation. Here, D_{ext} is some extreme fatigue damage

---

J.T.H. Horn is with the Centre for Autonomous Marine Operations and Systems (NTNU AMOS) at the Department of Marine Technology, NTNU, Norway, e-mail: (see http://www.ntnu.edu/employees/jan-tore.horn).

J.J. Jensen is with the Department of Mechanical Engineering at the Technical University of Denmark, DTU, and NTNU AMOS.

J. Amdahl is with NTNU AMOS, and the Department of Marine Technology, NTNU, Norway.

and $\mathbf{u} = [\bar{u}_1, \ldots, \bar{u}_m, \tilde{u}_1, \ldots, \tilde{u}_n]$ are standard normal random variables. The conventional Hasofer-Lind (HL) and modified HL (MHL) method as described in [3], has been used as iteration schemes. The equations to be satisfied at the design-point are [4]:

$$G(\mathbf{u}^*) = 0$$
$$\mathbf{u}^* + \lambda^* \nabla G(\mathbf{u}^*) = 0$$

where

$$\lambda^* = -\frac{\nabla G(\mathbf{u}^*)\mathbf{u}^*}{|\nabla G(\mathbf{u}^*)|^2}$$

and the gradient is defined as:

$$\nabla G(\mathbf{u}) = \left[\frac{\partial G}{\partial u_1}, \frac{\partial G}{\partial u_2}, \ldots, \frac{\partial G}{\partial u_{m+n}}\right]^T \tag{2}$$

Iterations on $\mathbf{u}$ is based on the function value of (1) and the gradient. The $(k+1)$ iteration point is found from a weighted linear function:

$$\mathbf{u}_{k+1} = \mathbf{a}_k + (1-\xi)\mathbf{d}_k \tag{3}$$

where

$$\mathbf{a}_k = [\mathbf{u}_k \nabla G(\mathbf{u}_k) - G(\mathbf{u}_k)] \frac{\nabla G(\mathbf{u}_k)^T}{|\nabla G(\mathbf{u}_k)|^2} \tag{4}$$

and

$$\mathbf{d}_k = \mathbf{u}_k - \mathbf{a}_k \tag{5}$$

which is illustrated in Fig. 3. For the HL method, $\xi = 1$, so that (3) reduces to $\mathbf{u}_{k+1} = \mathbf{a}_k$. With the MHL method, $\mathbf{u}_k$ is chosen along the line $\mathbf{d}_k$ by stepwise increasing ξ in (3) from 0.2 to 1.0 in order to minimize the following cost function [3]:

$$M(\mathbf{u}) = |\mathbf{u} - \frac{\nabla G(\mathbf{u})\mathbf{u}}{|\nabla G(\mathbf{u})|^2}\nabla G(\mathbf{u})|^2 + cG(\mathbf{u})^2 \tag{6}$$

In this particular case, $c \propto (D_{\text{ext}})^{-2}$ has given a reasonable cost function, putting most weight on the last term.

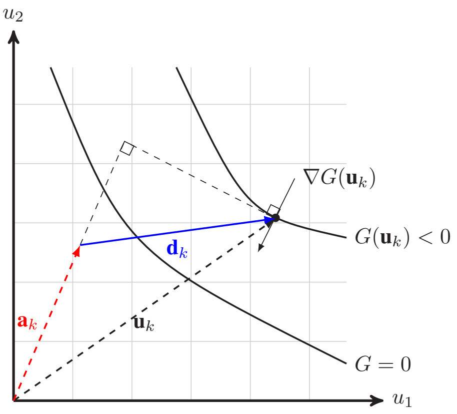

Fig. 3. Illustration of FORM iteration

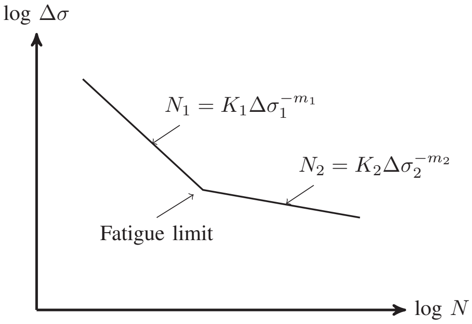

Fig. 4. S-N curves above and below the fatigue limit.

B. S-N curves

Fatigue damage is calculated using S-N curves obtained from [5] for a structure in seawater with cathodic protection, and the material parameters obtained are given in Table I for a bi-linear curve illustrated in Fig. 4. The fatigue damage is then obtained with a rainflow counting (RFC) method using the WAFO toolbox [6] in MATLAB. The Palmgren-Miner rule for accumulated damage is given as

$$D = \sum_j \frac{n_j}{N_j} = \sum_j n_j K_j^{-1} (\text{SCF} \cdot \Delta\sigma_j)^{m_j} \left(\frac{t}{t_{\text{ref}}}\right)^{k \cdot m_j} \tag{7}$$

where $\Delta\sigma_j$ is the rainflow filtered stress range for S-N curve j [7] and n_j is the rainflow counted number of cycles. The stress concentration factor (SCF) is taken as 1.0, using the base material cross section at the mudline which in this case has a diameter of 8m and thickness of 110mm.

TABLE I
PARAMETERS FOR BI-LINEAR S-N CURVE

m_1		3.0
m_2		5.0
$\log_{10} K_1$		11.764
$\log_{10} K_2$		15.606
Fatigue limit	[MPa]	52.63
SCF		1.0
t_{ref}	[mm]	25
k		0.2

C. Fatigue damage estimation using the reliability index

The traditional way of calculating the expected fatigue damage is to average over N statistically independent simulations:

$$D_e = \frac{1}{N}\sum_{i=1}^{N} D_i \tag{8}$$

which is equivalent to integrating over the PDF of the fatigue damage to get the expected value:

$$D_e = \int_0^\infty D f(D) dD \tag{9}$$

We now define the reliability index β through the standard normal cumulative density function (CDF), Φ:

$$P[D > D_i] = 1 - \frac{i}{N} = \Phi(-\beta_i) \tag{10}$$

resulting in

$$\beta_i = -\Phi^{-1}(P[D > D_i]) \approx -\Phi^{-1}(1 - \frac{i}{N}) \tag{11}$$

for sorted fatigue damage values so that $D_i \leq D_{i+1}$ and $i = 1, 2, .., N-1$. The fatigue damage PDF can now be expressed in terms of β using the formulation in (10):

$$\begin{aligned} f(D) = \frac{dF(D)}{dD} &= 1 - P[D > D_i] \\ &= -\frac{d\Phi(-\beta)}{d\beta}\frac{d\beta}{dD} \\ &= \frac{1}{\sqrt{2\pi}}\exp(-\frac{1}{2}\beta^2)\frac{d\beta}{dD} \end{aligned} \tag{12}$$

Note that we obtain a Gaussian distribution PDF for constant $d\beta/dD$. The expected fatigue damage in (9), can now be re-written as a summation:

$$\begin{aligned} D_e &= \int_0^\infty Df(D)dD \\ &= \frac{1}{\sqrt{2\pi}}\sum_{i=1}^{N} D_i(\beta_i)\exp(-\frac{1}{2}\beta_i^2)\Delta\beta_i \end{aligned} \tag{13}$$

It is clear that $D_e \to \infty$ since $\Delta\beta_N \to \infty$ when using (10). Instead, a linearization of the tail as described in the next section is performed. The first $N-1$ increments in β for the summation are evaluated as:

$$\Delta\beta_i = \begin{cases} \frac{1}{2}(\beta_{i+1} - \beta_i) & \text{for } i = 1 \\ \frac{1}{2}(\beta_{i+1} - \beta_{i-1}) & \text{for } 2 \leq i \leq N-2 \\ \beta_i - \beta_{i-1} & \text{for } i = N-1 \end{cases} \tag{14}$$

D. Tail linearization

It is assumed that for large β, the relationship with the fatigue damage is close to linear:

$$D(\beta) = A + B\beta \tag{15}$$

which means that the extreme fatigue damage values follow a Gaussian distribution. As a result, the last term of the summation in (13) for $i = N$, can be written as [2]:

$$\begin{aligned} &\frac{1}{\sqrt{2\pi}}D_N(\beta_N)\exp(-\frac{1}{2}\beta_N^2)\Delta\beta_N \\ &= \frac{1}{\sqrt{2\pi}}\int_{\beta_{N-1}}^{\infty} D(\beta)\exp(-\frac{1}{2}\beta^2)d\beta \\ &= A(1 - \Phi(\beta_{N-1})) + \frac{B}{\sqrt{2\pi}}\exp(-\frac{1}{2}\beta_{N-1}^2) \end{aligned} \tag{16}$$

which inserted in (13) gives

$$\begin{aligned} D_{SL} = &\frac{1}{\sqrt{2\pi}}\sum_{i=1}^{N-1} D_i(\beta_i)\exp(-\frac{1}{2}\beta_i^2)\Delta\beta_i \\ &+ A(1 - \Phi(\beta_{N-1})) + \frac{B}{\sqrt{2\pi}}\exp(-\frac{1}{2}\beta_{N-1}^2) \end{aligned} \tag{17}$$

where SL denotes a combination of summation and linearization. The constants A and B in (15) is found using the FORM analysis to obtain a sufficiently large extreme fatigue damage D_{ext} and a corresponding reliability index β_{FORM}. An example is shown in Fig. 5 where a linear function is fitted to the tail of the fatigue damage values. This particular case contains 10,000 simulations of simulation time $T_{\text{sim}} = 100\text{s}$. A FORM analysis yields the plotted coordinate for a yearly extreme damage and corresponds well to the simulated extremes and the hypothesis of a linear tail i.e. Gaussian distributed. The simulated fatigue damage is converted to an equivalent yearly damage with:

$$D_{\text{year}} = 365 \cdot 24 \cdot 60^2 \cdot \frac{D_{\text{sim}}}{T_{\text{sim}}} \tag{18}$$

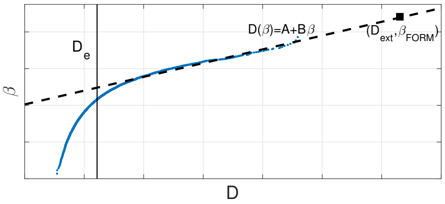

Fig. 5. Example linear tail fit

In order to obtain a proper linear fit, a sufficient amount of simulations has to be done. From Fig. 5, it is clear that the coordinate in addition to the FORM-evaluated point has to lie on the linear area of the results, meaning approximately $\beta > 1.2$. Also, since β_N is supposedly large, the second point has to be (D_{N-1}, β_{N-1}). Finally, combining $\beta_{N-1} > 1.2$ with (11) yields $N > 8$. The coefficients in (15) can now be written as:

$$B = \frac{D_{ext} - D_{N-1}}{\beta_{FORM} - \beta_{N-1}} \tag{19}$$

$$A = D_{N-1} - B\beta_{N-1} \tag{20}$$

E. Special case for Gaussian fatigue damage

In the special case that the fatigue damage is Gaussian distributed, (15) is a good approximation for $\beta \in \{-\infty, \dots, \infty\}$. As a result, the expected fatigue damage can be found as:

$$
\begin{aligned}
D_L =& \int_0^\infty Df(D)dD \\
=& \frac{1}{\sqrt{2\pi}} \int_0^\infty D \exp(-\frac{1}{2}\beta^2) \frac{d\beta}{dD} dD \\
=& \frac{1}{\sqrt{2\pi}} \int_{\beta'}^\infty D \exp(-\frac{1}{2}\beta^2) d\beta \\
=& \frac{1}{\sqrt{2\pi}} \int_{\beta'}^\infty (A + B\beta) \exp(-\frac{1}{2}\beta^2) d\beta \\
=& A \int_{\beta'}^\infty \frac{1}{\sqrt{2\pi}} \exp(-\frac{1}{2}\beta^2) d\beta \\
=& A(1 - \Phi(\beta')) + \frac{B}{\sqrt{2\pi}} \exp(-\frac{1}{2}\beta'^2)
\end{aligned}
\tag{21}
$$

and for $\beta' \to -\infty$:

$$D_L = A \tag{22}$$

Note that B disappears due to the integration of an odd function over the entire domain. The above result means that a good estimate of D_e can be found from only two pairs of (D_i, β_i), and the coefficients in (15) are now:

$$B = \frac{D_2 - D_1}{\beta_2 - \beta_1} \tag{23}$$

$$A = D_1 - B\beta_1 \tag{24}$$

which means that for $\beta' \to -\infty$:

$$D_L = \frac{D_1\beta_2 - D_2\beta_1}{\beta_2 - \beta_1} \tag{25}$$

where $D_2 > D_1$. For a good linear approximation, it is preferred that $D_2/D_1 \gg 1$, therefore, the FORM procedure may be used to find $\beta_2 = \beta_{\text{FORM}}$ for some extreme value of $D_2 = D_{\text{ext}}$. The remaining point for linear regression has to be found by several simulations which is demonstrated in Section IV-A.

F. Weakly non-Gaussian fatigue damage

Due to the utilization of bi-linear S-N curves, the fatigue damage might be slightly non-Gaussian or Weibull distributed with respect to β, which means that a quadratic polynomial description might be more appropriate than the linear representation in (15):

$$D(\beta) = A + B\beta + C\beta^2 \tag{26}$$

which inserted into (9) yields:

$$
\begin{aligned}
D_Q =& \int_0^\infty Df(D)dD \\
=& \frac{1}{\sqrt{2\pi}} \int_0^\infty D \exp(-\frac{1}{2}\beta^2) \frac{d\beta}{dD} dD \\
=& \frac{1}{\sqrt{2\pi}} \int_{\beta'}^\infty (A + B\beta + C\beta^2) \exp(-\frac{1}{2}\beta^2) d\beta \\
=& A\,(1 - \Phi(\beta')) + \frac{B}{\sqrt{2\pi}} \exp(-\frac{1}{2}\beta'^2) \\
&+ \frac{1}{\sqrt{2\pi}} \int_{\beta'}^\infty C\beta^2 \exp(-\frac{1}{2}\beta^2) d\beta \\
=& A\,(1 - \Phi(\beta')) + \frac{B}{\sqrt{2\pi}} \exp(-\frac{1}{2}\beta'^2) \\
&+ C\left(1 - \Phi(\beta') + \frac{\beta'}{\sqrt{2\pi}} \exp(-\frac{1}{2}\beta'^2)\right) \\
=& (A + C)(1 - \Phi(\beta')) + \frac{B + C\beta'}{\sqrt{2\pi}} \exp(-\frac{1}{2}\beta'^2)
\end{aligned}
\tag{27}
$$

and for $\beta' \to -\infty$:

$$D_Q = A + C \tag{28}$$

Typically, one could choose $\beta' = \beta_1$ from simulations. The constants A, B and C are found using a polynomial curve fitting to the data in MATLAB, including the FORM evaluated point which is crucial to obtain stable results for few seeds.

G. Procedure

The complete procedure for the SL method is summed up as:

1) Perform N simulations with a detailed simulation model and evaluate the first $N - 1$ terms in (13)
2) Use a simplified and computationally efficient model to find β_{FORM} and $\mathbf{u}^*$ for a given $D_{\text{ext}} > D_{N-1}$. It is preferred that $\beta_{\text{FORM}} > 2.5$
3) Do an iteration on the detailed model with $\mathbf{u} = \mathbf{u}^*$ to find an updated D_{ext}, which is valid for the detailed model, but with the same reliability index, β_{FORM}
4) Use the results in 1) and 3) to evaluate (17)

Details regarding the simulation models are given in the next section. The simulation procedure for the simplified model is illustrated in Fig. 6, where the yellow blocks represent codes developed in MATLAB for this particular set-up. First, the FORM-evaluated set of standard normal random variables, $\mathbf{u}$, is transformed to uniform random variables, $\boldsymbol{\epsilon}$, through

$$\boldsymbol{\epsilon} = 2\pi\Phi(\mathbf{u}) \tag{29}$$

in *fatigue.m*. Then, the calculated environmental forces and/or wave elevation from *force.m* are passed on to USFOS where the dynamic simulations are performed. Finally, desired response time-series are returned to MATLAB and *fatigue.m* for post-processing. The damage is then calculated and returned to *FORM.m* for evaluation.

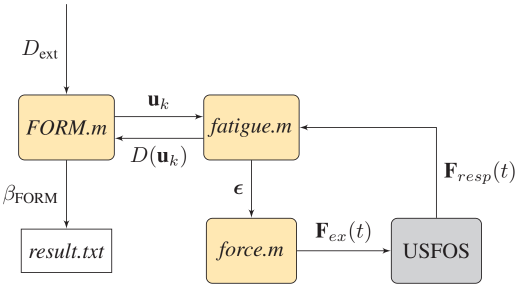

Fig. 6. Block diagram of simulation process for the simplified model

H. *Summary of methods for fatigue estimation*

The presented methods for fatigue damage calculation are summed up in Table II.

TABLE II
FATIGUE CALCULATION METHODS

Description	Symbol	Formulation
Conventional	D_C	$\frac{1}{N}\sum_{i=1}^{N} D_i$
Sum+Linear	D_{SL}	$\frac{1}{\sqrt{2\pi}}\sum_{i=1}^{N-1} D_i \exp(-\frac{1}{2}\beta_i^2)\Delta\beta_i$ $+ A(1-\Phi(\beta_{N-1})) + \frac{B}{\sqrt{2\pi}}\exp(-\frac{1}{2}\beta_{N-1}^2)$
Linear	D_L	$A(1-\Phi(\beta_1)) + \frac{B}{\sqrt{2\pi}}\exp(-\frac{1}{2}\beta_1^2)$
Quadratic	D_Q	$(A+C)(1-\Phi(\beta_1)) + \frac{B+C\beta_1}{\sqrt{2\pi}}\exp(-\frac{1}{2}\beta_1^2)$

In this work, it is found that the expressions for D_L and D_Q can be replaced by their asymptotic values in (22) and (28), respectively. This has lead to more stable estimations of the fatigue damage.

I. *Limitation of variables in FORM analysis*

To speed up the FORM analysis, iterations are only performed on the random variables contributing the most to the fatigue damage. In other words, a sensitivity evaluation based on the first iteration is carried out. The most significant variables are stored in $\mathbf{u}'$ after the first iteration, satisfying:

$$\min\left(\nabla G(\mathbf{u}')\right) > \nu|\nabla G(\mathbf{u}_1)| \tag{30}$$

for some constant ν so that $\mathbf{u}'$ only contains the significant values. Further, $\mathbf{u}_2 = \mathbf{u}'$ implying that the following simulations are only using the variables from $\mathbf{u}'$. For instance, wave components with small frequencies and/or small amplitudes will not have impact on the fatigue damage calculation, and the number of components will depend on the sea-state. In Fig. 7, an example is shown where 7 out of 19 wave components are found to be insignificant. For the disregarded variables, values from the first iteration are used for evaluation of β, and as constants in the remaining simulations. If deterministic wave amplitudes are used, it is assumed that the significant components are grouped.

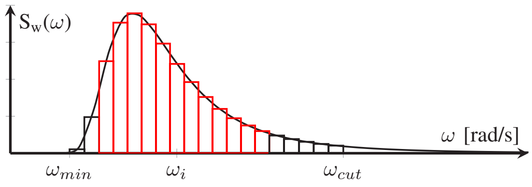

Fig. 7. Example discretized wave spectrum with significant wave components in red

III. SIMULATION MODELS

A. *Structural model*

The structural model is a monopile based on the 10 MW DTU reference wind turbine [8]. The transition piece and pile have a diameter of 8m and thickness of 110mm, and it is located at 30m water depth. The first and second natural periods are 4.8s and 1.0s, respectively. Rotor- and nacelle masses are lumped to the tower top,and the soil layers are modelled as non-linear springs all. An illustration of the model is shown in Fig. 8 with corresponding parameters in Table III.

To be able to perform the FORM analysis in reasonable time, a simplified model is used for the iterations. This is based on the assumption that the design-point is the same for the detailed and simple model. In other words, a sea-state

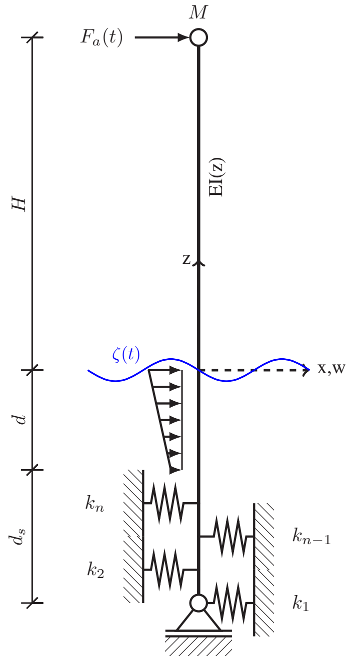

Fig. 8. Simplified wind turbine model

TABLE III
SIMULATION MODELS

H	[m]	115
d	[m]	30
d_s	[m]	42
M	[ton]	675

giving extreme fatigue on the simple model will also give extreme damage on the detailed model. Differences between the models are stated in Table IV. Note that the difference in simulation time are not very large, which means that very limited time can be used on the FORM analysis in order to justify the use of the presented method. If a complete wind turbine model including rotor had been used, simulation time would at least be doubled, and the proposed method is even more attractive. However, more work has to be done to find a simple aerodynamic model that matches the complete rotor dynamics by only using a single wind series, like e.g. [9].

TABLE IV
SIMULATION MODELS

	Detailed model	Simple model
Elements	21	12
Number of soil springs	26	6
Rotor	No	No
Aerodynamics	C_T	C_T
Hydrodynamics	2nd order	1st order
Controller	None	None
Real time/sim. time [s/s]	0.4	0.2

B. Hydrodynamic loads

The wave elevation in an irregular sea is described with [10]:

$$\zeta(t) = \sum_{i=1}^{m} \sqrt{2S_{\text{w}}(\omega_i)\Delta\omega}\cos(\omega_i t + \bar{\epsilon}_i) \tag{31}$$

where $\Delta\omega = \frac{2\pi}{T}$ [11] and $\omega_i = \omega_{min} + (i-1)\Delta\omega$. The maximum number of wave components can be found as $m = \frac{\omega_{cut} - \omega_{min}}{\Delta\omega} \leq 0.35T$ when $\omega_{min} = 0.3$[rad/s] and

$$\omega_{cut} = \min\left[2.5, \sqrt{\frac{2g}{H_S}}\right] \tag{32}$$

Here, the wave amplitudes are deterministic to limit the number of random variables, but they can also be modeled as Rayleigh distributed [12]. For small m, this should be done in order to obtain a Gaussian surface elevation. The phase angles are uniformly distributed and obtained from normally distributed variables with (29). For the simple model, only the wave components are given as input to USFOS, which automatically calculates the first order hydrodynamic forces. The detailed model utilizes second order hydrodynamic forces which is pre-calculated in MATLAB and given as a spatially time-variant interpolation grid as input to USFOS. Kinematics calculations are based on an FFT algorithm similar to what is used in [13]. From previous studies [13], it has been found that second order wave loads are only significant when $H_S > 5$, which means that these loads can be neglected in smaller sea-states, which increases the computational efficiency.

C. Simplified aerodynamic thrust model

The turbulent wind is found by realizing the Kaimal spectrum [14]:

$$S_{uu}(f) = \sigma_u^2\left(\frac{4L}{\bar{U}}\right)\left(1 + \frac{6fL}{\bar{U}}\right)^{-5/3} \tag{33}$$

where the standard deviation

$$\sigma_u = I(0.75\bar{U} + 5.6) \tag{34}$$

is given as a function of the mean wind speed, $\bar{U}$, and turbulence intensity, I, which is set to 0.14. The total wind speed is then:

$$U(t) = \bar{U} + V(t) \tag{35}$$

where the gust component, V, is found with:

$$V(t) = \sum_{i=1}^{n} \sqrt{S_{uu}(f_i)\Delta f/\pi}\cos(2\pi f_i t + \bar{\epsilon}_i) \tag{36}$$

where $\Delta f = \frac{1}{T}$ and $n = \frac{f_{cut} - f_{min}}{\Delta f} = \frac{1-0}{\Delta f} = T$. Which means that the number of components in the wind gust is equal to the simulation time for a high frequency cut-off of 1Hz. Higher frequencies are excluded to simulate the low-pass filtering effects of the rotor. The thrust force can now be found using:

$$F_a = \frac{1}{2}\rho_a \pi R^2 C_T(\beta, \lambda) U^2 \tag{37}$$

where C_T is the aerodynamic thrust coefficient dependent on pitch angle (β) and tip-speed ratio (λ), R is the rotor radius and ρ_a is the density of air. Here, it is assumed that the pitch angle, and tip-speed ratio $\lambda = \frac{\omega_R R}{U}$, can be written as functions of the rotor-induced lowpass-filtered wind speed, $\widetilde{U}$, and true wind speed U:

$$\beta \approx \beta(\widetilde{U}) = \begin{cases} 0, & \text{for } U_{\text{cut-in}} \leq \widetilde{U} < U_R \\ \frac{\widetilde{U} - U_R}{1.8\widetilde{U} - 6.7}\ \text{[rad]}, & \text{for } \widetilde{U} \geq U_R \end{cases} \tag{38}$$

$$\lambda \approx \lambda(U, \widetilde{U}) = \begin{cases} \lambda_{\text{opt}}\frac{\widetilde{U}}{U}, & \text{for } U_{\text{cut-in}} \leq \widetilde{U} < U_R \\ \lambda_{\text{opt}}\frac{U_R}{U}, & \text{for } \widetilde{U} \geq U_R \end{cases} \tag{39}$$

where $\lambda_{\text{opt}} = \frac{\omega_{\text{max}} R}{U_R} = 7.5$ is the optimal tip-speed ratio. The lowpass filtered wind speed is found with:

$$\dot{\widetilde{U}} = \frac{1}{\tau}\left(U - \widetilde{U}\right) \tag{40}$$

for some time constant τ, which has to be tuned according to a more detailed simulation model. It has been found that $\tau = 3$ gives sufficiently accurate thrust for all wind speeds in this case. The above equations are resulting in:

$$C_T'(U, \widetilde{U}) = \begin{cases} C_T(0, \lambda_{\text{opt}}\frac{\widetilde{U}}{U}), & \text{for } U_{\text{cut-in}} \leq \widetilde{U} < U_R \\ C_T(\frac{\widetilde{U} - U_R}{1.8\widetilde{U} - 6.7}, \lambda_{\text{opt}}\frac{U_R}{U}), & \text{for } \widetilde{U} \geq U_R \end{cases} \tag{41}$$

which is plotted in Fig. 9. Further, the thrust coefficient, $C_T(\beta, \lambda)$ can be approximated by the polynomial:

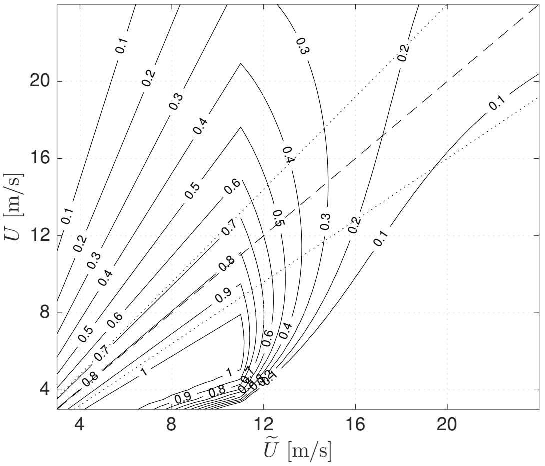

Fig. 9. Thrust coefficient, $C'_T(U,\widetilde{U})$, with dashed line for $\widetilde{U} = U$ and dotted lines for the most probable region: $\widetilde{U} = U(1 \pm 0.2)$

$$C_T(\beta,\lambda) \approx a_{00} + a_{01}\lambda + a_{02}\lambda^2 + a_{10}\beta + a_{20}\beta^2 + a_{11}\lambda\beta + a_{12}\lambda^2\beta + a_{21}\lambda\beta^2 \tag{42}$$

with the constants for the present turbine given in Table V. The modified expression for the aerodynamic thrust is then:

$$F_a = \frac{1}{2}\rho_a \pi R^2 C'_T(U,\widetilde{U})U^2 \tag{43}$$

TABLE V
THRUST COEFFICIENT PARAMETERS

a_{00}	-0.27127
a_{01}	0.19974
a_{02}	-0.007461
a_{10}	0.02822
a_{20}	-5.875e-05
a_{11}	-0.0088
a_{12}	-9.822e-05
a_{21}	-6.342e-05

The presented aerodynamic model is lacking the ability to capture transient load effects and other thrust variations due to the presence of a rotor, but it is considered to be sufficient for this initial study.

D. Deterministic 3P effects

To account for thrust variations that oscillates with three times the rotor frequency, given a three-bladed rotor, a deterministic time-series is added to the wind to create an equivalent wind speed. In reality, only the wind shear and tower shadow are deterministic effects, while the rotational sampling of the rotor is stochastic and hence neglected in this case. A sinusoidal function with amplitude of 8% of the instantaneous true wind speed and a frequency of three times the rotor frequency, ω_R, is added:

$$U_{\text{eq}} = U + 0.08U\sin(3\omega_R t) \tag{44}$$

where

$$\omega_R \approx \omega_R(\bar{U}) = \begin{cases} \lambda_{\text{opt}}\frac{\bar{U}}{R}, & \text{for } U_{\text{cut-in}} \leq \widetilde{U} < U_R \\ \lambda_{\text{opt}}\frac{U_R}{R}, & \text{for } \widetilde{U} \geq U_R \end{cases} \tag{45}$$

In other words, the rotational frequency of the rotor is assumed to be close to constant during the simulations, which might result in a slightly unrealistic load excitation at exactly $3\omega_R$.

E. Aerodynamic damping

Aerodynamic damping has a great influence on the fatigue damage on the tower and pile. Usually, the aerodynamic damping is accounted for in the structural damping matrix when a simple thrust model is used. Here, the thrust is found through an equivalent drag force on a cylinder at the rotor-nacelle assembly location. The thrust can then be transferred to the tower by a simple drag formulation including relative velocity:

$$F_{a,\text{rel}}(U,\widetilde{U}) = \frac{1}{2}\rho_a D C_D(U,\widetilde{U})\left[U - V_{\text{RNA}}\right]^2 L \tag{46}$$

By Fig. 10 it is clear that this approach is able to represent the expected aerodynamic damping which is reported to be 4-7% in most cases [15]. When only wave loads are considered, the structural damping is increased from 1 to 5% to account for damping contribution from an operational turbine.

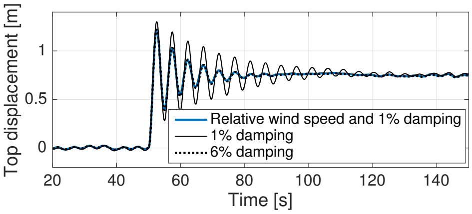

Fig. 10. Decay test at 16[m/s] wind speed with structural damping and relative wind speed comparison

F. Random variables

The total uniform random variables from wind and waves are collected as

$$\boldsymbol{\epsilon} = [\bar{\boldsymbol{\epsilon}}, \tilde{\boldsymbol{\epsilon}}] \tag{47}$$

where $\bar{\boldsymbol{\epsilon}} = [\bar{\epsilon}_1, ..., \bar{\epsilon}_m]$ are wave component phase angles and $\tilde{\boldsymbol{\epsilon}} = [\tilde{\epsilon}_1, ..., \tilde{\epsilon}_n]$ are wind component phase angles, if used.

IV. RESULTS

The three sea-states considered are shown in Table VI and represents typical FLS conditions at Dogger Bank along with their probability of occurrence, p. Expected relative contribution to the equivalent yearly fatigue damage is shown in Table VII, and it is clear that the largest sea-state is contributing the most although it has a lower probability of occurrence.

TABLE VI
SEA-STATES FOR FLS CONDITIONS

No.	H$_S$ [m]	T$_P$ [s]	U [m/s]	p [-]
1	1.5	4.7	6	0.1002
2	3.0	6.2	10	0.0314
3	4.8	7.5	14	0.0092

TABLE VII
RELATIVE FATIGUE CONTRIBUTIONS FROM SEA-STATES

	Waves only		Wind and waves	
Sea-state	$D_{\text{year,e}}$	$D_{\text{year,e}} \cdot p$	$D_{\text{year,e}}$	$D_{\text{year,e}} \cdot p$
1	0.011	0.001	0.016	0.0016
2	0.360	0.011	0.100	0.0031
3	1.330	0.012	0.830	0.0076

However, the statistics are limited to these three sea-states, and it is likely that the cumulative contribution from small sea-states will dominate.

When only wave loads are used, the aerodynamic damping is accounted for by increasing the structural damping to 5%. The damping is applied as Rayleigh damping with proper coefficients to obtain the wanted damping level at the first and second vibrational mode. Larger damping also gives a smoother response surface, which makes the FORM iterations converge faster. An example fatigue damage contour is shown in Fig. 11 where two of the largest wave components are varied from 0 to 2π. The contour confirms that the fatigue damage is very sensitive to the wave phase angles.

For validation of the results, 10,000 simulations have been run for the different sea-states, using approximately 120 CPU hours for each condition with the detailed model. The validation plots are presented in Fig. 12. By varying the SCF in the fatigue calculations, it is found that the curvature in highly dependent on the fatigue limit of the bi-linear S-N curve. For sea-state 3, the stress amplitudes are mainly located above the fatigue limit. This results in the same exponent for almost all rainflow counted stress ranges for this sea-state and a close to Gaussian distributed fatigue damage, especially for wave loads only. For the smaller sea-states, only some stress ranges are exceeding the fatigue limit, resulting in a larger variation between the different seeds and more samples in the distribution tail. These processes are closer to Rayleigh or Weibull distributions.

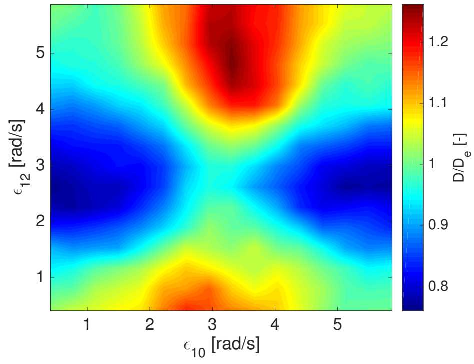

Fig. 11. Example response surface by varying two wave component phase angles for sea-state 3

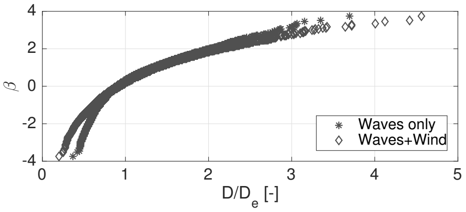

(a) Sea-state 1

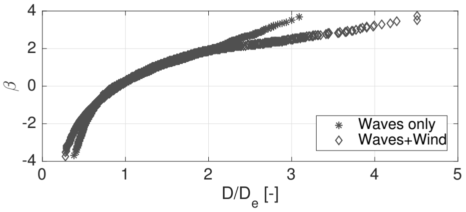

(b) Sea-state 2

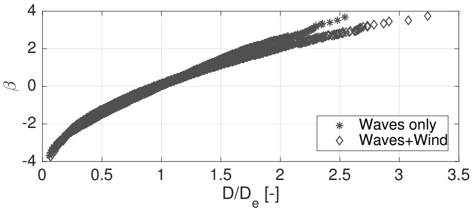

(c) Sea-state 3

Fig. 12. Fatigue damage results with 10,000 simulations for each sea-state and loading condition

The three presented methods for alternative fatigue damage estimation in Table II are fitted to the results from the wave only analysis by sea-state 1 and presented in Fig. 13. Here, 10 seeds are randomly drawn from the 10,000 existing simulations, and the different methods are applied. To conclude, the SL method and quadratic fit seems to represent the underlying distribution well, whereas the linear fit misses the distribution slightly, but may still be appropriate for finding the expected value since it crosses $\beta = 0$ almost exactly at $D/D_e = 1$.

A. Wave loads only

As an initial study, only wave forces was included in the model. To reduce the number of random variables, deterministic wave amplitudes are used and the simulation time is limited to 100 seconds, which gives a maximum of 35 insertions

TABLE VIII
FORM DESIGN-POINTS FOR WAVE LOADS

Sea-state	$D_{\text{year,ext}}$	β_{FORM}
1	0.03	3.15
2	0.80	2.55
3	2.40	2.40

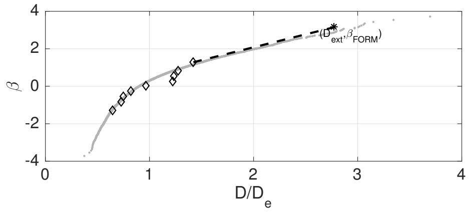

(a) Sum+linear fit

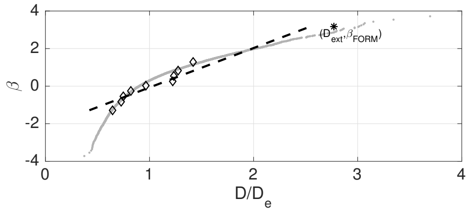

(b) Linear fit

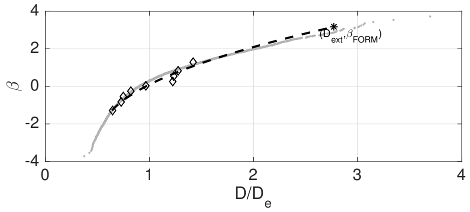

(c) Quadratic fit

Fig. 13. Example fits using the three presented methods using wave loads only and 10 simulations with sea-state 1. Underlying distribution and the FORM evaluated point is plotted.

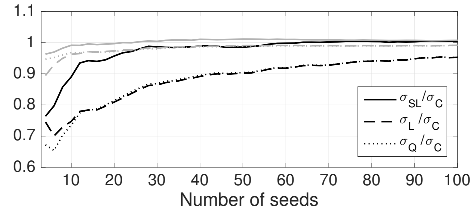

(a) Sea-state 1

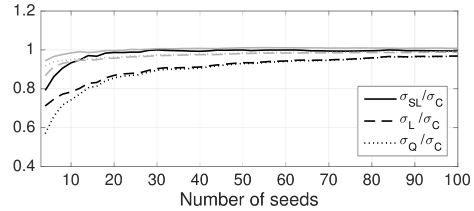

(b) Sea-state 2

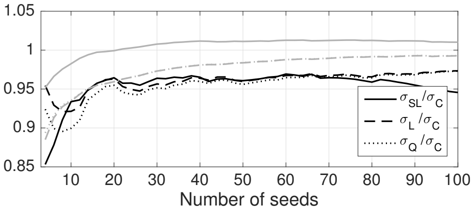

(c) Sea-state 3

Fig. 14. Standard deviations of fatigue damage estimation given number of seeds (N) of 100s simulations with only wave loads. Gray lines are the mean fatigue normalized with true damage.

in $\mathbf{u}$. However, by using (30), the number of variables are reduced to between 15 and 25, depending on the spectrum and significance threshold. The FORM evaluated design-points chosen for proper representation of the extremes are shown in Table VIII.

The complete results for wave loads are shown in Fig. 14 with number of utilized seeds in the fatigue estimation on the x-axis. For each number of seeds, $K = 300$ independent simulations are used to evaluate the mean fatigue and standard deviation. In most cases, the expected fatigue has converged after about 20 seeds for all methods. The most promising results are in sea-state 1 and 2, where the expected fatigue is converging quickly and the variance is lower than the variance using the conventional averaging, σ_C^2, defined as

$$\sigma_{C|N}^2 = \frac{1}{K}\sum_{i=1}^{K}(D_i - D_{C|N})^2 \qquad (48)$$

where $D_{C|N}$ is the mean fatigue for N simulations. Note that the linear and quadratic fit provides the best results when accurately estimating the expected fatigue while having relatively low variance, which is the suggested benefit by using these methods. The SL method is most beneficial for small N, when the two last terms in (17) are still contributing significantly. Interestingly, the SL method does not provide a sufficiently large reduction in the variance, which is due to variations in the MCS point for linearizing the tail. For sea-state 3, no large improvements are seen in the uncertainty of the results. An explanation for this is that the conventional method is already estimating the fatigue quite accurately for a relatively small number of seeds.

For the FORM method to be preferable, the time used for finding β_{FORM} must be smaller than additional Monte Carlo simulations to obtain a smaller variance with the conventional method. For sea-state 3, this is clearly not feasible, but it may be beneficial for sea-state 1, considering that finding β_{FORM} consumes the same time as 40-60 simulations, depending on the initiation point. With a large difference between the detailed and simple model, the argument of curve-fitting is even stronger.

B. Wave- and wind loads

When including wind loads, the simulation model has proved to be slightly more non-linear resulting in larger fatigue damage variations as seen in Fig. 12. Therefore, it is expected that the presented methods will be even more efficient. However, the inclusion of wind loads leads to a dramatic increase in random variables. For a simulation time of 100s, as much as 135 random variables has to be used to avoid repetition of the environmental loads. Even though the number is reduced to about 90-110 by using (30), the computational efforts to find β_{FORM} are still significant, meaning more than 100 simulations with the detailed model. For demonstration of the method, results in Fig. 15 are found using the second largest points in Fig. 12 as the FORM design-points.

The complete results are shown in Fig. 15 using the same approach as for the case with only wave loads. Here, the results are very similar to what is observed in the wave load case. Reduction of the uncertainty is seen for small number of seeds with the curve-fitting methods, but not large enough to justify using significant computational efforts on the FORM analysis.

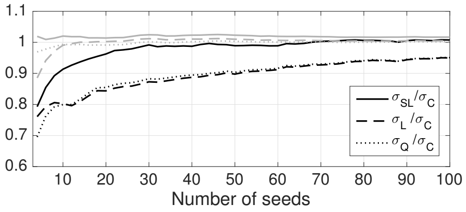

(a) Sea-state 1

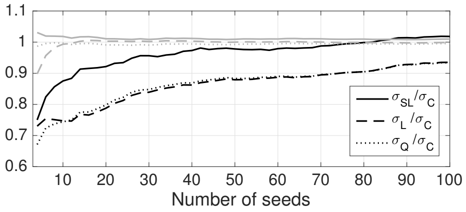

(b) Sea-state 2

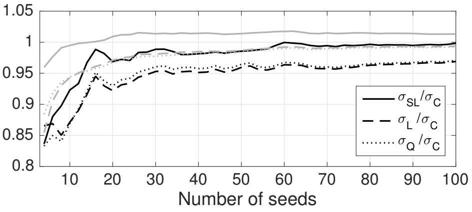

(c) Sea-state 3

Fig. 15. Standard deviations of fatigue damage estimation given number of seeds (N) of 100s simulations with wind and wave loads. Gray lines are the mean fatigue normalized with true damage.

V. CONCLUSION

To conclude, the fatigue damage estimation using a FORM procedure may lead to a reduced uncertainty if the FORM design-point is properly found and contributes significantly to the integration. Especially the linear and quadratic curve fitting methods have proven more reliable that conventional averaging. It has been found that the standard deviation is reduced up to 30% for load cases where the fatigue damage distribution deviates from the normal distribution.

The multi-step FORM procedure might be computationally efficient in a wide range of applications if the simulation model can be simplified sufficiently. For the presented procedure applied to wind turbines to be computationally competing with the conventional average of simulations, β_{FORM} for D_{ext} has to be found with relatively small efforts, or be known from previous analyses by e.g. scaling with respect to the significant wave height [16]. A simpler linear model corresponding to a wind turbine model with a more sophisticated aerodynamic model should be used in future work to reduce computational efforts and evaluate the applicability and effectiveness of the presented methods.

ACKNOWLEDGMENT

This work has been carried out at the Centre for Autonomous Marine Operations and Systems at the Norwegian University of Science and Technology (NTNU AMOS). The Norwegian Research Council is acknowledged as the main sponsor of NTNU AMOS. This work was supported by the Research Council of Norway through the Centres of Excellence funding scheme, Project number 223254 - NTNU AMOS.

REFERENCES

[1] D. Zwick and M. Muskulus, “The simulation error caused by input loading variability in offshore wind turbine structural analysis,” *Wind Energy*, vol. 18, no. 8, aug 2015.
[2] J. J. Jensen, “Fatigue damage estimation in non-linear systems using a combination of Monte Carlo simulation and the First Order Reliability Method,” *Marine Structures*, vol. 44, pp. 203–210, dec 2015.
[3] P.-L. Liu and A. Der Kiureghian, “Optimization algorithms for structural reliability,” *Structural Safety*, vol. 9, no. 3, pp. 161–177, feb 1991. [Online]. Available: http://www.sciencedirect.com/science/article/pii/0167473091900417
[4] H. Madsen, S. Krenk, and N. Lind, *Methods of Structural Safety*. Prentice-Hall, Inc., 1986.
[5] DNV GL, “RP-C203 Fatigue design of offshore steel structures,” Tech. Rep. April, 2005.
[6] WAFO-group, “WAFO - A Matlab Toolbox for Analysis of Random Waves and Loads,” 2000. [Online]. Available: http://www.maths.lth.se/matstat/wafo/
[7] T. Moan and A. Naess, *Stochastic Dynamics of Marine Structures*. Cambridge University Press, 2013.
[8] C. Bak, F. Zahle, R. Bitsche, A. Yde, L. C. Henriksen, A. Nata, and M. H. Hansen, “Description of the DTU 10 MW Reference Wind Turbine,” no. July, 2013.
[9] E. Smilden and L. Eliassen, “Wind Model for Simulation of Thrust Variations on a Wind Turbine,” *Energy Procedia*, 2016.
[10] O. M. Faltinsen, J. N. Newman, and T. Vinje, “Nonlinear wave loads on a slender vertical cylinder,” *Journal of Fluid Mechanics*, vol. 289, p. 179, apr 1995. [Online]. Available: http://journals.cambridge.org/abstract_S0022112095001297
[11] X. Y. Zheng, T. Moan, and S. T. Quek, “Numerical simulation of non-Gaussian wave elevation and kinematics based on two-dimensional fourier transform,” pp. 1–6, 2006.
[12] M. Tucker, P. Challenor, and D. Carter, “Numerical simulation of a random sea: a common error and its effect upon wave group statistics,” *Applied Ocean Research*, vol. 6, no. 2, pp. 118–122, apr 1984.
[13] J. T. H. Horn, J. R. Krokstad, and J. Amdahl, “Hydro-Elastic Contributions to Fatigue Damage on a Large Monopile,” *Energy Procedia*, 2016.
[14] DNV GL, “OS-J101 Design of Offshore Wind Turbine Structures,” Tech. Rep., 2014.
[15] T. Burton, D. Sharpe, N. Jenkins, and E. Bossanyi, *Wind Energy Handbook*. John Wiley & Sons, Ltd, 2002. [Online]. Available: http://dx.doi.org/10.1002/0470846062.ch4
[16] J. J. Jensen, “Extreme value predictions using Monte Carlo simulations with artificially increased load spectrum,” *Probabilistic Engineering Mechanics*, vol. 26, no. 2, pp. 399–404, apr 2011. [Online]. Available: http://www.sciencedirect.com/science/article/pii/S0266892010000767

Paper III

Long-Term Fatigue Damage Sensitivity to Wave Directionality in Extra Large Monopile Foundations

Jan-Tore Horn, Jørgen R. Krokstad, and Jørgen Amdahl

Journal of Engineering for the Maritime Environment, 2018

Abstract The fatigue damage sensitivity to wave directionality on large-diameter monopile foundations for use in the offshore wind turbine industry is investigated. A frequency domain approach with the Dirlik method is used for a fatigue damage estimate and evaluate the effect of wave spreading and swell separation compared to a total sea representation. 30 years of hindcast data from the Dogger Bank area is used to evaluate the long-term impact. Furthermore, a computationally efficient time domain model of a 10 MW offshore wind turbine is used to compare with the frequency domain results. Results show that benefits in terms of structural fatigue can be obtained with directional considerations.

Long-Term Fatigue Damage Sensitivity to Wave Directionality in Extra Large Monopile Foundations

Jan-Tore H. Horn [1,2], Jørgen R. Krokstad [2] and Jørgen Amdahl [1,2]

Abstract

The fatigue damage sensitivity to wave directionality on large-diameter monopile foundations for use in the offshore wind turbine industry is investigated. A frequency domain approach with the Dirlik method is used for a fatigue damage estimate and evaluate the effect of wave spreading and swell separation compared to a total sea representation. 30 years of hindcast data from the Dogger Bank area is used to evaluate the long-term impact. Furthermore, a computationally efficient time domain model of a 10 MW offshore wind turbine is used to compare with the frequency domain results. Results show that benefits in terms of structural fatigue can be obtained with directional considerations.

Keywords

Directionality, Fatigue, Hydrodynamics, Long-term statistics, Offshore environment, Offshore wind turbines, Swell

Introduction

The monopile foundation has proven to be the most cost-efficient solution in the offshore wind turbine industry due to its simple construction. As the rotor diameters and generator capacities are increasing to reduce the cost of energy, there is a need for large-diameter monopiles for up to 30-40 meters water depth. A consequence of the increasing submerged volume of the support structure is a higher sensitivity to wave loads for both FLS and ULS design considerations. This is in contrast to jacket foundations, where the wave load contribution is found to be significantly less than the wind loads[1], being less sensitive to wave directionality and swell separation.

The overall goal for the offshore wind industry is to reduce the levelized cost of energy (LCoE) to be able to compete with non-renewable sources of electricity. There are many ways to achieve cost reduction, but the focus here is on design conservatism. Being a low-margin industry, both investment and operational costs play an important role in the profitability of an offshore wind farm. Hence, accurate analysis models for use in the structural design are important. The topic of this paper is important for substructure designs that are driven by wave loads. Previous studies have been performed on hydrodynamic load models for monopile foundations, and the outcome has been compared with industry standards[2;3] and model tests[4]. These account for typical sea states for both FLS and ULS design, and findings include the importance of wave diffraction and non-linear load effects such as ringing[5]. In general, the purpose is to de-risk monopile support structures for larger turbines and greater water depths.

A previous study has been performed[6] to find reduction factors for fatigue damage for various types of wave directionality. Although the wave environment is somewhat idealized, the result indicates a large potential for reduced conservatism and correspond well with the short-term fatigue factors (FF) obtained in the present work. It has previously been demonstrated how a directional distribution can be used for probabilistic analyses[7], and the effects on selection and determination of the extreme design wave criteria[8;9]. These investigations have shown that care must be taken in a design process when using directional distribution of environmental conditions and directional bins. One might end up with a less reliable structure than intended for ULS design considerations. For FLS design, it will here be demonstrated how a directional consideration can increase the structural reliability and to what extent the circumferential fatigue damage depends on load directionality.

In the present work, both a frequency- and a time domain model are implemented in order to qualitatively compare the effects of wave directionality with the different approaches. The frequency domain model is expected to be a good approximation when evaluating the FLS conditions where the contribution from non-linear wave loads and structural response can be neglected.

Model Description

The computational model used in this work is the onshore DTU 10 MW reference wind turbine[10] mounted on an offshore monopile foundation. To keep the first natural period realistically low, the original tower is stiffened by increasing the thickness 20%. The turbine is located in 30 meters of water depth at Dogger Bank in the North Sea and 60 years of hindcast data are retrieved from the Norwegian Meteorological Institute[11] for an approximate location. The monopile has a simplified design with a constant outer diameter from 42 meters below the mudline to the tower

---

[1] Centre for Autonomous Marine Operations and Systems (NTNU AMOS)
[2] Department of Marine Technology, Norwegian University of Science and Technology, Trondheim, Norway

Corresponding author:
Jan-Tore H. Horn, NTNU AMOS, Department of Marine Technology, Otto Nielsen veg 10, 7491 Trondheim, Norway.
Email: jan-tore.horn@ntnu.no

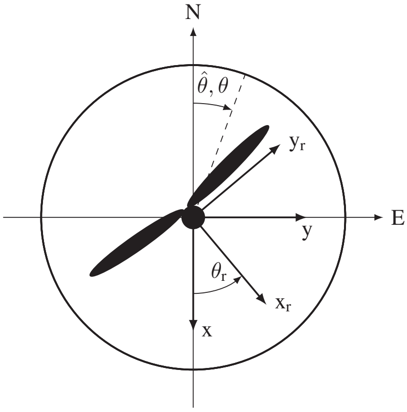

Figure 1. Directional definitions for environment (θ), monopile circumference ($\hat{\theta}$) and rotor plane (θ_r)

base at 10 meters above sea level (m.a.s.l.). The part from -10 to 10 m.a.s.l. is defined as the transition piece, which is stiffened by increasing the monopile thickness by 36%. Here, the monopile diameter and thickness are 8.0 and 0.11 meters, respectively, partly based on a preliminary design[12]. The structural model is illustrated in Fig. 2 with all components manufactured in steel, with a 8% density increase in the transition piece and tower to account for secondary structures. As a result, the first and second natural period of the system are approximately 4.4 and 0.9 seconds. The numerical analyses are carried out with USFOS[13]. with a computationally efficient model. Beams are used for the monopile and tower in the FEM analysis, while the soil stiffness is modelled using an equivalent cantilever beam tuned to properly represent realistic eigenmodes[3] and natural periods mentioned above. Wave loads are calculated by the Morison equation with correction for linear diffraction and a vertical stretching to the free surface.

This paper focuses on the effects of directionality on the environmental loads, it is therefore necessary to define the wind turbine operational conditions in relation to the north-east (NE) frame as well as the local frame (xy) and rotor-frame ($\mathrm{x_r y_r}$). These definitions are illustrated in Fig. 1.

Environmental conditions

The environmental conditions used in simulations are obtained from the hindcast data. The most important parameters for description of the offshore environment are given in Tab. 1, while the remaining parameters can be found in Tab. 2. It is assumed that the wind speed at 100 m.a.s.l. is equal the wind speed at hub height, which is located at 119 m.a.s.l. Also, no corrections are made to the hindcast data with respect to local bathymetry. Except for parameters related to current, spreading and spectral peak shape, information is readily available. Scatter diagrams and joint contour plots can be found in the appendix for the simulated data.

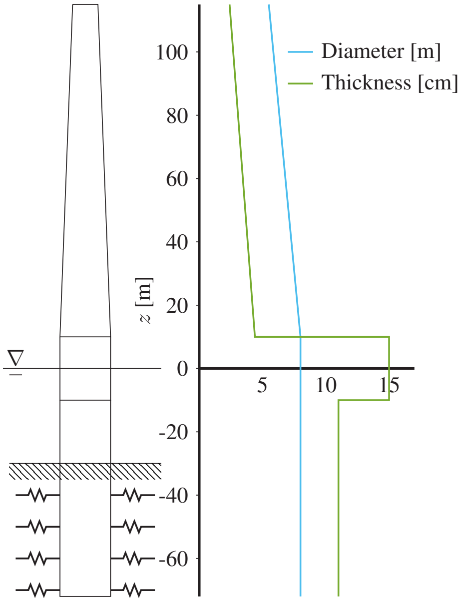

Figure 2. Structural dimensions of tower and monopile foundation

In Fig. 3, the circular probability density functions (PDF) of the some environmental parameters are presented. The most likely wind and wind sea direction is from the south-west, while swell is mostly coming from the northern North Sea. Is is clear that the total sea distribution is significantly influenced by the swell component. To get an idea about the direction of the most energetic waves, the directional data is weighted by the significant wave heights squared. The result is shown in Fig. 4 and by the available information, it is expected that the wave-induced fatigue damage will be largest at north or south side of the foundation.

This work will present results from five different variations on wave directionality in addition to the long-term mean direction variation:

- Long-crested total sea (L)
- Short-crested total sea (S)
- Long-crested wind sea and long-crested swell (LL)

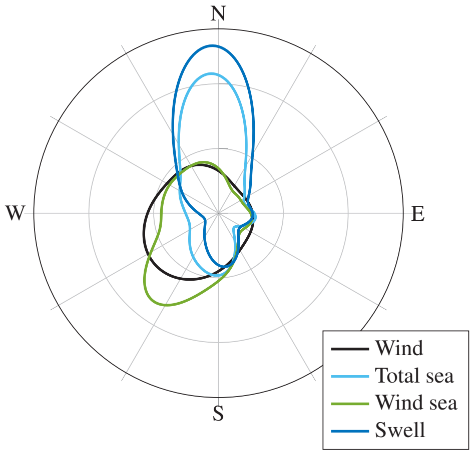

Figure 3. Directional marginal distributions of environmental parameters

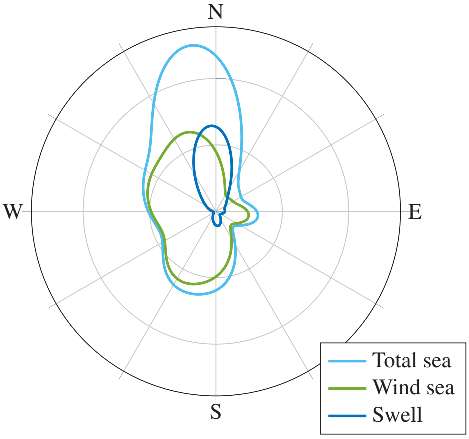

Figure 4. Directional marginal distributions of environmental parameters weighted with the square of the respective significant wave heights

Table 1. Primary parameters for description of environmental conditions

	Description	
Θ_u	Mean wind heading relative to N	[deg]
Θ	Mean total sea direction relative to N	[deg]
U	Mean wind speed at 100m.a.s.l.	[m/s]
H_S	Significant wave height for total sea	[m]
T_P	Peak period for total sea	[s]
γ	Peak shape parameter for total sea	[-]
h	Water depth	[m]

Table 2. Secondary parameters for description of environmental conditions

	Description	
Θ_w	Mean wind-sea direction relative to N	[deg]
Θ_s	Mean swell direction relative to N	[deg]
H_{S_w}	Significant wave height for wind sea	[m]
H_{S_s}	Significant wave height for swell	[m]
T_{P_w}	Peak period for wind sea	[s]
T_{P_s}	Peak period for swell	[s]
γ_w	Peak shape parameter for wind sea	[-]
γ_s	Peak shape parameter for swell	[-]
s	Spreading exponent for wind sea	[-]
X	Spreading parameter for swell	[-]
V_c	Current velocity	[m/s]
Θ_c	Current direction	[deg]

- Short-crested wind sea and long-crested swell (SL)
- Short-crested wind sea and short-crested swell (SS)

Availability

The availability of a wind turbine is defined as the proportion of the time it is capable of producing power. The aerodynamic damping level of the turbine decreases dramatically when the turbine is not operating, which is an important parameter for fatigue estimation. This relation is becoming more important as the wind turbines are getting larger, meaning that the relative difference between operational and non-operational damping level is increasing. It has been reported that current offshore wind farms have an availability between 90 and 95%[14], which is slightly less than land-based turbines. Final results are therefore presented using both 90 and 100% availability to find any impact on the fatigue damage using the different directional descriptions. To account for the fact that the unavailability may occur at any time during the total lifecycle, simulations with 0 and 100% availability are superimposed after weighting with the percentage of total availability. The fatigue damage is then found as:

$$D = D_\mathrm{unavail} \cdot (1-\alpha) + D_\mathrm{avail} \cdot \alpha \tag{1}$$

where α is the availability fraction.

Directional wave spectrum

According to design standards[15], the total wave spectrum can be modelled as a superposition of the wind sea and swell spectrum with their respective generalized spreading functions:

$$S_{\zeta\zeta}(\omega,\theta) = S_\mathrm{w}(\omega)\Delta_\mathrm{w}(\omega,\theta) + S_\mathrm{s}(\omega)\Delta_\mathrm{s}(\omega,\theta) \tag{2}$$

Tthe JONSWAP spectrum is used for both wind sea and swell spectrum, and the peak shape parameters is a function of the significant wave height and peak period[15]. The spreading function for wind sea in infinite water depth is given as a *cos-2s* distribution[16]:

$$\Delta_\mathrm{w}(\omega,\theta) = \frac{\Gamma[s(\omega)+1]}{2\sqrt{\pi}\Gamma[s(\omega)+1/2]} \cos^{2s(\omega)}\left(\frac{\theta-\Theta_\mathrm{w}}{2}\right) \tag{3}$$

for a frequency dependent spreading exponent s. For practical purposes, the spreading exponent is often considered frequency independent, which in general is more conservative[17]. The established frequency dependent spreading functions are all based on wave measurements and are on the form:

$$s(\omega) = s_p \left(\frac{\omega}{\omega_p}\right)^{\mu} \tag{4}$$

as seen in e.g.[18;19]. Observations have shown that the spreading exponent is decreasing for frequencies away from the peak frequency, and that it is in dependent on the wave age. For practical purposes, s is often regarded as a constant between 4 and 9[15]. Here a model described in Tucker[20] and implemented in Krokstad[17] is used, where:

$$s_p = \begin{cases} 6.97 & \text{for } \omega < 1.05\omega_p \\ 9.77 & \text{for } \omega \geq 1.05\omega_p \end{cases} \tag{5}$$

and

$$\mu = \begin{cases} 4.06 & \text{for } \omega < 1.05\omega_p \\ -1.91 & \text{for } \omega \geq 1.05\omega_p \end{cases} \tag{6}$$

Further, the directional distribution of the swell component can be approximated by a Poisson distribution[21], also assuming infinite water depth:

$$\Delta_\mathrm{s}(\omega,\theta) = \frac{1}{2\pi}\frac{1-X(\omega)^2}{1-2X(\omega)\cos(\theta-\Theta_\mathrm{s})+X(\omega)^2} \tag{7}$$

where

$$X(\omega) = X_p \left(\frac{\omega}{\omega_p}\right)^{\nu} \tag{8}$$

using $X_p = 0.9$[22], and

$$\nu = \begin{cases} 2.21 & \text{for } \omega < \omega_p \\ -0.35 & \text{for } \omega \geq \omega_p \end{cases} \tag{9}$$

When the swell is modelled as long-crested, $\Delta_\mathrm{s} = 1$ for $\theta = \Theta_\mathrm{s}$ and zero elsewhere.

SN-curves

Fatigue damage at the mudline is calculated using SN-curves in both the frequency- and the time domain with the SN-curves given in Tab. 3[23]. The predicted number of cycles until failure, N, is found with

$$\log N_n = \log K_n - \beta_n \log \left(\Delta\sigma (t/t_\mathrm{ref})^{k_t} \cdot \mathrm{SCF}\right) \tag{10}$$

for a given stress range $\Delta\sigma$ and material parameter β. Further, t is the cross section thickness, t_ref is the reference thickness and k_t is the thickness exponent. Here, $n = 1$ for a single-slope SN-curve and

$$n = \begin{cases} 1 & \text{for } \Delta\sigma \geq s_0 \\ 2 & \text{for } \Delta\sigma < s_0 \end{cases} \tag{11}$$

for two-slope SN-curves. For practical reasons, the single-slope SN-curves are used in frequency domain analyses, corresponding to elements without cathodic protection. The fatigue damage from the time domain simulations is estimated using rainflow counting and the Palmgren-Miner rule with the WAFO toolbox[24].

Table 3. Three different SN-curves

SN-curve		1	2	3
β_1		3	5	3
β_2		-	-	5
$\log K_1$		11.764	15.606	11.764
$\log K_2$		-	-	15.606
s_0	[MPa]	-	-	52.63
k_t		0.2	0.2	0.2
t_ref	[mm]	25	25	25
SCF		1.0	1.0	1.0

Wind sea and swell compared to total sea

To facilitate comparisons between directionally dependent sea state realizations, the energy in the wave spectrum must be conserved. From the hindcast generated wind sea and swell components, the total significant wave height can be found as[15]:

$$H_S = \sqrt{H_{S_\mathrm{w}}^2 + H_{S_\mathrm{s}}^2} \tag{12}$$

The above equation for significant wave height compares very well to the hindcast data for total sea. However, finding the equivalent total sea peak period from the swell and wind sea components is not straightforward. Therefore, a typical design approach is performed; the simulated total sea is based purely on the hindcast data with default peak shape factor[15]. As a consequence, the total spectral energy may differ between the total sea spectrum and the spectrum based on both wind sea and swell.

Fatigue factor

The fatigue factor (FF) from simulations using directional spreading is calculated as:

$$\mathrm{FF}_\mathrm{S} = \frac{\max[D_\mathrm{S}(\hat{\boldsymbol{\theta}})]}{\max[D_\mathrm{L}(\hat{\boldsymbol{\theta}})]} \tag{13}$$

for all directions of evaluation in the vector $\hat{\boldsymbol{\theta}}$ about the circumference of the foundation. The FF is an indication of how much the maximum circumferential fatigue damage has changed compared to analyses with long-crested total sea. A similar expression is used for all wave direction variations.

Frequency domain model

Mudline bending moment transfer function

Using the Morison equation as a basis, the linearized total complex force per unit length from an undisturbed wave field is given as:

$$\begin{aligned} f_x =& \zeta_a \rho \pi r^2 C_M a_x + \zeta_a^2 \rho r C_D |u_x| u_x \\ \approx& \zeta_a \left\{ \rho \pi r^2 C_M a_x + \rho r C_D \sqrt{\frac{8}{3\pi}} \sigma_u u_x \right\} \\ =& \zeta_a \cdot \bar{f}_x(\omega, \sigma_u) \end{aligned} \tag{14}$$

where r is the monopile radius and C_M is the mass coefficient corrected for diffraction and

$$u_x = -i\omega \frac{\cosh k(z+h)}{\sinh kh} \tag{15}$$

$$a_x = \omega^2 \frac{\cosh k(z+h)}{\sinh kh} \tag{16}$$

The drag coefficient is assumed to be constant equal to one, while the particle velocity standard deviation is found with:

$$\sigma_u^2(\theta) = \int_0^\infty \omega^2 S_{\zeta\zeta}(\omega, \theta) d\omega \tag{17}$$

Following the order of magnitude definition in Horn et al.[3] and Faltinsen[25], and assuming a rigid body, one degree-of-freedom system with no radiation effects, the moment transfer function is obtained as:

$$\bar{M}_\mathrm{y}(\omega) = \int_{-h}^{0} \bar{f}_x \cdot (z+h) \cdot dz + O(\epsilon^2 \delta^2) \tag{18}$$

and the following relation is utilized:

$$\int_{-h}^{0} (z+h) \cdot \frac{\cosh k(z+h)}{\sinh kh} dz = \frac{hk - \tanh \frac{hk}{2}}{k^2} \tag{19}$$

The resulting spectrum for the mudline bending moment can then be found as:

$$S_\mathrm{MM}(\omega, \theta) = |\bar{M}_\mathrm{y}(\omega)|^2 \cdot S_{\zeta\zeta}(\omega, \theta) \tag{20}$$

Dynamic amplification factor

An investigation on dynamic amplification of marine structures can be found in e.g. Horn et al.[26]. Due to the linear response characteristics of a mass-dominated structure, it is sufficient to use the single harmonic dynamic amplification factor (DAF)[27]:

$$DAF(\omega,\theta,U) = \frac{1}{\sqrt{(1-\Omega^2)^2 + (2\zeta\Omega)^2}} \tag{21}$$

where $\Omega = \frac{\omega}{\omega_1}$ and ω_1 is the first natural period of the system, neglecting contribution from higher modes. Estimating the damping level is not straightforward, especially in irregular seas. In general, the damping level is found as:

$$\zeta = \zeta_a(\theta,U) + \zeta_s + \bar{\zeta} \tag{22}$$

for a structural damping level ζ_s, here equal to 0.5%, wind- and directionally dependent aerodynamic damping ζ_a presented later, and some additional damping $\bar{\zeta}$, which is here calibrated to approximately 5% to account for damping induced by hydrodynamic loads in an irregular sea. The modified bending moment spectrum is then:

$$S_{\mathrm{MM}}(\omega,\theta,U) = |\bar{M}_{\mathrm{y}} \cdot DAF|^2 \cdot S_{\zeta\zeta} \tag{23}$$

Circumferential fatigue damage distribution

The axial stress at a location $\hat{\theta}$ on a cylindrical beam element due to axial load and bending moments can be expressed in the time domain as:

$$\begin{aligned} s_z(\hat{\theta}) &= \frac{N}{A} - \frac{M_y \cdot r\cos\hat{\theta}}{I_A} - \frac{M_x \cdot r\sin\hat{\theta}}{I_A} \\ &= \frac{N}{A} - \sum_{\theta\in\boldsymbol{\theta}} \frac{M_\theta \cdot r\cos(\hat{\theta}-\theta)}{I_A} \end{aligned} \tag{24}$$

for loads acting in directions contained in $\boldsymbol{\theta}$. Here, A is the cross sectional area, N is the axial force, I_A is the second area moment of the cross section and M_x, M_y and M_θ are the bending moments in x-, y- and θ-direction, respectively. Taking the variance yields:

$$\sigma_s^2(\hat{\theta}) = \sum_{\theta\in\boldsymbol{\theta}} \sigma_s^2(\hat{\theta}|\theta) \tag{25}$$

where

$$\sigma_s^2(\hat{\theta}|\theta) = \frac{r^2}{I_A^2} \cdot \sigma_{\mathrm{M}}^2(\theta) \cdot \cos^2(\hat{\theta}-\theta) \tag{26}$$

and the variance of the directionally dependent moments is found by integrating the response spectrum:

$$\sigma_{\mathrm{M}}^2(\theta) = \int_0^\infty S_{\mathrm{MM}}(\omega,\theta)d\omega \tag{27}$$

Dirlik method

The fatigue damage in the frequency domain is evaluated using the Dirlik method[28]. At a circumferential location $\hat{\theta}$, the damage due to a load acting in direction θ is:

$$\begin{aligned} D^{\mathrm{DK}}(\hat{\theta}|\theta) = C \cdot \sigma_s^\beta(\hat{\theta}|\theta) \Big[& G_1 Q^\beta \Gamma(1+\beta) \\ & + \sqrt{2}^\beta \Gamma(1+\frac{\beta}{2})(G_2|R|^\beta + G_3)\Big] \end{aligned} \tag{28}$$

where C$=\nu_p \cdot T \cdot K^{-1} \cdot (t/t_{\mathrm{ref}})^{\beta\cdot k_t} \cdot \mathrm{SCF}^\beta$, and the G_1, G_2, G_3, R and Q parameters read:[28;29]

$$\begin{aligned} G_1 &= \frac{2(x_m - \alpha_2^2)}{1+\alpha_2^2} & G_2 &= \frac{1-\alpha_2 - G_1 + G_1^2}{1-R} \\ G_3 &= 1 - G_1 - G_2 & R &= \frac{\alpha_2 - x_m - G_1^2}{1-\alpha_2-G_1+G_1^2} \\ Q &= \frac{1.25(\alpha_2 - G_3 - G_2 R}{G_1} \end{aligned} \tag{29}$$

Further, the α_2, x_m and ν_p parameters are calclutated as:

$$\begin{aligned} \alpha_2 &= \frac{m_2}{\sqrt{m_0 m_2}} & x_m &= \frac{m_1}{m_0}\Big(\frac{m_2}{m_4}\Big)^{\frac{1}{2}} \\ \nu_p &= \sqrt{\frac{m_4}{m_2}} \end{aligned} \tag{30}$$

by using the n$^{\mathrm{th}}$ spectral moment defined as:

$$m_n = \int_0^{2\pi}\int_0^\infty \omega^n S(\omega,\theta)d\omega d\theta \tag{31}$$

By integrating over the load directions for the sea state, a short-term fatigue damage is found as:

$$D_n^{\mathrm{DK}}(\hat{\theta}) = \frac{1}{2\pi}\int_{-\pi}^{\pi} D^{\mathrm{DK}}(\hat{\theta}|\theta)d\theta \tag{32}$$

Finally, the long-term fatigue damage is calculated by superposition over N individual sea states:

$$D^{\mathrm{DK}}(\hat{\theta}) = \sum_{n=1}^{N} D_n^{\mathrm{DK}}(\hat{\theta}) \tag{33}$$

Time domain model

Wave kinematics

The wave kinematics for time domain analysis are computed using the Matlab-based, in-house program WaveSim[3]. Wave loads to the first order are included, in addition to a vertical stretching of the first order kinematics to the linear free surface which introduces second order forcing terms[3].

Aerodynamics

When using constant wind, assuming stationary conditions and neglecting rotor-induced loads, there is no need for a rotor or control system. Instead a constant force is applied to account for the structural displacements due to mean aerodynamic thrust given by:

$$F_a = \frac{1}{2}\rho_a \pi R^2 C_T(U) U^2 \tag{34}$$

where R is the rotor radius and the thrust coefficient is taken as:

$$C_T(U) = \begin{cases} 0.8 & \text{for } 4 \leq U < 11 \\ 39e^{-0.37U} + 0.13 & \text{for } 11 \leq U \leq 25 \\ 0.0 & \text{else} \end{cases} \tag{35}$$

Aerodynamic damping is accounted for using dashpot dampers at the tower top during simulations. The rotor-induced damping is dependent on both wind speed and

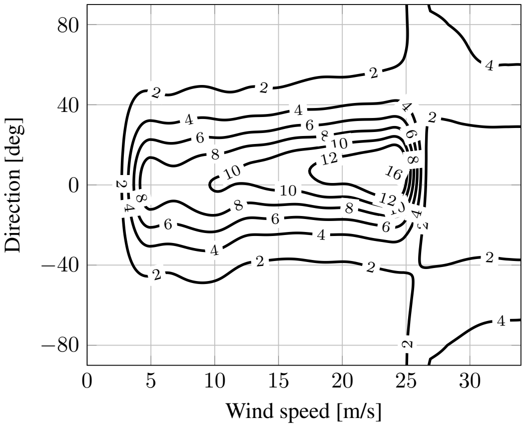

Figure 5. Aerodynamic damping coefficient ζ_a as a function of wind speed and vibration direction

vibrational direction. A complete model of the DTU 10 MW reference wind turbine[10] is used to estimate the damping on the present foundation. The results are presented in Fig. 5, and it is seen that there is a significant level of aerodynamic damping in operational conditions for vibrational modes aligned with the wind direction. Interestingly, there is a significant difference in damping level for a tower top vibrational direction of -15 and 15 degrees for higher wind speeds. This is simply due to the clockwise rotation of the turbine when looking downwind, introducing a larger drag on the blade due to the relative velocity. Also, above the cut-out wind speed, when the rotor is idling with a blade pitch angle of 82 degrees, there is larger side-to-side than fore-aft damping. This indicates that the blades can contribute to the aerodynamic damping even in non-operational conditions. In the frequency domain, the wind and directionally dependent damping is found by interpolation, while the applied dashpot damping in time domain is the fore-aft and side-to-side damping ratios only. As a result, the damping in time domain will decrease proportionally with cosine, meaning that the damping coefficient will be over-predicted for small to intermediate wind-wave misalignment angles. The lower limit of aerodynamic damping is 1%.

Theoretical fatigue factors

In this section a theoretical fatigue damage reduction will be derived using a spectral method and narrow-banded response. Due to the non-linearity of separating the swell component from the fatigue damage expression, this is only done for long- and short-crested waves with the same wave spectrum and frequency independent spreading. First, the fatigue factor, FF, for a single sea state is derived in Eqn. (36). Here, the FF is evaluated in the same direction as the mean direction of the incoming waves, i.e. $\hat{\theta} = 0$ and $\bar{\theta} = 0$, where $\bar{\theta}$ is the mean direction. The closed-form solution in Eqn. (36) corresponds exactly to the wave kinematics factor (WKF) for long-crested waves[15] reproduced in Eqn. (37), with the relationship $\text{FF} = \text{WKF}^{\beta}$. Some example values are given in Tab. 4 for the FF in a single sea-state. These values indicate that in a short-term perspective, a large reduction in the fatigue damage can be expected when using short-crested sea, depending on the bandwidth of the directional spreading.

Table 4. Theoretical short-term fatigue factors for short-crested compared to long-crested waves using two SN-curves (SN) and three spreading exponents (s)

		s		
		4	6	9
SN	1	0.59	0.67	0.75
	2	0.41	0.52	0.62

$$FF = \frac{D_{\text{S}}}{D_{\text{L}}}(\hat{\theta} = 0|\bar{\theta} = 0) = \frac{\sigma^{\beta}_{\text{s,SC}}}{\sigma^{\beta}_{\text{s,LC}}}(\hat{\theta} = 0|\bar{\theta} = 0) \tag{36a}$$

$$= \frac{\left[\int_{-\pi}^{\pi} \sigma^2_{\text{M,SC}}(\theta) \cdot \cos^2(\theta) d\theta\right]^{\beta/2}}{\sigma^{\beta}_{\text{M,LC}}} \tag{36b}$$

$$= \left[\int_{-\pi}^{\pi} \Delta_{\text{w}}(\theta) \cdot \cos^2(\theta) d\theta\right]^{\beta/2} \tag{36c}$$

$$= \left[\frac{\Gamma(s+1)}{2\sqrt{\pi}\Gamma(s+1/2)} \int_{-\pi}^{\pi} \cos^{2s}(\frac{\theta}{2}) \cos^2(\theta) d\theta\right]^{\beta/2} \tag{36d}$$

$$= \left[\frac{\Gamma(s+1)}{\Gamma(s+1/2)} \cdot \frac{(s^2+s+1)\Gamma(s+1/2)}{\Gamma(s+3)}\right]^{\beta/2} \tag{36e}$$

$$= \left[\frac{s^2+s+1}{(s+1)(s+2)}\right]^{\beta/2} \tag{36f}$$

$$\text{WKF} = \sqrt{\frac{s^2+s+1}{(s+1)(s+2)}} \tag{37}$$

Now, the long-term FF will be derived under the assumption that the wave loads are uniformly distributed from all directions. Since the environmental loads are assumed to have the same severity in all directions, so will the fatigue damage. Hence, setting $\hat{\theta} = 0$ as the point of evaluation is sufficient. The fatigue factors for N uniformly distributed environmental conditions from north to south is then given as:

$$\frac{D_{\text{S}}}{D_{\text{L}}}(\hat{\theta} = 0) = \frac{\sum_{n=1}^{N} \sigma^{\beta}_{\text{s,SC}}(\bar{\theta}_n)}{\sum_{n=1}^{N} \sigma^{\beta}_{\text{s,LC}}(\bar{\theta}_n)} \tag{38a}$$

$$= \frac{\sum_{n=1}^{N} \left[\int_{-\pi}^{\pi} \Delta_{\text{w}}(\theta) \cdot \cos^2(\theta - \bar{\theta}_n) d\theta\right]^{\beta/2}}{\sum_{n=1}^{N} \left[\cos^2(\bar{\theta}_n)\right]^{\beta/2}} \tag{38b}$$

Here, no closed-form solution is available, but the FF has converged for $N > 20$. The numerically evaluated factors are found in Tab. 5, and as expected, the fatigue reduction is smaller in a long-term perspective compared to a single sea state. It is also seen that the FF is less dependent on the wave spreading exponent. For offshore wind turbines, the fatigue damage is expected to have a significant contribution from high-cycle fatigue, meaning that the FFs for $\beta = 5$ may dominate the results when a quasi-static response assumption is valid. Hence, there is a potential for reducing the FLS design conservatism.

Table 5. Theoretical long-term fatigue factors for short-crested compared to long-crested waves for two SN-curves (SN) and three spreading exponents (s)

		s		
		4	6	9
SN	1	0.86	0.88	0.90
	2	0.60	0.66	0.73

From the fatigue factors in Tab. 5, one can show that use of the wave kinematics factor in Eqn. (37) is conservative for $\beta = 5$ and non-conservative for $\beta = 3$, meaning that the WKF should be applied with care in a long-term directionally dependent fatigue evaluation.

Long-term fatigue damage predictions

Results are presented for frequency domain analysis using the latest 30 years of raw data and time domain simulations with five years of data, or approximately 15,000 individual sea states. The computational efforts are very small in the frequency domain, but the time domain simulations through five years requires over 3,000 CPU-hours, even with a computationally efficient model with a real- to simulation time ratio of 18:1.

The complete multivariate results are found in the appendix, where the correlations between fatigue factors and environmental conditions are visualized.

Frequency domain analysis

Results from simulations with a constant sprading exponent are shown in the rosette in Fig. 6. The corresponding fatigue factors are found in Tab. 6, including fatigue factors when including frequency wave spreading. For the single slope SN-curve with $\beta = 3$ there is no change in the long-term fatigue damage using a short-crested formulation for the total sea. Theoretically a damage reduction of 10% is expected, but due to non-uniform directional environmental loads, the total maximum fatigue does not change significantly. This is true for both constant an frequency dependent spreading. When using a larger material exponent as in SN-curve 2, the effect of wave spreading is beneficial in terms of reduced fatigue damage. Explained by the increased importance of reduced loading and less impact from directional components away from the main propagation direction.

When swell is separated from the spectrum, meaning that the wind sea and swell spectrum are superimposed, there is a benefit in spread energy, but there is also a larger probability of significant misalignment angles between the swell- and wind direction. For swell significant wave height comparable to the wind sea wave height, this may excite low-damped vibrational modes.This effect is not captured completely in the frequency domain as the structure is assumed to be excited in-line with the individual wave components, while in time domain such components may rather contribute to excitation of other low-damped directions. Significant reduced fatigue damage is observed, when the swell is modelled as short-crested. Now, more of the energy from the swell is propagating in directions affected by the aerodynamic damping, and hence reducing the response.

Table 6. Fatigue factors from frequency domain analyses with single-slope SN-curves (SN) and 100% availability. Normalized w.r.t. long-crested sea (L)

	Spreading							
	$s = 9$				$s(\omega)$			
SN	LL	S	SL	SS	LL	S	SL	SS
1	0.90	1.00	1.04	0.92	0.90	1.02	1.11	0.99
2	0.76	0.83	0.81	0.67	0.76	0.79	0.84	0.70

Total fatigue damage using 90% availability is presented in Fig. 7. The fatigue has increased by approximately 40-50% for SN-curve 2 by comapring Fig. 6b and 7b, stating the importance of including unavailability. Relative

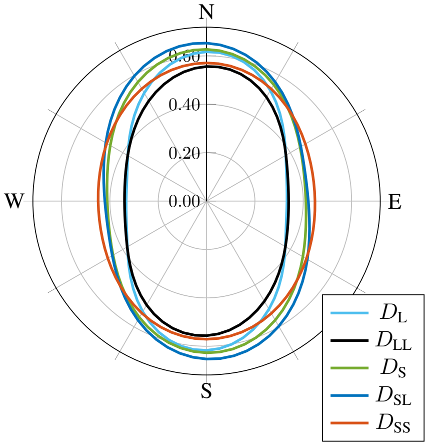

(a) SN-curve 1

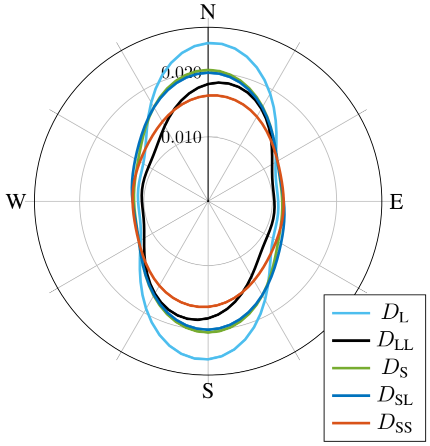

(b) SN-curve 2

Figure 6. 20-year circumferential fatigue damage at mudline using Dirlik method in the frequency domain and 20 years of data with spreading exponent $s = 9$.

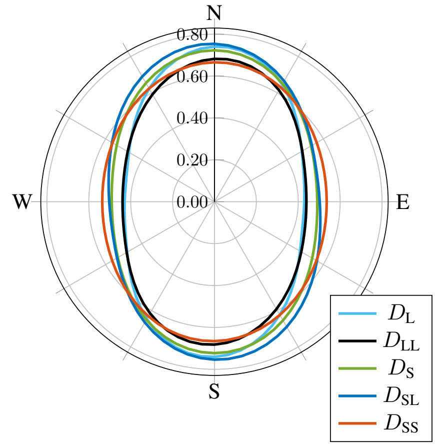

(a) SN-curve 1

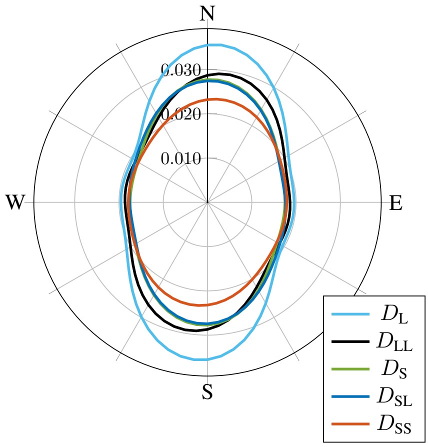

(b) SN-curve 2. S and SL configuration overlap.

Figure 7. 20-year circumferential fatigue damage at mudline using Dirlik method in the frequency domain and 20 years of data with 90% availability and spreading exponent $s = 9$

differences with respect to long-crested sea are found in Tab. 7 and show that spreading is increasingly important when considering availability, in terms of reducing the expected fatigue damage.

Table 7. Fatigue factors from frequency domain analyses with SN-curve 1, 90% availability and spreading exponent $s = 9$. Normalized w.r.t. long-crested sea (L)

SN	LL	S	SL	SS
1	0.92	0.97	1.02	0.89
2	0.82	0.77	0.76	0.65

Time domain analysis

Results from time domain analysis confirm qualitatively what was observed in frequency domain. Hence, the simple one degree-of-freedom frequency is a good indicator for variations in fatigue. The circumferential fatigue damage from time domain simulations is plotted in Fig. 8, which shows a high degree of correlation with Fig. 6b indicating that the high-cycle part of the SN-curve is dominating the results. The corresponding fatigue factors are presented in Tab. 8, showing slight fatigue reductions, especially when modelling the swell as short-crested. Note that the circumferential distribution in shifted slightly counterclockwise, because the wind turbine model used in time domain simulations are only able to translate in one direction at the time, meaning that more wave components will excite lightly damped vibrational directions. Comparing with Fig. 3 and 4, the maximum fatigue occurs at the location excited by most wave energy, but has the largest probability of misaligned wind and waves.

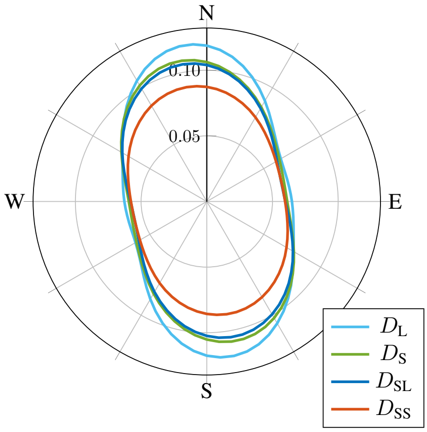

Figure 8. 20-year circumferential fatigue damage at mudline using dynamic time domain simulations and 5 years of data. SN-curve 3 and spreading exponent $s = 9$.

Table 8. Fatigue factors from time domain analyses with bi-linear SN-curve and spreading exponent $s = 9$. Normalized w.r.t. long-crested sea (L)

S	SL	SS
0.90	0.88	0.74

Discussions and conclusions

It is concluded that the effects of wave spreading and swell separation on the long-term fatigue damage are somewhat smaller than initially expected. It may even result in lower fatigue life when a low-cycle SN-curve is used for members without corrosion protection. However, the more realistic high-cycle and bi-linear SN-curves show a fatigue damage reduction potential of up to 35%, which is of significance. From the current analyses, it is clear that any benefit from wave directionality on the structural fatigue damage is site dependent as the statistical correlation between wind and swell direction is an important parameter for dynamic amplification and rotor-induced damping. Therefore, any cost reductions related to less conervative environmental modelling for both FLS and ULS design must be performed with respect to the governing measurements or hindcast data. For the present case, a 35% increase in fatigue damage is equivalent to a thickness reduction of approximately 6% if one assume that the dynamic behaviour of the system does not change and SN-curve 2 is used. As the cost of the foundation is directly related to the wall thickness of the monopile, it will contribute to lowering the levelized cost of energy. Of course, one needs to include the response due to turbulent wind when assessing the overall cost reduction.

It would be of interest to compare the presented results with a water depth dependent spreading function. Such a correction should account for the fact that incoming waves may develop a narrower spreading when propagating to shallower waters and introduce different frequency dependencies on the spreading exponent. This is especially important for extreme sea states, but to a lesser degree when fatigue is of primary interest. The spreading effect on fatigue damage is expected to have a significant effect when the turbine is idling above the cut-out wind speed of 25m/s as indicated in the scatter plots in the appendix. Therefore, the validity of spreading in extreme sea needs to be validated by on-site measurements.

For wind sea, the spectral peak period is the main contributor to response excitation, while the misalignment angle is more important for swell, whose direction is statistically independent of the wind and wind sea direction. When the turbine is operating, and aerodynamic damping is significant, both the swell direction and a peak period close to the natural period is important for fatigue damage through dynamic amplification. Introduction of unavailability is important for fatigue damage from the operational periods. When the turbine is in a non-operational condition, the fatigue reduction effect of directionality in all its presented forms are more evident.

In further work it is recommended to include the directional formulations presented in this paper in a fully coupled aero-servo-hydro-elastic simulation in order to quantify the overall effects when loads from turbulent wind are included.

Acknowledgements

This work has been carried out at the Centre for Autonomous Marine Operations and Systems (NTNU AMOS). The Norwegian Research Council is acknowledged as the main sponsor of NTNU AMOS. This work was supported by the Research Council of Norway through the Centres of Excellence funding scheme, Project number 223254 - NTNU AMOS. The authors would also like to thank the Norwegian Meteorological Institute for access to hindcast data.

References

1. Dong W, Moan T and Gao Z. Long-term fatigue analysis of multi-planar tubular joints for jacket-type offshore wind turbine in time domain. *Engineering Structures* 2011; 33(6): 2002–2014. DOI:10.1016/j.engstruct.2011.02.037.
2. Bachynski EE and Ormberg H. Hydrodynamic modeling of large-diameter bottom-fixed offshore wind turbines. In *Proceedings of the ASME 34th International Conference on Ocean, Offshore and Arctic Engineering*. St. Johns, Canada: ASME.
3. Horn JTH, Krokstad JR and Amdahl J. Hydro-Elastic Contributions to Fatigue Damage on a Large Monopile. *Energy Procedia* 2016; .
4. Fürst Frimann-Dahl J. Master thesis: Experimental Validation and Design Review of Wave Loads on Large-Diameter Monopiles. Technical report, Norwegian University of Science and Technology, 2015.
5. Krokstad J, Stansberg C, Nestegaard A et al. A New Nonslender Ringing Load Approach Verified Against Experiments. *Journal of Offshore Mechanics and Arctic Engineering* 1998; 120(1): 20. DOI:10.1115/1.2829515.
6. Vugts JH. Fatigue damage assessments and the influence of wave directionality. *Applied Ocean Research* 2005; 27(3): 173–185. DOI:10.1016/j.apor.2005.11.003.
7. Mathisen J, Ronold KO and Sigurdsson G. Probabilistic Modelling for Reliability Analysis of Jackets. In *23rd International Conference on Offshore Mechanics and Arctic Engineering, Volume 2*. ASME. ISBN 0-7918-3744-0, pp. 231–239. DOI:10.1115/OMAE2004-51227.
8. Sterndorff MJ and Sørensen JD. A Rational Procedure for Determination of Directional Individual Wave Heights. In *Proceedings of the 20th International Conference on Ocean, Offshore and Arctic Engineering - OMAE 2001*. Rio de Janeiro, Brazil: ASMA.
9. Ewans K and Jonathan P. The Effect of Directionality on Northern North Sea Extreme Wave Design Criteria. *Journal of Offshore Mechanics and Arctic Engineering* 2008; 130(4): 041604. DOI:10.1115/1.2960859.
10. Bak C, Zahle F, Bitsche R et al. Description of the DTU 10 MW Reference Wind Turbine. Technical report, DTU, 2013.
11. Reistad M, Breivik Ø, Haakenstad H et al. A high-resolution hindcast of wind and waves for the North Sea, the Norwegian Sea, and the Barents Sea. *Journal of Geophysical Research: Oceans* 2011; 116(5): 1–18. DOI:10.1029/2010JC006402. `1111.0770`.
12. Velarde J. Master thesis: Design of monopile foundations to support the DTU 10MW wind turbine. Technical report, Norwegian Univeristy of Science and Technology, 2016.
13. USFOS. User Manual. Technical report, 2014. URL `http://www.usfos.no`.
14. GL Garrad Hassan. A guide to UK offshore wind operations and maintenance. Technical report, 2013.
15. DNV GL. RP-C205 Environmental conditions and environmental loads. Technical report, 2010.
16. Simanesew A, Krogstad HE, Trulsen K et al. Development of frequency-dependent ocean wave directional distributions. *Applied Ocean Research* 2016; 59: 304–312. DOI:10.1016/j.apor.2016.06.011. URL `http://dx.doi.org/10.1016/j.apor.2016.06.011`.
17. Krokstad JR. Sensitivity of Directional Spreading for Low-Frequency Motions in Short-Crested Waves. *Proceedings of the Fourth (1994) InteTlUltional Offshore and Polar Engineering Conference* 1994; lll: 564–574.
18. Mitsuyasu H, Tasai F, Suhara T et al. Observations of the directional spectrum of ocean waves using a coverleaf buoy, 1975. DOI:10.1175/1520-0485.
19. Hasselmann DE, Dunckel M and Ewing JA. Directional Wave Spectra Observed during JONSWAP 1973. *Journal of Physical Oceanography* 1980; 10.
20. Tucker MJ. *Waves in Ocean Engineering, Measurements, Analysis, Interpretation*. Ellis Horwood Limited, 1991.
21. Krogstad HE, Barstow SF, Haug O et al. Directional distributions in wave spectra. In *Proceedings of the*

International Symposium on Ocean Wave Measurement and Analysis.

22. Bitner-Gregersen EM and Hagen Ø. Directional spreading in two-peak spectrum at the Norwegian continental shelf. In *Proceedings of the International Conference on Offshore Mechanics and Arctic Engineering*.
23. DNV GL. RP-C203 Fatigue design of offshore steel structures. Technical Report April, 2005.
24. WAFO-group. WAFO - A Matlab Toolbox for Analysis of Random Waves and Loads, 2000. URL `http://www.maths.lth.se/matstat/wafo/`.
25. Faltinsen OM, Newman JN and Vinje T. Nonlinear wave loads on a slender vertical cylinder. *Journal of Fluid Mechanics* 1995; 289: 179. DOI:10.1017/S0022112095001297.
26. Horn JTH, Amdahl J and Haver SK. Dynamic Amplification of Drag Dominated Structures in Irregular Seas. In *Proceedings of OCEANS'15 MTS/IEEE Washington Conference & Exhibition*. IEEE conference proceedings. ISBN 978-0-933957-43-5.
27. ABS. Guidance Notes on Dynamic Analysis Procedure for Self- Elevating Drilling Units. Technical report, 2014.
28. Dirlik T. *Application of Computers in Fatigue Analysis*. PhD Thesis, The University of Warwick, 1985.
29. Mršnik M, Slavič J and Boltežar M. Frequency-domain methods for a vibration-fatigue-life estimation - Application to real data. *International Journal of Fatigue* 2013; 47: 8–17. DOI:10.1016/j.ijfatigue.2012.07.005.

Appendix

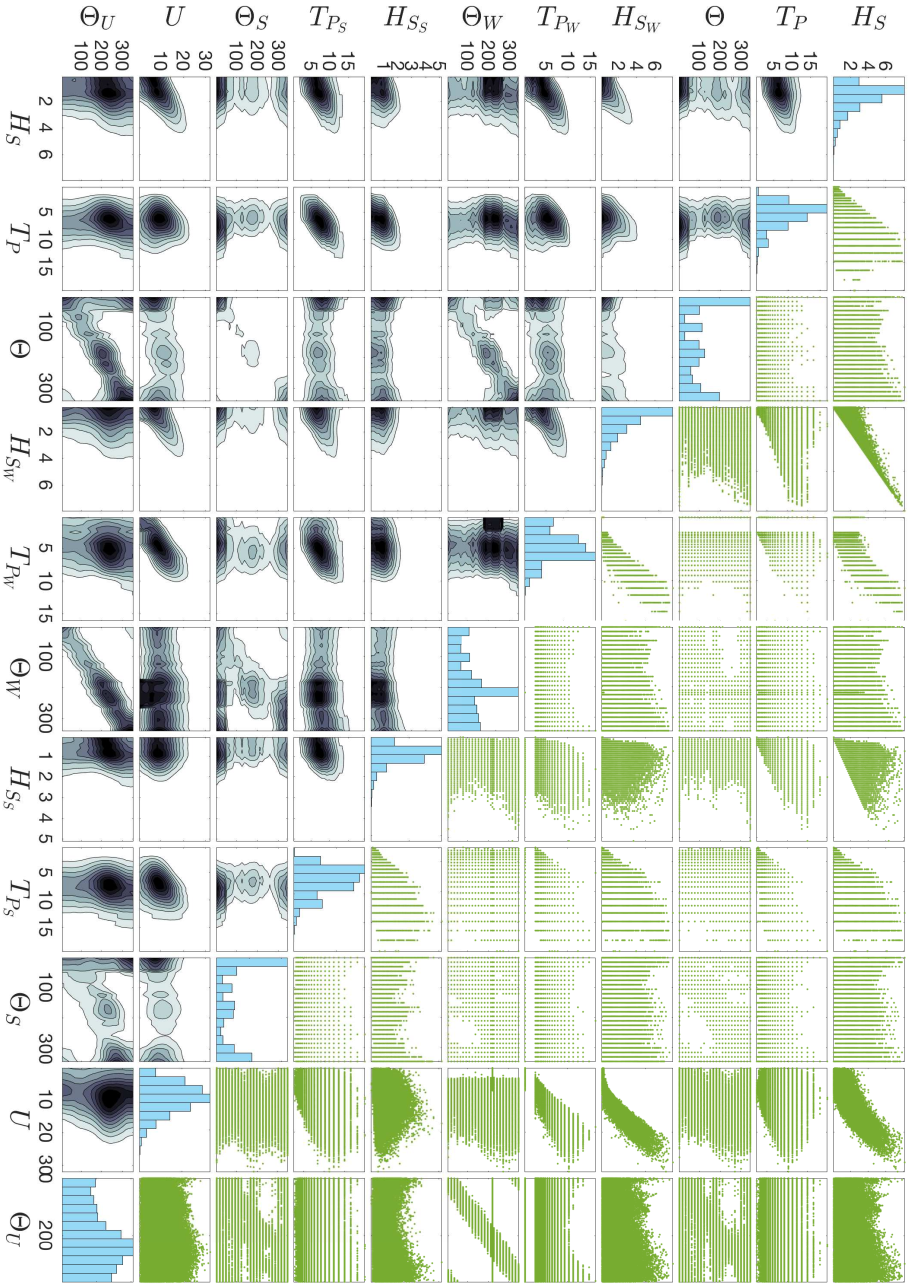

Figure 9. 30 years of unfiltered hindcast data at Dogger Bank with marginal histograms and qualitative joint contour plots

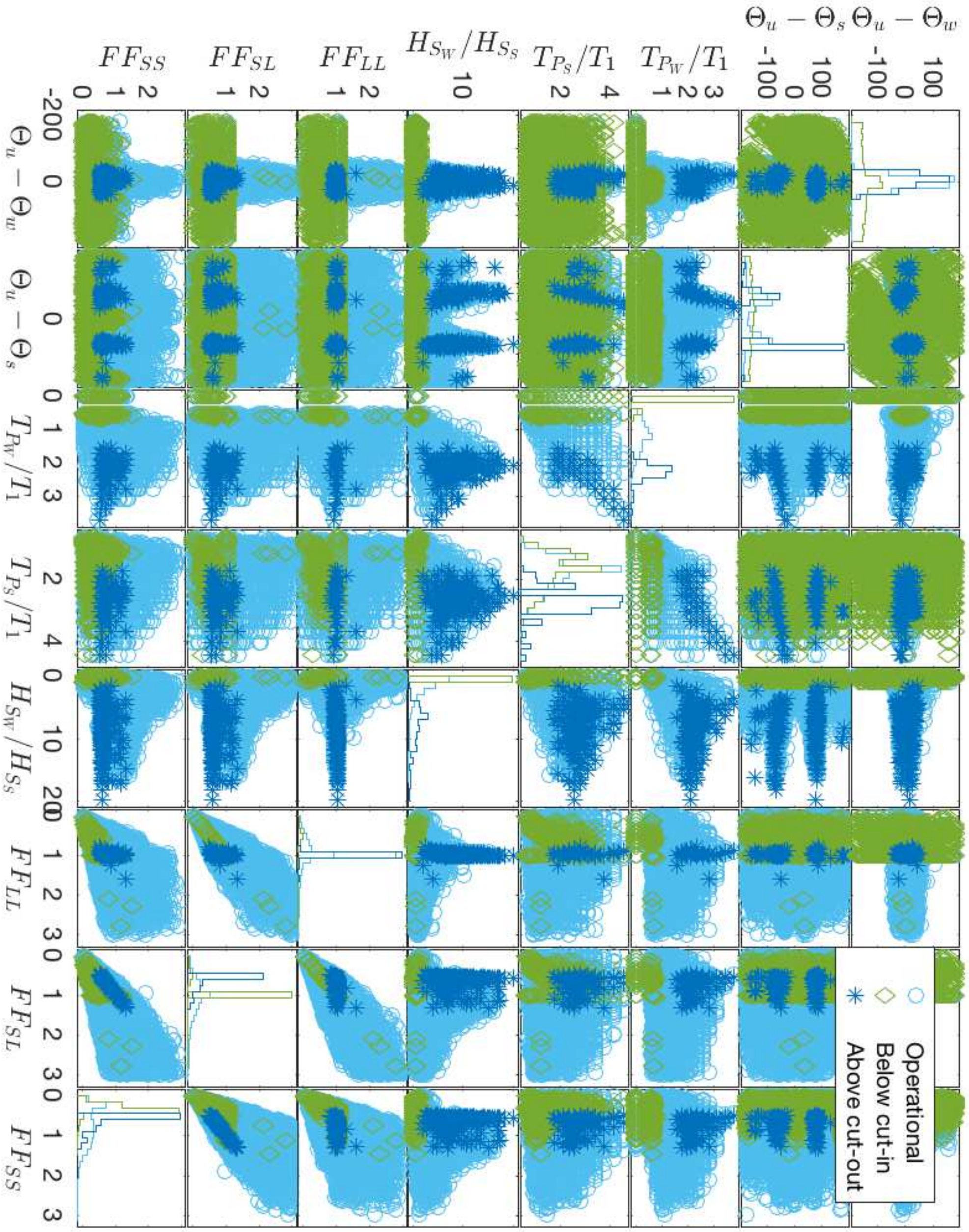

Figure 10. Correlations between environmental parameters and fatigue factors with 100% availability. T_1 is the first natural period.

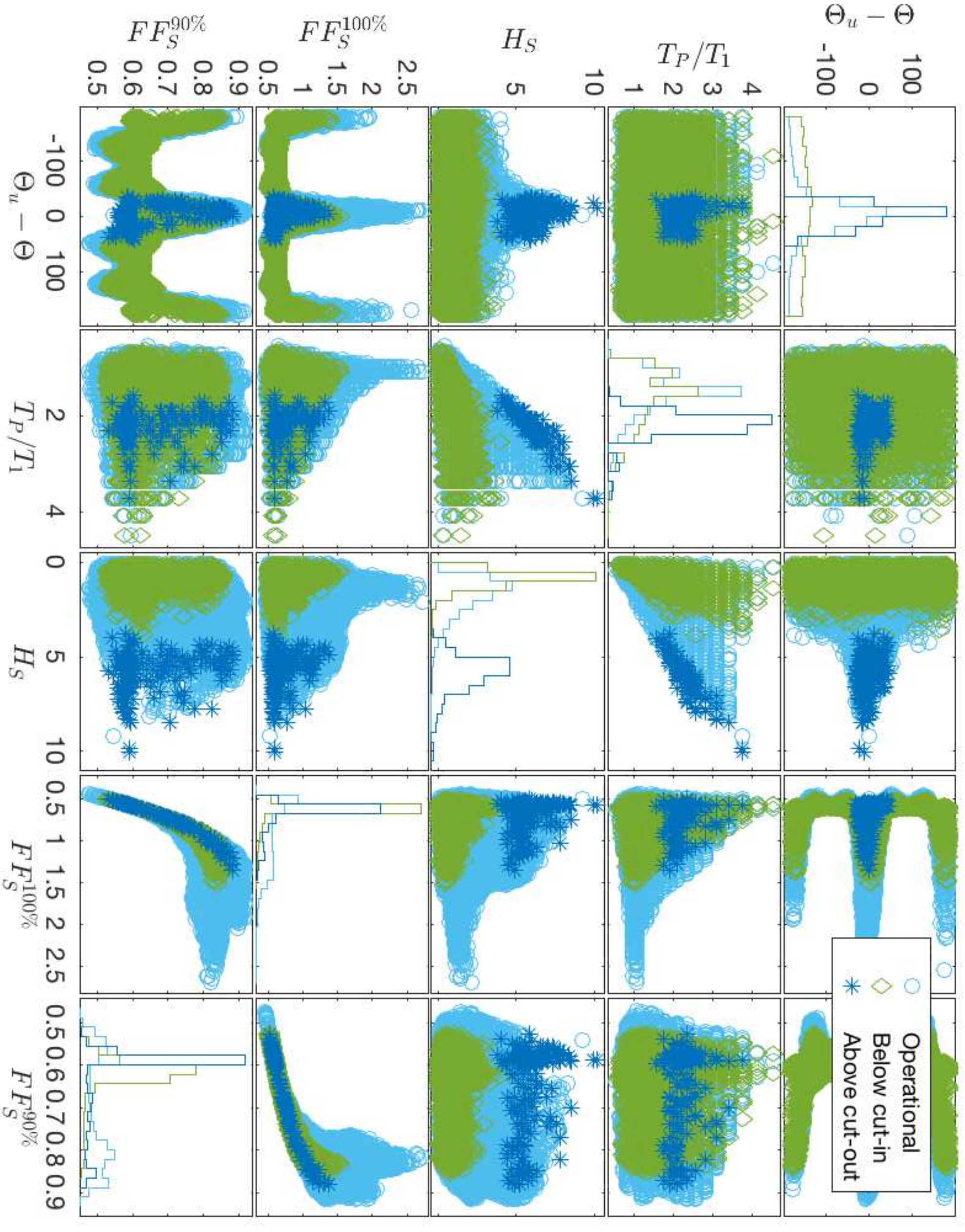

Figure 11. Correlations between environmental parameters and fatigue factors with 90% and 100% availability for short-crested total sea. T_1 is the first natural period.

Paper IV

A new combination of conditional environmental distributions

Jan-Tore Horn et al.

Applied Ocean Research, 2018

Abstract In this paper, a joint distribution of all relevant environmental parameters used in design of offshore structures including directional components is presented, along with a novel procedure for dependency modelling between wind and wind sea. Probabilistic directional models are rarely used for response calculation and reliability assessments of stationary offshore structures. However, very few locations have the same environment from all compass directions in combination with a rotationally symmetric structure. The scope of this work is to present a general environmental joint distribution with directional descriptions for long term design of stationary offshore structures such as offshore wind turbines. Wind, wind sea and swell parameters will be investigated for a chosen location in the central North Sea.

A New Combination of Conditional Environmental Distributions

Jan-Tore Horn[a,b,*], Elzbieta Bitner-Gregersen[c], Jørgen R. Krokstad[b], Bernt J. Leira[b], Jørgen Amdahl[a,b]

[a] *Centre for Autonomous Marine Operations and systems (NTNU AMOS), NTNU, Trondheim, Norway*
[b] *Department of Marine Technology, NTNU, Trondheim, Norway*
[c] *DNV GL, Veritasveien 1, Høvik, Norway*

Abstract

In this paper, a joint distribution of all relevant environmental parameters used in design of offshore structures including directional components is presented, along with a novel procedure for dependency modelling between wind and wind sea. Probabilistic directional models are rarely used for response calculation and reliability assessments of stationary offshore structures. However, very few locations have the same environment from all compass directions in combination with a rotationally symmetric structure. The scope of this work is to present a general environmental joint distribution with directional descriptions for long term design of stationary offshore structures such as offshore wind turbines. Wind, wind sea and swell parameters will be investigated for a chosen location in the central North Sea.

Keywords: joint distribution; environmental parameters; directional effects; design; offshore wind turbines

---

1. Introduction

The present work presents a general multi-dimensional joint distribution which is fitted to data from the site of a future offshore wind farm in the central North Sea. The aim is to obtain a statistical representation of combinations of all relevant environmental variables for design of offshore wind turbines where absolute and relative load directions are important for response analyses. The proposed model is useful for full long term analyses to calibrate simplified design methods, and finding probable combinations of environmental parameters for extreme sea states and simplified ULS design [1]. Environmental variables include wind, wind sea, swell and tide, as well as their respective directions. A conditional modelling approach [2] will be utilized, due to its robustness for description of simultaneous information in data. Copula-based methods may be an alternative, but still need further exploration [3, 4, 5].

---

[*] Corresponding author

Email address: `jan-tore.horn@ntnu.no` (Jan-Tore Horn)

Preprint submitted to Applied Ocean Research *June 5, 2018*

Depending on the desired accuracy of the structural response and reliability estimations, the joint environmental distributions can be extended to high dimensions corresponding to the available site-specific data. Accounting for environmental variable correlations has shown to reduce design conservatism [6] for structures related to oil and gas extraction on the Norwegian continental shelf. Joint modelling of offshore environmental processes has evolved over the years to facilitate probabilistic analysis of structures. Early adoptions include a bottom-fixed structure accounting for wave height and current [7]. A comprehensive omni-directional model including wind, wave, current and tidal elevation can be found in e.g. [8], and it is often referred to by standards for joint modelling of environmental processes [9]. A similar model is used in e.g. [10], adopted for the northern North Sea and more recently in [11] for several locations. In [12], an extension is added to model the mean and standard deviation of the wind and wave direction. Later, a model for description of combined sea (wind sea and swell) and relative directions was presented in e.g. [13]. It is still a challenge to model directional processes. For instance, consistency with regard to combining omni-directional and multi-directional data must be considered in probabilistic design [14].

For offshore wind turbines, the structural dynamics with a power-producing rotor will introduce directionally dependent response characteristics [15, 16, 17]. Hence, a statistical description of both absolute and relative directions of the load processes is of importance. A continuous wave directional distribution can be found in e.g. [18] and combined with a structural resistance in [19] as a function of the absolute direction. Further, a model for relative wind-wave direction was proposed in [20], but lacks relation to the earth-fixed coordinate system, which will be introduced in the present work.

In [21] and [22], the absolute wind direction was modelled using the von Mises distribution [23, 24], which has proven suitable for circular distributions. Furthermore, a relation between wind speed and direction was presented in [25]. This dependency will be also explored in this paper, with a slightly more pragmatic approach and in combination with other relevant offshore environmental processes.

The present study proposes a new combination of conditional environmental distributions which can be found in the literature and verifies it by environmental data from the North Sea. The paper is organized as follows: First, the example offshore site is presented along with the data characteristics before and after pre-processing. Secondly, the full environmental join distribution is constructed along with evaluation of the goodness of the conditional fittings. Finally, an error test of the complete distribution is performed.

2. Offshore site

Hindcast data for description of the wind and wave environment used in the study is provided by the Norwegian Meteorological Institute [26] for the location shown in Fig. 1. The data contains information about the wind speed, wind direction and significant wave height, peak period, and direction for both wind sea and swell. The data are sampled every third hour and cover the historical period of approximately 60 years.

The hindcast data are pre-processed in order to remove ties due to discrete frequencies in the hindcast model, and to make the data independent and identically distributed (iid). This is done by de-seasonalizing the raw data with a moving average algorithm. Deseasoning is one of the suggested pre-processing methods when using data from measure-

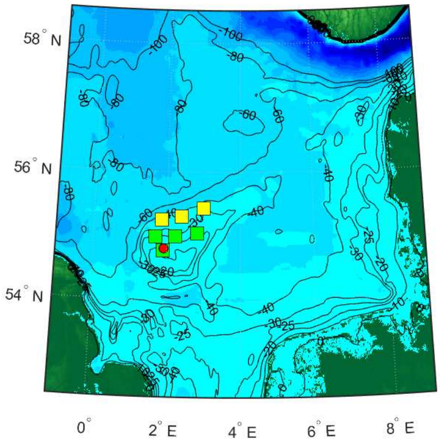

Figure 1: Planned (green) and possible (yellow) offshore wind farms at Dogger Bank with location for hindcast data (red)

ments [27]. Note that directional data is not pre-processed. The effects of pre-processing can be seen in Fig. 2 and 3. It is clear that the de-seasonalizing algorithm reduces the tail-distribution of the wind speed and significant wave height, yielding smaller extreme values. The average conditional exceedance rate (ACER) approach as described in [28] is plotted in Fig. 3 for two values of the conditioning parameter k. In the ACER method, k consecutive peaks over a given exceedance level will be considered dependent and only the first peak will be counted. It is seen that de-seasonalizing has a large effect on the high-percentile values, but the ACER method varies from the wind speed to the wave height, indicating a higher inter-dependency in the wave height hindcast data. This is reflected in Tab. 1 where the ACER method has a much larger impact on the extreme values for wave height.

	V [m/s]		H_S^w [m]	
k	1	2	1	2
Raw	32.74	32.61	9.07	8.68
De-seasoned	30.35	29.96	8.62	7.94

Table 1: 50-year values using the ACER method with and without de-seasonalizing

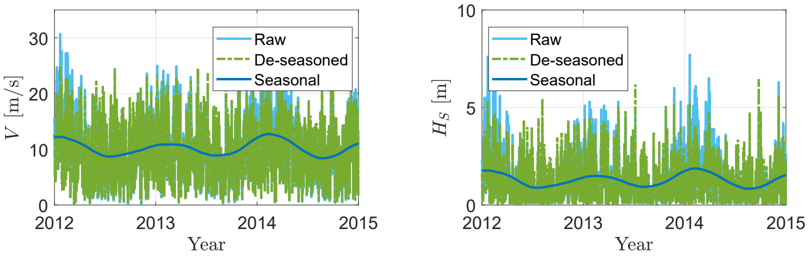

(a) Wind speed (b) Wind sea significant wave height

Figure 2: De-seasonalizing of wind and wind sea

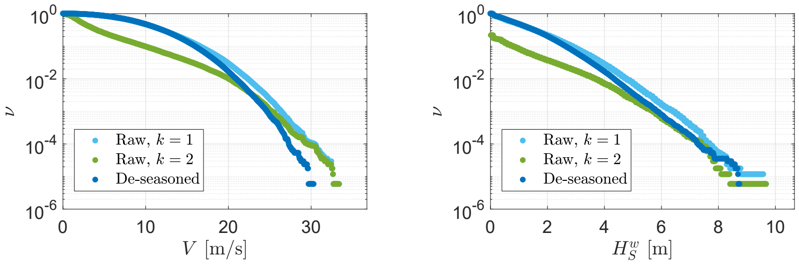

(a) Wind speed (b) Wind sea significant wave height

Figure 3: Upcrossing rates by ACER method and de-seasonalizing

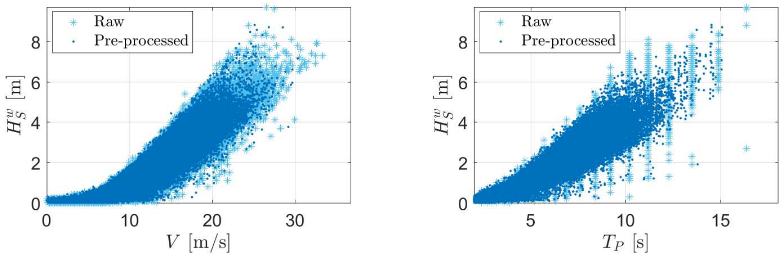

(a) (b)

Figure 4: Hindcast data before and after pre-processing using a de-seasoning algorithm

Scatters of the data before and after pre-processing are shown in Fig. 4 for wind speed, significant wave height and peak period for wind sea. The pre-processed data appears to be more densely distributed, and the ties created by binning of the peak period are removed solely by de-seasonalizing.

3. Environmental joint distribution

Before constructing the environmental joint distribution, some observations and assumptions are made regarding the measurement data. First, the wind sea and swell components of the wave environment are assumed to be uncorrelated and treated separately. This has no effect on extreme wave heights or the distribution tail, but the average wind sea significant wave height is smaller than the expected total sea significant wave height. Thus, the separation is expected to reduce conservatism related to fatigue, but retains the extreme wave loads. Due to the sheltering effect of the British Islands, the wave climate in the central North Sea is mostly dominated by wind sea [29], and the swell is mainly propagating in a southerly direction [17]. Second, the astronomical tide is assumed uncorrelated with both the wind sea and swell. It should be noted that the design standards require the storm surge component of the water level and wind generated current to be accounted for. However, these effects are not considered in the present work, but would otherwise be included as wind sea dependent parameters. As a result, the complete joint distribution can be written as:

$$f_{\mathbf{X}_e} = f_{\mathbf{X}_w} \cdot f_{\mathbf{X}_s} \cdot f_{H_t} \tag{1}$$

where the wind sea and swell parameters are gathered in:

$$\begin{aligned} \mathbf{X}_w &= [V, \Theta_v, H_S^w, T_P^w, \Theta_w^r] \\ \mathbf{X}_s &= [H_S^s, T_P^s, \Theta_s] \end{aligned} \tag{2}$$

respectively, and described in Tab. 2 with distribution types used for marginal and conditional formulations. Note that the wind speed and direction are obtained from hindcast data at 100 meter above sea level (m.a.s.l.) for compatibility with future offshore wind farms, and to reduce the uncertainty that arises from manual extrapolation of the wind speed at 10 m.a.s.l. An average power-law exponent for wind speed extrapolation from 10 to 100 m.a.s.l. of 0.07 (18% increase) and a standard deviation of 0.05 is observed in the hindcast data. This uncertainty is removed when using the 100 m.a.s.l. values directly. The dependencies between the environmental parameters are modelled using conditional fitting parameters, which is the industry standard [9]. Other approaches have been investigated, such as copula-based methods [4], but the traditional method with parameter fitting has proven the most robust and practical.

The parameter dependencies can be revealed by investigating bi-variate histograms of the raw data and the correlation coefficients. For simplicity, each parameter can only depend on one other parameter, but multi-dimensional dependencies are still captured in an indirect manner. In Tab. 3, an overview is given for the dependency modelling. For instance, H_S^w is depending on V, but not vice versa. The dependencies are chosen based on the physics of environmental phenomena and by trials aiming to provide the description with minimal amount of conditional parameters. For instance, the wind

Table 2: Marginal distribution types and description of environmental parameters

	Parameter		Distribution	Description	Unit
Wind sea	V	v	3-p Weibull	Wind speed at 100 m.a.s.l.	[m/s]
	Θ_v	θ_v	von Mises mix	Wind direction at 100 m.a.s.l.	[deg]
	H_S^w	h_w	3-p Weibull	Significant wave height for wind sea	[m]
	T_P^w	t_w	Lognormal	Peak period for wind sea spectrum	[m]
	Θ_w^r	θ_w	Trunc. Normal	Relative wind-wave direction	[deg]
Swell	H_S^s	h_s	3-p Weibull	Significant wave height for swell	[m]
	T_P^s	t_s	Lognormal	Peak period for swell spectrum	[s]
	Θ_s	θ_s	von Mises mix	Swell direction	[deg]
	H_t	H	Normal mix	Water level	[m]

direction is dependent on wind speed and not the other way around as it turned out easier to make a bounded variable conditioned on an unbounded one. More discussions on dependency modelling can be found in e.g. [20].

Table 3: Dependency table with dependent variable in rows and independent in columns

	V	Θ_v	H_S^w	T_P^w	Θ_r^w	H_S^s	T_P^s	Θ_s	H_t
V	1								
Θ_v	1	1							
H_S^w	1		1						
T_P^w			1	1					
Θ_r^w			1		1				
H_S^s						1			
T_P^s						1	1		
Θ_s						1		1	
H_t									1

The distribution parameters, e.g. the mean value, standard deviation etc., in the conditional PDFs are fitted to the pre-processed hindcast data with a least-squares algorithm and a general non-linear regression line given by:

$$p(x) = p_1 + p_2 \cdot x^{p_3} + p_4 \exp[p_5(x + p_6)^{p_7}] \tag{3}$$

for a given parameter p as a function of x with the fitting constants $p_{1,\dots,7}$. This is an extended fitting function to those presented in e.g. [9, 12]. Since there is no need to fit seven constants for each distribution parameter, the distribution parameter regression lines are constructed individually to obtain a reasonable function for extrapolation to be presented in the next subsections. Resulting fitting parameters can be found in the appendix.

3.1. Wind and wind sea

The model for wind sea parameters is assumed to only depend on the wind speed. Also, the peak period is assumed independent of the wind speed, which is often a good assumption [11, 20]. It has also been observed that the relative direction between wind and wind sea can be described with a Normal distribution. The wind sea joint distribution is then approximated as:

$$f_{\mathbf{X}_w} \approx f_V \cdot f_{\Theta_v|V} \cdot f_{H_S^w|V} \cdot f_{T_P^w|H_S^w} \cdot f_{\Theta_w^r|H_S^w} \tag{4}$$

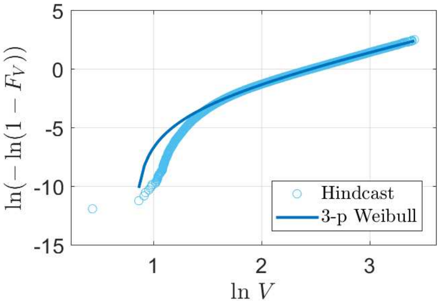

Figure 5: Wind speed data with Weibull fit

Figure 5 shows the quantile plot of the wind speed marginal distribution using the 3-parameter Weibull distribution. The wind direction is dependent on the wind speed and found to be well approximated by a combination of von Mises distributions, using the von Mises mixture distribution:

$$f_{\Theta_v|V}(\theta_v|v) = \sum_{i=1}^{n_{\theta_v}} w_i(v) \cdot f_{\Theta_v}^{(i)}(\theta_v) = \sum_{i=1}^{n_{\theta_v}} w_i(v) \frac{e^{\kappa_i \cos(\theta_v - \mu_i)}}{2\pi I_0(\kappa_i)} \tag{5}$$

where $\sum_i w_i(u) \approx 1$ and I_0 is the modified Bessel function of order zero. For the marginal distribution in Fig. 6, $n_{\theta_v} = 3$ has proven sufficient. The figure also show the contribution from each component and both the location (μ) and the concentration parameter (κ) are kept independent of wind speed in the conditional model. The wind speed dependent weights can be found in Fig. 7, while the remaining values can be found in the appendix.

The wind speed-conditioned directional distribution in Fig. 8 shows that strong winds are more likely to originate from the south west, which is well captured by the model.

The wind sea significant wave height conditioned on the wind speed follows a three parameter Weibull distribution as illustrated with some examples in Fig. 9a obtained with the fitted parameters in Fig. 9b. Describing the parameters in a three-parameter Weibull distribution conditionally is not presented elsewhere in the literature and may prove challenging. A good fit is observed for most H_S^w values, using a two-step fitting procedure; first, an estimation of the location parameter (γ) is performed [30] for each wind speed bin and a continuous fit is made based on Eq. 3. Second, a 2-parameter Weibull fit is performed in the same bins, correcting the data with the analytic location parameter obtained in the previous step. As a result, simple expressions are obtained as a function of the wind speed, with fitting constants given in the Appendix. Care should

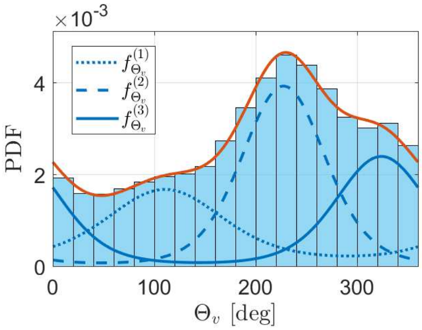

Figure 6: Marginal directional wind distribution with each von Mises component

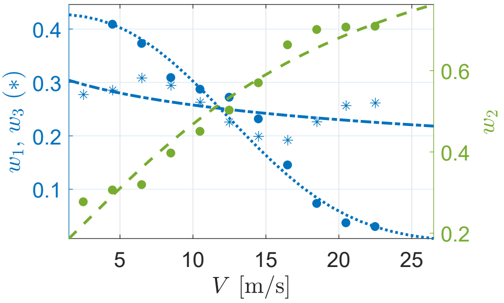

Figure 7: Fitting of weighting parameters for wind speed direction

be taken in modelling the location parameter in order to capture the smallest values of the significant wave height, which are most probably occurring for low wind speeds as seen in Fig. 9b.

The wave peak period is dependent on the significant wave height. The fitted parameters are found in Fig. 10b and the conditional quantile plots can be found in Fig. 10a. For small wave heights, it appears that some large values of the peak period does not satisfy a Lognormal assumption. These data are probably representing swell periods, which are unsuccessfully separated from the wind sea during generation of hindcast data. Such data are also visible in Fig. 4, where some outliers in terms of small steepness are observed. Further, the wind-wave relative direction is modelled with a Normal distribution truncated on ±90 degrees relative to the wind direction. The quantile plots in Fig. 11a shows a good fit with the parameters in Fig. 11b. Interestingly, the standard deviation is independent of the wave height, while the mean relative direction is decreasing linearly, due to a higher probability of time lag between the wind and wave directional changes for high sea states. In other words, the relative probability of misaligned wind and wind sea is increasing with increasing wave height.

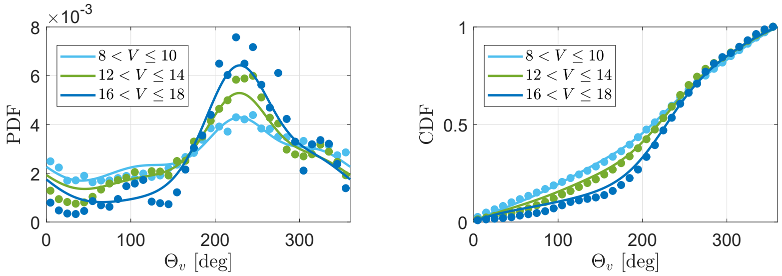

(a) PDF (b) CDF

Figure 8: Fitting goodness of wind direction conditioned on the wind speed

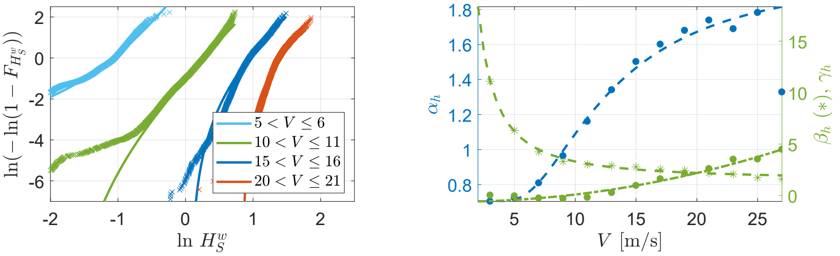

(a) (b)

Figure 9: Wind sea significant wave height

3.2. Swell

The joint distribution for swell is assumed independent of the wind sea variables and approximated as:

$$f_{\mathbf{X}_s} \approx f_{H_S^s} \cdot f_{T_P^s|H_S^s} \cdot f_{\Theta_s|H_S^s} \tag{6}$$

where the swell peak period is conditioned on the swell significant wave height and the direction of propagation is dependent on significant wave height. The 3-parameter Weibull distribution provides a good fit for the swell significant wave height as seen in Fig. 12a when $H_S^s > e^{-1} \approx 0.37$ meter. Furthermore, the swell directional distribution in Fig. 12b is approximated by a bimodal von Mises mixture distribution, representing the swell from the northern and southern North Sea. In [29], typical swell directions can be found, indicating that swell from north originates from heavy weather in the north Atlantic sea. However, the Dogger Bank area is still dominated by wind sea due to a high degree of energy dissipation in the swell before reaching the area of interest. Swell from the south and other directions is less likely, but present in the hindcast data. Of course, the swell separation technique used by the wave spectral model by which the

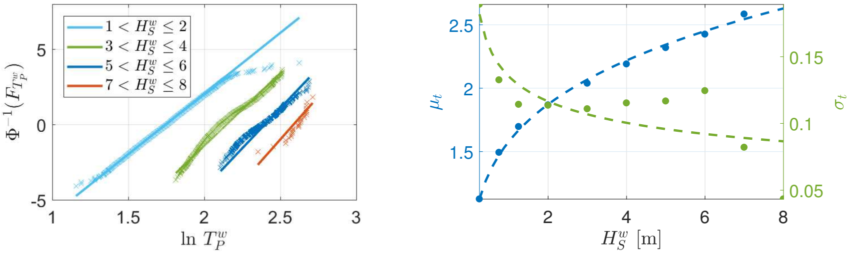

(a) (b)

Figure 10: Wind sea peak period

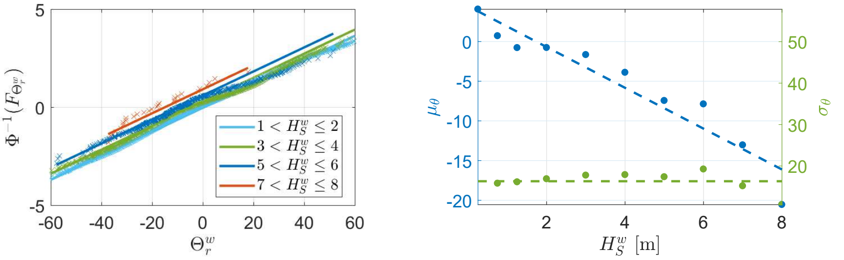

(a) (b)

Figure 11: Wind sea relative direction

data were simulated might affect the predicted direction as well as the period and wave height combinations, introducing uncertainties in the data and the fitted model. It can therefore be argued that modelling the swell directional distributions may require some additional considerations, especially for the direction. The directional dependency on the swell wave height is modelled in a similar manner as the conditional wind direction, with two dominating directions:

$$f_{\Theta_s|H_S^s}(\theta_s|h_s) = \sum_{i=1}^{2} w_i(h_s) \cdot f_{\Theta_s}^{(i)}(\theta_s) = \sum_{i=1}^{2} w_i(h_s) \frac{e^{\kappa_i \cos(\theta_s - \mu_i)}}{2\pi I_0(\kappa_i)} \tag{7}$$

The first direction is from south, with a wide spread as seen in Fig. 12b, resulting in a close to uniform distribution. The second is from north, which is more narrow banded. With a least-squares fitting method, the best weighting parameters are found given the μ and κ parameters in the von Mises distribution obtained from the marginal fit. The result is shown in Fig. 14 with power function fits, and fitting parameters can be found in the appendix. As expected, the northern direction ($\Theta_s^{(2)}$) dominates for larger H_S^s.

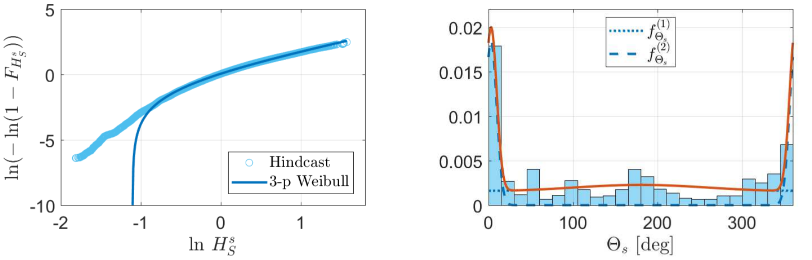

(a) Swell significant wave height (b) Marginal swell directional distribution

Figure 12: Swell wave height and directional distribution

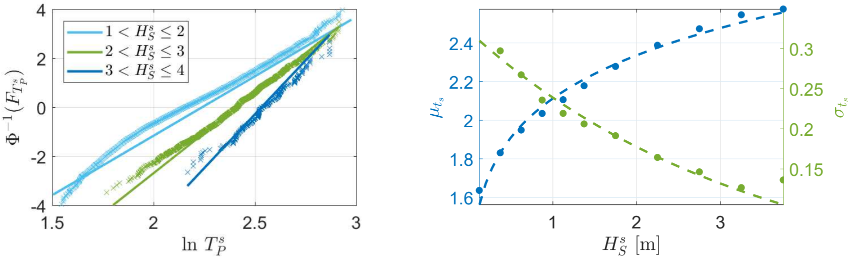

(a) Swell peak period (b) Swell peak period parameters

Figure 13: Swell peak period with fitted function for the swell wave height dependent parameters

The swell peak period dependence on the swell significant wave height is well captured by a conditional Lognormal distribution as seen in Fig. 13a and 13b for quantile plots and parameter fitting, respectively.

3.3. Tide

As tidal current is not expected to lead to an increased loading at the bottom-fixed wind turbines at the present site, at least in a linear manner, it is neglected in this study. However, the water level variation induced by tides may affect the wave loads significantly due to the shallow water depths and is therefore included.

The tide is modelled as an independent process. By only accounting for tidal variations due to the astronomical tide, this is expected to be a good approximation. However, this may be non-conservative for three-hour analysis of extreme sea-states, as the storm duration is typically longer than three hours when including the temporal evolution. To account for the possibility of having a high sea state in combination with a high astronomical tide, the industry standards typically require extreme conditions to be modelled in combination with an high water level [27]. Other important environmental phenomena

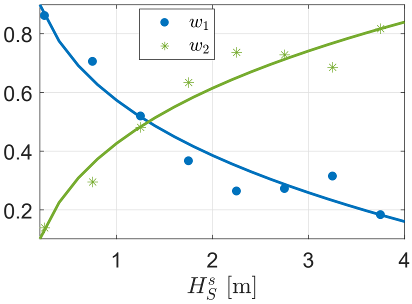

Figure 14: Weighting parameters for 2-folded von Mises mixture distribution of swell direction with fitting functions

leading to currents and water level variations such as storm surge is not accounted for in the present work, but should rather be included in the description of the wind sea, wind speed dependent. The water level data is retrieved from `www.worldtide.info` for the actual location, transformed to values representative for three hour durations for compatibility with the hindcast data, and fitted to a Gaussian mixture model as illustrated in Fig. 15. Here, two components are needed for a good fit, and the tidal water level distribution is modelled as:

$$f_{H_t} \sim \sum_{i=1}^{2} w_i \cdot \mathcal{N}(\mu_i, \sigma_i^2) \tag{8}$$

with the fitting parameters given in the appendix.

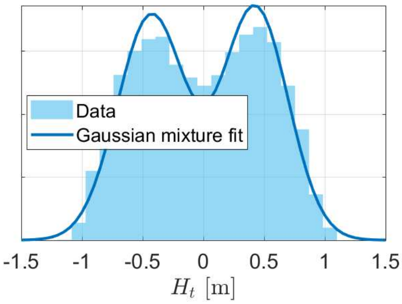

Figure 15: Tidal elevation

4. Simulation results

With an environmental model that contains a large number of variables where many of them are uncorrelated, numerical integration over the complete domain in combination with response calculation of offshore structures may become computationally too demanding and impractical to perform. Also, direct integration would not yield any error estimation. The efficiency of methods based on Monte Carlo simulation (MCS) does, however, not depend on the sampling domain. Latin Hypercube sampling (LHS) is another way of sampling from a high-dimensional domain and has proven efficient in terms of probability density estimation and in applications related to structural reliability analysis [31]. Hence, MCS or LHS with variance reduction techniques and various means of importance sampling related to the system dynamics are promising tools for use in probabilistic design where the stochastic variables are described by a joint probability model. See e.g. [32] and [33] for examples of application.

The obtained joint probability density function is tested against the pre-processed hindcast data by a Monte Carlo simulation. All 2D combinations in the data are compared with a root-mean-square-error (RMSE) estimate given as:

$$RMSE = \sqrt{\sum_j \sum_i (X_{ij} - Y_{ij})^2} \tag{9}$$

for fractions of empirical data X and simulated data Y in bin (i,j), an approach similar to [3]. Each data set is divided into the same 50 equally spaced intervals, so that $i, j = 1, \ldots, 50$. Results from 150 000 MCS are shown in Tab. 4. Except for the marginal swell directional distribution, the RMSE values are in general low, indicating good representation of both marginals on the diagonal and joint distributions elsewhere.

The resulting marginals are presented in the form of histograms to illustrate the similarities between the pre-processed hindcast data and simulated data. The wind speed and wind direction show a very good fit in Fig. 16. In Fig. 17, the wind sea parameters are compared, showing only a slight deviation for small values of the significant wave height and peak period. Swell sea and tidal elevation are presented in Fig. 18, and again the agreement is good, although the directional hindcast data is not completely described by a 2-fold von Mises distribution due to some irregularities.

Table 4: RMSE from simulations

	V	Θ_v	H_S^w	T_P^w	Θ_w^r	H_S^s	T_P^s	Θ_s	H_t
V	0.012	0.006	0.018	0.021	0.013	0.012	0.022	0.044	-
Θ_v	-	0.013	0.007	0.009	0.029	0.014	0.009	0.047	-
H_S^w	-	-	0.027	0.036	0.015	0.014	0.042	0.054	-
T_P^w	-	-	-	0.029	0.013	0.013	0.045	0.046	-
Θ_w^r	-	-	-	-	0.011	0.015	0.016	0.064	-
H_S^s	-	-	-	-	-	0.036	0.019	0.054	-
T_P^s	-	-	-	-	-	-	0.025	0.051	-
Θ_s	-	-	-	-	-	-	-	0.191	-
H_t	-	-	-	-	-	-	-	-	0.029

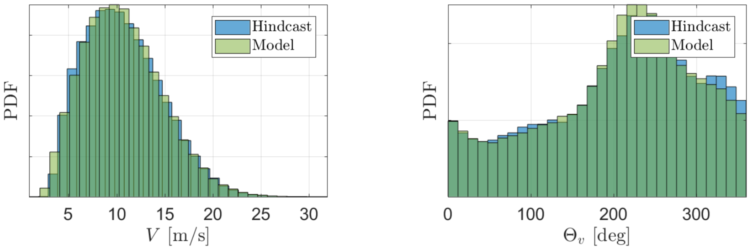

(a) (b)

Figure 16: Pre-prcessed wind data compared to results from MCS

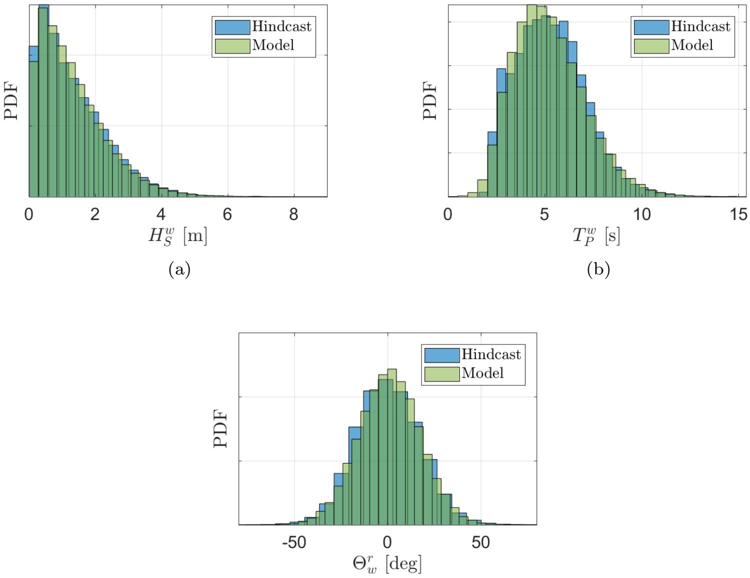

(a) (b)

(c)

Figure 17: Pre-prcessed wind sea data compared to results from MCS

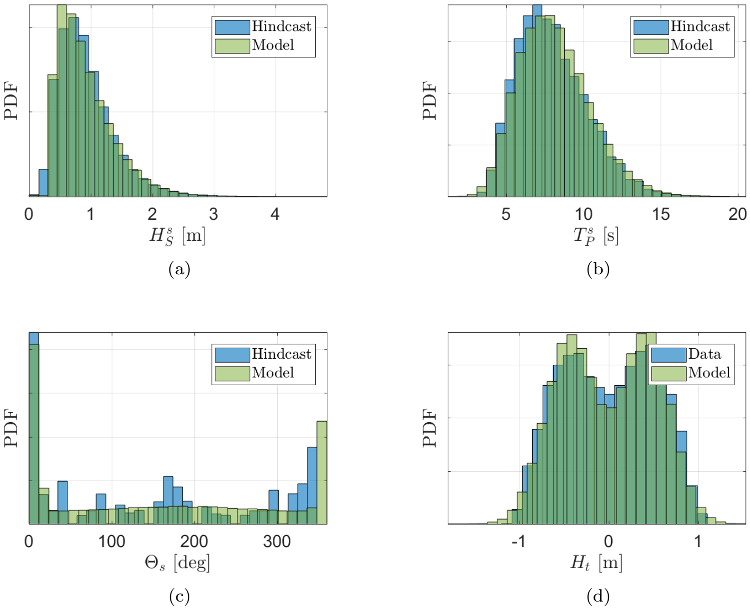

(a) (b) (c) (d)

Figure 18: Pre-prcessed swell and tidal data compared to results from MCS

4.1. Environmental contours

To further compare the fitted model with the hindcast data, several environmental contours calculated using IFORM [1] have been established. The results are shown in Fig. 19a for 2D contours for wind speed and wind sea significant wave height and for peak period in Fig. 19b. From Fig. 19a, it can be observed that the model will allow slightly higher extreme wave heights for approximately $8 < V < 18$ than the hindcast data suggests. This is partly a result of the statistical uncertainty when fitting a distribution to hindcast data as higher classes of wave heights given wind speed include less observations. To investigate the assumption of independent wind sea and swell, the corresponding wave heights and contour lines are plotted in Fig. 19c. Overall, the hindcast data seems to lie inside the contour lines, without excessive out-crossings of the 50-year contour line. To illustrate some 3D effects, the significant wave height and peak period for wind sea is plotted in Fig. 19d for $22 < V < 24$. This domain contains very few data points and are subject to statistical uncertainty due to limited numbers of observations. Therefore, larger variations are observed in the peak period for a given wave height when extrapolating to 10 and 50 year return periods.

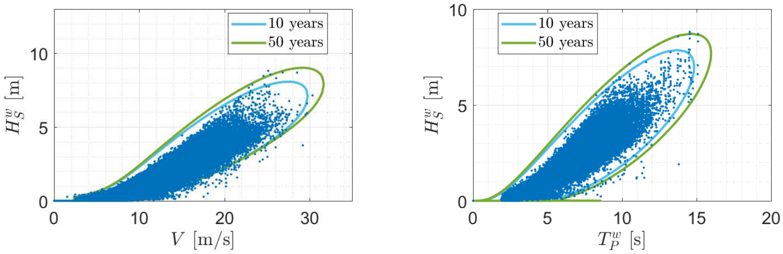

(a) V and H_S^w joint distribution

(b) T_P^w and H_S^w joint distribution

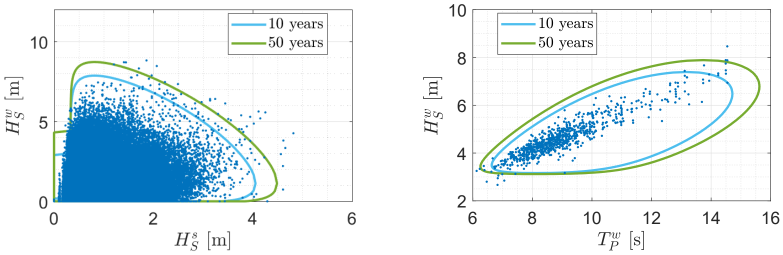

(c) H_S^s and H_S^w joint distribution

(d) T_P^w and H_S^w joint distribution for $22 < V < 24\text{m/s}$

Figure 19: Contour lines for environmental conmbinations with 10 and 50 year return periods including pre-processed hindcast data

5. Conclusion

A method for obtaining an analytic probabilistic description of the environmental parameters including directional effects is proposed and verified by hindcast data from a specific location in the North Sea. The model provides a good representation of the wind, wind sea and swell environment at the considered location. The model is meant to be used for calculations of environmental loads of marine structures, e.g. offshore wind turbines, in probabilistic design. A paper demonstrating its application will follow. A conservative description of the peak period for a given significant wave height is also demonstrated by use of the contour plots, which is a good tool for design of dynamically sensitive offshore structures subjected to higher order loading, like bottom-fixed monopile-mounted wind turbines [34].

A von Mises mixture distribution conditioned on the wind speed is successfully adopted for modelling the wind direction, and has proven very flexible for multi-directional processes. As a first approach, only conditioning the weights of the main wind directions in the folded von Mises distribution has proven very effective. The continuous directional distribution of wind speed which is proposed can be used in probabilistic analysis of rotationally symmetric structures or as a response parameter for non-symmetric structures.

To the authors' knowledge, a 3-parameter Weibull distribution of significant wave height conditioned on the wind speed has been established for the first time, and an efficient fitting method is presented in order to obtain a satisfactory fit. Also, a separate joint distribution for swell is useful especially for fatigue design and will allow to capture important response for structures sensitive to environmental directions, such as offshore wind turbines. In a similar manner, a description of the current velocity and direction may be included in the proposed joint model if such data exists.

Acknowledgement

This work has been carried out at the Centre for Autonomous Marine Operations and Systems (NTNU AMOS). The Norwegian Research Council is acknowledged as the main sponsor of NTNU AMOS. This work was supported by the Research Council of Norway through the Centres of Excellence funding scheme, Project number 223254 - NTNU AMOS. The authors would like to thank the Norwegian Meteorological Institute for providing hindcast data.

References

[1] S. Haver, S. R. Winterstein, Environmental contour lines: A method for estimating long term extremes by a short term analysis, Transactions - Society of Naval Architects and Marine Engineers 116 (2009) 116–127.

[2] E. M. Bitner-Gregersen, Joint Met-ocean Description for Design and Operations of Marine Structures, Applied Ocean Research 51 (2015) 279–292. `doi:10.1016/j.apor.2015.01.007`.

[3] E. Vanem, Copula-based Bivariate Modelling of Significant Wave Height and Wave Period and the Effects of Climate Change on the Joint Distribution, in: Proceedings of the 35th International Conference on Ocean, Offshore and Arctic Engineering, ASME, Busan, South Korea, 2016, pp. 1–12.

[4] E. Vanem, Joint statistical models for significant wave height and wave period in a changing climate, Marine Structures 49 (2016) 180–205. `doi:10.1016/j.marstruc.2016.06.001`.

[5] Y. Zhang, M. Beer, S. T. Quek, Long-term performance assessment and design of offshore structures, Computers & Structures 154 (2015) 101–115. `doi:10.1016/j.compstruc.2015.02.029`.

[6] E. M. Bitner-Gregersen, S. Haver, R. Løseth, Ultimate Limit States with Combined Load Processes, in: Proceedings of the 2nd Offshore and Polar Engineering Conference, 1992.

[7] J. Heideman, O. Hagen, C. Cooper, F.-E. Dahl, Joint Probability of Extreme Waves and Currents on Norwegian Shelf, Journal of Waterway, Port, Coastal, and Ocean Engineering 115 (4) (1989) 534–546.

[8] E. M. Bitner-Gregersen, S. Haver, Joint Environmental Model for Reliability Calculations, in: Proceedings of the First International Offshore and Polar Engineering Conference, 1991.

[9] DNV GL, RP-C205 Environmental conditions and environmental loads, Tech. rep. (2017).

[10] K. Johannessen, T. S. Meling, S. Haver, Joint Distribution for Wind and Waves in the Northern North Sea, International Journal of Offshore and Polar Engineering 12 (1) (2002) 1–8.

[11] L. Li, Z. Gao, T. Moan, Joint Environmental Data at Five European Offshore Sites for Design of Combined Wind and Wave Energy Devices, Journal of Offshore Mechanics and Arctic Engineering 137 (June) (2015) 1–16.

[12] E. M. Bitner-Gregersen, Distribution of Multidirectional Environmental Effects, in: Proceedings of the 15th International Conference on Ocean, Offshore and Arctic Engineering, ASME, Florence, Italy, 1996.

[13] E. M. Bitner-Gregersen, Joint Probabilistic Description for Combined Seas, in: Proceedings of the 24th International Conference on Offshore Mechanics and Arctic Engineering, 2005. `doi:10.1115/OMAE2005-67382`.

[14] G. Z. Forristall, On the Use of Directional Wave Criteria, Journal of Waterway, Port, Coastal, and Ocean Engineering 130 (6) (2004) 312–321.

[15] E. E. Bachynski, M. I. Kvittem, C. Luan, T. Moan, Wind-Wave Misalignment Effects on Floating Wind Turbines: Motions and Tower Load Effects, Journal of Offshore Mechanics and Arctic Engineering 136 (4) (2014) 41902.

[16] L. Barj, S. Stewart, G. Stewart, M. Lackner, J. Jonkman, A. Robertson, D. Matha, Wind/wave misalignment in the loads analysis of a floating offshore wind turbine, in: 32nd ASME Wind Energy Symposium, 2014. `doi:10.2514/6.2014-0363`.

[17] J.-T. Horn, J. R. Krokstad, J. Amdahl, Long-Term Fatigue Damage Sensitivity to Wave Directionality in Extra Large Monopile Foundations, Journal of Engineering for the Maritime Environment`doi:10.1177/1475090217727136`.

[18] J. Vega, Modeling Long Term Distribution of Mean Wave Direction, in: Proceedings of the 12th International Congress of the International Maritime Association of the Mediterranean, 2007, pp. 839–846.

[19] J. Mathisen, K. O. Ronold, G. Sigurdsson, Probabilistic Modelling for Reliability Analysis of Jackets, in: Proceedings of the 23rd International Conference on Offshore Mechanics and Arctic Engineering, ASME, 2004, pp. 231–239. `doi:10.1115/OMAE2004-51227`.

[20] J.-T. Horn, J. R. Krokstad, J. Amdahl, Joint Probability Distribution of Environmental Conditions for Design of Offshore Wind Turbines, in: Proceedings of the 36th International Conference on Ocean, Offshore and Arctic Engineering, Trondheim, Norway, 2017.

[21] N. Masseran, A. M. Razali, K. Ibrahim, M. T. Latif, Fitting a mixture of von Mises distributions in order to model data on wind direction in Peninsular Malaysia, Energy Conversion and Management 72 (2013) 94–102. `doi:10.1016/j.enconman.2012.11.025`.

[22] J. A. Carta, C. Bueno, P. Ramírez, Statistical modelling of directional wind speeds using mixtures of von Mises distributions: Case study, Energy Conversion and Management 49 (5) (2008) 897–907.

[23] M. Abramowitz, I. A. Stegun, Handbook of Mathematical Functions, 1965.

[24] C. Forbes, M. Evans, N. Hastings, B. Peacock, von Mises Distribution, in: Statistical Distributions, John Wiley & Sons, Inc., 2010, pp. 191–192. `doi:10.1002/9780470627242.ch45`.

[25] J. A. Carta, P. Ramírez, C. Bueno, A joint probability density function of wind speed and direction for wind energy analysis, Energy Conversion and Management 49 (6) (2008) 1309–1320. `doi:10.1016/j.enconman.2008.01.010`.

[26] M. Reistad, Ø. Breivik, H. Haakenstad, O. J. Aarnes, B. R. Furevik, J. R. Bidlot, A high-resolution hindcast of wind and waves for the North Sea, the Norwegian Sea, and the Barents Sea, Journal of Geophysical Research: Oceans 116 (5) (2011) 1–18. `doi:10.1029/2010JC006402`.

[27] DNV GL, Loads and site conditions for wind turbines, Tech. Rep. November (2016).

[28] A. Naess, O. Karpa, Statistics of bivariate extreme wind speeds by the ACER method, Journal of Wind Engineering and Industrial Aerodynamics 139 (2015) 82–88. `doi:10.1016/j.jweia.2015.01.011`.

[29] A. Semedo, R. Vettor, Ø. Breivik, A. Sterl, M. Reistad, C. G. Soares, D. Lima, The wind sea and swell waves climate in the Nordic seas, Ocean Dynamics 65 (2) (2015) 223–240. `doi:10.1007/s10236-014-0788-4`.

[30] R. L. Smith, J. C. Naylor, A Comparison of Maximum Likelihood and Bayesian Estimators for the Three- Parameter Weibull Distribution, Journal of the Royal Statistical Society. Series C (Applied Statistics) 36 (3) (1987) 358–369.

[31] A. Olsson, G. Sandberg, O. Dahlblom, On Latin hypercube sampling for structural reliability analysis, Structural Safety 25 (1) (2003) 47–68. `doi:10.1016/S0167-4730(02)00039-5`.

[32] Y. M. Low, A variance reduction technique for long-term fatigue analysis of offshore structures using Monte Carlo simulation, Engineering Structures 128 (2016) 283–295. `doi:10.1016/j.engstruct.2016.09.047`.

[33] Y. Gao, Y. M. Low, An efficient importance sampling method for long-term fatigue assessment of deepwater risers with time domain analysis, Probabilistic Engineering Mechanics 45 (2016) 102–114. `doi:10.1016/j.probengmech.2016.04.003`.

[34] J. Krokstad, C. Stansberg, A. Nestegaard, T. Marthinsen, A New Nonslender Ringing Load Approach Verified Against Experiments, Journal of Offshore Mechanics and Arctic Engineering 120 (1) (1998) 20–29. `doi:10.1115/1.2829515`.

Appendix

Table 5: Fitting constants

Var.	Par.	Arg.	Marg.	p_1	p_2	p_3	p_4	p_5	p_6	p_7
V	α	-	9.49e+00	9.49e+00	0	1	0	1	0	1
	β	-	2.19e+00	2.19e+00	0	1	0	1	0	1
	γ	-	2.28e+00	2.28e+00	0	1	0	1	0	1
Θ_v	w_1	v	2.77e-01	0	0	1	4.28e-01	-1.06e-03	1	2.52e+00
	w_2	v	4.33e-01	0	0	1	1	-1.62e+03	1.89e+01	-2.28e+00
	w_3	v	2.90e-01	0	0	1	2.26e+00	-1.63e+00	5.88e+00	1.03e-01
	μ_1	-	1.11e+02	1.11e+02	0	1	0	1	0	1
	μ_2	-	2.27e+02	2.27e+02	0	1	0	1	0	1
	μ_3	-	3.24e+02	3.24e+02	0	1	0	1	0	1
	κ_1	-	1.02e+00	1.02e+00	0	1	0	1	0	1
	κ_2	-	2.02e+00	2.02e+00	0	1	0	1	0	1
	κ_3	-	1.73e+00	1.73e+00	0	1	0	1	0	1
H_S^w	α	v	1.56e+00	7.04e-01	0	0	1.32e+00	-1.23e+02	0	-2.00e+00
	β	v	1.43e+00	1.51e+00	4.41e+01	-1.39e+00	0	1	0	1
	γ	v	-9.39e-02	-5.94e-01	6.96e-03	2.00e+00	0	1	0	1
T_P^w	μ	h	1.61e+00	0	1.58e+00	2.45e-01	0	1	0	1
	σ	h	3.54e-01	0	1.35e-01	-2.14e-01	0	1	0	1
Θ_w^r	μ	h	2.38e-01	4.45e+00	-2.57e+00	1	0	1	0	1
	σ	h	1.71e+01	1.63e+01	0	1	0	1	0	1
H_S^s	α	-	6.38e-01	6.38e-01	0	1	0	1	0	1
	β	-	1.32e+00	1.32e+00	0	1	0	1	0	1
	γ	-	3.32e-01	3.32e-01	0	1	0	1	0	1
T_P^s	μ	h_s	2.03e+00	0	2.11e+00	1.45e-01	0	1	0	1
	σ	h_s	2.81e-01	0	0	1	3.22e-01	-2.97e-01	0	1
Θ_s	w_1	h_s	6.93e-01	1.53e+00	-9.53e-01	2.60e-01	0	1	0	1
	w_2	h_s	3.07e-01	-5.26e-01	9.53e-01	2.60e-01	0	1	0	1
	μ_1	-	1.80e+02	1.80e+02	0	1	0	1	0	1
	μ_2	-	3.00e+00	3.00e+00	0	1	0	1	0	1
	κ_1	-	1.71e-01	1.71e-01	0	1	0	1	0	1
	κ_2	-	7.42e+01	7.42e+01	0	1	0	1	0	1
H_t	w_1	-	5.01e-01	5.01e-01	0	1	0	1	0	1
	w_2	-	4.99e-01	4.99e-01	0	1	0	1	0	1
	μ_1	-	4.27e-01	4.27e-01	0	1	0	1	0	1
	μ_2	-	-4.30e-01	-4.30e-01	0	1	0	1	0	1
	σ_1	-	7.35e-02	7.35e-02	0	1	0	1	0	1
	σ_2	-	7.79e-02	7.79e-02	0	1	0	1	0	1

Paper V

Extreme response estimation of offshore wind turbines with an extended contour-line method

Jan-Tore Horn and Steven R. Winterstein

Journal of Physics: Conference Series, 2018

Abstract The contour-line method is a simplified approach for finding the long-term extreme values by a small number of short-term analyses. It is assumed the response with a return period of T years occurs during a sea-state with a shorter or equal return period. This provides good extreme response estimates for structures dominated by wave loads and have a monotonic response behaviour. For an offshore wind turbine, the power production stops at a certain wind speed to reduce wear, changing the dynamics of the system dramatically, from wind to wave load dominated. Also, there is a non-negligible probability for the turbine being unable to operate although the wind speeds would suggest so, due to e.g. grid- or mechanical failure. Therefore, the original contour-line method for extreme response estimation is not applicable without some modifications to account for changing dynamics. In the present work, it is suggested to treat the operational and non-operational conditions as two sub-populations and estimate the Tyear response in each population by a standard contour-line method. Next, the results from each sub-population are combined in order to estimate the total T-year response in consistent manner.

Extreme response estimation of offshore wind turbines with an extended contour-line method

Jan-Tore Horn[1] **and Steven R. Winterstein**[2]

[1]Centre for Autonomous Marine Operations and Systems (NTNU AMOS), Department of Marine Technology, NTNU, Otto Nielsens veg 10, 7491 Trondheim, Norway
[2] Probability-Based Engineering, Menlo Park, CA, USA

E-mail: `jan-tore.horn@ntnu.no`

Abstract. The contour-line method is a simplified approach for finding the long-term extreme values by a small number of short-term analyses. It is assumed the response with a return period of T years occurs during a sea-state with a shorter or equal return period. This provides good extreme response estimates for structures with a response behaviour monotonically increasing with the severity of the sea-state. For an offshore wind turbine, the power production stops at a certain wind speed to reduce wear, changing the dynamics of the system dramatically, from wind to wave load dominated. Also, there is a non-negligible probability for the turbine being unable to operate although the wind speeds would suggest so, due to e.g. grid- or mechanical failure. Therefore, the original contour-line method for extreme response estimation is not applicable without some modifications to account for changing dynamics. In the present work, it is suggested to treat the operational and non-operational conditions as two sub-populations and estimate the T-year response in each population by a standard contour-line method. Next, the results from each sub-population are combined in order to estimate the total T-year response in consistent manner.

1. Introduction

A method for long term extreme value analysis of a system with multiple sub-populations of dynamic response characteristics is presented. The approach is suggested in [1] to combine environmental sub-populations related to load directions and sub-populations related to different response models. Offshore wind turbines (OWTs) have, simply formulated, two dynamic response models; one for operating turbine, and one for an idle or parked turbine. Depending on the response parameter of interest, both sub-populations may be important to consider in both FLS and ULS design.

The present work investigates whether such an approach is feasible on a large, bottom-fixed, monopile-mounted OWT in a water depth of 30 meters. Typical responses of interest are; forces and moments in the transition between tower and foundation, soil deformation, blade root loads, bending moments in the foundation and nacelle accelerations affecting the drive train loads. Here, the two latter responses will be investigated. The long-term extreme values are to be found with environmental contours and the inverse first-order reliability method (IFORM) [2] for parked and operational turbine, and verified with an extreme value distribution based on a full long-term analysis (FLTA). The method has previously been used on OWTs for assessing extreme loads during operation in e.g. [3, 4].

The issue with applying simplified methods for extreme value analyses of OWTs are presented along with suggested remedies for the response discontinuities in [5, 6]. For comparison, the present work will also use the contour-line method, but instead of modifications, the original method presented in [2] will be performed on several sub-domains of the problem. Hence, the response discontinuities presented in e.g. [7] will not be present in the chosen sub-populations. The final step is to combine the results to obtain a extreme response consistent with the required exceedance probability, a non-trivial problem illustrated in [8] for responses dependent on load directionality.

This paper will first present approaches used for long term extreme value analyses and combined responses. Next, the response sub-populations, environmental- and numerical model will be presented. Finally. results and discussions will evaluate the applicability and consequences of the suggested approach.

2. Extreme response estimation

Two methods for estimation of extreme response will presented. The full long-term analysis (FLTA) taking into account weighted response contributions from the complete environmental domain is considered exact and will be used to verify the IFORM-based environmental contour method (ECM).

2.1. Full long-term analysis

For sub-population 1, the CDF of the maximum response in a 1-hour sea state using an FLTA is found by numerical integration as [9]:

$$F^{(1)}_{X_{1h}}(x) = \exp\left\{ \int_v \int_h \ln F^{(1)}_{X_{1h}|V,H_S,T_P}(x|v,h,t_e)\, f^{(1)}_{V,H_S}(v,h)\, dv\, dh \right\} \tag{1}$$

where the wind speed and significant wave height are described by their joint distribution, while the expected peak period t_e is used. Similarly for sub-population 2:

$$F^{(2)}_{X_{1h}}(x) = \exp\left\{ \int_h \int_t \ln F^{(2)}_{X_{1h}|V,H_S,T_P}(x|v_e,h,t)\, f_{H_S,T_P}(h,t)\, dt\, dh \right\} \tag{2}$$

where the significant wave height and peak period are described by their joint distribution, while the expected wind speed v_e is used for response calculations. Here, Eq. (1) and (2) are evaluated numerically using the bins in Tab. 1 and 90 10-minute simulations are performed in each bin for sufficiently accurate results. It is assumed that the extreme value in each 10-minute simulation is Gumbel distributed, so that the 1-hour extreme value distribution for each simulation bin is found by a power of six:

$$F_{X_{1h}|V,H_S,T_P} = \left[F_{X_{10min}|V,H_S,T_P}\right]^6 \tag{3}$$

Parameter	Min	Max	Step
V [m/s]	4	36	1
H_S [m]	0	10	0.5
T_P [s]	2	18	1

Table 1: Bins for FLTA

2.2. Environmental contour method

The ECM is a method for estimating the extreme response by limiting the number of sea-states. The method is very useful when extreme responses are dominated by a small number of environmental conditions. More specifically, the extreme response with a return period of T years is approximated by a sea-state with a similar return period. The environmental parameters describing this sea-state is here v_T for wind speed, h_T for significant wave height and t_T for peak period. When the CDF of the 1-hour extreme response for this sea-state is established by e.g. time-domain simulations, the extreme response x_T is found by:

$$x_T \approx F^{-1}_{X_{1h}|V,H_S,T_P}(\alpha|v_T, h_T, t_T) \tag{4}$$

for some appropriate fractile α. For a range of wave-driven offshore problems, typical α values have been found in the range 0.75-0.95 [10]. Note that only 2D environmental domains will be considered in the present work, meaning that one of the three environmental parameters will be replaced by their expected value conditioned on the remaining parameters, as described in detail later.

2.3. Combined extreme response

For each operational sub-population, the extreme response functions are evaluated separately, and later combined into a total extreme response. Let X_{1h} denote the 1-hour extreme response of a given parameter, $F_{X_{1h}}$ is its cumulative distribution and $G_{X_{1h}} = 1 - F_{X_{1h}}$ is the complementary CDF (CCDF). The total response CDF is simply found by a weighted sum of the contributing populations:

$$F_{X_{1h}}(x) = \sum_i p_i \, F^{(i)}_{X_{1h}}(x) \tag{5}$$

and simlarly with the CCDFs:

$$G_{X_{1h}}(x) = \sum_i p_i \, G^{(i)}_{X_{1h}}(x) \tag{6}$$

where p_i is the probability of sub-population i. The CDF conditioned on response sub-population i can be evaluated accurately with an FLTA, or with the ECM [10]. The objective is to extended the latter for use with offshore wind turbines, which is done with an alternative approach in [5, 6].

3. Proposed method

The proposed procedure for estimating long term extremes using the ECM in several response sub-populations is:

a) Estimate extreme response x_T in each sub-population for two return periods, say $T_1 = 50$ and $T_2 = 500$. Use the ECM and Eq. 4, assuming only this population is acting.
b) Estimate the response CCDF $G^C_{X_{1h}}(x)$, where C denotes *contour*, for each sub-population using the obtained responses. Use the relation $G^C_{X_{1h}}(x_T) = 1/(T \cdot 365 \cdot 24)$ for finding the two fitting points used for linear fitting.
c) Find the total $G^C_{X_{1h}}(x)$ using Eq. 6.

Of course, the response CCDFs can be found with more fitting points from the ECM and a curved CCDF may be obtained. However, the linear assumption is used in the present work for simplicity. The linear fit can for instance be performed using:

$$-\log_{10} G^C_{X_{1h}}(x) = A\, B^{c(x)}; \;\; c(x) = \frac{\ln x - \ln x_{T_1}}{\ln x_{T_2} - \ln x_{T_1}} \tag{7}$$

where $A = \log_{10} T_1$ and $AB = \log_{10} T_2$. The choices of fitting form, and the return periods T_1 and T_2 used in these fits, are discussed further in [1].

4. Sub-populations

The system dynamics of an OWT is considerably different between parked and operational state. Hence, it is natural to divide the lifetime into fractions as function of the up-time of the turbine. The sub-populations defining the dynamic response models are illustrated in Fig. 1 with corresponding probabilities of occurrence, and are defined as:

1. Operational turbine within operational wind speed limits
2. Parked turbine due to general unavailability independent of wind speeds
3. Parked turbine due to wind exceeding operational wind speed limit (25 m/s)
4. Parked turbine due to wind below lower operational wind speed (4 m/s)

To limit the number of sub-populations, the CDFs from population 3 and 4 are taken as constants. Assuming that $p_4 F_{X_{1h}}^{(4)} \approx p_4$ is expected to be a good approximation due to small response in this population. Also, it is assumed that the extreme response for $V > 25$ is mostly covered by sub-population 2, so that we can assume $p_3 F_{X_{1h}}^{(3)} \approx 0$. The actual contribution from sub-population 3 is left for future work. Hence, only sub-populations 1 and 2 will be evaluated here. The total availability is set to 90% in accordance with [11].

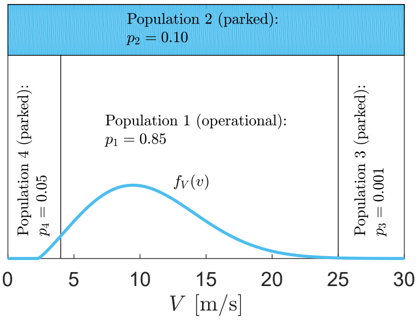

Figure 1: Sub-populations with lifetime fractions p_i

5. Environmental model

The environmental parameters to be considered are the hub-height mean wind speed, significant wave height and peak period. Turbulence intensity is set to 10%, and the wind field is calculated with TurbSim [12] using the Kaimal spectrum. For the irregular waves, the JONSWAP spectrum with long-crested formulation with co-directional wind and waves. Due to dynamic properties in the two sub-populations and to limit the problem to two environmental dimensions in each sub-population, slightly different environmental descriptions are used. For sub-population 1, meaning operational turbine, the wind speed and significant wave height are assumed to be the governing parameters and will be treated as stochastic, while for the peak period, the expected value is used. For sub-population 2, and parked turbine, wave loads are assumed to be dominating, meaning that the significant wave height and peak period are stochastic, while the wind speed is the expected wind speed conditioned on the peak period.

5.1. Joint distributions

The joint distribution of hub-height mean wind speed and significant wave height is:

$$f_{V,H_S}(v,h) = f_V(v;\alpha_v,\beta_v,\gamma_v)\, f_{H_S|V}(h;\alpha_h(u),\beta_h(u),\gamma_h(u)) \tag{8}$$

where both are assumed to be Weibull distributed with three parameters α, β and γ. To be used with sub-population 1, the joint distribution is modified as:

$$f^{(1)}_{V,H_S}(v,h) = \begin{cases} \frac{f_{V,H_S}(v,h)}{F_V(25)-F_V(4)} & \text{for } 4 \leq v \leq 25 \\ 0 & \text{else} \end{cases} \tag{9}$$

to account for operational wind speed limits. Further, the significant wave height and peak period joint distribution is given as:

$$f_{H_S,T_P}(h,t) = \int_0^\infty f_{V,H_S}(v,h)\,dv\, f_{T_P|H_S}(t;\mu_{\log t}(h),\sigma_{\log t}(h)) \tag{10}$$

where the peak period distribution condition on significant wave height is assumed lognormally distributed.

5.2. Wind

The chosen location for the environmental basis is Dogger Bank in the central North Sea [13], where the parameters in the 3-parameter Weibull-distributed wind speed are found as:

$$\alpha_v = 9.5 \tag{11a}$$
$$\beta_v = 2.2 \tag{11b}$$
$$\gamma_v = 2.3 \tag{11c}$$

5.3. Wind sea

The significant wave height is described with a 3-parameter Weibull distribution with the parameters conditioned on the wind speed v as:

$$\alpha_h(v) = 0.70 + 1.3\,e^{-120\,v^{-2}} \tag{12a}$$
$$\beta_h(v) = 1.5 + 44\,v^{-1.4} \tag{12b}$$
$$\gamma_h(v) = -0.60 + 0.007\,v^2 \tag{12c}$$

Further, the peak period is lognormally distributed with the mean and variance conditioned on the significant wave height as:

$$\mu_{\log t}(h) = 1.6\,h^{0.24} \tag{13a}$$
$$\sigma_{\log t}(h) = 0.14\,h^{-0.21} \tag{13b}$$

For sub-population 1, the wave peak period is modelled deterministically as a function of the mean wind speed v using the curve-fitted relation:

$$t_e = 1.99 + 0.17\,v_e^{1.24} \tag{14}$$

The inverse relation is used in sub-population 2, where the mean wind speed is a function of the peak period.

5.4. Environmental contours

In Fig. 2, the two-dimensional 50- and 500-year environmental contour-lines created using the Rosenblatt transform [14] are shown for both sub-populations. Specific sea-states to be checked when using the ECM are outlined.

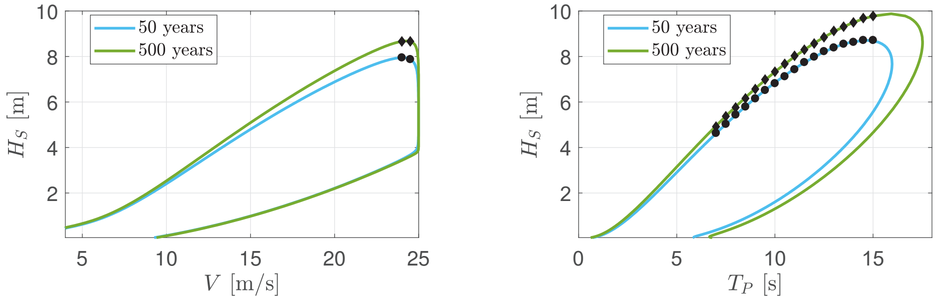

(a) Sub-population 1

(b) Sub-population 2

Figure 2: 2D environmental contours including points used with IFORM

6. Numerical OWT model

The numerical model is an FEM model in USFOS/vpOne of the 10MW DTU reference wind turbine [15] mounted on a monopile in 30 meters water depth at Dogger Bank in the central North Sea. See Fig. 3 for illustration and main dimensions of tower and foundation. First fore-aft natural period is 4.4 seconds. For the load calculations, unsteady BEM theory [16] is used for the blades, and for wave loads; the first order wave theory with a vertical stretching to the free surface [17]. When the turbine is parked, or idling, the blade pitch is set to 82 degrees with respect to incoming wind direction, resulting in a slowly rotating rotor and small wind loads.

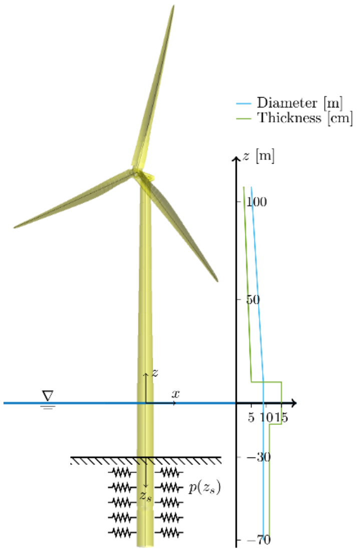

Figure 3: Illustration of numerical FEM model in USFOS/vpOne

7. Results

In this section, results from the combined extreme response analyses using the ECM and the FLTA are presented.

7.1. Nacelle acceleration

The environmental contours and isoquants for the nacelle tower-top acceleration are shown in Fig. 4. For each combination of significant wave height and peak period, 90 10-minute simulations are performed in order to predict the 1-hour response at a fractile of $\alpha = 0.8$ with sufficient confidence. The discretization are performed with a step of 0.5m for H_S, and 1s for T_P, excluding combinations outside the 500 year environmental contour. For sub-population 1, the response is mostly affected by wind loads at lower wind speeds, but wave driven for approximately $H_S > 2$m. When the turbine is parked, an amplification in the response is seen around $T_P = 5$s, where the first natural period of the turbine is excited. Elsewhere, responses systematically increase with H_S and decrease with T_P.

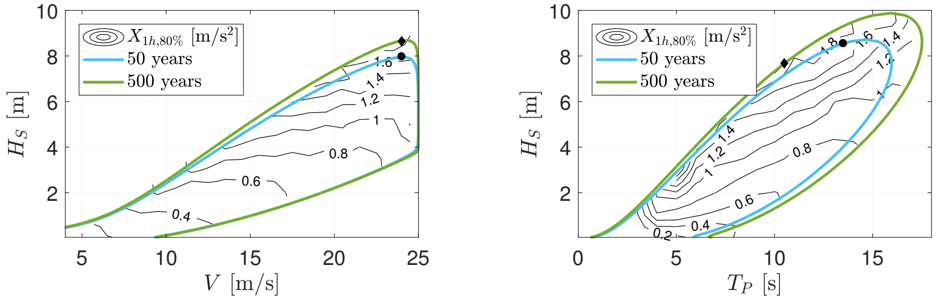

(a) Sub-population 1 (b) Sub-population 2

Figure 4: Isoquants for short-term nacelle acceleration with the fractile $\alpha = 0.8$ in Eq. (4). Sea-states leading to the most severe responses on the two contours are highlighted.

In Fig. 5, the results from the combined extreme value analysis is presented. In Fig. 5a, the exact CCDFs along with the linear curve-fits using the sea-states marked in Fig 4a and the optimal fractiles in Tab. 2. It is seen that a linear fit is a good approximation for response values with high return periods. The combined response using Eq. 6 is shown in Fig. 5b, indicating that the correct 50-year nacelle acceleration is slightly above 1.8m/s^2.

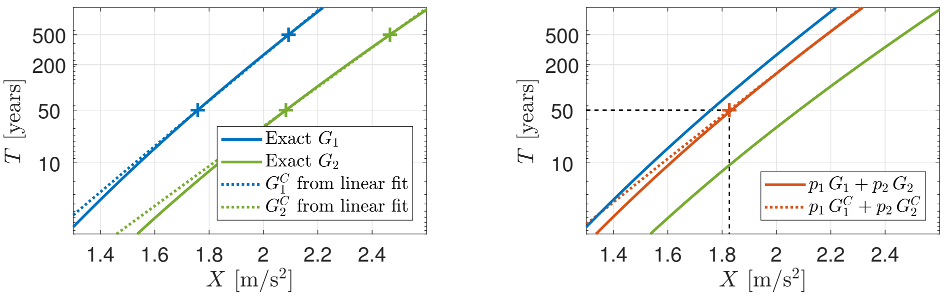

(a) (b)

Figure 5: Response CCDFs and combined extreme response for nacelle acceleration. Sub-population 1 in blue and sub-population 2 in green.

T [years]	α_1	α_2
50	0.93	0.95
500	0.97	0.97

Table 2: Optimal fractiles for extreme nacelle acceleration

The response fractiles in Tab. 2 are the fractiles needed to best approximate the CCDFs between 50 and 500 years return period. The fractiles needed in both sub-populations are quite similar, with higher fractiles for longer return periods. Also, fractiles for longer return periods are excpected to increase due to more dominant response variability, which is indeed reflected in Tab. 2. Figure 6 show the Gumbel fits for the sea-states used with ECM. It is found that 90 10-minute simulations are sufficient to predict the 10-minute extremes. The 1-hour extreme distribution is then found by applying Eq. 3. For future work, the accuracy of such a transformation may be investigated, compared to performing 1-hour simulations.

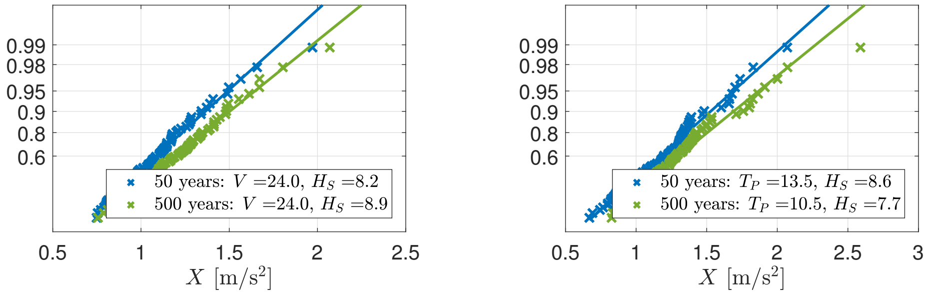

(a) (b)

Figure 6: CDFs and Gumbel fits for 10-minute extreme nacelle acceleration with sea-states chosen for T-year response estimates with ECM.

7.2. Bending moment

Isoquants for the extreme bending moment at mudline is shown in Fig. 7 for both populations using the same simulations as for the nacelle acceleration case. The response dependency on the environmental parameters are similar to the nacelle acceleration. However, the operational case is dominating due to the large static moment induced by the mean wind speed. Also, H_S is the most important parameter for the non-operational turbine as seen by the dominating sea-states in Fig. 7. The exact and ECM-created CCDFs are shown in Fig. 8a for the bending moment at mudline and combined CCDF is plotted in Fig. 8b using the optimal fractiles in Tab. 3. In contrast to the nacelle acceleration, the operational sub-population is dominant and the combined response is very little affected by the parked turbine. Also, for the extreme bending moment, considering only sub-population 1 is slightly conservative.

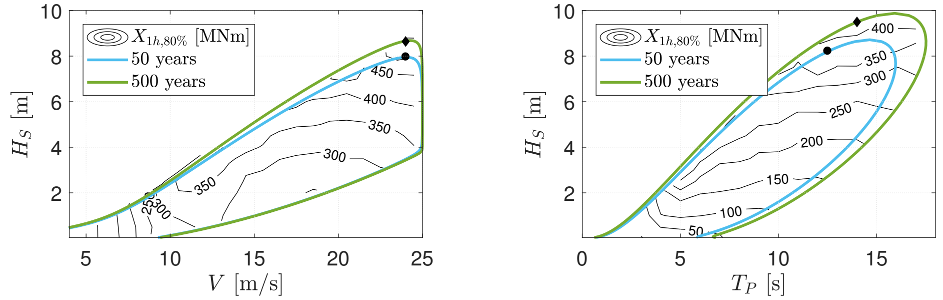

(a) Sub-population 1

(b) Sub-population 2

Figure 7: Isoquants for short-term mudline bending moment with the fractile $\alpha = 0.8$ in Eq. 4.

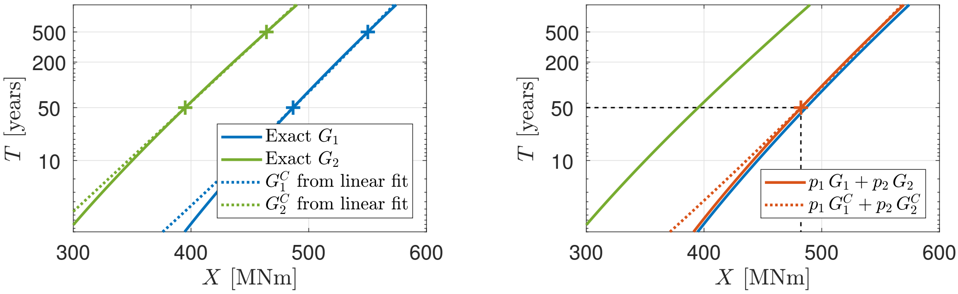

(a)

(b)

Figure 8: Response CCDFs and combined extreme response for bending moment at mudline. Sub-population 1 in blue and sub-population 2 in green.

T [years]	α_1	α_2
50	0.83	0.88
500	0.92	0.92

Table 3: Optimal fractiles for extreme bending moment

8. Conclusion

A method for estimation of the T-year extreme response from several response sub-populations is presented. The method is applied to an offshore wind turbine with different response characteristics during operational and parked state. Compared to an FLTA, the environmental contour method is very efficient and can provide good results given appropriate response fractiles.

For response parameters dominated by the operational state of the offshore wind turbine, using the extreme values assuming the turbine is 100% operational will yield an upper bound of the extreme response. Similarly, for response parameters dominated by a parked turbine, an upper bound is obtained by assuming a turbine which is always idling. In the latter case, the upper bound is expected to be quite conservative due to the small probability of this sub-population. Depending on which response parameter that is important for ULS design, combining all sub-populations may both increase or decrease the true 50-year response compared to a fully operational turbine, as seen in the presented results. Although the relative differences are minor in the present case, the method is useful to establish this fact, and may be used for more response parameters and other types of offshore wind turbine structures.

It is worthwhile to mention that the low-damped parked turbine state is expected to contribute more to the combined response if a wave load model of higher order is used, see e.g. [17, 18].

Acknowledgments

This work has been carried out at the Centre for Autonomous Marine Operations and Systems (NTNU AMOS). The Norwegian Research Council is acknowledged as the main sponsor of NTNU AMOS. This work was supported by the Research Council of Norway through the Centres of Excellence funding scheme, Project number 223254 - NTNU AMOS.

References

[1] Steven R. Winterstein. Environmental Contours : Including the Effects of Directionality and other sub-populations. Technical Report August, Menlo Park, CA, 2017.

[2] Steven R. Winterstein, T. C. Ude, C. A. Cornell, P. Bjerager, and S. Haver. Environmental parameters for extreme response: Inverse FORM with omission factors. In *Proc. 6th Int. Conf. on Structural Safety and Reliability, Innsbruck, Austria*, 1993.

[3] Puneet Agarwal and Lance Manuel. Simulation of offshore wind turbine response for long-term extreme load prediction. *Engineering Structures*, 31(10):2236–2246, 2009.

[4] K. Saranyasoontorn and L. Manuel. Efficient models for wind turbine extreme loads using inverse reliability. *Journal of Wind Engineering and Industrial Aerodynamics*, 92(10):789–804, 2004.

[5] Qinyuan Li, Zhen Gao, and Torgeir Moan. Modified environmental contour method for predicting long-term extreme responses of bottom-fixed offshore wind turbines. *Marine Structures*, 48:15–32, 2016.

[6] Qinyuan Li, Zhen Gao, and Torgeir Moan. Modified environmental contour method to determine the long-term extreme responses of a semi-submersible wind turbine. *Ocean Engineering*, 142(July):563–576, 2017.

[7] Korn Saranyasoontorn and Lance Manuel. On assessing the accuracy of offshore wind turbine reliability-based design loads from the environmental contour method. 15(2):132–140, 2005.

[8] George Z. Forristall. On the Use of Directional Wave Criteria. *Journal of Waterway, Port, Coastal, and Ocean Engineering*, 130(6):312–321, 2004.

[9] Torgeir Moan and Arvid Naess. *Stochastic Dynamics of Marine Structures.* Cambridge University Press, 2013.

[10] Sverre Haver and Steven R. Winterstein. Environmental contour lines: A method for estimating long term extremes by a short term analysis. *Transactions - Society of Naval Architects and Marine Engineers*, 116:116–127, 2009.

[11] DNV GL. Loads and site conditions for wind turbines. Technical Report November, 2016.

[12] N.D Kelley and Bonnie Jonkman. Overview of the TurbSim Stochastic Inflow Turbulence Simulator. 2007.

[13] Jan Tore Horn, Jørgen R. Krokstad, and Jørgen Amdahl. Joint Probability Distribution of Environmental Conditions for Design of Offshore Wind Turbines. In *Proceedings of the 36th International Conference on Ocean, Offshore and Arctic Engineering*, Trondheim, Norway, 2017.

[14] H.O. Madsen, S. Krenk, and N.C. Lind. *Methods of Structural Safety.* Prentice-Hall, Inc., 1986.

[15] Christian Bak, Frederik Zahle, Robert Bitsche, Anders Yde, Lars Christian Henriksen, Anand Nata, and Morten Hartvig Hansen. Description of the DTU 10 MW Reference Wind Turbine. Technical report, DTU, 2013.

[16] Martin O L Hansen. *Aerodynamics of wind turbines, Second edition*, volume 9781849770. 2013.

[17] Jan Tore Horn, Jørgen R. Krokstad, and Jørgen Amdahl. Hydro-Elastic Contributions to Fatigue Damage on a Large Monopile. *Energy Procedia*, 2016.

[18] Signe Schløer, Henrik Bredmose, and Harry B. Bingham. The influence of fully nonlinear wave forces on aero-hydro-elastic calculations of monopile wind turbines. *Marine Structures*, 50:162–188, 2016.

Paper VI

Fatigue reliability assessment of offshore wind turbines with stochastic availability

Jan-Tore Horn and Bernt J. Leira

Accepted to: Reliability Engineering & System Safety, 2018

Abstract In this paper, the impact on lifetime estimation of an offshore wind turbine by introduc- ing a stochastic model for the availability is investigated. Offshore bottom-fixed wind turbines typically have an average downtime of 4-10% due to e.g. grid- or mechanical fail- ures including a potentially long response time for recovery. During the non-operational conditions, the fatigue damage in the foundation is accumulating significantly faster. Designing the wind farm based on a conservative downtime fraction will lead to design conservatism with respect to the foundation, which will be quantified in this paper using a structural reliability analysis. The variability in the long-term fatigue damage is found with a joint distribution of all relevant environmental parameters and a Monte Carlo sampling procedure.

Fatigue reliability assessment of offshore wind turbines with stochastic availability

Jan-Tore Horn[a,b,*], Bernt J. Leira[b]

[a] *Centre for Autonomous Marine Operations and systems (NTNU AMOS), NTNU, Trondheim, Norway*
[b] *Department of Marine Technology, NTNU, Trondheim, Norway*

Abstract

In this paper, the impact on lifetime estimation of an offshore wind turbine by introducing a stochastic model for the availability is investigated. Offshore bottom-fixed wind turbines typically have an average downtime of 4-10% due to e.g. grid- or mechanical failures including a potentially long response time for recovery. During the non-operational conditions, the fatigue damage in the foundation is accumulating significantly faster. Designing the wind farm based on a conservative downtime fraction will lead to design conservatism with respect to the foundation, which will be quantified in this paper using a structural reliability analysis.

Keywords: offshore wind turbines; reliability; downtime; fatigue

1. Introduction

The overall costs of an offshore wind farm is highly dependent on the substructure designed to keep the turbine in place or floating in a safe and reliable manner during the operational lifetime. To date, the simplistic monopile foundation has proven to be the most cost efficient solution in water depths up to at least 40 meters. In the present work, an extra large monopile foundation supporting a 10MW wind turbine is chosen as the basis for the dynamic system for which the long term structural fatigue is to be evaluated.

When moving the wind energy industry offshore to larger water depths and further away from the mainland, additional considerations must be made with respect to environmental loading from waves, currents and tides [1]. Comparing to an onshore turbine, the load situation for which the design criteria are to be met, is much more complex. Depending on the desired accuracy of the structural response and reliability estimations, the environmental loading parameters can be extended to a large number of dimensions. If design conservatism can be reduced by including extra loading parameters and stochastic descriptions, methods should be readily available for spending computational efforts to improve the system knowledge and decrease modelling uncertainties. A general method

---

[*] Corresponding author
Email address: `jan-tore.horn@ntnu.no` (Jan-Tore Horn)

involving efficient use of idle computing resources rather than a case-optimized method is used for the present long-term analyses.

Fatigue life estimation of offshore wind turbines requires simulations of the response due to combined external loads according to design load case (DLC) 1.2 in [1]. Other load cases may also contribute to the overall fatigue damage, but DLC 1.2 is expected to be the main contributor. For an offshore wind turbine, this means to simulate with a sufficient amount of external conditions to represent the expected fatigue damage during the operational lifetime (see e.g. [2]). Due to many types of external parameters (wind, wave height, wave direction, current etc.) a full fatigue limit state (FLS) analysis may become computationally demanding. As a result, there has been an effort to develop simplified methods for quick load analysis in the frequency domain [3, 4, 5]. In addition, efforts has been made to reduce the number of load cases and total simulation length while maintaining the accuracy [6, 7].

The present work uses a high dimensional joint distribution fitted to data from a likely site of a future offshore wind farm in the central North Sea. Environmental parameters include wind, wind-genereted sea (wind sea), swell and tide as well as their respective directional statistics. Further, the distribution is used for generating short-term sea states in a long-term analysis of the turbine in question by means of Gibbs sampling and cluster computing. Removing the need for binning the data and finding the probability of occurrence for each sea state are some of the advantages when using a direct sampling from the joint distribution. It is also of great interest to obtain an estimation of the estimated fatigue error incorporated in the structural reliability, which only can be obtained by an analysis in the entire variable domain. Furthermore, there is no need to discretize the domain where the load effects are unknown as these will be accounted for automatically if the number of samples are sufficiently large. For instance, if the tidal parameters do not contribute to the response, the result is a faster convergence of the load effects. Finally, when the convergence criteria of the investigated response is met, sensitivity factors and response characteristics for the fatigue damage with respect to input parameters are estimated using the probabilistic analysis tool PROBAN [8].

The availability of an offshore wind turbine (OWT) is a measure of the ratio between the duration for which the turbine is unable to produce energy and the total time for possible power production. While parked, the dynamic characteristics changes significantly. For bottom-fixed OWTs the damping level is dramatically reduced, resulting in an increased fatigue damage accumulation [9]. Unless data on the actual downtime fraction is available, the availability is taken as 90 or 100%, whichever is most conservative [1]. The purpose of this paper is to reduce the potential design conservatism related to the availability parameter by means of probabilistic analysis.

The paper is built up as follows; first, the design basis including the environmental- and numerical model is presented. Second, the simulation procedures and sub-populations required to perform long-term reliability analyses are discussed. Finally, the reliability analysis is performed, with an investigation of the most dominating parameters and the impact of availability on the failure probability.

2. Offshore site and environmental model

Hindcast data for description of the wind and wave environment is provided by the Norwegian Meteorological Institute and the NORA10 database [10] for the location shown in Fig. 1. The data contains information about the wind speed, wind direction and significant wave height, peak period, and direction for both wind sea and swell. The data is valid for periods of 3 hour durations and some of the available parameters are listed in Tab. 1 with corresponding probability distributions.

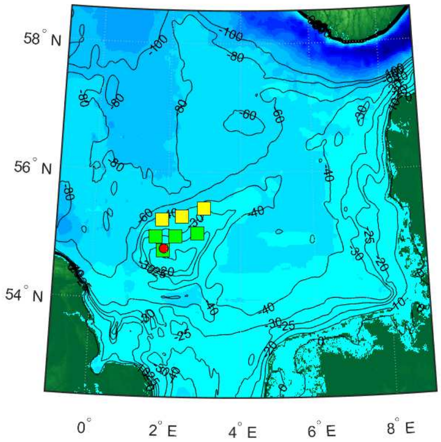

Figure 1: Planned (green) and possible (yellow) offshore wind farms at Dogger Bank with location for hindcast data (red)

The complete environmental joint distribution is modelled as:

$$f_{\mathbf{X}_e} = f_{\mathbf{X}_w} \cdot f_{\mathbf{X}_s} \cdot f_{H_t} \tag{1}$$

where the wind sea variables are gathered in:

$$\mathbf{X}_w = [V, \Theta_v, H_S^w, T_P^w, \Theta_w^r] \tag{2}$$

where descriptions can be found in Tab. 1, and

$$\mathbf{X}_s = [H_S^s, T_P^s, \Theta_s] \tag{3}$$

for swell. The variable dependencies are described with:

$$f_{\mathbf{X}_w} \approx f_V \cdot f_{\Theta_v|V} \cdot f_{H_S^w|V} \cdot f_{T_P^w|H_S^w} \cdot f_{\Theta_w^r|H_S^w} \tag{4}$$

for wind sea, and

$$f_{\mathbf{X}_{\mathrm{s}}} \approx f_{H_S^{\mathrm{s}}} \cdot f_{T_P^{\mathrm{s}}|H_S^{\mathrm{s}}} \cdot f_{\Theta_s|H_S^s} \tag{5}$$

for swell. The distribution types are given in Tab. 1 and chosen based on a previous study [11] where the von Mises distribution was found very useful for modelling directions. Furthermore, is was found that a 3-parameter Weibull distribution was necessary in order to model the wave heights accurately. A normal distribution truncated at ±90 degrees proved suitable for modelling the relative wind-wave direction for wind-generated sea.

Table 1: Marginal distribution types and description of environmental parameters

Parameter		Distribution	Description	Unit
V	v	3-p Weibull	Wind speed at 100 meters	[m/s]
Θ_v	θ_v	von Mises mix	Wind direction at 100 meters	[deg]
H_S^w	h_w	3-p Weibull	Significant wave height for wind sea	[m]
T_P^w	t_w	Lognormal	Peak period for wind sea spectrum	[s]
Θ_w^r	θ_w	Trunc. normal	Relative wind-wave direction	[deg]
H_S^s	h_s	3-p Weibull	Significant wave height for swell	[m]
T_P^s	t_s	Lognormal	Peak period for swell spectrum	[s]
Θ_s	θ_s	von Mises mix	Swell direction	[deg]
H_t	H	Normal mix	Water level	[m]

3. Numerical wind turbine model

The numerical model is a bottom-fixed monopile-mounted turbine with tower and rotor-nacelle assembly (RNA) as described in [12]. To obtain a realistic natural period, the tower thickness is increased with 20% [13]. The final dimensions of the monopile and transition piece can be found in Fig. 2. The resulting first fore-aft and side-side natural periods are approximately 4.4 seconds, while the periods related to the second vibrational model are about 0.9 seconds in both directions. Consequently, the system is stiff, but still subjected to significant dynamic response from both wind and waves. The model has been validated in previous work, see e.g. [14]. The controller is an extended version of [15] with the possibility of increasing the fore-aft aerodynamic damping and avoid rotational speeds coinciding with the natural periods of the system. For integration in time-domain and calculation of aerodynamic loads, the finite-element method code USFOS/vpOne is used [16, 17], while the hydrodynamic loads are calculated by an external routine and imported to the FEM code on an equivalent wave kinematics grid for load calculation with the Morison equation. The method has been used as verified in previous studies (see [18, 19, 20]). The turbulent wind field is created with TurbSim [21] using the Kaimal spectrum and a turbulence intensity of 10%. For a parked/idling turbine, the blades are pitched to 82 degrees relative to the rotor plane, inducing only a slow rotation of the rotor.

4. Sub-populations

Due to several different states related to the turbine operation and downtime, an offshore wind turbine have sub-populations of significantly different response characteristics. Four different sub-populations are suggested, which are presented in Fig. 3 and defined as:

1. Operational turbine within operational wind speed limits
2. Parked turbine due to general unavailability independent of wind speed
3. Parked turbine due to wind exceeding the operational wind speed limit (25 m/s)

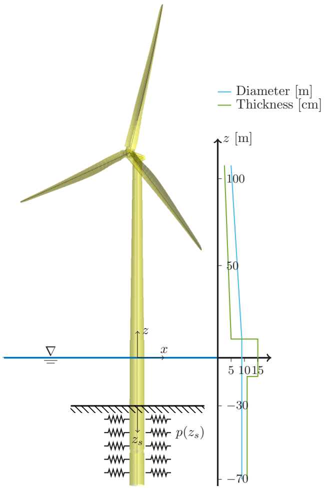

Figure 2: Numerical model. Diameter is varying from 5.4 meters in the top to 9.0 meters at the bottom. Thickness varies between 38 and 150 mm.

4. Parked turbine due to wind below the lower operational wind speed (4 m/s)

The fractions p_i satisfies $\sum_i p_i(\alpha) = 1$ for a given level of availability $\alpha \in [0, 1]$. Thus, the total fatigue damage can be found as:

$$D = \sum_i p_i \, D_i \tag{6}$$

Since the availability parameter α is independent of the response statistics from Monte Carlo simulations (MCS), it can be modelled as a random variable in the reliability analysis. Typically, the downtime of an offshore wind turbine is $4 - 10\%$ [22, 23] due to some failure, assumed to be uncorrelated with the environment. Hence, a probabilistic model of the availability using the beta distribution is introduced; $\alpha \sim \mathcal{B}[\mu_\alpha, \sigma_\alpha]$. The beta distribution is often used in modelling of the availability and corresponding costs in electrical systems [24] when both the failure rate and downtime are exponentially distributed [25]. Several distributions for component reliability are presented in e.g. [26] for wind turbine applications, one of which is the beta distribution. It is seen that the beta distribution is very flexible for modelling of failure rates compared to the Weibull, exponential and normal distributions. Hence, the beta distribution is chosen for the present work and examples of the stochastic modelling of α is shown in Fig. 4. Here, the uncertainty related to the choice of availability distribution is neglected. To underline the importance of modelling the availability, an example is shown in Tab. 2 for the individual populations considering the long-term fatigue damage at mudline for the presented model.

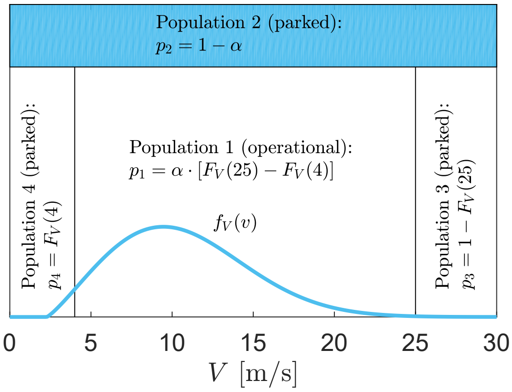

Figure 3: Sub-populations, with fractions as functions of the wind speed marginal cumulative distribution F_V and an availability parameter α

The fatigue contribution coefficient (FCC) is defined as:

$$\text{FCC}_i = \frac{p_i \cdot E[D_i]}{\sum_j p_j \cdot E[D_j]} \tag{7}$$

and the example show that the FCC is significantly larger than the probability of occurrence for the unavailable population, p_2, meaning that a small variation in α may be amplified in the structural reliability analysis. As a consequence, durations where the turbine is parked will have a damage accumulation rate of almost four times that of a parked turbine, on average. The results throughout this paper are focusing on sub-populations 1 and 2 due to the domination over sub-populations 3 and 4 in fatigue damage contributions.

Population	p_i [%]	FCC$_i$ [%]
1	89.6	76.0
2	7.0	21.0
3	0.1	2.6
4	3.3	0.4

Table 2: Population fractions and fatigue contribution coefficients (FCC) for $\alpha = 0.93$

5. Fatigue damage estimation

The fatigue damage for the long-term stochastic environmental variables contained in $\mathbf{x}$ and the short-term random variables in $\boldsymbol{\epsilon}$, e.g. wave and wind component phases

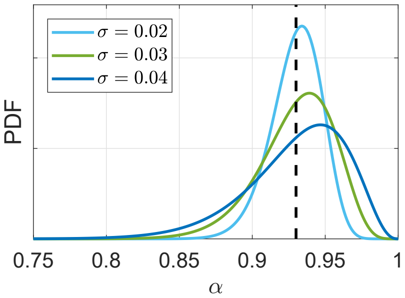

Figure 4: Example beta-distributions for the availability parameter α, with $E[\alpha] = \mu = 0.93$. σ denotes the standard deviation in the beta-distribution.

and amplitudes, is given as:

$$d(\mathbf{x}, \boldsymbol{\epsilon}) = \sum_{s \in \mathbf{s}(\mathbf{x}, \boldsymbol{\epsilon})} \frac{s^{m_1}}{K_1} \mathcal{H}(s - s_0) + \frac{s^{m_2}}{K_2} \mathcal{H}(s_0 - s) \tag{8}$$

where $\mathbf{s} = \boldsymbol{\Delta\sigma}\,(t/t_{\text{ref}})^k\, X_S\, X_L$ is the rainflow-counted [27] stress ranges for a single stationary time-domain simulation with a duration of T_{sim} seconds, corrected for local plate thickness (t), stress uncertainty (X_S) and load model uncertainty (X_L). Furthermore, $\mathcal{H}$ is the Heaviside function, s_0 is the stress limit, the m's and K's are material parameters, and t_{ref} and k are constants to account for the plate thickness t. For probabilistic analysis, uncertainty in the SN-curve is accounted for by introducing a mean and variance on $\log K_{1,2}$ [28]. The short-term variability can be overcome by M repeated simulations with different seeds, i.e. uncorrelated sampling of $\boldsymbol{\epsilon}$ for a given $\mathbf{x}$. Some other aspects of reducing the short-term variability are discussed in [29] with a probability-based approach, and in [30] with emphasis on simulation length. The 1-year fatigue damage for the variables in $\mathbf{x}$ is found with:

$$d(\mathbf{x}) = \frac{365 \cdot 24 \cdot 3600}{M \cdot T_{\text{sim}}} \cdot \sum_{i=1}^{M} d(\mathbf{x}, \boldsymbol{\epsilon}_i) \tag{9}$$

With reference to Eq. (9), industry standards [31] recommend that either $M = 6$ and $T_{\text{sim}} = 600$s, or $M = 1$ and $T_{\text{sim}} = 3600$s to predict sufficiently accurate short-term results. In this work, focus is on evaluating the long-term fatigue, which can be expressed as an integral over the dimensions in $\mathbf{x}$:

$$D = \int_{-\infty}^{\infty} d(\mathbf{x}) \cdot f_{\mathbf{X}}(\mathbf{x}) d\mathbf{x} \tag{10}$$

which evaluated using N Monte Carlo simulations is simply the arithmetic mean:

$$D^{\text{mcs}} = \frac{1}{N} \sum_{i=1}^{N} d(\mathbf{x}_i) \tag{11}$$

To limit the scope of this paper, no importance sampling or other means of variance reduction techniques are used for the long-term fatigue estimate, and $d(\mathbf{x})$ will be evaluated according to Eq. (9) with $M = 1$ and $T_{\text{sim}} = 600$.

6. Reliability analysis

In this study, the foundation fatigue is the only considered contribution to the structural reliability. Then, the failure probability for n years of operation is:

$$p_f = P\left[\Delta \leq n \sum_i p_i \, D_i\right] \tag{12}$$

where $\Delta \sim \text{Logn}[1.0, 0.3^2]$ (as suggested in [32]) is accounting for the uncertainty in the Palmgren-Miner summation of the rainflow-counted stress cycles, and D_i is the 1-year fatigue damage for sub-population i for a given structural component. It is important that the Miner sum uncertainty (Δ) is applied to the sum of all contributing populations. Finding the failure probability in each sub-population and then the union of failure in all populations would be non-conservative. The failure probability expressed as:

$$p_f = P[g \leq 0] \tag{13}$$

where $g = \Delta - n \sum p_i \, D_i$, can be evaluated by e.g. FORM/SORM analysis [33] or Monte Carlo simulations. The reliability index denoted β is frequently used in this paper, which is a measure of the shortest distance to the failure surface. For the FORM analysis, the reliability index β is:

$$\beta = -\Phi^{-1}(p_f) \tag{14}$$

6.1. Uncertainty from SN-curve

If the uncertainty in the SN-curve is to be accounted for, the reliability is traditionally performed with the Weibull-distributed long-term stress range as a basis for the fatigue damage [34, 32]. The fatigue damage from a Weibull distributed stress range; $\Delta\sigma \sim \text{Weibull}[a, b]$, yields the closed-form solution [35]:

$$\begin{aligned} D_i = & \nu_i \, T \, X_D \left\{ \frac{[\, a_i \, X_S \, X_L \, (t/t_{\text{ref}})^k \,]^{m_1}}{K_1} \Gamma \left[1 + \frac{m_1}{b_i}, \left(\frac{s_0}{a_i}\right)^{b_i}\right] \right. \\ & \left. + \frac{[\, a_i \, X_S \, X_L \, (t/t_{\text{ref}})^k \,]^{m_2}}{K_2} \gamma \left[1 + \frac{m_2}{b_i}, \left(\frac{s_0}{a_i}\right)^{b_i}\right] \right\} \end{aligned} \tag{15}$$

for sub-population i, where $\Gamma[\cdot, \cdot]$ and $\gamma[\cdot, \cdot]$ are the upper incomplete gamma functions and incomplete gamma functions, respectively. Furthermore, X_D is the fatigue uncertainty related to number of MCS, T is one year in seconds and ν is the sub-population dependent mean stress cycle rate found from simulations. An overview of the stochastic and deterministic parameters used in the reliability analysis is given in Tab. 3. The SN-curve used is the curve denoted D in [28] for steel in seawater with cathodic protection. The variance on the material parameters $\log K_1$ and $\log K_2$ are suggested in

[28]. Furthermore, the standard deviation on the stress uncertainty X_S and load model uncertainty X_L is chosen as 0.1, partly based on [36] and [37].

Although the response characteristics in the present case do not yield a perfectly Weibull distributed stress range. In Fig. 5, example Weibull fits are shown. A 2-parameter Weibull distribution is fitted to the distribution tail using two fitting points in the upper range of the data. The fatigue damage error using the fitted Weibull stress range and direct evaluation of the Palmgren-Miner was found to be less than 5% in all cases. For fatigue calculations, it is important that the stress range representation is correct for the stress ranges that contribute the most to the total fatigue damage. As indicated in Fig. 6, the fatigue damage derived from approximately $\Delta\sigma > 10$ [MPa] or $\log \Delta\sigma > 2.3$ is dominating, meaning that the Weibull fit should be accurate in this range. Hence, it is assumed that the 2-parameter Weibull with tail weighting is sufficient in all present cases to satisfy this requirement. Also, the advantage with 2-parameter Weibull is the closed-form solution to the Palmgren-Miner summation as presented in Eq. (15).

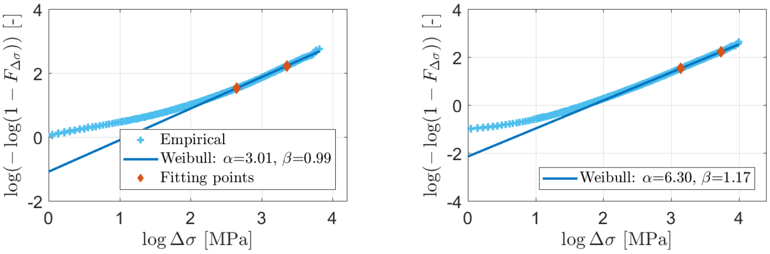

(a) Population 1

(b) Population 2

Figure 5: A two-parameter Weibull distribution (solid line) is fitted to the simulated/empirical data (crosses) using two fitting point at $1 - F_{\Delta\sigma} = 10^{-2}$ and 10^{-4}.

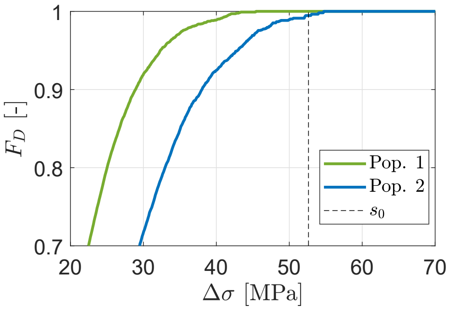

Figure 6: Contributions to fatigue damage from sub-populations

Variable	Distribution	Expected value	Standard deviation
$\boldsymbol{\alpha}$	**Beta**	$\boldsymbol{\mu_\alpha}$	$\boldsymbol{\sigma_\alpha}$
Δ	Lognormal	1	0.3
s_0	Fixed	52.63	-
m_1	Fixed	3	-
m_2	Fixed	5	-
$\log K_1$	Normal	12.164	0.2
$\log K_2$	Normal	16.106	0.2
X_S	Lognormal	1.5	0.1
X_L	Lognormal	1.0	0.1
X_D	Normal	1.0	$\boldsymbol{\sigma_D}$
t_{ref}	Fixed	0.025	-
k	Fixed	0.2	-
ν_1	Normal	0.755	0.020
ν_2	Normal	0.262	0.005

Table 3: Stochastic variables for probabilistic analysis of fatigue damage. Note that an expected stress correction factor X_S of 1.5 is introduced to account for e.g. thickness variation, ovality and girth welds in the foundation [28].

7. Results

In this section, the convergence of fatigue damage, foundation reliability and the impact of the availability model on the structural reliability is presented. The fatigue damage and failure probabilities are given at the most critical circumferential location in the foundation at sea-bed level.

7.1. Fatigue damage convergence

For each sub-population, simulations are performed until a user-specified convergence criteria is met as illustrated in Fig. 7. When a satisfying confidence interval is obtained, a probabilistic model of the stress range can be established as described above.

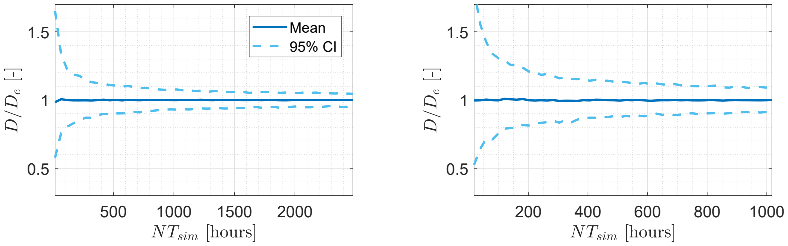

(a) Population 1

(b) Population 2

Figure 7: Convergence of fatigue in dimensioning location at mudline as function of simulation hours. D_e is the expected fatigue damage.

By assuming a normally distributed X_D to account for uncertainty in fatigue damage related to the number of MCS, the following relation is found:

$$\sigma_{D_1} \approx 4.62\, N^{-0.63} \tag{16a}$$

$$\sigma_{D_2} \approx 3.17\, N^{-0.49} \tag{16b}$$

Note that the convergence in sub-population 1 is faster than in sub-population 2, due to slightly smaller response variability. For the presented results, no uncertainty related to fatigue damage convergence is accounted for, meaning that $N \to \infty$ and $\sigma_D = 0$ for both sub-populations. Furthermore, as seen in Fig. 6, accumulated fatigue in the foundation is dominated by low-amplitude stress ranges in both sub-populations. In practice, only the high-cycle part of the SN-curve with $m = 5$ is utilized.

7.2. Combined failure probability

With reference to Fig. 8 it is found that all three methods give similar results, although the SORM method is slightly closer to the MCS solution than FORM. The total failure probability is significantly higher than the direct summation of the failure probabilities in sub-populations 1 and 2 due to a large number of shared stochastic variables related to the SN-curve, Miner sum and other uncertainties.

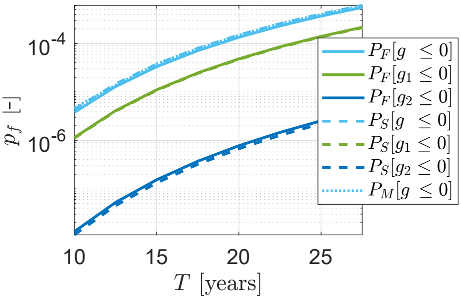

Figure 8: Failure probability for system(g), sub-population 1 (g_1) and sub-population 2 (g_2). Subscript F represents FORM calculation, S denotes SORM, and M is MCS. The failure probability is for $\mu_\alpha = 0.94$ and $\sigma_\alpha = 0.04$.

7.3. Impact on reliability and lifetime estimate

In Fig. 9, results from a parameter study of the beta-distributed availability are presented. Using common practice, there is no uncertainty in the availability and a characteristic value of 0.9 is used [1]. This corresponds to a beta-distribution with mean value of 0.9 and zero standard deviation. The figure shows how the estimated failure probability changes with different availability distributions. For instance, the accumulated failure probability can be reduced from $5 \cdot 10^{-4}$ with the deterministic model to $3.6 \cdot 10^{-4}$ if a mean value of 0.94 and standard deviation of 0.04 are used. With this availability model, we can read from Fig. 9 that there is a 10% probability that the availability is less than 0.9. It can be interpreted as if 10% of the turbines in a farm will have an availability of

0.9 or less. With a deterministic model, it is assumed that every single turbine has an availability of 0.9. The results show that a deterministic availability model is likely to yield pessimistic lifetime estimates.

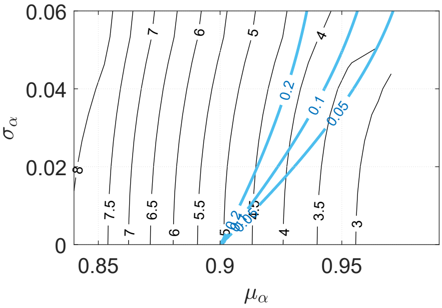

Figure 9: Cumulative failure probability for $n = 25$ years normalized with 10^{-4}, for the beta-distributed availability with variation in mean (μ_α) and standard deviation (σ_α). In blue: $P[\alpha < 0.90]$.

175 In Fig. 10, the temporal evolution of the reliability index β is shown for several models for the beta-distributed availability. The additional lifetime is then calculated based on the difference between time before down-crossing of $\beta_{lim} = 3.1$ - the reliability index corresponding to a cumulative failure probability of 10^{-3}, and the lifetime using deterministic availability.

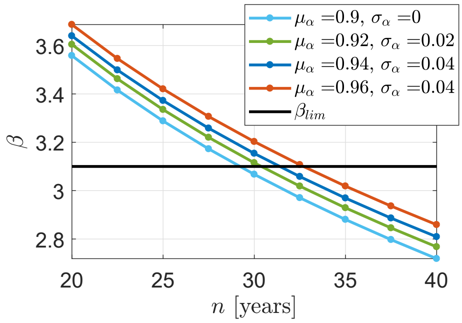

Figure 10: Increased reliability index β for different stochastic models of α.

180 Figure 11 shows the additional lifetime compared to 90% deterministic availability as a function of the stochastic availability model. Isoquants for $P[\alpha < 0.90]$ indicate combinations of μ_α and σ_α which have the same probability of superseding 90% availability. For instance, choosing a stochastic model of the availability with a mean of 94% and 10% probability of being below 90% ($P[\alpha < 0.90] = 0.1$]), an additional 2.3 years of expected 185 lifetime is obtained.

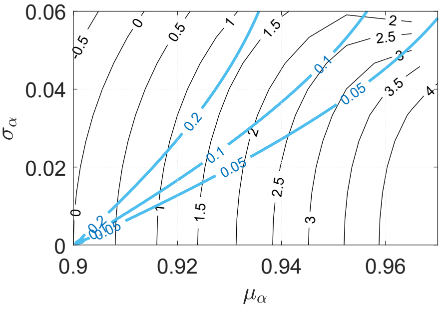

Figure 11: Increased lifetime in years compared to deterministic $\alpha = 0.90$. Blue lines for $P[\alpha < 0.90] \in [0.05, 0.1, 0.2]$.

For comparison, a similar study using a deterministic availability of 85% is shown in Fig. 12. By investigating the isoquant for $P[\alpha < 0.85] = 0.1$ and comparing with Fig. 11, it is clear that there is a slight benefit using the stochastic modelling for lower values of the deterministic availability.

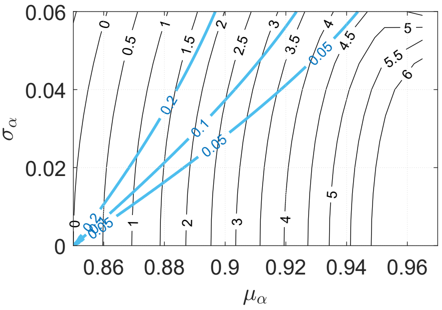

Figure 12: Increased lifetime in years compared to deterministic $\alpha = 0.85$. Blue lines for $P[\alpha < 0.85] \in [0.05, 0.1, 0.2]$.

8. Conclusion

The framework presented in this paper allows for the availability of an offshore wind turbine to be modelled as a stochastic variable, and thus reducing the failure probability and increasing the operational lifetime. An increase of approximately 10% in operational lifetime is proven for the present case if a deterministic availability of 90% is replaced with a beta-distributed availability model using expected availability of 94% and a standard deviation of 4%. In other words, the duration of assumed lost power production using a deterministic availability of 90% can almost be reclaimed by performing a reliability analysis, depending on the distribution of α.

As wind turbines in the same wind farm will most likely experience different downtime portions, the presented approach is useful for preventing unintentional design conservatism. Also, having fatigue response models for the different sub-populations may prove useful for estimates of remaining useful lifetime when using the actual availability from monitoring of the turbines.

Acknowledgement

This work has been carried out at the Centre for Autonomous Marine Operations and Systems (NTNU AMOS). The Norwegian Research Council is acknowledged as the main sponsor of NTNU AMOS. This work was supported by the Research Council of Norway through the Centres of Excellence funding scheme, Project number 223254 - NTNU AMOS.

References

[1] DNV GL, Loads and site conditions for wind turbines, 2016.

[2] J. Velarde, E. E. Bachynski, Design and fatigue analysis of monopile foundations to support the DTU 10 MW offshore wind turbine, Energy Procedia 137 (2017) 3–13. `doi:10.1016/j.egypro.2017.10.330`.
URL `https://doi.org/10.1016/j.egypro.2017.10.330`

[3] S. Schløer, H. Bredmose, H. B. Bingham, The influence of fully nonlinear wave forces on aero-hydro-elastic calculations of monopile wind turbines, Marine Structures 50 (2016) 162–188. `doi:10.1016/j.marstruc.2016.06.004`.

[4] L. Ziegler, S. Voormeeren, S. Schafhirt, M. Muskulus, Sensitivity of Wave Fatigue Loads on Offshore Wind Turbines under Varying Site Conditions, Energy Procedia 80 (2015) 193–200. `doi:10.1016/j.egypro.2015.11.422`.
URL `http://linkinghub.elsevier.com/retrieve/pii/S1876610215021542`

[5] M. I. Kvittem, T. Moan, Frequency Versus Time Domain Fatigue Analysis of a Semi-Submersible Wind Turbine Tower (2014).

[6] D. Zwick, M. Muskulus, Simplified fatigue load assessment in offshore wind turbine structural analysis, Wind Energy 19 (2016) 265–278.

[7] Y. M. Low, A variance reduction technique for long-term fatigue analysis of offshore structures using Monte Carlo simulation, Engineering Structures 128 (2016) 283–295. `doi:10.1016/j.engstruct.2016.09.047`.

[8] DNV GL, PROBAN – General purpose probabilistic analysis program (1996).

[9] J.-T. Horn, J. R. Krokstad, J. Amdahl, Long-Term Fatigue Damage Sensitivity to Wave Directionality in Extra Large Monopile Foundations, Journal of Engineering for the Maritime Environment 232 (2018) 37–49. `doi:10.1177/1475090217727136`.

[10] M. Reistad, Ø. Breivik, H. Haakenstad, O. J. Aarnes, B. R. Furevik, J. R. Bidlot, A high-resolution hindcast of wind and waves for the North Sea, the Norwegian Sea, and the Barents Sea, Journal of Geophysical Research: Oceans 116 (5) (2011) 1–18. `doi:10.1029/2010JC006402`.

[11] J.-T. Horn, E. M. Bitner-Gregersen, J. R. Krokstad, B. J. Leira, J. Amdahl, A new combination of conditional environmental distributions, Applied Ocean Research 73 (2018) 17–26.

[12] C. Bak, F. Zahle, R. Bitsche, A. Yde, L. C. Henriksen, A. Nata, M. H. Hansen, Description of the DTU 10 MW Reference Wind Turbine, Tech. rep., DTU (2013).

[13] E. E. Bachynski, H. Ormberg, Hydrodynamic modeling of large-diameter bottom-fixed offshore wind turbines, in: Proceedings of the ASME 34th International Conference on Ocean, Offshore and Arctic Engineering, ASME, St. Johns, Canada, 2015.

[14] S. H. Sørum, J.-T. Horn, J. Amdahl, Comparison of numerical response predictions for a bottom-fixed offshore wind turbine, Energy Procedia 137 (2017) 89–99. `doi:10.1016/j.egypro.2017.10.336`.

[15] M. O. L. Hansen, Aerodynamics of wind turbines, Second edition, Vol. 9781849770, 2013.
URL `http://dx.doi.org/10.4324/9781849770408`

[16] M. O. L. Hansen, T. Holmås, K. Aas-Jakobsen, J. Amdahl, vpOne - a new FEM based servo-, hydro- and aeroelastic code for wind turbines, in: Offshore Wind Energy, 2009.

[17] W. Popko, F. Vorpahl, A. Zuga, M. Kohlmeier, J. Jonkman, A. Robertson, T. J. Larsen, A. Yde, K. Saetertrø, K. M. Okstad, J. Nichols, T. A. Nygaard, Z. Gao, D. Manolas, K. Kim, Q. Yu, W. Shi, H. Park, A. Vásquez-Rojas, J. Dubois, D. Kaufer, P. Thomassen, M. J. De Ruiter, T. Van Der Zee, J. M. Peeringa, H. Zhiwen, H. Von Waaden, Offshore Code Comparison Collaboration Continuation (OC4), Phase I—Results of Coupled Simulations of an Offshore Wind Turbine with Jacket Support Structure, Journal of Ocean and Wind Energy 1 (1) (2013) 1–11.

[18] J. T. Horn, J. R. Krokstad, J. Amdahl, Hydro-Elastic Contributions to Fatigue Damage on a Large Monopile, Energy Procedia 94 (2016) 102–114.

[19] E. Baekkedal, Alternative methods for realizing the sea spectrum for time-domain simulations of marine structures in irregular seas (2014).

[20] J.-T. H. Horn, Stochastic Dynamic Analysis of Offshore Bottom-Fixed Structures, Tech. rep., NTNU/AMOS (2015).

[21] N. Kelley, B. Jonkman, Overview of the TurbSim stochastic inflow turbulence simulator, Tech. rep. (2007).

[22] GL Garrad Hassan, A Guide to UK Offshore Wind Operations and Maintenance, Tech. rep., Scottish Enterprise and The Crown Estate (2013).

[23] S. Faulstich, B. Hahn, P. J. Tavner, Wind turbine downtime and its importance for offshore deployment, Wind Energy`doi:10.1002/we.421`.

[24] J. Sauvé, R. Rebouças, A. Moura, C. Bartolini, A. Boulmakoul, D. Trastour, Business-driven Decision Support for Change Management: Planning and Scheduling of Changes, in: Proceedings of the 17th IFIP/IEEE International Conference on Distributed Systems: Operations and Management, Springer-Verlag, Berlin, Heidelberg, 2006, pp. 173–184.

[25] M. Abramowitz, I. A. Stegun, Handbook of Mathematical Functions, 1965.

[26] M. N. Scheu, A. Kolios, T. Fischer, F. Brennan, Influence of statistical uncertainty of component reliability estimations on offshore wind farm availability, Reliability Engineering & System Safety (2017) 1–12`doi:10.1016/j.ress.2017.05.021`.

[27] S. D. Downing, D. F. Socie, Simple rainflow counting algorithms, International Journal of Fatigue 4 (1) (1982) 31–40.

[28] DNV GL, RP-C203 Fatigue design of offshore steel structures, 2005.

[29] J. T. Horn, J. J. Jensen, Reducing uncertainty of Monte Carlo estimated fatigue damage in offshore wind turbines using FORM, in: Practical Design of Ships and other Floating Structures - PRADS, Copenhagen, 2016.

[30] D. Zwick, M. Muskulus, The simulation error caused by input loading variability in offshore wind turbine structural analysis, Wind Energy 18 (8). `doi:10.1002/we.1767`.

[31] DNV GL, OS-J101 Design of Offshore Wind Turbine Structures, 2014.

[32] DNV GL, RP-C210 Probabilistic methods for planning of inspection for fatigue cracks in offshore structures, 2015.

[33] H. Madsen, S. Krenk, N. Lind, Methods of Structural Safety, Prentice-Hall, Inc., 1986.

[34] E. Ayala-Uraga, T. Moan, Fatigue reliability-based assessment of welded joints applying consistent fracture mechanics formulations, International Journal of Fatigue 29 (3) (2007) 444–456. `doi:10.1016/j.ijfatigue.2006.05.010`.

[35] K. Nolte, J. Hansford, Closed-Form Expressions for Determining the Fatigue Damage of Structures Due to Ocean Waves, in: Society of Petroleum Engineers Journal, Vol. 17, 1977, pp. 431–440. `doi:10.2118/6250-PA`.

[36] J. D. Sørensen, Reliability assessment of wind turbines, in: 12th International Conference on Applications of Statistics and Probability in Civil Engineering, ICASP12, Vancouver, Canada, 2015.

[37] S. Ambühl, F. Ferri, J. P. Kofoed, J. D. Sørensen, Fatigue reliability and calibration of fatigue design factors of wave energy converters, International Journal of Marine Energy 10 (2015) 17–38. `doi:10.1016/j.ijome.2015.01.004`.

Paper VII

Impact of model uncertainties on the fatigue reliability of offshore wind turbines

Jan-Tore Horn, Jørgen R. Krokstad, and Bernt J. Leira

Marine Structures, 2018

Abstract The impact of environmental load uncertainties on the spatial fatigue reliability of offshore wind turbine foundations is discussed and exemplified. Design procedures are utilizing overall- or partial safety factors to include different model- and statistical uncertainties. Uncertainties in the final design are to a high degree related to decisions taken during the design process, such as; load models, analysis methods and statistical descriptions. Furthermore, to benefit from more elaborate methods, strategies to account for reduced uncertainties by increased knowledge must be adopted. This is especially important for the offshore wind energy industry, where the aim is to produce renewable energy at a competitive cost level. The challenges and consequences of using a detailed design basis are exemplified and discussed through structural reliability analyses. Epistemic load effect uncertainties related to the foundation fatigue will be presented for a detailed wind directional model, wind-wave misalignment, and a second order wave load model. It will be shown that all of these represent important uncertainties to consider during the fatigue design of an offshore wind farm.

Impact of model uncertainties on the fatigue reliability of offshore wind turbines

Jan-Tore Horn[a,b,*], Jørgen R. Krokstad[b], Bernt J. Leira[b]

[a] *Centre for Autonomous Marine Operations and Systems (NTNU AMOS), NTNU, Trondheim, Norway*
[b] *Department of Marine Technology, NTNU, Trondheim, Norway*

Abstract

The impact of environmental load uncertainties on the spatial fatigue reliability of offshore wind turbine foundations is discussed and exemplified. Design procedures are utilizing overall or partial safety factors to include different model- and statistical uncertainties. Uncertainties in the final design are related to decisions taken during the design process, such as; load models, analysis methods and statistical descriptions. Furthermore, to benefit from more elaborate methods, strategies to account for reduced uncertainties by increased knowledge must be adopted. This is especially important for the offshore wind energy industry, where the aim is to produce renewable energy at a competitive cost level. The challenges and consequences of using a detailed design basis are exemplified and discussed through structural reliability analyses. Epistemic load effect uncertainties related to the foundation fatigue will be presented for a detailed wind directional model, wind-wave misalignment, and a second order wave load model. It will be shown that all of these represent important uncertainties to consider during the fatigue design of an offshore wind farm.

Keywords: Offshore wind turbines; reliability; fatigue; misalignment; wave loads; uncertainties; directions

---

1. Introduction

It is important to be aware of design conservatism and lack of knowledge as the offshore wind energy industry is expanding with an increasing number of offshore farms. Several rules and regulations, e.g. [1, 2, 3], have been developed in order to mitigate the risk involved in construction, transport, installation and operation of offshore wind turbines.

Increased accuracy in modelling the environmental loads may both increase and decrease the long term load effects determining the survivability of the structure. For instance, it was demonstrated in [4] that separating between wind sea and swell was beneficial with respect to the foundation fatigue. On the other hand, more detailed wave

---

[*] Corresponding author
Email address: `jan-tore.horn@ntnu.no` (Jan-Tore Horn)

load models may increase loads, and hence the risk of failure, as seen in e.g. [5, 6, 7, 8]. It is then expected that methods beyond state-of-the-art will introduce over-conservatism unless the safety factors are re-calibrated for detailed time-domain analyses.

Safety factors found in guidelines and literature are to be used in combinations with characteristic values of their respective load effects. For instance, the characteristic SN-curve used in fatigue design is defined as the mean value minus two standard deviations [9], in order to ensure conservatism. Then, a characteristic fatigue damage can be found whose value is increased with a design fatigue factor (DFF) to obtain the governing fatigue result. However, safety factors do not consider the dynamic characteristics of the structure in combination with the accuracy of the engineering load models. In other words, a more accurate method, giving higher load amplitudes (or stress ranges), is not automatically rewarded with a lower safety factor.

In order to bypass the use of general safety factors, probabilistic analyses can be performed to document a sufficient level of structural safety. Probabilistic fatigue limit state (FLS) analyses are performed using long term response statistics in combination with uncertainties related to the engineering models, which are accounted for by stochastic variables in the structural reliability analyses (SRA). Relevant literature on general SRA can be found in e.g. [10, 11], where [10] has a relatively pragmatic approach suitable for new readers. In [12], an overview of probabilistic design of wind turbines is presented, including uncertainties related to environmental models and stress calculation. Load effect uncertainties can be a function of available in-situ measurements, as presented in [13]. Further, given a set of load effect- and model uncertainties, safety factors for a given level of reliability can be calculated as demonstrated in e.g. [14].

Uncertainties related to design of offshore wind turbines, may be divided into aleatory and epistemic (see e.g. [15, 16]). Aleatory, or statistical, uncertainties include variation due to the stochastic nature of the wind and wave loading. This include both long-term variation related to temporal weather changes and the short-term randomness of wave elevation and wind gusts. A significant amount of computational efforts to cover all environmental combinations during the 20-25 years of operational lifetime may be required. Second, epistemic, or systematic, uncertainties are related to the engineering models. Here, these are defined as the physical models of and the statistical models of the environmental processes. These uncertainties can be mitigated with high-fidelity models of the physical processes, but also in terms of access to extensive in-situ measurements of the metocean parameters to fit accurate statistical models demonstrated in e.g. [17].

The paper is structured as follows: first, the environmental and numerical model is briefly presented. Second, a model for the spatial fatigue damage used in the reliability analysis is presented. Finally, some cases with increased model accuracies are compared to a state-of-the-art base case analysis to illustrate how the foundation reliability is affected.

2. Environment

Hindcast data for description of the wind and wave environment is provided by the Norwegian Meteorological Institute and the NORA10 database [18] for Dogger Bank. The data contains information about the wind speed, wind direction and significant wave height, peak period, and directions. The data is valid for periods of 3 hour durations and contains information for the previous 60 years. Some of the available parameters are listed in Tab. 1. The amount of available data is sufficient for providing an accurate statistical description of the weather at the chosen site. Discussions regarding the statistical uncertainty of the environment can be found in e.g. [17]. These aleatory uncertainties are not accounted for in this paper, and the environmental model is assumed to reflect the true environment. The environmental joint distribution is then modelled as:

$$f_{\mathbf{X}_e} = f_{\Theta_v} \cdot f_{V|\Theta_v} \cdot f_{H_S|V} \cdot f_{T_P|H_S} \cdot f_{\Theta_r} \tag{1}$$

Details on the the distribution types are given in Tab. 1, but the reader is referred to [17] for details regarding construction of the conditional model, where good resemblance with the hindcast data is demonstrated. Note that the wind-wave misalignment Θ_r, is de-coupled from the wind speed and significant wave height, for simplicity. As seen in [17], this is a reasonable assumption for the site in question. It can be explained by the dynamics of wind direction changes and the inherent inertia of the misalignment angle, which is present for all wind-wave conditions.

Table 1: Marginal distribution types and description of environmental parameters

Parameter		Distribution	Description	Unit
V	v	2-p Weibull	Wind speed at 100 meters	[m/s]
Θ_v	θ_v	von Mises mix	Wind direction at 100 meters	[deg]
H_S	h	3-p Weibull	Significant wave height for wind sea	[m]
T_P	t	Lognormal	Peak period for wind sea spectrum	[m]
Θ_r	θ	Normal	Relative wind-wave direction	[deg]

3. Numerical model

The numerical model represents a bottom-fixed monopile-mounted turbine with tower and rotor-nacelle assembly as described in [19]. The dimensions of the monopile and transition piece can be found in Fig. 1. To maintain a realistic natural period while increasing the overall height of the structure, the tower thickness is increased by 20% [20]. The resulting first fore-aft and side-to-side natural periods are approximately 4.4 seconds, while the periods related to the second vibrational model are about 0.9 seconds in both directions. Consequently, the system is stiff, but still subjected to significant dynamic response from both wind and waves. The controller is an extended version of [21] with the possibility of increasing the fore-aft aerodynamic damping and avoid rotational speeds coinciding with the natural periods of the system. For integration in time-domain and calculation of aerodynamic loads, the finite-element method (FEM) code USFOS/vpOne is used [22, 23, 24], while the hydrodynamic loads are calculated by an external Matlab/Octave routine and imported to the FEM code. The turbulent wind field is created with TurbSim [25] using the Kaimal spectrum and a turbulence intensity of 10%. For a parked/idling turbine, the blades are pitched to 82 degrees relative to the rotor plane, inducing only a slow rotation of the rotor. All fatigue damage results are based on the bending stresses at the mudline for this model.

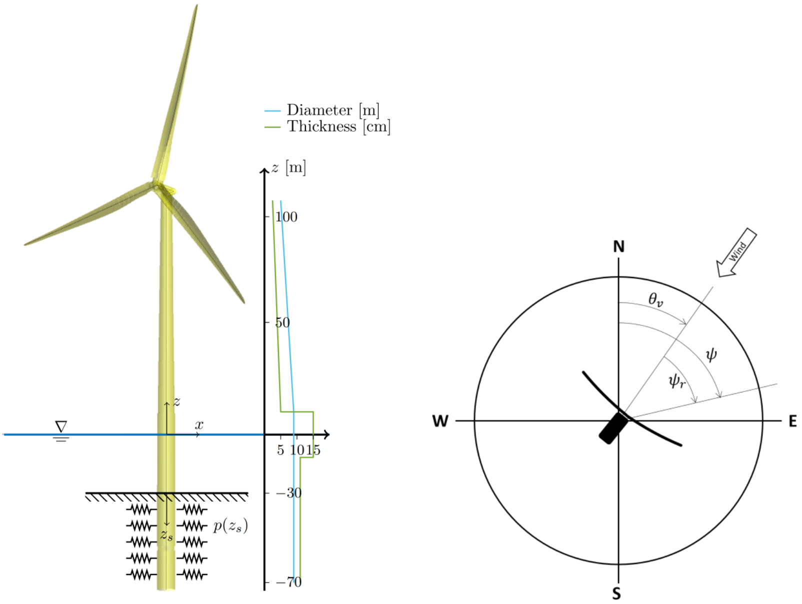

(a) Numerical model with dimensions

(b) Definition of wind direction and location on pile, absolute (ψ) and relative (ψ_r)

Figure 1: Numerical wind turbine model geometry

4. Fatigue limit state

In this section, a novel method for the spatial fatigue reliability of a monopile foundation is presented. The method utilizes the fact that the current foundation is radially symmetric, and assumes uniform soil conditions in all directions.

The failure function for fatigue at a location ψ along the pile circumference, after n years in service is:

$$g(\psi) = \Delta - n\left[\alpha\, d_{op}(\psi) + (1-\alpha)\, d_{id}(\psi)\right] \tag{2}$$

where α is the fraction of the time of which the wind turbine is operational, d_{op} and d_{id} is the expected yearly fatigue damage accumulation for an operational and idling turbine, respectively. Furthermore, Δ is the maximum allowable utilization of the material fatigue life, including uncertainties related to the Palmgren-Miner summation of stress cycles. The probability of failure can then be found by evaluating

$$p_f = P[g \leq 0] \tag{3}$$

by some appropriate reliability method, such as the first- or second order reliability method (FORM/SORM), or Monte Carlo simulations (MCS) [11]. The corresponding reliability index is $\beta = -\Phi^{-1}(p_f)$, where Φ^{-1} is the inverse standard normal cumulative density function (CDF).

The fact that the current wind turbine is considered to be rotationally symmetric, means that one only needs to perform simulations for a single direction, and superposition the results according to the relative direction: $\psi_r = \psi - \theta_v$. Hence the fatigue damage at ψ can be found as:

$$d(\psi) = \int_v \int_{\theta_v} d(\psi_r|v)\, f_{V,\Theta_v}(v, \theta_v)\, d\theta_v\, dv \tag{4}$$

where $d(\psi_r|v)$ is the fatigue damage during operation or idling at ψ_r given the wind speed v. The total fatigue damage is then found by integrating over all wind speeds and directions along with the probability density function f_{V,Θ_v}. Further, is can be shown that the fatigue damage can be expressed in terms of a closed form solution as [26, 27]:

$$\begin{aligned} d(\psi_r|v) =& \nu\, T \left\{ \frac{[\, a\, X_M\, X_L\, (t/t_{\mathrm{ref}})^k\,]^{m_1}}{K_1} \Gamma \left[1 + \frac{m_1}{b}, \left(\frac{\Delta\sigma_0}{a} \right)^b \right] \right. \\ &+ \left. \frac{[\, a\, X_M\, X_L\, (t/t_{\mathrm{ref}})^k\,]^{m_2}}{K_2} \gamma \left[1 + \frac{m_2}{b}, \left(\frac{\Delta\sigma_0}{a} \right)^b \right] \right\} \end{aligned} \tag{5}$$

when the stress range is Weibull distributed with scale parameter $a = a(\psi_r, v)$ and shape parameter $b = b(\psi_r, v)$. The remaining parameters are; average number of stress cycles $\nu = \nu(\psi_r, v)$, pile thickness t, stress calculation uncertainty in the numerical model X_M, and load effect uncertainty X_L. Furthermore, $\Delta\sigma_0$, K_i and m_i are material parameters related to the SN-curve, and k and t_{ref} are parameters to account for actual plate thickness. All parameters are listed in Tab. 1. The stress range distribution includes uncertainties related to the significant wave height and peak period for a given wind speed, which is found by evaluating

$$\Delta\sigma(\psi_r, v) = \int_h \int_t \Delta\sigma(\psi_r, v|h, t)\, f_{H_S,T_P}(h, t)\, dt\, dh \tag{6}$$

using Monte Carlo simulations until the scale and shape parameters (a and b) for each wind speed has met the convergence criteria, a coefficient-of-variance (CoV) less than 0.05 is chosen in this case. An example of statistical uncertainty related to the number of simulations can be found in e.g. [28] when using a response surface method. As a result, there are some statistical uncertainties related to the Weibull parameters, which are neglected in the present study to limit the scope. Example Weibull fits are shown in Fig. 2, where a 2-parameter Weibull distribution is fitted to the distribution tail using two fitting points in the upper range of the data. It was observed that the fatigue damage error computed using the fitted Weibull stress range and direct evaluation of the Palmgren-Miner was less than 5% in all cases. For fatigue calculations, it is important that the stress range representation is correct for the stress ranges contributing the most to the total fatigue. As indicated in Fig. 3, the fatigue damage derived from approximately $\Delta\sigma > 10$ [MPa] or $\log \Delta\sigma > 2.3$ is dominating, meaning that the Weibull fit should be accurate in this range. Also, note that there is a very small contribution from the low-cycle part of the SN-curve ($\Delta\sigma > \Delta\sigma_0$). It is assumed that the 2-parameter

Weibull with tail weighting is sufficient in all present cases to satisfy this requirement, although a 3-parameter Weibull may yield even more accurate results. The advantage with 2-parameter Weibull is the closed-form solution to the Palmgren-Miner summation as presented in Eq. (5).

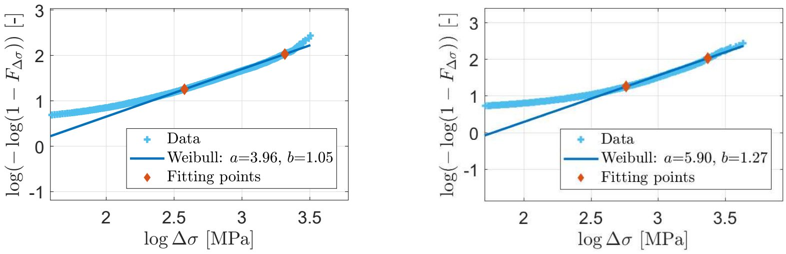

(a) Wind speed of 14m/s and misalignment angle of 0 degrees

(b) Wind speed of 20m/s and misalignment angle of -40 degrees

Figure 2: Example stress range distributions with Weibull fits in the tail, for the critical location on the pile circumference for operational turbine

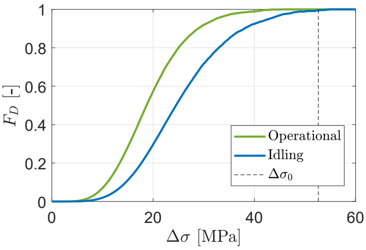

Figure 3: Cumulative fatigue damage contribution from stress ranges for an operational and idling turbine. The stress limit Δs_0 for the two-slope SN-curve is shown.

The scale and shape parameters are then found as a function of wind speed and relative pile location as shown in Fig. 4 and 5 for operational and idling turbine, respectively. It is suggested that an exponential response surface is used:

$$a(\psi_r, v) = \frac{\exp(p_0 + p_1\,v + p_2\,v^2)}{1 + p_3\,(v - v_0)^2} \cdot (\cos 2\psi_r + 1) + \exp(p_4 + p_5\,v) \tag{7}$$

for a and the ratio a/b with fitting parameters $p_{0,\ldots,5}$ and a dominating wind speed v_0 to account for additional excitation at the wind speed where resonance is most likely. The fitting function is strictly positive, differentiable, and periodic with respect to relative location ψ_r. It was proven to be well-suited for representing the Weibull parameters of the stress ranges as function of wind speed and relative pile location. Final fitting constants can be found in Tab. 3. Note that a similar expression will not be used for the zero-crossing frequency ν, which will be treated as an independent variable due to relatively small changes in terms of V and ψ_r. Instead, the zero-crossing frequency for operational (ν_{op}) and idling (ν_{id}) turbine can be found in Tab. 2, derived from Fig. 4c and 5c, respectively. The procedure for obtaining the response surface in the (v, ψ_r)-domain is summed up in the flowchart in Fig. 6.

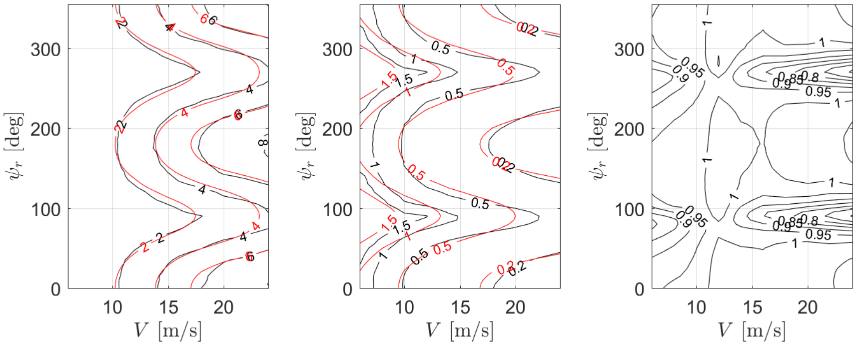

(a) $a(\psi_r, v)$

(b) $b(\psi_r, v)/a(\psi_r, v)$

(c) $\nu(\psi_r, v)$

Figure 4: Response contours for operational turbine in co-directional sea. Result from MCS in the full environmental domain by Eq. (6) in black and periodic surface fit in red.

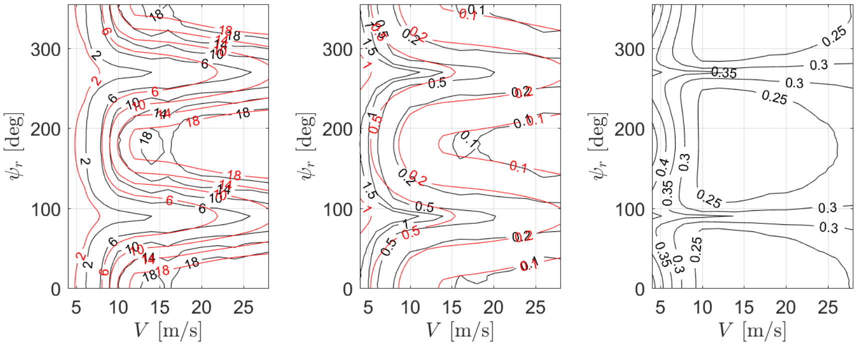

(a) $a(\psi_r, v)$ (b) $b(\psi_r, v)/a(\psi_r, v)$ (c) $\nu(\psi_r, v)$

Figure 5: Response contours for idle turbine in co-directional sea. Result from MCS in the full environmental domain by Eq. (6) in black and surface fit in red.

Variable	Distribution	Expected value	Standard deviation
Δ	Lognormal	1	0.3
α	Beta	0.94	0.04
$\Delta\sigma_0$	Fixed	52.63	-
m_1	Fixed	3	-
m_2	Fixed	5	-
$\log K_1$	Normal	12.164	0.2
$\log K_2$	Normal	16.106	0.2
X_M	Lognormal	1.0	0.1
$X_{L,a}$	Lognormal	1.0	0.03
$X_{L,h}$	Fixed	1.0	-
ν_{id}	Lognormal	0.27	0.05
ν_{op}	Lognormal	0.96	0.06
t	Fixed	0.11	-
t_{ref}	Fixed	0.025	-
k	Fixed	0.2	-

Table 2: Stochastic variables for the base case probabilistic analysis in FLS.

Table 3: Fitting constants

Turbine state	Parameter	p_0	p_1	p_2	p_3	p_4	p_5	v_0
Operational	a	-5.12	0.600	-1.51	0.00	-1.42	0.121	10
Operational	a/b	-3.09	0.370	-0.890	0.00	-1.36	0.103	10
Idling	a	-3.0	0.57	-0.94	0.12	0.083	0.078	10
Idling	a/b	-1.5	0.29	-0.34	0.036	-0.37	0.069	10

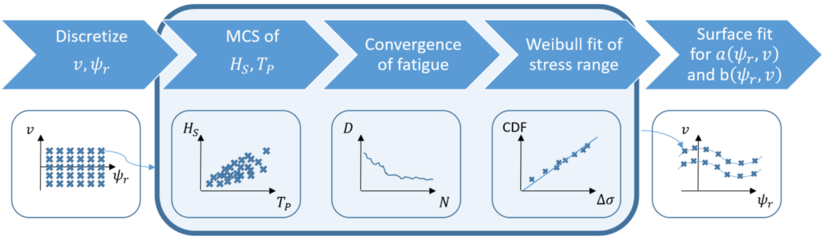

Figure 6: Steps to obtain the response surface used in the present fatigue reliability methodology

5. Case studies

Three case studies will be presented with respect to the impact on fatigue reliability; wind directional model, wind-wave misalignment and wave load effect.

5.1. Base case

The base case contains the uncertainties in Tab. 2, no wind-wave misalignment, linear wave theory, and independent wind speed and direction:

$$f_{V,\Theta_v} = f_V \cdot f_{\Theta_v} \tag{8}$$

5.2. Uncertainty in wind speed and -direction

When modelling the joint wind speed and wind direction, two approaches are possible as illustrated in Fig. 7. Either the Weibull parameters describing the wind speed distribution is dependent on the wind direction as in Fig. 7a, or the wind directional distribution is dependent on the wind speed as illustrated in Fig. 7b. The latter description is elaborated on in [17]. For the present case, the wind speed distribution is modelled as dependent on the direction, so that:

$$f_{V,\Theta_v} = f_{V|\Theta_v} \cdot f_{\Theta_v} \tag{9}$$

Hence, the Fourier fit of the scale and shape parameter as shown in Fig. 7a is used, combined with the marginal wind directional distribution, which is the red curve in Fig. 7b.

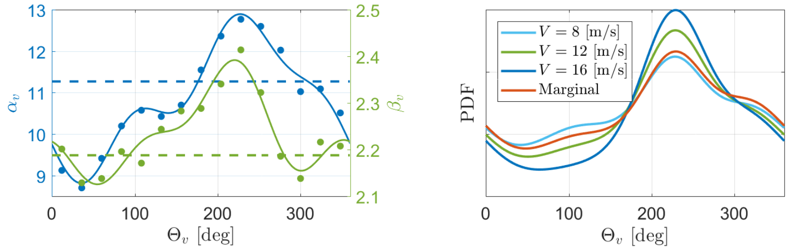

(a) Wind speed Weibull parameters as function of wind direction with Fourier fit (solid), compared to marginal values (dashed)

(b) Wind directional distribution for different wind speeds using a mixed von Mises distribution [17].

Figure 7: Dependency between wind speed and wind direction

The effect on the reliability when solving Eq. (3) using Monte Carlo simulations (MCS) is shown in Fig. 8. It is clear that the wind directional model does not affect the average reliability on the pile circumference, but since high wind speeds are more likely to originate from the south-west, a fatigue damage concentration is found at approximately $\psi = 50$ and $\psi = 230$ degrees. The difference from the base case at $\psi = 230$ corresponds to about 2 years of operational lifetime, meaning that the fatigue life calculated using decoupled wind speed and direction is non-conservative. Consequently, one must consider the multi-directionality of the metocean conditions as required in [3], but also with the distribution parameters as functions of the wind direction. Otherwise, an additional safety factor should be applied, calibrated to approximately $1 + 2/25 = 1.08$ in this specific case.

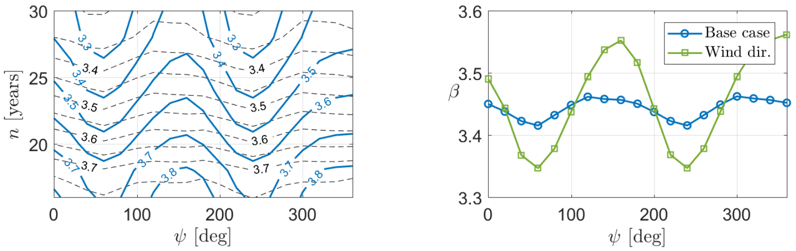

(a) Reliability index as function of years in operation and location on pile. Base case in dashed for comparison.

(b) Reliability index for 25 years in operation

Figure 8: Effect on reliability index when introducing dependency between wind speed and direction.

5.3. Uncertainty in the load effect induced by misalignment

Here, the fatigue damage uncertainty, or reliability, due to the wind-wave misalignment is presented. As illustrated in Fig. 9a, the fatigue damage increases approximately with the square of the misalignment angle. Interestingly, the effect is larger to one side due to the directionally dependent damping induced by the rotation of the rotor [4]. In Fig. 9b, the fatigue damage is weighted according to the probability of occurrence, described by the marginal distribution of wind speed and misalignment angle. Not surprisingly, misalignment will contribute significantly to the estimated fatigue, as we also can see from the reliability estimate later on.

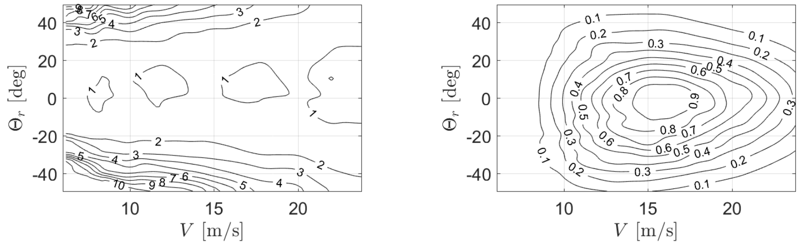

(a) Contours of fatigue normalized for each wind speed

(b) Contours of fatigue damage weighted according to joint probability of wind speed and misalignment angle

Figure 9: Effect of misalignment on the maximum fatigue damage around the pile circumference.

To account for the effect of wind-wave misalignment on the stress range along the pile circumference, some corrections are made to Eq. (7):

$$\begin{aligned} a_{mis}(\psi_r, v, \theta_r) = & \frac{\exp(p_0 + p_1\, v + p_2\, v^2)}{1 + p_3\,(v - v_0)^2} \cdot (\gamma_a(v, \theta_r)\, \cos 2(\psi_r - \psi_r^c) + 1) \\ & + \gamma_c(v, \theta_r)\, \exp(p_4 + p_5\, v) \end{aligned} \tag{10}$$

where ψ_r^c is the phase-shift of the most critical fatigue damage location on the pile due to increasing transverse motions. A regression analysis is shown in Fig. 10b, which includes all wind speeds. Note that as the misalignment angle increases, the location accumulating the most fatigue damage is shifting even further, meaning that the turbine is vibrating more sideways than what is expected when only considering the misalignment angle. Furthermore, γ_a is to correct for the amplitude increase ($d_M - d_m$) as illustrated in Fig. 10a, and γ_c is accounting for the increase in average fatigue, μ_d. There are more differences than change in amplitude and mean value, which are neglected in this study to keep Eq. (10) fairly simple. A two-step procedure is performed for the fitting procedure, to obtain a reasonable fit with limited data. First, Eq. (7) is fitted for the zero-misalignment cases. Second, the corrections to the stress amplitude and mean are fitted to the following equation:

$$\gamma(v, \theta_r) = p_1\, \sin^{p_2}(\theta_r - p_3) + 1 \tag{11}$$

which is periodic, with maximum value for $\theta_r = p_3 + \pi/2$. In this case, a total of 100 10-minute simulations are performed for each combination of v and θ_r, including variations in H_S and T_P by Eq. (6). The resulting parameters can be found in Tab. 4 as functions of the wind speed.

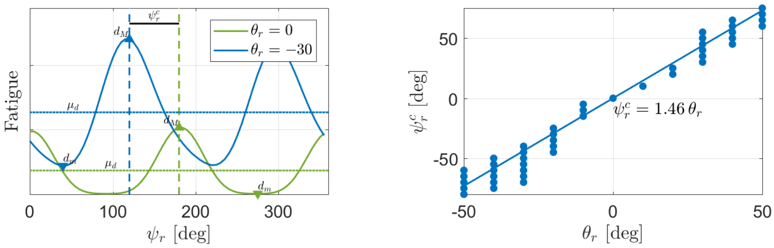

(a) Circumferential fatigue distribution for a single wind speed for two different misalignment angles. The means (μ_d), peaks (d_M), troughs (d_m) and angular correction (ψ_r^c) is shown.

(b) Correlation between misalignment angle and the circumferential location of maximum fatigue damage with fitted linear regression function

Figure 10: Effects of wind-wave misalignment

Table 4: Misalignment correction parameters as function of wind speed

Parameter	p_1	p_2	p_3
γ_a	$3.24\ \exp(-0.069\,v)$	4	$1.09\ \exp(0.085\,v)$
γ_c	$1.84\ \exp(-0.062\,v)$	2	$1.75\ \exp(0.067\,v)$

The results in Fig. 11 show that the misalignment is a significant contributor to the foundation reliability with the present formulations. Figure 11a, shows that a turbine subjected to misalignment conditions during its lifetime, will have an expected lifetime of approximately 7 years less compared to a turbine only operating in co-directional sea. In Fig. 11b, the circumferential fatigue reliability after 25 years in operation is shown, indicating a significant change in the reliability index when accounting for misalignment, both in magnitude and how the fatigue distributes over the circumference.

From this study, a partial safety factor can be derived regarding uncertainty in load effects from misalignment. Assuming that the base case represents a design fatigue analysis, and a reliability index of 3.4 is the reference for 25 years, a case-specific partial safety factor of $1 + 7/25 = 1.28$ must be applied to the case with co-directional sea to reflect the increased fatigue accumulation.

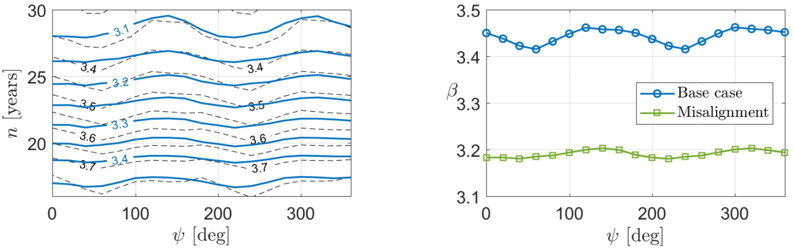

(a) Reliability index as function of years in operation and location on pile. Base case in dashed.

(b) Reliability index for 25 years in operation

Figure 11: Effect of misalignment on the foundation fatigue reliability index.

5.4. Uncertainty in wave loads

The final case study is related to the impact of higher order wave loads on the fatigue of the foundation. Several previous studies have concluded that second or higher order loads will have little impact on the design fatigue in the foundation and tower, see e.g. [5, 6]. While others show that non-linear loads can potentially reduce the lifetime significantly [29, 30]. This section studies the structural reliability impact of a second order load model compared to linear wave loads on the foundation fatigue damage.

In [31], investigations were made on the fatigue sensitivity to wave kinematics models and coefficients in the Morison equation [32] used for applying the wave loads. Further, [33] performed a sensitivity study on the fatigue where the MacCamy and Fuchs [34] load model was used to account for linear diffraction, including a frequently used second order kinematics model [35, 36] without any correction for diffraction forces. The studies are limited to a few sea states and little variation in the significant wave height and peak period for each wind speed. To the authors knowledge, no comprehensive studies have been performed accounting for the statistical uncertainty of the steepness of the sea state for a given wind speed, which is important for the magnitude of the higher order loading [37]. Also, no previous study has included the second order diffraction terms in relation to the wave load uncertainty, which may be of importance, depending on the size of the monopile [38], damping level and the modal shapes of the structure.

Here, the panel code Wamit is used for generating wave loads. For first order loads, the resulting pressure on the foundation can be found with:

$$p^{(1)}(z,t) = \mathcal{R}\left\{ \sum_j \zeta_{a,j} \sum_i n_{x,i}\, A_i\, p^{(1)}_{i,j}(z)\, e^{i\omega_j\, t - i\epsilon_j} \right\} \tag{12}$$

where $p_{i,j}$ represent the pressure at panel i due the the excitation frequency ω_j. Furthermore, A_i is the panel area, $n_{x,i}$ is the vector normal to the panel, and $\zeta_{a,j}$ is the wave amplitude corresponding to frequency ω_j, generated using the JONSWAP spectrum with default peak shape parameter [39]. The first order loads are calculated to the mean surface and no surface effects from wave elevation is present. The outer summation can be evaluated efficiently by using an inverse fast Fourier transform (FFT) [40]. For the second order sum-frequency force, a similar approach is used. The pressure due to sum-frequency components is then:

$$p^{+}(z,t) = \mathcal{R}\left\{ \sum_{k} \sum_{j} \zeta_{a,j}\, \zeta_{a,k} \sum_{i} n_{x,i}\, A_i\, p^{+}_{i,j,k}(z)\, e^{i(\omega_j+\omega_k)\,t}\, e^{-i(\epsilon_j+\epsilon_k)} \right\} \tag{13}$$

where the two outer summations can be evaluated efficiently with a two-dimensional inverse FFT as in e.g. [41]. The second order pressure is then found as:

$$p(z) = \begin{cases} p^{(1)}(z) + p^{+}(z) & \text{if } -h < z \leq 0 \\ p^{(1)}(0) & \text{if } 0 < z \leq \eta \end{cases} \tag{14}$$

for the first order surface elevation η. The horizontal force is then consistent to the second order, including the second order contribution from the surface elevation (see e.q. [6]).

In order to estimate the impact of uncertainty of wave-induced load effects on the foundation fatigue, the uncertainty introduced in the stress range in the foundation must be assessed. This is done in a similar manner as in [29], finding the load effect uncertainty as the ratio of the damage equivalent loads (DEL) between identical runs with non-linear and linear wave load model. The DEL is taken as the fatigue damage obtained from the rainflow-counted stress range at the mudline for zero misalignment $\Delta\sigma_y$. It is expected that this is a conservative measure for the load effect uncertainty on the pile circumference. Note that no further changes are made to the response surface presented in Section 4. After simplifying the expression by removing constant material parameters, the wave load uncertainty can be expressed as:

$$X_{L,h} = \frac{\left(\frac{1}{N}\sum_{i=1}^{N} \Delta\sigma_{y,NL,i}^{m_2}\right)^{1/m_2}}{\left(\frac{1}{N}\sum_{i=1}^{N} \Delta\sigma_{y,L,i}^{m_2}\right)^{1/m_2}} \tag{15}$$

where NL denotes non-linear loads with sum-frequency panel pressures and L is linear wave loading. Furthermore, $m_2 = 5$ is the material parameter for the high-cycle part of the SN-curve, which is dominating in this case. Due to significant aerodynamic damping from the large rotor during operation (demonstrated in [4]) and interaction between aerodynamic and hydrodynamic load effects, the load effect uncertainty must be found for operational and idling states of the turbine separately. Due to the higher possibility of transient responses during the low damped state for an idling turbine, the load effect uncertainty is larger for an idling turbine. In Fig. 12, the wave load effect uncertainty for an operational turbine is visualized as a function of H_S and T_P using the expected wind speed, while the uncertainty for an idling turbine is found in Fig. 13. By utilizing the statistical dependency between wind speed, significant wave height and peak period, the wave load effect uncertainty is re-sampled to a function of wind speed only, which is given in Fig. 14. Clearly, the uncertainty increases for an idling turbine. The functions given in Fig. 14 replaces the default mean and standard deviation of $X_{L,h}$ in Tab. 2.

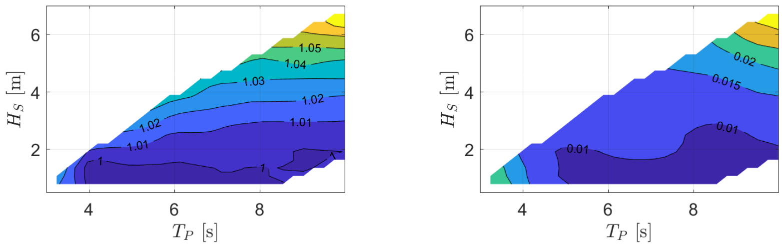

(a) Mean (b) Standard deviation

Figure 12: Wave load effect uncertainty for operational turbine for most likely T_P-values in $4 < V < 25$.

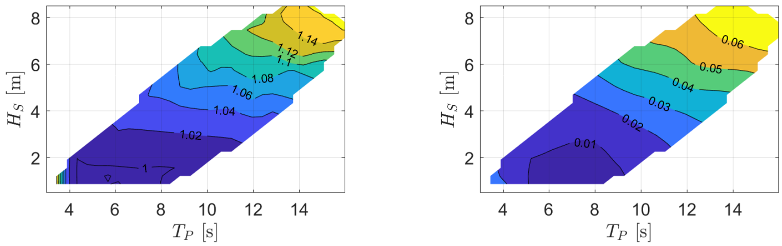

(a) Mean (b) Standard deviation

Figure 13: Wave load effect uncertainty for idling turbine

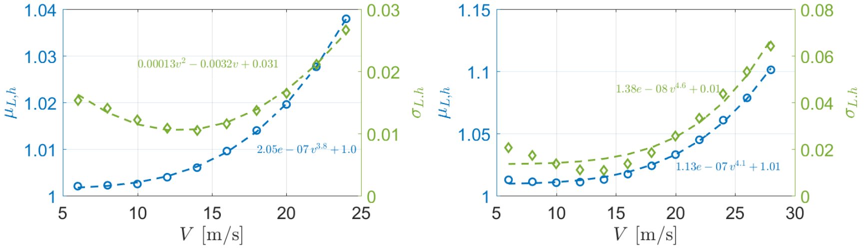

(a) Operational turbine (b) Idling turbine

Figure 14: Wave load effect uncertainty as function of wind speed with fitted curves. Mean value in blue on the left axis and standard deviation in green on the right axis.

The resulting reliability, with and without accounting for the uncertainty in the wave load model, is shown in Fig. 15. A lifetime reduction of approximately 5 years is found when using the second order load model compared to the linear wave load model, indicating a case-specific partial safety factor of approximately 1.2. The second order wave loading results in a more wide-band loading characteristics, increasing the number of high-frequency stress ranges around the natural frequency. Of course, these results would depend on the dynamic properties of the monopile, and is expected to increase for a softer design, i.e. higher natural period for the first vibrational mode.

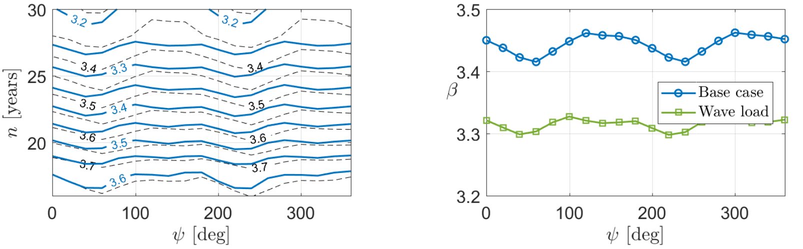

(a) Reliability index as function of years in operation and location on pile. Base case in dashed.

(b) Reliability index for 25 years in operation

Figure 15: Effect of wave load effect uncertainty on the foundation reliability index.

5.5. *All combined*

In Fig. 16a, all the above uncertainties are accounted for and compared to the base case. By comparing the isoquants for e.g. $\beta = 3.3$, a reduced lifetime of about 10 years is observed, which can be translated to an indicative, case-specific safety factor of $1 + 10/25 = 1.4$. The importance of the wind directional model on the critical fatigue reliability is shown in Fig. 16b, where a significant decrease in the reliability index is observed at $\psi = 60$ and 240 degrees.

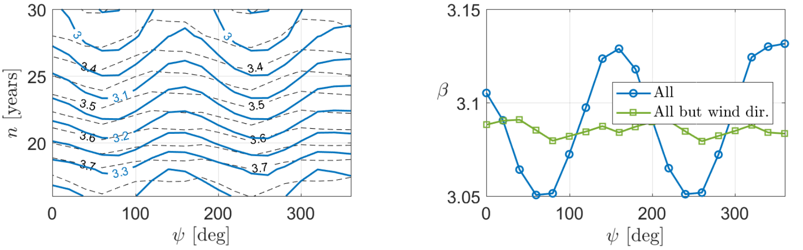

(a) Reliability index as function of years in operation and location on pile. Base case in dashed.

(b) Reliability index for 25 years in operation for all considered uncertainties, with and without wind direction and speed coupling.

Figure 16: Effect of all presented load effect uncertainties on the foundation reliability index.

6. Conclusions

All presented models are believed to represent the reality in a better way than current state-of-the-art models, and all have shown to reduce the structural reliability. It was found that wind-wave misalignment has a significant negative impact on the fatigue life due to dynamic effects. Some indicative, case-specific safety factors that describe the difference between the base case and the higher fidelity case have been found. Although these are only qualitative factors to illustrate the potential over-conservatism, it is clear that the reduced uncertainty in high-fidelity models requires a re-calibration of safety factors in order to be beneficial for the designer. Calibrating new safety factors for bottom-fixed offshore wind turbines may be very elaborate and will require a complete reliability study with time-domain methods like presented in this paper. However, the upside in terms of reduced conservatism will likely justify the investment in computational resources, which easily can be scaled by cloud solutions.

Some limitations in this study include a simplified model for the impact of misalignment of the circumferentially distributed fatigue, and a wave load effect uncertainty independent of the wind-wave misalignment which may be of importance as also noted in [30]. Additionally, the model uncertainty due to soil conditions should be considered in future work, as the soil characteristics may alter the dynamic properties of the system significantly.

Acknowledgement

This work has been carried out at the Centre for Autonomous Marine Operations and Systems (NTNU AMOS). The Norwegian Research Council is acknowledged as the main sponsor of NTNU AMOS. This work was supported by the Research Council of Norway through the Centres of Excellence funding scheme, Project number 223254 - NTNU AMOS.

References

[1] International Electrotechnical Commission, IEC 61400-3, Wind turbinesPart 3: design requirements for offshore wind turbines, Tech. rep. (2009).

[2] DNV GL, Support structures for wind turbines, 2016.

[3] DNV GL, Loads and site conditions for wind turbines, 2016.

[4] J.-T. Horn, J. R. Krokstad, J. Amdahl, Long-Term Fatigue Damage Sensitivity to Wave Directionality in Extra Large Monopile Foundations, Journal of Engineering for the Maritime Environment 232 (2018) 37–49. `doi:10.1177/1475090217727136`.

[5] S. Schløer, H. Bredmose, H. B. Bingham, The influence of fully nonlinear wave forces on aero-hydro-elastic calculations of monopile wind turbines, Marine Structures 50 (2016) 162–188. `doi:10.1016/j.marstruc.2016.06.004`.

[6] J. T. Horn, J. R. Krokstad, J. Amdahl, Hydro-Elastic Contributions to Fatigue Damage on a Large Monopile, Energy Procedia 94 (2016) 102–114.

[7] P. Agarwal, L. Manuel, Incorporating irregular nonlinear waves in coupled simulation and reliability studies of offshore wind turbines, Applied Ocean Research 33 (3) (2011) 215–227. `doi:10.1016/j.apor.2011.02.001`.

[8] M. Moarefzadeh, R. Melchers, Nonlinear wave theory in reliability analysis of offshore structures, Probabilistic Engineering Mechanics 21 (2) (2006) 99–111. `doi:10.1016/j.probengmech.2005.04.002`.

[9] DNV GL, RP-C203 Fatigue design of offshore steel structures, 2005.

[10] P. Toft-Christensen, Y. Murotsu, Application of Structural Systems Reliability Theory, Springer, 1986.

[11] H. Madsen, S. Krenk, N. Lind, Methods of Structural Safety, Prentice-Hall, Inc., 1986.

[12] J. D. Sørensen, H. S. Toft, Probabilistic Design of Wind Turbines, Energies 3 (2) (2010) 241–257. `doi:10.3390/en3020241`.

[13] S. Ambühl, F. Ferri, J. P. Kofoed, J. D. Sørensen, Fatigue reliability and calibration of fatigue design factors of wave energy converters, International Journal of Marine Energy 10 (2015) 17–38. `doi:10.1016/j.ijome.2015.01.004`.

[14] S. Marquez-Dominguez, J. D. Sorensen, Fatigue Reliability and Calibration of Fatigue Design Factors for Offshore Wind Turbines, Energies 5 (6) (2012) 1816–1834. `doi:10.3390/en5061816`.

[15] M. H. Faber, On the Treatment of Uncertainties and Probabilities in Engineering Decision Analysis, Journal of Offshore Mechanics and Arctic Engineering 127 (3) (2005) 243–248.

[16] M. Paté-Cornell, Uncertainties in risk analysis: Six levels of treatment, Reliability Engineering & System Safety 54 (2) (1996) 95–111. `doi:https://doi.org/10.1016/S0951-8320(96)00067-1`.

[17] J.-T. Horn, E. M. Bitner-Gregersen, J. R. Krokstad, B. J. Leira, J. Amdahl, A new combination of conditional environmental distributions, Applied Ocean Research 73 (2018) 17–26.

[18] M. Reistad, Ø. Breivik, H. Haakenstad, O. J. Aarnes, B. R. Furevik, J. R. Bidlot, A high-resolution hindcast of wind and waves for the North Sea, the Norwegian Sea, and the Barents Sea, Journal of Geophysical Research: Oceans 116 (5) (2011) 1–18. `doi:10.1029/2010JC006402`.

[19] C. Bak, F. Zahle, R. Bitsche, A. Yde, L. C. Henriksen, A. Nata, M. H. Hansen, Description of the DTU 10 MW Reference Wind Turbine, Tech. rep., DTU (2013).

[20] E. E. Bachynski, H. Ormberg, Hydrodynamic modeling of large-diameter bottom-fixed offshore wind turbines, in: Proceedings of the ASME 34th International Conference on Ocean, Offshore and Arctic Engineering, ASME, St. Johns, Canada, 2015.

[21] M. H. Hansen, L. C. Henriksen, M. Hartvig, L. Christian, Basic DTU Wind Energy Controller, no. January, 2013.

[22] M. O. L. Hansen, T. Holmås, K. Aas-Jakobsen, J. Amdahl, vpOne - a new FEM based servo-, hydro- and aeroelastic code for wind turbines, in: Offshore Wind Energy, 2009.

[23] S. H. Sørum, J.-T. Horn, J. Amdahl, Comparison of numerical response predictions for a bottom-fixed o ff shore wind turbine, Energy Procedia.

[24] W. Popko, F. Vorpahl, A. Zuga, M. Kohlmeier, J. Jonkman, A. Robertson, T. J. Larsen, A. Yde, K. Saetertrø, K. M. Okstad, J. Nichols, T. A. Nygaard, Z. Gao, D. Manolas, K. Kim, Q. Yu, W. Shi, H. Park, A. Vásquez-Rojas, J. Dubois, D. Kaufer, P. Thomassen, M. J. De Ruiter, T. Van Der Zee, J. M. Peeringa, H. Zhiwen, H. Von Waaden, Offshore Code Comparison Collaboration Continuation (OC4), Phase IResults of Coupled Simulations of an Offshore Wind Turbine with Jacket Support Structure, Journal of Ocean and Wind Energy 1 (1) (2013) 1–11.

[25] N. Kelley, B. Jonkman, Overview of the TurbSim stochastic inflow turbulence simulator, Tech. rep. (2007).

[26] K. Nolte, J. Hansford, Closed-Form Expressions for Determining the Fatigue Damage of Structures Due to Ocean Waves, in: Society of Petroleum Engineers Journal, Vol. 17, 1977, pp. 431–440. `doi:10.2118/6250-PA`.

[27] E. Ayala-Uraga, T. Moan, Fatigue reliability-based assessment of welded joints applying consistent fracture mechanics formulations, International Journal of Fatigue 29 (3) (2007) 444–456. `doi:10.1016/j.ijfatigue.2006.05.010`.

[28] H. S. Toft, L. Svenningsen, W. Moser, J. D. Sørensen, M. L. Thøgersen, Assessment of wind turbine structural integrity using response surface methodology, Engineering Structures 106 (2016) 471–483. `doi:10.1016/j.engstruct.2015.10.043`.

[29] L. Colone, A. Natarajan, N. Dimitrov, Impact of turbulence induced loads and wave kinematic models on fatigue reliability estimates of o ff shore wind turbine monopiles, Ocean Engineering 155 (2018) 295–309. `doi:10.1016/j.oceaneng.2018.02.045`.

[30] E. Marino, A. Giusti, L. Manuel, Offshore wind turbine fatigue loads: The influence of alternative wave modeling for different turbulent and mean winds, Renewable Energy 102. `doi:10.1016/j.renene.2016.10.023`.

[31] H. F. Veldkamp, J. van der Tempel, Influence of wave modelling on the prediction of fatigue for offshore wind turbines, Wind Energy 8 (1) (2004) 49–65. `doi:10.1002/we.138`.

[32] J. Morison, J. Johnson, S. Schaaf, The Force Exerted by Surface Waves on Piles, Journal of Petroleum Technology 2 (05) (1950) 149–154. `doi:10.2118/950149-G`.

[33] M. B. V. D. Meulen, T. Ashuri, G. J. W. V. Bussel, D. P. Molenaar, Influence of Nonlinear Irregular Waves on the Fatigue Loads of an Offshore Wind Turbine, The Science of Making Torque from Wind

(2012) 1–10doi:10.13140/2.1.3034.5606.

[34] R. C. MacCamy, R. A. Fuchs, Wave Forces on Piles: A Diffraction Theory (1954).

[35] N. Sharma, R. G. Dean, Second-Order Directional Seas and Associated Wave Forces, Society of Petroleum Engineers Journal (February) (1981) 129–140.

[36] J. N. Sharma, R. G. Dean, Contributions to second order directional sea simulation and wave forces, in: Proceedings of the International Conference on Offshore Mechanics and Arctic Engineering - OMAE, Vol. 5, San Diego, CA, 2007, pp. 361–370. doi:10.1115/OMAE2007-29634.

[37] G. Z. Forristall, Wave crest distributions: Observations and second-order theory, Journal of Physical Oceanography 30 (8) (2000) 1931–1943.

[38] R. Eatock Taylor, S. M. Hung, Second order diffraction forces on a vertical cylinder in regular waves., Appl. Ocean Res. 9 (1 , Jan. 1987) (1987) 19–30. doi:10.1016/0141-1187(87)90028-9.

[39] DNV GL, RP-C205 Environmental conditions and environmental loads, Tech. rep. (2017).

[40] M. Tucker, P. Challenor, D. Carter, Numerical simulation of a random sea: a common error and its effect upon wave group statistics, Applied Ocean Research 6 (2) (1984) 118–122. doi:10.1016/0141-1187(84)90050-6.

[41] X. Y. Zheng, T. Moan, S. T. Quek, Numerical simulation of non-Gaussian wave elevation and kinematics based on two-dimensional fourier transform (2006) 1–6.

Previous PhD theses published at the Department of Marine Technology
(earlier: Faculty of Marine Technology)
NORWEGIAN UNIVERSITY OF SCIENCE AND TECHNOLOGY

Report No.	Author	Title
	Kavlie, Dag	Optimization of Plane Elastic Grillages, 1967
	Hansen, Hans R.	Man-Machine Communication and Data-Storage Methods in Ship Structural Design, 1971
	Gisvold, Kaare M.	A Method for non-linear mixed -integer programming and its Application to Design Problems, 1971
	Lund, Sverre	Tanker Frame Optimalization by means of SUMT-Transformation and Behaviour Models, 1971
	Vinje, Tor	On Vibration of Spherical Shells Interacting with Fluid, 1972
	Lorentz, Jan D.	Tank Arrangement for Crude Oil Carriers in Accordance with the new Anti-Pollution Regulations, 1975
	Carlsen, Carl A.	Computer-Aided Design of Tanker Structures, 1975
	Larsen, Carl M.	Static and Dynamic Analysis of Offshore Pipelines during Installation, 1976
UR-79-01	Brigt Hatlestad, MK	The finite element method used in a fatigue evaluation of fixed offshore platforms. (Dr.Ing. Thesis)
UR-79-02	Erik Pettersen, MK	Analysis and design of cellular structures. (Dr.Ing. Thesis)
UR-79-03	Sverre Valsgård, MK	Finite difference and finite element methods applied to nonlinear analysis of plated structures. (Dr.Ing. Thesis)
UR-79-04	Nils T. Nordsve, MK	Finite element collapse analysis of structural members considering imperfections and stresses due to fabrication. (Dr.Ing. Thesis)
UR-79-05	Ivar J. Fylling, MK	Analysis of towline forces in ocean towing systems. (Dr.Ing. Thesis)
UR-80-06	Nils Sandsmark, MM	Analysis of Stationary and Transient Heat Conduction by the Use of the Finite Element Method. (Dr.Ing. Thesis)
UR-80-09	Sverre Haver, MK	Analysis of uncertainties related to the stochastic modeling of ocean waves. (Dr.Ing. Thesis)
UR-81-15	Odland, Jonas	On the Strength of welded Ring stiffened cylindrical Shells primarily subjected to axial Compression
UR-82-17	Engesvik, Knut	Analysis of Uncertainties in the fatigue Capacity of

		Welded Joints
UR-82-18	Rye, Henrik	Ocean wave groups
UR-83-30	Eide, Oddvar Inge	On Cumulative Fatigue Damage in Steel Welded Joints
UR-83-33	Mo, Olav	Stochastic Time Domain Analysis of Slender Offshore Structures
UR-83-34	Amdahl, Jørgen	Energy absorption in Ship-platform impacts
UR-84-37	Mørch, Morten	Motions and mooring forces of semi submersibles as determined by full-scale measurements and theoretical analysis
UR-84-38	Soares, C. Guedes	Probabilistic models for load effects in ship structures
UR-84-39	Aarsnes, Jan V.	Current forces on ships
UR-84-40	Czujko, Jerzy	Collapse Analysis of Plates subjected to Biaxial Compression and Lateral Load
UR-85-46	Alf G. Engseth, MK	Finite element collapse analysis of tubular steel offshore structures. (Dr.Ing. Thesis)
UR-86-47	Dengody Sheshappa, MP	A Computer Design Model for Optimizing Fishing Vessel Designs Based on Techno-Economic Analysis. (Dr.Ing. Thesis)
UR-86-48	Vidar Aanesland, MH	A Theoretical and Numerical Study of Ship Wave Resistance. (Dr.Ing. Thesis)
UR-86-49	Heinz-Joachim Wessel, MK	Fracture Mechanics Analysis of Crack Growth in Plate Girders. (Dr.Ing. Thesis)
UR-86-50	Jon Taby, MK	Ultimate and Post-ultimate Strength of Dented Tubular Members. (Dr.Ing. Thesis)
UR-86-51	Walter Lian, MH	A Numerical Study of Two-Dimensional Separated Flow Past Bluff Bodies at Moderate KC-Numbers. (Dr.Ing. Thesis)
UR-86-52	Bjørn Sortland, MH	Force Measurements in Oscillating Flow on Ship Sections and Circular Cylinders in a U-Tube Water Tank. (Dr.Ing. Thesis)
UR-86-53	Kurt Strand, MM	A System Dynamic Approach to One-dimensional Fluid Flow. (Dr.Ing. Thesis)
UR-86-54	Arne Edvin Løken, MH	Three Dimensional Second Order Hydrodynamic Effects on Ocean Structures in Waves. (Dr.Ing. Thesis)
UR-86-55	Sigurd Falch, MH	A Numerical Study of Slamming of Two-Dimensional Bodies. (Dr.Ing. Thesis)
UR-87-56	Arne Braathen, MH	Application of a Vortex Tracking Method to the Prediction of Roll Damping of a Two-Dimension Floating Body. (Dr.Ing. Thesis)

UR-87-57	Bernt Leira, MK	Gaussian Vector Processes for Reliability Analysis involving Wave-Induced Load Effects. (Dr.Ing. Thesis)
UR-87-58	Magnus Småvik, MM	Thermal Load and Process Characteristics in a Two-Stroke Diesel Engine with Thermal Barriers (in Norwegian). (Dr.Ing. Thesis)
MTA-88-59	Bernt Arild Bremdal, MP	An Investigation of Marine Installation Processes – A Knowledge - Based Planning Approach. (Dr.Ing. Thesis)
MTA-88-60	Xu Jun, MK	Non-linear Dynamic Analysis of Space-framed Offshore Structures. (Dr.Ing. Thesis)
MTA-89-61	Gang Miao, MH	Hydrodynamic Forces and Dynamic Responses of Circular Cylinders in Wave Zones. (Dr.Ing. Thesis)
MTA-89-62	Martin Greenhow, MH	Linear and Non-Linear Studies of Waves and Floating Bodies. Part I and Part II. (Dr.Techn. Thesis)
MTA-89-63	Chang Li, MH	Force Coefficients of Spheres and Cubes in Oscillatory Flow with and without Current. (Dr.Ing. Thesis
MTA-89-64	Hu Ying, MP	A Study of Marketing and Design in Development of Marine Transport Systems. (Dr.Ing. Thesis)
MTA-89-65	Arild Jæger, MH	Seakeeping, Dynamic Stability and Performance of a Wedge Shaped Planing Hull. (Dr.Ing. Thesis)
MTA-89-66	Chan Siu Hung, MM	The dynamic characteristics of tilting-pad bearings
MTA-89-67	Kim Wikstrøm, MP	Analysis av projekteringen for ett offshore projekt. (Licenciat-avhandling)
MTA-89-68	Jiao Guoyang, MK	Reliability Analysis of Crack Growth under Random Loading, considering Model Updating. (Dr.Ing. Thesis)
MTA-89-69	Arnt Olufsen, MK	Uncertainty and Reliability Analysis of Fixed Offshore Structures. (Dr.Ing. Thesis)
MTA-89-70	Wu Yu-Lin, MR	System Reliability Analyses of Offshore Structures using improved Truss and Beam Models. (Dr.Ing. Thesis)
MTA-90-71	Jan Roger Hoff, MH	Three-dimensional Green function of a vessel with forward speed in waves. (Dr.Ing. Thesis)
MTA-90-72	Rong Zhao, MH	Slow-Drift Motions of a Moored Two-Dimensional Body in Irregular Waves. (Dr.Ing. Thesis)
MTA-90-73	Atle Minsaas, MP	Economical Risk Analysis. (Dr.Ing. Thesis)
MTA-90-74	Knut-Aril Farnes, MK	Long-term Statistics of Response in Non-linear Marine Structures. (Dr.Ing. Thesis)
MTA-90-75	Torbjørn Sotberg, MK	Application of Reliability Methods for Safety Assessment of Submarine Pipelines. (Dr.Ing.

		Thesis)
MTA-90-76	Zeuthen, Steffen, MP	SEAMAID. A computational model of the design process in a constraint-based logic programming environment. An example from the offshore domain. (Dr.Ing. Thesis)
MTA-91-77	Haagensen, Sven, MM	Fuel Dependant Cyclic Variability in a Spark Ignition Engine - An Optical Approach. (Dr.Ing. Thesis)
MTA-91-78	Løland, Geir, MH	Current forces on and flow through fish farms. (Dr.Ing. Thesis)
MTA-91-79	Hoen, Christopher, MK	System Identification of Structures Excited by Stochastic Load Processes. (Dr.Ing. Thesis)
MTA-91-80	Haugen, Stein, MK	Probabilistic Evaluation of Frequency of Collision between Ships and Offshore Platforms. (Dr.Ing. Thesis)
MTA-91-81	Sødahl, Nils, MK	Methods for Design and Analysis of Flexible Risers. (Dr.Ing. Thesis)
MTA-91-82	Ormberg, Harald, MK	Non-linear Response Analysis of Floating Fish Farm Systems. (Dr.Ing. Thesis)
MTA-91-83	Marley, Mark J., MK	Time Variant Reliability under Fatigue Degradation. (Dr.Ing. Thesis)
MTA-91-84	Krokstad, Jørgen R., MH	Second-order Loads in Multidirectional Seas. (Dr.Ing. Thesis)
MTA-91-85	Molteberg, Gunnar A., MM	The Application of System Identification Techniques to Performance Monitoring of Four Stroke Turbocharged Diesel Engines. (Dr.Ing. Thesis)
MTA-92-86	Mørch, Hans Jørgen Bjelke, MH	Aspects of Hydrofoil Design: with Emphasis on Hydrofoil Interaction in Calm Water. (Dr.Ing. Thesis)
MTA-92-87	Chan Siu Hung, MM	Nonlinear Analysis of Rotordynamic Instabilities in Highspeed Turbomachinery. (Dr.Ing. Thesis)
MTA-92-88	Bessason, Bjarni, MK	Assessment of Earthquake Loading and Response of Seismically Isolated Bridges. (Dr.Ing. Thesis)
MTA-92-89	Langli, Geir, MP	Improving Operational Safety through exploitation of Design Knowledge - an investigation of offshore platform safety. (Dr.Ing. Thesis)
MTA-92-90	Sævik, Svein, MK	On Stresses and Fatigue in Flexible Pipes. (Dr.Ing. Thesis)
MTA-92-91	Ask, Tor Ø., MM	Ignition and Flame Growth in Lean Gas-Air Mixtures. An Experimental Study with a Schlieren System. (Dr.Ing. Thesis)
MTA-86-92	Hessen, Gunnar, MK	Fracture Mechanics Analysis of Stiffened Tubular Members. (Dr.Ing. Thesis)

MTA-93-93	Steinebach, Christian, MM	Knowledge Based Systems for Diagnosis of Rotating Machinery. (Dr.Ing. Thesis)
MTA-93-94	Dalane, Jan Inge, MK	System Reliability in Design and Maintenance of Fixed Offshore Structures. (Dr.Ing. Thesis)
MTA-93-95	Steen, Sverre, MH	Cobblestone Effect on SES. (Dr.Ing. Thesis)
MTA-93-96	Karunakaran, Daniel, MK	Nonlinear Dynamic Response and Reliability Analysis of Drag-dominated Offshore Platforms. (Dr.Ing. Thesis)
MTA-93-97	Hagen, Arnulf, MP	The Framework of a Design Process Language. (Dr.Ing. Thesis)
MTA-93-98	Nordrik, Rune, MM	Investigation of Spark Ignition and Autoignition in Methane and Air Using Computational Fluid Dynamics and Chemical Reaction Kinetics. A Numerical Study of Ignition Processes in Internal Combustion Engines. (Dr.Ing. Thesis)
MTA-94-99	Passano, Elizabeth, MK	Efficient Analysis of Nonlinear Slender Marine Structures. (Dr.Ing. Thesis)
MTA-94-100	Kvålsvold, Jan, MH	Hydroelastic Modelling of Wetdeck Slamming on Multihull Vessels. (Dr.Ing. Thesis)
MTA-94-102	Bech, Sidsel M., MK	Experimental and Numerical Determination of Stiffness and Strength of GRP/PVC Sandwich Structures. (Dr.Ing. Thesis)
MTA-95-103	Paulsen, Hallvard, MM	A Study of Transient Jet and Spray using a Schlieren Method and Digital Image Processing. (Dr.Ing. Thesis)
MTA-95-104	Hovde, Geir Olav, MK	Fatigue and Overload Reliability of Offshore Structural Systems, Considering the Effect of Inspection and Repair. (Dr.Ing. Thesis)
MTA-95-105	Wang, Xiaozhi, MK	Reliability Analysis of Production Ships with Emphasis on Load Combination and Ultimate Strength. (Dr.Ing. Thesis)
MTA-95-106	Ulstein, Tore, MH	Nonlinear Effects of a Flexible Stern Seal Bag on Cobblestone Oscillations of an SES. (Dr.Ing. Thesis)
MTA-95-107	Solaas, Frøydis, MH	Analytical and Numerical Studies of Sloshing in Tanks. (Dr.Ing. Thesis)
MTA-95-108	Hellan, Øyvind, MK	Nonlinear Pushover and Cyclic Analyses in Ultimate Limit State Design and Reassessment of Tubular Steel Offshore Structures. (Dr.Ing. Thesis)
MTA-95-109	Hermundstad, Ole A., MK	Theoretical and Experimental Hydroelastic Analysis of High Speed Vessels. (Dr.Ing. Thesis)
MTA-96-110	Bratland, Anne K., MH	Wave-Current Interaction Effects on Large-Volume Bodies in Water of Finite Depth. (Dr.Ing. Thesis)
MTA-96-111	Herfjord, Kjell, MH	A Study of Two-dimensional Separated Flow by a Combination of the Finite Element Method and

		Navier-Stokes Equations. (Dr.Ing. Thesis)
MTA-96-112	Æsøy, Vilmar, MM	Hot Surface Assisted Compression Ignition in a Direct Injection Natural Gas Engine. (Dr.Ing. Thesis)
MTA-96-113	Eknes, Monika L., MK	Escalation Scenarios Initiated by Gas Explosions on Offshore Installations. (Dr.Ing. Thesis)
MTA-96-114	Erikstad, Stein O., MP	A Decision Support Model for Preliminary Ship Design. (Dr.Ing. Thesis)
MTA-96-115	Pedersen, Egil, MH	A Nautical Study of Towed Marine Seismic Streamer Cable Configurations. (Dr.Ing. Thesis)
MTA-97-116	Moksnes, Paul O., MM	Modelling Two-Phase Thermo-Fluid Systems Using Bond Graphs. (Dr.Ing. Thesis)
MTA-97-117	Halse, Karl H., MK	On Vortex Shedding and Prediction of Vortex-Induced Vibrations of Circular Cylinders. (Dr.Ing. Thesis)
MTA-97-118	Igland, Ragnar T., MK	Reliability Analysis of Pipelines during Laying, considering Ultimate Strength under Combined Loads. (Dr.Ing. Thesis)
MTA-97-119	Pedersen, Hans-P., MP	Levendefiskteknologi for fiskefartøy. (Dr.Ing. Thesis)
MTA-98-120	Vikestad, Kyrre, MK	Multi-Frequency Response of a Cylinder Subjected to Vortex Shedding and Support Motions. (Dr.Ing. Thesis)
MTA-98-121	Azadi, Mohammad R. E., MK	Analysis of Static and Dynamic Pile-Soil-Jacket Behaviour. (Dr.Ing. Thesis)
MTA-98-122	Ulltang, Terje, MP	A Communication Model for Product Information. (Dr.Ing. Thesis)
MTA-98-123	Torbergsen, Erik, MM	Impeller/Diffuser Interaction Forces in Centrifugal Pumps. (Dr.Ing. Thesis)
MTA-98-124	Hansen, Edmond, MH	A Discrete Element Model to Study Marginal Ice Zone Dynamics and the Behaviour of Vessels Moored in Broken Ice. (Dr.Ing. Thesis)
MTA-98-125	Videiro, Paulo M., MK	Reliability Based Design of Marine Structures. (Dr.Ing. Thesis)
MTA-99-126	Mainçon, Philippe, MK	Fatigue Reliability of Long Welds Application to Titanium Risers. (Dr.Ing. Thesis)
MTA-99-127	Haugen, Elin M., MH	Hydroelastic Analysis of Slamming on Stiffened Plates with Application to Catamaran Wetdecks. (Dr.Ing. Thesis)
MTA-99-128	Langhelle, Nina K., MK	Experimental Validation and Calibration of Nonlinear Finite Element Models for Use in Design of Aluminium Structures Exposed to Fire. (Dr.Ing. Thesis)
MTA-99-	Berstad, Are J., MK	Calculation of Fatigue Damage in Ship Structures.

129		(Dr.Ing. Thesis)
MTA-99-130	Andersen, Trond M., MM	Short Term Maintenance Planning. (Dr.Ing. Thesis)
MTA-99-131	Tveiten, Bård Wathne, MK	Fatigue Assessment of Welded Aluminium Ship Details. (Dr.Ing. Thesis)
MTA-99-132	Søreide, Fredrik, MP	Applications of underwater technology in deep water archaeology. Principles and practice. (Dr.Ing. Thesis)
MTA-99-133	Tønnessen, Rune, MH	A Finite Element Method Applied to Unsteady Viscous Flow Around 2D Blunt Bodies With Sharp Corners. (Dr.Ing. Thesis)
MTA-99-134	Elvekrok, Dag R., MP	Engineering Integration in Field Development Projects in the Norwegian Oil and Gas Industry. The Supplier Management of Norne. (Dr.Ing. Thesis)
MTA-99-135	Fagerholt, Kjetil, MP	Optimeringsbaserte Metoder for Ruteplanlegging innen skipsfart. (Dr.Ing. Thesis)
MTA-99-136	Bysveen, Marie, MM	Visualization in Two Directions on a Dynamic Combustion Rig for Studies of Fuel Quality. (Dr.Ing. Thesis)
MTA-2000-137	Storteig, Eskild, MM	Dynamic characteristics and leakage performance of liquid annular seals in centrifugal pumps. (Dr.Ing. Thesis)
MTA-2000-138	Sagli, Gro, MK	Model uncertainty and simplified estimates of long term extremes of hull girder loads in ships. (Dr.Ing. Thesis)
MTA-2000-139	Tronstad, Harald, MK	Nonlinear analysis and design of cable net structures like fishing gear based on the finite element method. (Dr.Ing. Thesis)
MTA-2000-140	Kroneberg, André, MP	Innovation in shipping by using scenarios. (Dr.Ing. Thesis)
MTA-2000-141	Haslum, Herbjørn Alf, MH	Simplified methods applied to nonlinear motion of spar platforms. (Dr.Ing. Thesis)
MTA-2001-142	Samdal, Ole Johan, MM	Modelling of Degradation Mechanisms and Stressor Interaction on Static Mechanical Equipment Residual Lifetime. (Dr.Ing. Thesis)
MTA-2001-143	Baarholm, Rolf Jarle, MH	Theoretical and experimental studies of wave impact underneath decks of offshore platforms. (Dr.Ing. Thesis)
MTA-2001-144	Wang, Lihua, MK	Probabilistic Analysis of Nonlinear Wave-induced Loads on Ships. (Dr.Ing. Thesis)
MTA-2001-145	Kristensen, Odd H. Holt, MK	Ultimate Capacity of Aluminium Plates under Multiple Loads, Considering HAZ Properties. (Dr.Ing. Thesis)
MTA-2001-146	Greco, Marilena, MH	A Two-Dimensional Study of Green-Water

		Loading. (Dr.Ing. Thesis)
MTA-2001-147	Heggelund, Svein E., MK	Calculation of Global Design Loads and Load Effects in Large High Speed Catamarans. (Dr.Ing. Thesis)
MTA-2001-148	Babalola, Olusegun T., MK	Fatigue Strength of Titanium Risers – Defect Sensitivity. (Dr.Ing. Thesis)
MTA-2001-149	Mohammed, Abuu K., MK	Nonlinear Shell Finite Elements for Ultimate Strength and Collapse Analysis of Ship Structures. (Dr.Ing. Thesis)
MTA-2002-150	Holmedal, Lars E., MH	Wave-current interactions in the vicinity of the sea bed. (Dr.Ing. Thesis)
MTA-2002-151	Rognebakke, Olav F., MH	Sloshing in rectangular tanks and interaction with ship motions. (Dr.Ing. Thesis)
MTA-2002-152	Lader, Pål Furset, MH	Geometry and Kinematics of Breaking Waves. (Dr.Ing. Thesis)
MTA-2002-153	Yang, Qinzheng, MH	Wash and wave resistance of ships in finite water depth. (Dr.Ing. Thesis)
MTA-2002-154	Melhus, Øyvin, MM	Utilization of VOC in Diesel Engines. Ignition and combustion of VOC released by crude oil tankers. (Dr.Ing. Thesis)
MTA-2002-155	Ronæss, Marit, MH	Wave Induced Motions of Two Ships Advancing on Parallel Course. (Dr.Ing. Thesis)
MTA-2002-156	Økland, Ole D., MK	Numerical and experimental investigation of whipping in twin hull vessels exposed to severe wet deck slamming. (Dr.Ing. Thesis)
MTA-2002-157	Ge, Chunhua, MK	Global Hydroelastic Response of Catamarans due to Wet Deck Slamming. (Dr.Ing. Thesis)
MTA-2002-158	Byklum, Eirik, MK	Nonlinear Shell Finite Elements for Ultimate Strength and Collapse Analysis of Ship Structures. (Dr.Ing. Thesis)
IMT-2003-1	Chen, Haibo, MK	Probabilistic Evaluation of FPSO-Tanker Collision in Tandem Offloading Operation. (Dr.Ing. Thesis)
IMT-2003-2	Skaugset, Kjetil Bjørn, MK	On the Suppression of Vortex Induced Vibrations of Circular Cylinders by Radial Water Jets. (Dr.Ing. Thesis)
IMT-2003-3	Chezhian, Muthu	Three-Dimensional Analysis of Slamming. (Dr.Ing. Thesis)
IMT-2003-4	Buhaug, Øyvind	Deposit Formation on Cylinder Liner Surfaces in Medium Speed Engines. (Dr.Ing. Thesis)
IMT-2003-5	Tregde, Vidar	Aspects of Ship Design: Optimization of Aft Hull with Inverse Geometry Design. (Dr.Ing. Thesis)
IMT-	Wist, Hanne Therese	Statistical Properties of Successive Ocean Wave

2003-6		Parameters. (Dr.Ing. Thesis)
IMT-2004-7	Ransau, Samuel	Numerical Methods for Flows with Evolving Interfaces. (Dr.Ing. Thesis)
IMT-2004-8	Soma, Torkel	Blue-Chip or Sub-Standard. A data interrogation approach of identity safety characteristics of shipping organization. (Dr.Ing. Thesis)
IMT-2004-9	Ersdal, Svein	An experimental study of hydrodynamic forces on cylinders and cables in near axial flow. (Dr.Ing. Thesis)
IMT-2005-10	Brodtkorb, Per Andreas	The Probability of Occurrence of Dangerous Wave Situations at Sea. (Dr.Ing. Thesis)
IMT-2005-11	Yttervik, Rune	Ocean current variability in relation to offshore engineering. (Dr.Ing. Thesis)
IMT-2005-12	Fredheim, Arne	Current Forces on Net-Structures. (Dr.Ing. Thesis)
IMT-2005-13	Heggernes, Kjetil	Flow around marine structures. (Dr.Ing. Thesis
IMT-2005-14	Fouques, Sebastien	Lagrangian Modelling of Ocean Surface Waves and Synthetic Aperture Radar Wave Measurements. (Dr.Ing. Thesis)
IMT-2006-15	Holm, Håvard	Numerical calculation of viscous free surface flow around marine structures. (Dr.Ing. Thesis)
IMT-2006-16	Bjørheim, Lars G.	Failure Assessment of Long Through Thickness Fatigue Cracks in Ship Hulls. (Dr.Ing. Thesis)
IMT-2006-17	Hansson, Lisbeth	Safety Management for Prevention of Occupational Accidents. (Dr.Ing. Thesis)
IMT-2006-18	Zhu, Xinying	Application of the CIP Method to Strongly Nonlinear Wave-Body Interaction Problems. (Dr.Ing. Thesis)
IMT-2006-19	Reite, Karl Johan	Modelling and Control of Trawl Systems. (Dr.Ing. Thesis)
IMT-2006-20	Smogeli, Øyvind Notland	Control of Marine Propellers. From Normal to Extreme Conditions. (Dr.Ing. Thesis)
IMT-2007-21	Storhaug, Gaute	Experimental Investigation of Wave Induced Vibrations and Their Effect on the Fatigue Loading of Ships. (Dr.Ing. Thesis)
IMT-2007-22	Sun, Hui	A Boundary Element Method Applied to Strongly Nonlinear Wave-Body Interaction Problems. (PhD Thesis, CeSOS)
IMT-2007-23	Rustad, Anne Marthine	Modelling and Control of Top Tensioned Risers. (PhD Thesis, CeSOS)
IMT-2007-24	Johansen, Vegar	Modelling flexible slender system for real-time simulations and control applications
IMT-2007-25	Wroldsen, Anders Sunde	Modelling and control of tensegrity structures.

		(PhD Thesis, CeSOS)
IMT-2007-26	Aronsen, Kristoffer Høye	An experimental investigation of in-line and combined inline and cross flow vortex induced vibrations. (Dr. avhandling, IMT)
IMT-2007-27	Gao, Zhen	Stochastic Response Analysis of Mooring Systems with Emphasis on Frequency-domain Analysis of Fatigue due to Wide-band Response Processes (PhD Thesis, CeSOS)
IMT-2007-28	Thorstensen, Tom Anders	Lifetime Profit Modelling of Ageing Systems Utilizing Information about Technical Condition. (Dr.ing. thesis, IMT)
IMT-2008-29	Refsnes, Jon Erling Gorset	Nonlinear Model-Based Control of Slender Body AUVs (PhD Thesis, IMT)
IMT-2008-30	Berntsen, Per Ivar B.	Structural Reliability Based Position Mooring. (PhD-Thesis, IMT)
IMT-2008-31	Ye, Naiquan	Fatigue Assessment of Aluminium Welded Box-stiffener Joints in Ships (Dr.ing. thesis, IMT)
IMT-2008-32	Radan, Damir	Integrated Control of Marine Electrical Power Systems. (PhD-Thesis, IMT)
IMT-2008-33	Thomassen, Paul	Methods for Dynamic Response Analysis and Fatigue Life Estimation of Floating Fish Cages. (Dr.ing. thesis, IMT)
IMT-2008-34	Pákozdi, Csaba	A Smoothed Particle Hydrodynamics Study of Two-dimensional Nonlinear Sloshing in Rectangular Tanks. (Dr.ing.thesis, IMT/ CeSOS)
IMT-2007-35	Grytøyr, Guttorm	A Higher-Order Boundary Element Method and Applications to Marine Hydrodynamics. (Dr.ing.thesis, IMT)
IMT-2008-36	Drummen, Ingo	Experimental and Numerical Investigation of Nonlinear Wave-Induced Load Effects in Containerships considering Hydroelasticity. (PhD thesis, CeSOS)
IMT-2008-37	Skejic, Renato	Maneuvering and Seakeeping of a Singel Ship and of Two Ships in Interaction. (PhD-Thesis, CeSOS)
IMT-2008-38	Harlem, Alf	An Age-Based Replacement Model for Repairable Systems with Attention to High-Speed Marine Diesel Engines. (PhD-Thesis, IMT)
IMT-2008-39	Alsos, Hagbart S.	Ship Grounding. Analysis of Ductile Fracture, Bottom Damage and Hull Girder Response. (PhD-thesis, IMT)
IMT-2008-40	Graczyk, Mateusz	Experimental Investigation of Sloshing Loading and Load Effects in Membrane LNG Tanks Subjected to Random Excitation. (PhD-thesis, CeSOS)
IMT-2008-41	Taghipour, Reza	Efficient Prediction of Dynamic Response for Flexible amd Multi-body Marine Structures. (PhD-

		thesis, CeSOS)
IMT-2008-42	Ruth, Eivind	Propulsion control and thrust allocation on marine vessels. (PhD thesis, CeSOS)
IMT-2008-43	Nystad, Bent Helge	Technical Condition Indexes and Remaining Useful Life of Aggregated Systems. PhD thesis, IMT
IMT-2008-44	Soni, Prashant Kumar	Hydrodynamic Coefficients for Vortex Induced Vibrations of Flexible Beams, PhD thesis, CeSOS
IMT-2009-45	Amlashi, Hadi K.K.	Ultimate Strength and Reliability-based Design of Ship Hulls with Emphasis on Combined Global and Local Loads. PhD Thesis, IMT
IMT-2009-46	Pedersen, Tom Arne	Bond Graph Modelling of Marine Power Systems. PhD Thesis, IMT
IMT-2009-47	Kristiansen, Trygve	Two-Dimensional Numerical and Experimental Studies of Piston-Mode Resonance. PhD-Thesis, CeSOS
IMT-2009-48	Ong, Muk Chen	Applications of a Standard High Reynolds Number Model and a Stochastic Scour Prediction Model for Marine Structures. PhD-thesis, IMT
IMT-2009-49	Hong, Lin	Simplified Analysis and Design of Ships subjected to Collision and Grounding. PhD-thesis, IMT
IMT-2009-50	Koushan, Kamran	Vortex Induced Vibrations of Free Span Pipelines, PhD thesis, IMT
IMT-2009-51	Korsvik, Jarl Eirik	Heuristic Methods for Ship Routing and Scheduling. PhD-thesis, IMT
IMT-2009-52	Lee, Jihoon	Experimental Investigation and Numerical in Analyzing the Ocean Current Displacement of Longlines. Ph.d.-Thesis, IMT.
IMT-2009-53	Vestbøstad, Tone Gran	A Numerical Study of Wave-in-Deck Impact usin a Two-Dimensional Constrained Interpolation Profile Method, Ph.d.thesis, CeSOS.
IMT-2009-54	Bruun, Kristine	Bond Graph Modelling of Fuel Cells for Marine Power Plants. Ph.d.-thesis, IMT
IMT 2009-55	Holstad, Anders	Numerical Investigation of Turbulence in a Sekwed Three-Dimensional Channel Flow, Ph.d.-thesis, IMT.
IMT 2009-56	Ayala-Uraga, Efren	Reliability-Based Assessment of Deteriorating Ship-shaped Offshore Structures, Ph.d.-thesis, IMT
IMT 2009-57	Kong, Xiangjun	A Numerical Study of a Damaged Ship in Beam Sea Waves. Ph.d.-thesis, IMT/CeSOS.
IMT 2010-58	Kristiansen, David	Wave Induced Effects on Floaters of Aquaculture Plants, Ph.d.-thesis, CeSOS.

IMT 2010-59	Ludvigsen, Martin	An ROV-Toolbox for Optical and Acoustic Scientific Seabed Investigation. Ph.d.-thesis IMT.
IMT 2010-60	Hals, Jørgen	Modelling and Phase Control of Wave-Energy Converters. Ph.d.thesis, CeSOS.
IMT 2010- 61	Shu, Zhi	Uncertainty Assessment of Wave Loads and Ultimate Strength of Tankers and Bulk Carriers in a Reliability Framework. Ph.d. Thesis, IMT/ CeSOS
IMT 2010-62	Shao, Yanlin	Numerical Potential-Flow Studies on Weakly-Nonlinear Wave-Body Interactions with/without Small Forward Speed, Ph.d.thesis,CeSOS.
IMT 2010-63	Califano, Andrea	Dynamic Loads on Marine Propellers due to Intermittent Ventilation. Ph.d.thesis, IMT.
IMT 2010-64	El Khoury, George	Numerical Simulations of Massively Separated Turbulent Flows, Ph.d.-thesis, IMT
IMT 2010-65	Seim, Knut Sponheim	Mixing Process in Dense Overflows with Emphasis on the Faroe Bank Channel Overflow. Ph.d.thesis, IMT
IMT 2010-66	Jia, Huirong	Structural Analysis of Intect and Damaged Ships in a Collission Risk Analysis Perspective. Ph.d.thesis CeSoS.
IMT 2010-67	Jiao, Linlin	Wave-Induced Effects on a Pontoon-type Very Large Floating Structures (VLFS). Ph.D.-thesis, CeSOS.
IMT 2010-68	Abrahamsen, Bjørn Christian	Sloshing Induced Tank Roof with Entrapped Air Pocket. Ph.d.thesis, CeSOS.
IMT 2011-69	Karimirad, Madjid	Stochastic Dynamic Response Analysis of Spar-Type Wind Turbines with Catenary or Taut Mooring Systems. Ph.d.-thesis, CeSOS.
IMT - 2011-70	Erlend Meland	Condition Monitoring of Safety Critical Valves. Ph.d.-thesis, IMT.
IMT – 2011-71	Yang, Limin	Stochastic Dynamic System Analysis of Wave Energy Converter with Hydraulic Power Take-Off, with Particular Reference to Wear Damage Analysis, Ph.d. Thesis, CeSOS.
IMT – 2011-72	Visscher, Jan	Application of Particla Image Velocimetry on Turbulent Marine Flows, Ph.d.Thesis, IMT.
IMT – 2011-73	Su, Biao	Numerical Predictions of Global and Local Ice Loads on Ships. Ph.d.Thesis, CeSOS.
IMT – 2011-74	Liu, Zhenhui	Analytical and Numerical Analysis of Iceberg Collision with Ship Structures. Ph.d.Thesis, IMT.
IMT – 2011-75	Aarsæther, Karl Gunnar	Modeling and Analysis of Ship Traffic by Observation and Numerical Simulation. Ph.d.Thesis, IMT.

Imt – 2011-76	Wu, Jie	Hydrodynamic Force Identification from Stochastic Vortex Induced Vibration Experiments with Slender Beams. Ph.d.Thesis, IMT.
Imt – 2011-77	Amini, Hamid	Azimuth Propulsors in Off-design Conditions. Ph.d.Thesis, IMT.
IMT – 2011-78	Nguyen, Tan-Hoi	Toward a System of Real-Time Prediction and Monitoring of Bottom Damage Conditions During Ship Grounding. Ph.d.thesis, IMT.
IMT-2011-79	Tavakoli, Mohammad T.	Assessment of Oil Spill in Ship Collision and Grounding, Ph.d.thesis, IMT.
IMT-2011-80	Guo, Bingjie	Numerical and Experimental Investigation of Added Resistance in Waves. Ph.d.Thesis, IMT.
IMT-2011-81	Chen, Qiaofeng	Ultimate Strength of Aluminium Panels, considering HAZ Effects, IMT
IMT-2012-82	Kota, Ravikiran S.	Wave Loads on Decks of Offshore Structures in Random Seas, CeSOS.
IMT-2012-83	Sten, Ronny	Dynamic Simulation of Deep Water Drilling Risers with Heave Compensating System, IMT.
IMT-2012-84	Berle, Øyvind	Risk and resilience in global maritime supply chains, IMT.
IMT-2012-85	Fang, Shaoji	Fault Tolerant Position Mooring Control Based on Structural Reliability, CeSOS.
IMT-2012-86	You, Jikun	Numerical studies on wave forces and moored ship motions in intermediate and shallow water, CeSOS.
IMT-2012-87	Xiang ,Xu	Maneuvering of two interacting ships in waves, CeSOS
IMT-2012-88	Dong, Wenbin	Time-domain fatigue response and reliability analysis of offshore wind turbines with emphasis on welded tubular joints and gear components, CeSOS
IMT-2012-89	Zhu, Suji	Investigation of Wave-Induced Nonlinear Load Effects in Open Ships considering Hull Girder Vibrations in Bending and Torsion, CeSOS
IMT-2012-90	Zhou, Li	Numerical and Experimental Investigation of Station-keeping in Level Ice, CeSOS
IMT-2012-91	Ushakov, Sergey	Particulate matter emission characteristics from diesel enignes operating on conventional and alternative marine fuels, IMT
IMT-2013-1	Yin, Decao	Experimental and Numerical Analysis of Combined In-line and Cross-flow Vortex Induced Vibrations, CeSOS

IMT-2013-2	Kurniawan, Adi	Modelling and geometry optimisation of wave energy converters, CeSOS
IMT-2013-3	Al Ryati, Nabil	Technical condition indexes doe auxiliary marine diesel engines, IMT
IMT-2013-4	Firoozkoohi, Reza	Experimental, numerical and analytical investigation of the effect of screens on sloshing, CeSOS
IMT-2013-5	Ommani, Babak	Potential-Flow Predictions of a Semi-Displacement Vessel Including Applications to Calm Water Broaching, CeSOS
IMT-2013-6	Xing, Yihan	Modelling and analysis of the gearbox in a floating spar-type wind turbine, CeSOS
IMT-7-2013	Balland, Océane	Optimization models for reducing air emissions from ships, IMT
IMT-8-2013	Yang, Dan	Transitional wake flow behind an inclined flat plate-----Computation and analysis, IMT
IMT-9-2013	Abdillah, Suyuthi	Prediction of Extreme Loads and Fatigue Damage for a Ship Hull due to Ice Action, IMT
IMT-10-2013	Ramìrez, Pedro Agustìn Pèrez	Ageing management and life extension of technical systems- Concepts and methods applied to oil and gas facilities, IMT
IMT-11-2013	Chuang, Zhenju	Experimental and Numerical Investigation of Speed Loss due to Seakeeping and Maneuvering. IMT
IMT-12-2013	Etemaddar, Mahmoud	Load and Response Analysis of Wind Turbines under Atmospheric Icing and Controller System Faults with Emphasis on Spar Type Floating Wind Turbines, IMT
IMT-13-2013	Lindstad, Haakon	Strategies and measures for reducing maritime CO2 emissons, IMT
IMT-14-2013	Haris, Sabril	Damage interaction analysis of ship collisions, IMT
IMT-15-2013	Shainee, Mohamed	Conceptual Design, Numerical and Experimental Investigation of a SPM Cage Concept for Offshore Mariculture, IMT
IMT-16-2013	Gansel, Lars	Flow past porous cylinders and effects of biofouling and fish behavior on the flow in and around Atlantic salmon net cages, IMT
IMT-17-2013	Gaspar, Henrique	Handling Aspects of Complexity in Conceptual Ship Design, IMT
IMT-18-2013	Thys, Maxime	Theoretical and Experimental Investigation of a Free Running Fishing Vessel at Small Frequency of Encounter, CeSOS
IMT-19-2013	Aglen, Ida	VIV in Free Spanning Pipelines, CeSOS

IMT-1-2014	Song, An	Theoretical and experimental studies of wave diffraction and radiation loads on a horizontally submerged perforated plate, CeSOS
IMT-2-2014	Rogne, Øyvind Ygre	Numerical and Experimental Investigation of a Hinged 5-body Wave Energy Converter, CeSOS
IMT-3-2014	Dai, Lijuan	Safe and efficient operation and maintenance of offshore wind farms ,IMT
IMT-4-2014	Bachynski, Erin Elizabeth	Design and Dynamic Analysis of Tension Leg Platform Wind Turbines, CeSOS
IMT-5-2014	Wang, Jingbo	Water Entry of Freefall Wedged – Wedge motions and Cavity Dynamics, CeSOS
IMT-6-2014	Kim, Ekaterina	Experimental and numerical studies related to the coupled behavior of ice mass and steel structures during accidental collisions, IMT
IMT-7-2014	Tan, Xiang	Numerical investigation of ship's continuous- mode icebreaking in leverl ice, CeSOS
IMT-8-2014	Muliawan, Made Jaya	Design and Analysis of Combined Floating Wave and Wind Power Facilities, with Emphasis on Extreme Load Effects of the Mooring System, CeSOS
IMT-9-2014	Jiang, Zhiyu	Long-term response analysis of wind turbines with an emphasis on fault and shutdown conditions, IMT
IMT-10-2014	Dukan, Fredrik	ROV Motion Control Systems, IMT
IMT-11-2014	Grimsmo, Nils I.	Dynamic simulations of hydraulic cylinder for heave compensation of deep water drilling risers, IMT
IMT-12-2014	Kvittem, Marit I.	Modelling and response analysis for fatigue design of a semisubmersible wind turbine, CeSOS
IMT-13-2014	Akhtar, Juned	The Effects of Human Fatigue on Risk at Sea, IMT
IMT-14-2014	Syahroni, Nur	Fatigue Assessment of Welded Joints Taking into Account Effects of Residual Stress, IMT
IMT-1-2015	Bøckmann, Eirik	Wave Propulsion of ships, IMT
IMT-2-2015	Wang, Kai	Modelling and dynamic analysis of a semi-submersible floating vertical axis wind turbine, CeSOS
IMT-3-2015	Fredriksen, Arnt Gunvald	A numerical and experimental study of a two-dimensional body with moonpool in waves and current, CeSOS
IMT-4-2015	Jose Patricio Gallardo Canabes	Numerical studies of viscous flow around bluff bodies, IMT

IMT-5-2015	Vegard Longva	Formulation and application of finite element techniques for slender marine structures subjected to contact interactions, IMT
IMT-6-2015	Jacobus De Vaal	Aerodynamic modelling of floating wind turbines, CeSOS
IMT-7-2015	Fachri Nasution	Fatigue Performance of Copper Power Conductors, IMT
IMT-8-2015	Oleh I Karpa	Development of bivariate extreme value distributions for applications in marine technology,CeSOS
IMT-9-2015	Daniel de Almeida Fernandes	An output feedback motion control system for ROVs, AMOS
IMT-10-2015	Bo Zhao	Particle Filter for Fault Diagnosis: Application to Dynamic Positioning Vessel and Underwater Robotics, CeSOS
IMT-11-2015	Wenting Zhu	Impact of emission allocation in maritime transportation, IMT
IMT-12-2015	Amir Rasekhi Nejad	Dynamic Analysis and Design of Gearboxes in Offshore Wind Turbines in a Structural Reliability Perspective, CeSOS
IMT-13-2015	Arturo Jesùs Ortega Malca	Dynamic Response of Flexibles Risers due to Unsteady Slug Flow, CeSOS
IMT-14-2015	Dagfinn Husjord	Guidance and decision-support system for safe navigation of ships operating in close proximity, IMT
IMT-15-2015	Anirban Bhattacharyya	Ducted Propellers: Behaviour in Waves and Scale Effects, IMT
IMT-16-2015	Qin Zhang	Image Processing for Ice Parameter Identification in Ice Management, IMT
IMT-1-2016	Vincentius Rumawas	Human Factors in Ship Design and Operation: An Experiential Learning, IMT
IMT-2-2016	Martin Storheim	Structural response in ship-platform and ship-ice collisions, IMT
IMT-3-2016	Mia Abrahamsen Prsic	Numerical Simulations of the Flow around single and Tandem Circular Cylinders Close to a Plane Wall, IMT
IMT-4-2016	Tufan Arslan	Large-eddy simulations of cross-flow around ship sections, IMT

IMT-5-2016	Pierre Yves-Henry	Parametrisation of aquatic vegetation in hydraulic and coastal research,IMT
IMT-6-2016	Lin Li	Dynamic Analysis of the Instalation of Monopiles for Offshore Wind Turbines, CeSOS
IMT-7-2016	Øivind Kåre Kjerstad	Dynamic Positioning of Marine Vessels in Ice, IMT
IMT-8-2016	Xiaopeng Wu	Numerical Analysis of Anchor Handling and Fish Trawling Operations in a Safety Perspective, CeSOS
IMT-9-2016	Zhengshun Cheng	Integrated Dynamic Analysis of Floating Vertical Axis Wind Turbines, CeSOS
IMT-10-2016	Ling Wan	Experimental and Numerical Study of a Combined Offshore Wind and Wave Energy Converter Concept
IMT-11-2016	Wei Chai	Stochastic dynamic analysis and reliability evaluation of the roll motion for ships in random seas, CeSOS
IMT-12-2016	Øyvind Selnes Patricksson	Decision support for conceptual ship design with focus on a changing life cycle and future uncertainty, IMT
IMT-13-2016	Mats Jørgen Thorsen	Time domain analysis of vortex-induced vibrations, IMT
IMT-14-2016	Edgar McGuinness	Safety in the Norwegian Fishing Fleet – Analysis and measures for improvement, IMT
IMT-15-2016	Sepideh Jafarzadeh	Energy effiency and emission abatement in the fishing fleet, IMT
IMT-16-2016	Wilson Ivan Guachamin Acero	Assessment of marine operations for offshore wind turbine installation with emphasis on response-based operational limits, IMT
IMT-17-2016	Mauro Candeloro	Tools and Methods for Autonomous Operations on Seabed and Water Coumn using Underwater Vehicles, IMT
IMT-18-2016	Valentin Chabaud	Real-Time Hybrid Model Testing of Floating Wind Tubines, IMT
IMT-1-2017	Mohammad Saud Afzal	Three-dimensional streaming in a sea bed boundary layer
IMT-2-2017	Peng Li	A Theoretical and Experimental Study of Wave-induced Hydroelastic Response of a Circular Floating Collar
IMT-3-2017	Martin Bergström	A simulation-based design method for arctic maritime transport systems

IMT-4-2017	Bhushan Taskar	The effect of waves on marine propellers and propulsion
IMT-5-2017	Mohsen Bardestani	A two-dimensional numerical and experimental study of a floater with net and sinker tube in waves and current
IMT-6-2017	Fatemeh Hoseini Dadmarzi	Direct Numerical Simualtion of turbulent wakes behind different plate configurations
IMT-7-2017	Michel R. Miyazaki	Modeling and control of hybrid marine power plants
IMT-8-2017	Giri Rajasekhar Gunnu	Safety and effiency enhancement of anchor handling operations with particular emphasis on the stability of anchor handling vessels
IMT-9-2017	Kevin Koosup Yum	Transient Performance and Emissions of a Turbocharged Diesel Engine for Marine Power Plants
IMT-10-2017	Zhaolong Yu	Hydrodynamic and structural aspects of ship collisions
IMT-11-2017	Martin Hassel	Risk Analysis and Modelling of Allisions between Passing Vessels and Offshore Installations
IMT-12-2017	Astrid H. Brodtkorb	Hybrid Control of Marine Vessels – Dynamic Positioning in Varying Conditions
IMT-13-2017	Kjersti Bruserud	Simultaneous stochastic model of waves and current for prediction of structural design loads
IMT-14-2017	Finn-Idar Grøtta Giske	Long-Term Extreme Response Analysis of Marine Structures Using Inverse Reliability Methods
IMT-15-2017	Stian Skjong	Modeling and Simulation of Maritime Systems and Operations for Virtual Prototyping using co-Simulations
IMT-1-2018	Yingguang Chu	Virtual Prototyping for Marine Crane Design and Operations
IMT-2-2018	Sergey Gavrilin	Validation of ship manoeuvring simulation models
IMT-3-2018	Jeevith Hegde	Tools and methods to manage risk in autonomous subsea inspection,maintenance and repair operations
IMT-4-2018	Ida M. Strand	Sea Loads on Closed Flexible Fish Cages
IMT-5-2018	Erlend Kvinge Jørgensen	Navigation and Control of Underwater Robotic Vehicles

IMT-6-2018	Bård Stovner	Aided Intertial Navigation of Underwater Vehicles
IMT-7-2018	Erlend Liavåg Grotle	Thermodynamic Response Enhanced by Sloshing in Marine LNG Fuel Tanks
IMT-8-2018	Børge Rokseth	Safety and Verification of Advanced Maritime Vessels
IMT-9-2018	Jan Vidar Ulveseter	Advances in Semi-Empirical Time Domain Modelling of Vortex-Induced Vibrations
IMT-10-2018	Chenyu Luan	Design and analysis for a steel braceless semi-submersible hull for supporting a 5-MW horizontal axis wind turbine
IMT-11-2018	Carl Fredrik Rehn	Ship Design under Uncertainty
IMT-12-2018	Øyvind Ødegård	Towards Autonomous Operations and Systems in Marine Archaeology
IMT-13-2018	Stein Melvær Nornes	Guidance and Control of Marine Robotics for Ocean Mapping and Monitoring
IMT-14-2018	Petter Norgren	Autonomous Underwater Vehicles in Arctic Marine Operations: Arctic marine research and ice monitoring
IMT-15-2018	Minjoo Choi	Modular Adaptable Ship Design for Handling Uncertainty in the Future Operating Context
MT-16-2018	Ole Alexander Eidsvik	Dynamics of Remotely Operated Underwater Vehicle Systems
IMT-17-2018	Mahdi Ghane	Fault Diagnosis of Floating Wind Turbine Drivetrain- Methodologies and Applications
IMT-18-2018	Christoph Alexander Thieme	Risk Analysis and Modelling of Autonomous Marine Systems
IMT-19-2018	Yugao Shen	Operational limits for floating-collar fish farms in waves and current, without and with well-boat presence
IMT-20-2018	Tianjiao Dai	Investigations of shear interaction and stresses in flexible pipes and umbilicals
IMT-21-2018	Sigurd Solheim Pettersen	Resilience by Latent Capabilities in Marine Systems
IMT-22-2018	Thomas Sauder	Fidelity of cyber-physical empirical methods. Application to the active truncation of slender marine structures
IMT-23-2018	Jan-Tore Horn	Statistical and Modelling Uncertainties in the Design of Offshore Wind Turbines